

Dissertation

zur Erlangung des akademischen Grades Doktor der
Ingenieurwissenschaften (Dr.-Ing.) der Technischen Fakultät der
Christian-Albrechts-Universität zu Kiel

Methodology of ZnO Based 1D Microstructures: From Synthesis to Application

Sören Kaps

Kiel
2014

Durchgeführt in der Arbeitsgruppe Funktionale Nanomaterialien

1. Gutachter: Prof. Dr. Rainer Adlung
 2. Gutachter: Prof. Dr. Hermann Kohlstedt
- Datum der mündlichen Prüfung: 27.01.2015

KURZFASSUNG

ZnO gehörte in den vergangenen Dekaden zu den Materialien, die am intensivsten untersucht wurden. Durch die große Menge an möglichen Herstellungsverfahren sowie die einzigartige Kombination von Eigenschaften ist ZnO ein vielversprechendes Material für ein weites Anwendungsfeld. Diese Arbeit beschäftigt sich mit der Entwicklung von Anwendungen, die auf eindimensionalen ZnO-Mikrostrukturen basieren.

Die Entwicklung beginnt mit der Einführung eines neuen Syntheseverfahrens, der Flammentransportsynthese (FTS). Die FTS erlaubt die Herstellung unterschiedlicher Nano- und Mikrostrukturen bestehend aus diversen Metalloxiden. Je nach gewählten Syntheseparametern können dabei unterschiedliche Strukturen erstellt werden, wie zum Beispiel Durchdringungsnetzwerke, Kern-Stachel-Partikel und große eindimensionale Einkristalle. Diese Strukturen wurden mit aktuellen Methoden charakterisiert, um ihre kristallinen, elektrischen und piezoelektrischen Eigenschaften zu untersuchen. Röntgenbeugungsuntersuchungen zeigten exzellente kristalline Eigenschaften und das Fehlen einer Vordehnung in den eindimensionalen ZnO Mikronadeln. Transmissionselektronenmikroskopieuntersuchungen zeigten die Existenz von Zwillingsgrenzen in den Stacheln von Kern-Stachel-Partikeln.

Elektromechanische Messungen wurden benutzt, um das Vorhandensein einer Vordehnung in ZnO Mikronadeln zu demonstrieren, die auf ein Substrat aufgebracht wurden. Elektromechanische Messungen in einem Rasterelektronenmikroskop erlaubten die präzise Messung der piezoresistiven Eigenschaften einzelner ZnO Mikronadeln. Die hydrophilen und hydrophoben Benetzungszustände von ZnO wurden untersucht und ein theoretisches Modell wurde eingeführt, das die Benetzung von ultrahydrophoben Oberflächen beschreibt. Auf ZnO Mikronadeln basierende magnetoelektrische Sensoren wurden realisiert und untersucht. Das neue Konzept der piezotronischen Messung wurde angewendet und mit der klassischen piezoelektrischen Auswertung verglichen. Dabei stellte sich heraus, dass sich mit der piezotronischen Messung kleinere Magnetfelder messen lassen als mit der piezoelektrischen Messung. Dadurch ist die Piezotronik ein vielversprechendes Messkonzept für eine Vielzahl weiterer Anwendungen.

ABSTRACT

ZnO is among the most studied materials in the past decades. A large number of synthesis routes and a unique combination of properties offer a wide range of possible applications. This work focuses on the development of applications using 1D ZnO micro- and nanostructures.

The development starts with the introduction of a new synthesis process, flame transport synthesis (FTS). The FTS allows the fabrication of various metal oxide micro- and nanostructures. Depending on the used parameter set the structural type can be modified leading to different morphologies, e.g., interconnected networks, core spike particles or large 1D single crystals. These resulting structures were characterized by state of the art methods to determine their crystalline, electric and piezoelectric properties. X-ray diffraction analysis revealed excellent crystalline properties and the absence of pre-strain in 1D ZnO microrods. TEM investigations showed the existence of twin boundaries in the spikes of core spike particles. Electromechanical measurements were used to demonstrate the pre-strain in ZnO microrods when attached to a plane substrate.

Electromechanical measurements inside SEM allowed the precise measurement of the piezoresistive properties of individual ZnO microrods. The hydrophobic and hydrophilic wetting states of ZnO are discussed and a theoretical model is introduced which expands the common wetting theory and explains the wetting of superhydrophobic surfaces. Magnetoelectric sensors based on ZnO microrods are realized and investigated. The new concept of piezotronic measurements is applied for the sensors and is compared to the classical piezoelectric measurement concept. The comparison revealed a lower limit of detection for the piezotronic sensor, which makes it a promising candidate for new applications.

CONTENTS

I	Theoretical Considerations	3
1	Piezoelectric Materials	3
1.1	Piezoelectricity	3
1.2	Piezoresistivity	6
1.3	Semiconductor contacts	8
1.4	Piezotronics	13
1.5	Zinc Oxide	15
1.6	Wetting	17
2	Magnetostrictive Materials	19
2.1	Magnetostriction	19
2.2	Mechanical resonance	22
2.3	FeCoSiB	24
3	Magneto-Electric Composites	25
II	Synthesis	29
4	Vapor Liquid Solid	31
4.1	Standard Routine	34
4.2	Obtained Structures	36
5	Flame Transport	39
5.1	Synthesis Route 1: Coating	40
5.2	Synthesis Route 2: Crucible	42
5.3	Synthesis Route 3: Flame Spraying	48
6	Sputter Deposition	50
6.1	Deposition Chamber	52
6.2	Load Lock Chamber and Transfer System	55
6.3	Control Unit	56
6.4	Standard Sputtering Procedure	57
7	Summary of the Synthesis	59

III	Characterization	61
8	Crystalline Properties	62
8.1	X-Ray Nano Beam Diffraction	62
8.2	Morphologic Investigations of ZnO Nanospikes	65
9	Electromechanical Characterization	67
9.1	Electric contact	67
9.2	Piezoelectricity and Piezotronics	71
9.3	SEM in-situ push pull	84
9.4	Comparison of the Used Methods	87
10	Summary of the Characterization	88
IV	Effects and Applications	89
11	Water jet reflection as probe for superhydrophobic surfaces	90
12	Magnetic Field Sensors	99
12.1	Magneto-Electric Test Setup	99
12.2	2-1 ME Composites	110
V	Summary and Outlook	135
	List of Publications	138
	List of Patents	139
	Supervised Theses	140
	Bibliography	141
VI	Supplementary Information	151
A	VLS parameters	151
B	Matlab Functions	154
C	Labview	165
D	Water jet reflection equations	176

GLOSSARIES

ACRONYMS

AC	Alternating Current
AD	Analogue-Digital Converter
AFM	Atomic Force Microscopy
CB	Cassie-Baxter
DC	Direct Current
E-PTP	Electronic Push-To-Pull
FTS	Flame Transport Synthesis
IV	Current-Voltage
LG	Liquid-Gas Interface
MBE	Molecular Beam Epitaxy
ME	Magneto Electric
NRA	Nuclear Reaction Analysis
PFM	Piezoelectric Force Microscopy
PID	Proportional-Integral-Derivative Controller
PL	Photo Luminescence Analysis
PLD	Pulsed Laser Deposition
PVB	Poly Vinyl Butyral
SCR	Space Charge Region
SEM	Scanning Electron Microscopy
SG	Solid-Gas Interface
SL	Solid-Liquid Interface
SPIS	Slow Positron Implantation Spectroscopy
TEM	Transmission Electron Microscopy
UHV	Ultra High Vacuum
UV	Ultraviolet
VLS	Vapor Liquid Solid
VS	Vapor Solid
XRD	X-Ray Diffraction

SYMBOLS

α_{ME}	Magnetoelectric Voltage Coefficient
A^*	Effective Richardson Constant
\AA	Ångström, Unit Length Equal to $10^{-10}m$
d_B	Bending Distance
B	Magnetic Field - Flux Density per Area
ζ	Damping Ratio
ρ	Density
d	Piezoelectric Constant
D	Charge Density Displacement
Φ_{Bn}	Energy Barrier Height
E_g	Band Gap Energy
χ	Electron Affinity
E	Energy
E_{EB}	Exciton Binding Energy
E_F	Fermi Energy
E_{vac}	Vacuum Energy
E_V	Valence Band Energy
Φ_m	Metal Work Function
Φ_s	Semiconductor Work Function
ε	Permittivity
e	Piezoelectric Coefficient
ε_r	Relative Permittivity
ε_0	Vacuum Permittivity
\mathcal{E}	Electric Field
ω_0	Angular Eigenfrequency
ω_r	Angular Resonance Frequency
f_0	Eigenfrequency
F	Force
f	Frequency
f_r	Resonance Frequency
G	Electrical Conductance
G	Gauge Factor
\hbar	Reduced Planck Constant
H_C	Coercive Field
H	Magnetic Field
H_S	Saturation Field
I	Electrical Current
J	Current Density
J_F	Forward Current Density

J_R	Reverse Current Density
κ	Coupling Factor
k	Boltzmann Constant
k	Spring Constant
λ_{\parallel}	Longitudinal Magnetostriction
λ	Magnetostriction
λ_{\perp}	Transverse Magnetostriction
l	Length
m^*	Effective Mass
μ	Mobility
m	Mass
N_C	Density of States in Conduction Band
N_D	Donor Concentration
n_{th}	Thermionically Emitted Electron Density
P	Electric Polarization
p	Piezomagnetic Coefficient
q	Electric Charge
Q	Quality Factor
R_C	Specific Contact Resistance
R	Electric Resistance
R^2	Coefficient of Determination
s	Elastic Compliance
S	Strain
σ	Stress
T_C	Curie Temperature
T	Temperature
Θ	Contact Angle
t_{gr}	Growth Time
\bar{t}	Mean Free Collision Time
τ	Shear Stress
t	Thickness
t_{Film}	Thickness of Film
t_R	Thickness Ratio
t	Time
U	Voltage
ν	Poisson Ratio
v	Velocity
V	Volume
ω	Angular Frequency
W	Width
x	Place
Y	Young's modulus

INTRODUCTION

In the last decades the development of new techniques allowed a miniaturization of many kinds of technical devices. The basic concept of miniaturization is the perpetuation of the functionality with a decreasing feature size. The most prominent example is the development of microchips which were strongly improved by reducing the feature size from 800 *nm* in 1993 to 22 *nm* in 2014 [1]. The improvement of microchips is therefore a direct result of the structure size since it allows the integration of a larger number of transistors in a microprocessor [2]. Besides the advantage of a smaller size many material properties can be affected by the structural size. Some of these effects originating from these micro- and nanostructures have been used for centuries, e.g., in the red color of window glass which is a result of the plasmon resonance of small gold particles [3], but most of them require new methods which were mainly introduced in the second half of the 20th century. Other effects which originate from small structures are the superparamagnetism of small particles [4], the high surface to volume ratio which can be used to improve gas sensors [5–8] and mechanical stability that is a result of the increased flexibility of nanofibers [9–11]. Thus new or improved applications can be realized by reducing the size of a structure and thus changing the material properties. The main challenge towards a miniaturization is the development of new methods for the synthesis and the characterization of micro- and nanostructures.

The presented work was carried out as a part of the collaborative research center *SFB 855 biomagnetic sensing* which aimed to measure and understand the magnetic fields generated by the human body. The concept of magnetoelectric (ME) sensors consisting of a magnetostrictive and a piezoelectric phase was selected to realize the measurement of magnetic fields. The interdisciplinary concept of the collaborative research center separates this overall goal in individual problems. Different material combinations and different geometries are investigated by the appropriate research groups of physicists, electrical engineers and material scientists. The aim of the presented work is the synthesis, characterization and integration of a 1D piezoelectric phase in ME sensors and the investigation of the piezotronic effect as a new measurement method for ME devices.

Piezoelectric ZnO is an excellent material for the realization of new applications which base on micro- and nanostructured devices and ME sensors. On the one

hand many different synthesis routes are available to produce various types of structures [12]. On the other hand ZnO offers excellent piezoelectric characteristics and a unique combination of properties and thus a large number of possible uses.

Common synthesis routes do not provide a possibility to create 1D ZnO microrods in a fast and cost effective way. This lack of methods demands the modification of existing processes or the introduction of new processes. Systems for two different synthesis will be developed and discussed: the conventional Vapor-Liquid-Solid (VLS) synthesis and a new concept named Flame-Transport-Synthesis (FTS). The resulting ZnO structures are investigated using state of the art methods. The crystalline structure is investigated by transmission electron microscopy (TEM) and X-ray diffraction. For an integration in a electromechanic device like a ME sensor the creation of reliable electrical contacts is substantial. Therefore a variable, computer controlled two source sputter deposition is required for the establishment of electrical contacts. The conception, construction and development of the sputter deposition setup will be discussed. The electric properties of metal-ZnO contacts and their influence on a electromechanical device is investigated by current-voltage (IV) characterization. After successful creation of reliable electrical contacts the piezoelectric and piezoresistive properties of ZnO microrods are investigated. This requires the construction of a characterization setup which allows the precise deformation of the microrods while simultaneously measuring the piezoelectric and piezoresistive response. In order to investigate environmental influences the effect of external light, which is known to affect the oxygen vacancy concentration, is studied. The resulting change in resistivity, surface dipole moment and corresponding wetting states is discussed. To investigate the possible application in ME sensors the ZnO microrods are combined with commercial magnetostrictive foil. The investigation of the response to a magnetic field requires the development of a ME characterization setup whose conception and construction is described. The new concept of piezotronic measurements is investigated and compared to the conventional piezoelectric measurement.

This work is separated in four main parts. The first part provides the theoretical background and summarizes the recent status of literature. The second part focuses on the synthesis and processing of ZnO microstructures. The third part describes the electromechanical, piezoelectric, piezoresistive and piezotronic characterization and the fourth part addresses wetting effects and the application of 1D ZnO microrods in ME sensors.

PART I

THEORETICAL CONSIDERATIONS

This part describes the theoretical concepts which form the basis of this work. The methods and theories explained are a selection from recent literature and should provide all necessary information to understand the following chapters. The individual chapters briefly summarize the single topics and always refer to literature which can be used to obtain a more detailed description.

1 PIEZOELECTRIC MATERIALS

1.1 PIEZOELECTRICITY

The piezoelectric effect is well understood and applied in a large variety of applications. Among many others the application of the piezoelectric effect ranges from electric cigarette lighters [13] over pressure sensors [14–16] and microphones [17–19] to Knock sensors [20–22]. Besides these, energy harvesting applications using piezoelectric materials are currently under a strong debate [23–27].

The direct piezoelectric effect describes a property of a crystalline material where a mechanical stress σ creates a charge separation and thus an electric polarization

$$P_i = d_{ijk}\sigma_{jk} \tag{1.1}$$

with the piezoelectric coefficients d_{ijk} . The effect was discovered in 1880 by Pierre and Jacques Curie [28] when working with tourmaline crystals. The origin of the effect is the separation of positive and negative charge centers when applying stress to the crystal. This implies that piezoelectricity can only be observed in crystals lacking a center of symmetry. Indeed all non-centrosymmetric crystal classes show the piezoelectric effect, except for the cubic class 432 where the effect is cancelled out by other symmetries [29].

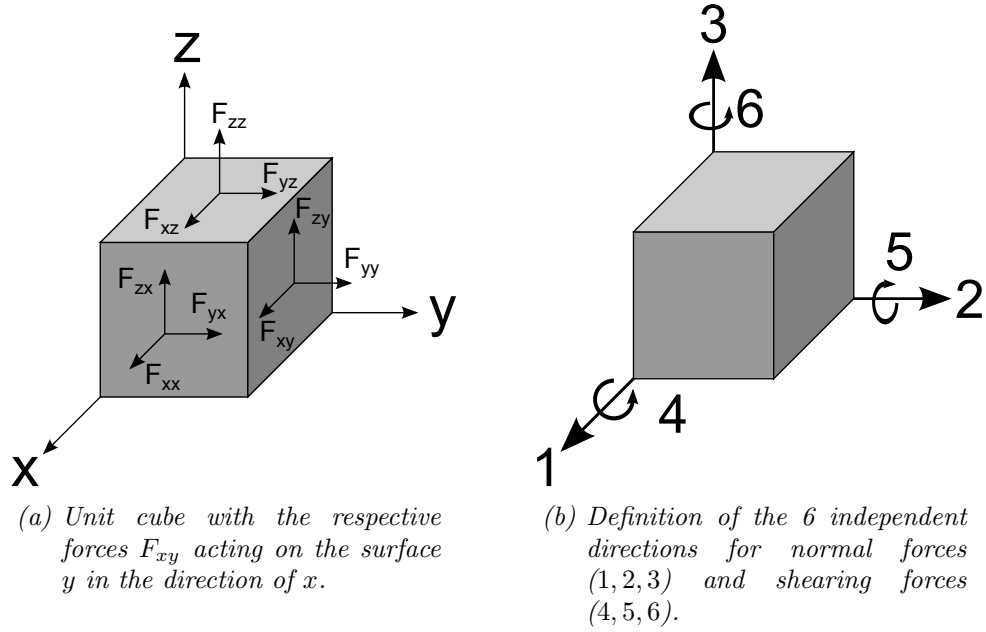


Figure 1.1: Evaluation of the normal and shear directions on a unit cube.

The inverse piezoelectric effect was predicted by Lippmann [30] in 1881 and observed again by the Curie brothers [31]. It describes the mechanical strain of a material when exposed to an electrical field. The constitutive *Equation* (1.2) and *Equation* (1.3) describe the direct and indirect piezoelectric effect with the electric displacement D_i , the piezoelectric coefficients d_{ijk} , the mechanical stress σ , the dielectric permittivity at a constant stress ε_{ij}^σ , the electric field \mathcal{E} , the mechanical strain S and the elastic modulus at constant electric field $s^\mathcal{E}$.

$$D_i = d_{ijk}\sigma_{jk} + \varepsilon_{ij}^\sigma \mathcal{E}_j \quad (1.2)$$

$$S_{ij} = d_{ijk}\mathcal{E}_k + s_{ijkl}^\mathcal{E}\sigma_{kl} \quad (1.3)$$

Equation (1.2) and *Equation (1.3)* can be rewritten in the matrix notation.

$$D_i = d_{ik}\sigma_k + \varepsilon_{ij}^{\sigma}\mathcal{E}_j \quad (1.4)$$

$$S_k = d_{ki}\mathcal{E}_i + s_{kl}^{\sigma}\sigma_l \quad (1.5)$$

The index notations i, j, k, l represent the direction of the respective variable. The used nomenclature is depicted in *Figure 1.1*. The force on the surfaces of a unit cube can act in three independent directions as shown in *Figure 1.1(a)*. Since the forces partially lead to a shear with respect to the same axis 6 independent forces remain resulting in the normal stress/strain direction 1, 2, 3 and the shear directions 4, 5, 6, as shown in *Figure 1.1(b)*. Thus $i, j \in \{1, 2, 3\}$ and $k, l \in \{1, 2, 3, 4, 5, 6\}$. Accordingly the piezoelectric coefficients can be expressed as

$$d_{ik}^{\mathcal{E}} = \frac{\partial D_i}{\partial \sigma_k} \quad (1.6)$$

for a constant electric field, and

$$d_{ik}^{\sigma} = \frac{\partial S_k}{\partial \mathcal{E}_i} \quad (1.7)$$

for a constant mechanical stress. The piezoelectric coefficients e and d are coupled by the elastic constants and can be described as

$$e_{ik}^{\mathcal{E}} = \frac{\partial D_i}{\partial S_k} \quad (1.8)$$

and

$$e_{ik}^S = -\frac{\partial \sigma_k}{\partial \mathcal{E}_i}. \quad (1.9)$$

ZnO is well described in terms of piezoelectricity. A collection of the reported piezoelectric coefficients for ZnO is depicted in *Table 1.1*. The relatively high piezoelectric coefficients in c-axis direction together with the preferred growth in the same direction make ZnO an excellent candidate for piezoelectric sensors based on single crystalline microrods.

1.2 PIEZORESISTIVITY

The term piezoresistivity falsely suggests a direct relation to piezoelectricity. Indeed all semiconducting materials can have piezoresistive properties. Especially the non-piezoelectric silicon is the material with the best description of piezoresistive properties and applications. Piezoresistivity is an effect which causes a change in resistivity when experiencing strain. The effect was first observed by Lord Kelvin in 1856 and is nowadays used in pressure sensors [39,40], rotation rate sensors [41–43], biological sensors [44–46], flow sensors [47–49] and other MEMS devices [50–52].

A resistor with length l and cross-sectional area A has a resistance of

$$R = \rho \cdot \frac{l}{A} \quad (1.10)$$

with ρ being the bulk resistivity. Thus a change in resistivity or geometry will change the resistance of a sample. Whereas the geometric resistance change, e.g.,

Table 1.1: Piezoelectric coefficients of ZnO [12]

$e_{31} [\frac{C}{m^2}]$	$e_{33} [\frac{C}{m^2}]$	Used Method
-0.62	0.96	Resonance-antiresonance method on ZnO single crystal [32]
-0.51	1.22	Acoustic investigation technique on ZnO film deposited by RF magnetron sputtering on sapphire substrate [33]
-0.39	0.92	Calculation using modern ab initio [34]
-0.53	1.19	Calculation using ab initio quantum-mechanical level by using through the Berry-phase scheme applied to delocalized crystalline orbitals and through the definition of well-localized Wannier functions [35]
-0.51	1.21	Calculation based on ab initio using the Berry-phase approach to polarization in solids [36]
-0.55	1.19	Calculation using ab initio periodic linear combination of atomic orbitals LCAO method, based mainly on the Hartree-Fock Hamiltonian, with an all-electron Gaussian-type basis set [37]
-0.66	1.30	Calculation using a plane-wave pseudopotential implementation of density-functional theory and density-functional linear response within the local-density approximation [38]

in metals, is referred as a strain gauge, piezoresistivity describes only the change in the resistivity. The resistivity can be described as

$$\frac{1}{\rho} = q n \mu \quad (1.11)$$

with charge per unit charge carrier q , charge carrier density n and mobility μ . The mobility of the charge carriers is defined as

$$\mu = \frac{q\bar{t}}{m^*} \quad (1.12)$$

with mean free time between charge carrier collisions \bar{t} and effective mass m^* . Since both mean free collision time and effective mass depend on the average atomic spacing in a semiconductor, a change in mobility and therefore in resistivity is observed when straining a semiconductor. The exact quantum physical description of the involved effects is discussed in details elsewhere [53]. The resulting change in resistance ΔR is proportional to the applied strain $\Delta L/L$ and can be written as

$$\frac{\Delta R}{R} = G \cdot \frac{\Delta L}{L} \quad (1.13)$$

introducing G as gauge factor. In single crystals the anisotropy of the piezoresistivity is described by piezoresistive coefficients π_{ijkl} to connect the directions of the mechanical stress σ with current density J and the electric field as

$$\mathcal{E}_i = \rho_{ij} J_j + \pi_{ijkl} J_j \sigma_{kl}. \quad (1.14)$$

The notation for the direction is the same as for piezoelectric coefficients, see *Figure 1.1(b)*. The piezoresistive coefficients are no constants and depend on doping [54, 55] and temperature [55, 56]. For silicon the reported values vary from $\pi = -102.2 \cdot 10^{-11} Pa^{-1}$ for n-type silicon to $\pi = 138.1 \cdot 10^{-11} Pa^{-1}$ for p-type silicon [57]. Due to the strong piezoelectric effect in ZnO which is well described in literature only a few reports about piezoresistivity in ZnO are available. The reported gauge factors vary from $1 \lesssim G \lesssim 100$ for ZnO nanowire composites [58] and $G \approx 350$ for Sb-doped ZnO nanobelts [59].

1.3 SEMICONDUCTOR CONTACTS

To understand the mechanisms of charge transfer at the interface between a metal and a semiconductor complex knowledge of both metals and semiconductors is necessary. The following is a brief introduction and description of the fundamental mechanisms which are important to understand further effects like piezotronics.

The rectifying properties of metal-semiconductor contacts have been applied since the early 20th century. The theory of these contacts was first described by Schottky [60] in 1938, who explained the mechanism by a space charge region causing a potential barrier for the charge carriers, named Schottky barrier. Contacts between metal and semiconductor do not always show a rectifying behavior. Depending on the combination of materials only a negligible contact resistance can be observed independent from the polarity, this is called ohmic contact. In this chapter the formation of Schottky and ohmic contacts will be explained using energy band diagrams.

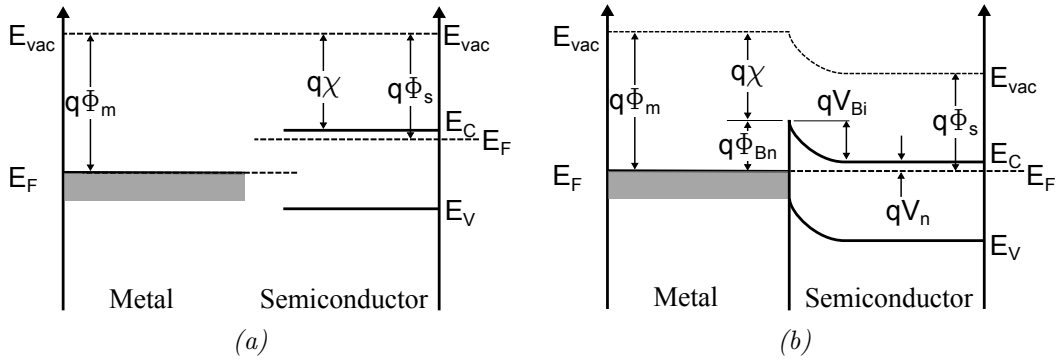


Figure 1.2: Metal-Semiconductor band diagram a) before and b) after contact formation.

Figure 1.2(a) shows the energy band diagram of an isolated metal with the work function $q\Phi_m$ next to an isolated n-type semiconductor with work function $q\Phi_s$. Whereas the work function is defined as the energy difference between vacuum level E_{vac} and Fermi level E_F , the electron affinity of a semiconductor $q\chi$ is the difference between vacuum level and conduction band edge E_C . If a contact is established between metal and semiconductor, compare Figure 1.2(b), the Fermi

levels approach leading to an energy barrier with height $q\Phi_{Bn}$ for electrons in the metal defined as

$$q\Phi_{Bn} = q\Phi_m - q\chi. \quad (1.15)$$

Electrons in the conduction band of the semiconductor are affected by the built in potential V_{Bi} written as

$$V_{Bi} = \Phi_{Bn} - V_n \quad (1.16)$$

when trying to move to the metal, where V_n is the difference between Fermi

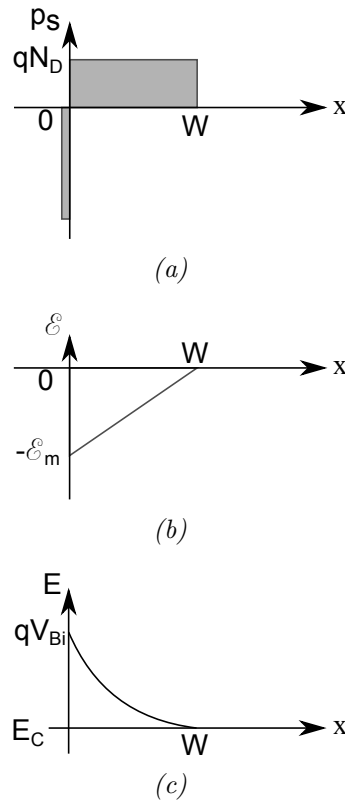


Figure 1.3: Space charge region of a semiconductor in contact to a perfectly conducting metal. a) Charge distribution b) Electric field distribution c) Conduction band bending

level and conduction band edge. The built in potential affects the shape of the conduction band which results in a space charge region in the semiconductor. *Figure 1.3* depicts the details of a space charge region with width

$$W = \sqrt{\frac{2\epsilon_s(V_{Bi} - V)}{qN_D}} \quad (1.17)$$

of a semiconductor with donor concentration N_D and dielectric permittivity ϵ_s in contact to a perfectly conducting metal. The charge distribution as shown in *Figure 1.3(a)* inside the space charge region ($0 < x < W$) equals qN_D , whereas it becomes 0 beyond the space charge region ($x > W$). The maximum electric field \mathcal{E}_m , see *Figure 1.3(b)*, is located at the interface and the electric field is linearly decreasing, becoming $\mathcal{E} = 0$ at $x = W$. This results in a bending of the conduction band of the semiconductor, see *Figure 1.3(c)*, and the build-in potential qV_{Bi} .

1.3.1 SCHOTTKY CONTACT

A metal-semiconductor contact with a large barrier height ($\Phi_{\text{Bn}} \gg kT$) is called Schottky contact. The dominating charge transport mechanism at room temperature is the thermionic emission of majority carriers from the semiconductor to the metal. The thermionically emitted electron density n_{th} is defined as

$$n_{th} = N_c \exp\left(-\frac{q\Phi_{\text{Bn}}}{kT}\right) \quad (1.18)$$

with the effective density of states in the conduction band N_c , the Boltzmann constant k and the temperature T . *Figure 1.4(a)* shows the energy band diagram of a metal-semiconductor contact with the thermal distribution of electrons marked blue without an applied bias. The current densities from metal to semiconductor J_R and from semiconductor to metal J_F are equal in size leading to zero net current. When a forward bias voltage V_F is applied, see *Figure 1.4(b)*, J_F is increasing whereas J_R remains constant. Thus a large net current flows from the semiconductor to the metal. If a reverse bias voltage V_R is applied, see *Figure 1.4(c)*, J_F is decreasing and J_R is remaining constant. This leads to a small net current from the metal to the semiconductor. The current density J of a Schottky contact can be calculated as

$$J = J_s \exp\left(\frac{qV}{kT} - 1\right) \quad (1.19)$$

with bias voltage V and the saturation current density J_s defined as

$$J_s = A^*T^2 \exp\left(-\frac{q\Phi_{\text{Bn}}}{kT}\right) \quad (1.20)$$

with the effective Richardson constant A^* and the energy barrier $q\Phi_{\text{Bn}}$.

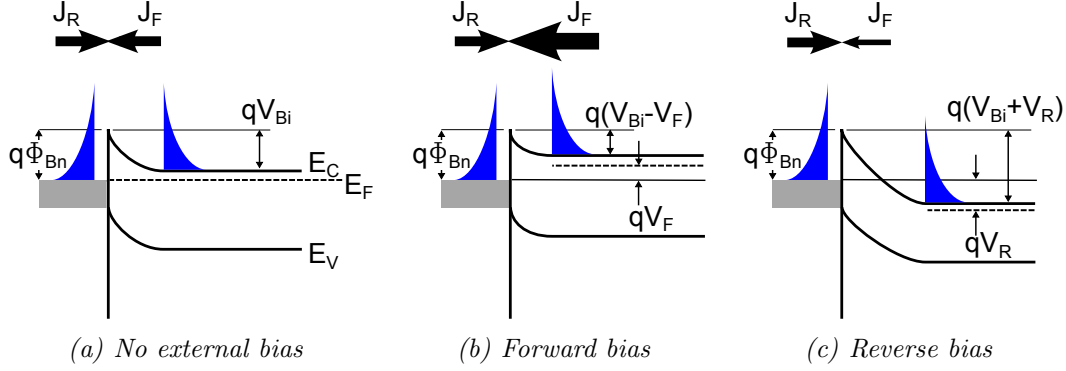


Figure 1.4: Energy band diagram for a Schottky contact for different bias voltages. Blue area shows the electron distribution. The size of the black arrows indicates the current density in forward direction (J_F) and reverse direction (J_R).

1.3.2 OHMIC CONTACT

Metal-semiconductor contacts with a negligible resistance compared to the series resistance of the semiconductor are called ohmic contacts. The specific contact resistance is defined as

$$R_C = \left(\frac{\partial V}{\partial J} \right)_{V=0} \Omega \text{ cm}^2. \quad (1.21)$$

Since the thermionic emission is dominant at low doping concentrations Equation (1.19) can be applied resulting in

$$R_C = \frac{k}{qA^*T} \exp\left(\frac{q\Phi_{Bn}}{kT}\right). \quad (1.22)$$

Thus a small barrier height Φ_{Bn} is necessary to obtain a small contact resistivity. Despite the thermionic emission tunneling processes become important for high doping concentrations. The tunneling current is proportional to the tunneling probability and the resulting specific contact resistance for high doping is described by

$$R_C \propto \exp\left(\frac{4\sqrt{m_n \epsilon_s} \Phi_{Bn}}{\sqrt{N_D} \hbar}\right), \quad (1.23)$$

with the donor concentration N_D and the effective mass m_n .

For n-type semiconductors this means that ohmic contacts can be realized when the contacted metal has a relatively low Φ_m . As a rule of thumb it is often referred

Table 1.2: Contact type for different metal semiconductor combinations

Semiconductor	Φ_D	Contact
n-type	$\Phi_D > 0$	Schottky
	$\Phi_D < 0$	ohmic
p-type	$\Phi_D > 0$	ohmic
	$\Phi_D < 0$	Schottky

that the difference in work functions $q\Phi_D = q(\Phi_m - \Phi_s)$ predicts the type of contact formation as listed in *Table 1.2*.

1.3.3 CURRENT VOLTAGE CHARACTERISTICS

The electrical properties of a sample and its contacts are usually investigated by measuring current-voltage curves. In this part the typical characteristics are depicted using ZnO as an example material. When establishing contacts to n-conducting ZnO, which has a work function of $q\Phi_{ZnO} \approx 4.3 \text{ eV}$, most noble metals will form a Schottky contact since their work functions are typically higher. For aluminum the formation of ohmic contacts to ZnO was observed. In the case of ZnO-Al contacts the ohmic behavior is not only related to the relatively low work function of Al (4.1 eV), but also to the interfacial oxide formation of Al_2O_3 , which facilitates the tunneling of charge carriers [61,62]. To prevent the Al contact from oxidation it is typically covered with a noble metal, e.g. Au.

Since two contacts are required for contacting a device, there exist three different IV-characteristics as depicted in *Figure 1.5*. Two Al contacts will lead to two ohmic contacts as depicted in *Figure 1.5(b)*. Two Au contacts will show a Schottky-Schottky type IV-curve, see *Figure 1.5(c)*. If only one side is contacted by Au and the other by Al the IV-curve looks similar to a classical diode, as depicted in *Figure 1.5(a)*. In this work the ohmic contacts to ZnO were established by RF sputtering of Al followed by DC sputtering of Au to prevent oxidation of the contact, as further described in *chapter 9.1*. The formation of Schottky contacts was realized by DC sputtering of Au or the use of Ag glue.

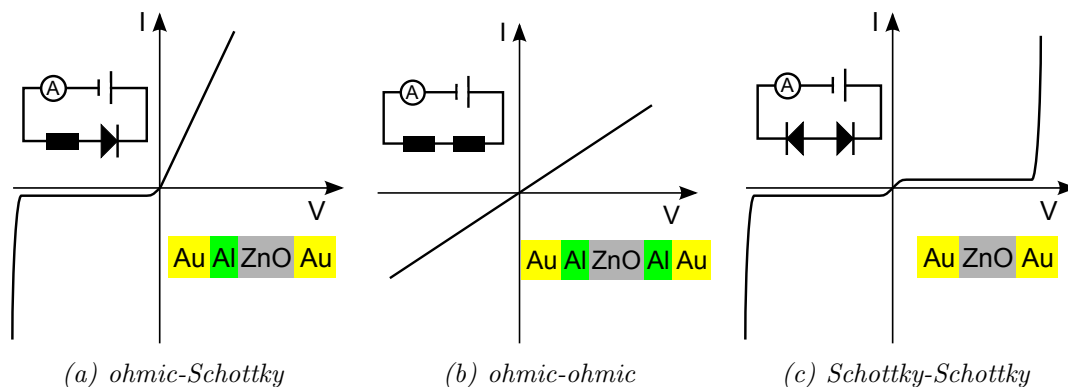


Figure 1.5: Typical IV curves for a ZnO sample with different contacts. The left insets illustrate the equivalent circuit whereas the lower right insets depict contact materials which would lead to the shown characteristic.

1.4 PIEZOTRONICS

In piezotronics the piezoelectric potential is used to affect the barrier height of a Schottky contact which leads to a change in current when applying a constant supply voltage. The effect was first observed by Wang in 2007 [63] who applied the piezotronic effect in ZnO strain sensors. As mentioned in *chapter 1.3*, semiconductors can build a Schottky contact to metals if certain prerequisites are met. The Schottky contact obeys a diode like IV-characteristic which is a result of the change in barrier height by an external voltage. For piezotronics the piezoelectric effect, as described in *chapter 1.1*, replaces the external voltage and changes the barrier height of the Schottky contact. This allows to directly utilize the current through the piezoelectric material as a measure for its strain.

Figure 1.6 shows the details of a Schottky contact which is analogue to the classical Schottky description depicted in *Figure 1.3* with additional piezoelectric charges at the interface. These additional charges, compare red area in *Figure 1.6(a)*, create a superposing depletion zone with the width W_p . The change in the electric field in this zone, see *Figure 1.6(b)*, affects the energy band diagram (*Figure 1.6(c)*) and changes the potential barrier height.

Following the theory of thermionic emission, as described by Zhang [64], the total potential barrier height for electrons Φ_{BnT} is the sum of the potential barrier

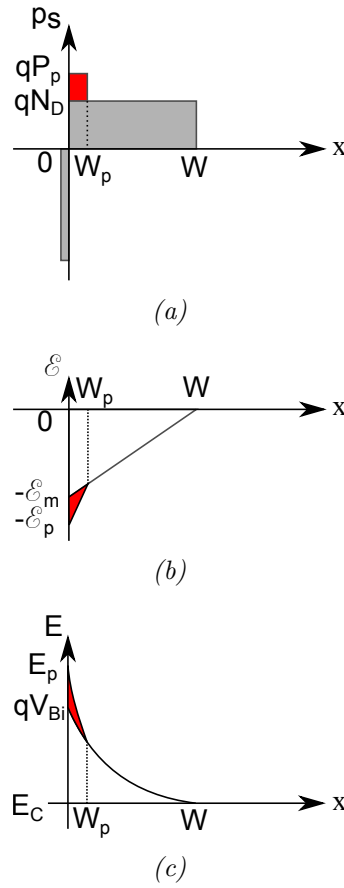


Figure 1.6: Influence of the piezoelectric potential on the space charge region of a semiconductor in contact to a perfectly conducting metal. The red areas indicate the influence of the piezoelectric effect. a) Charge distribution b) Electric field distribution c) Conduction band bending.

height in the absence of piezoelectric charges Φ_{Bn0} and the piezoelectric charge contribution Φ_{BnP}

$$\Phi_{\text{BnT}} = \Phi_{\text{Bn0}} + \Phi_{\text{BnP}}, \quad (1.24)$$

with the piezoelectric potential barrier

$$\Phi_{\text{BnP}} = \frac{qP_p W_p^2}{2\epsilon_s}. \quad (1.25)$$

A quantitative description of the current density for a piezotronic Schottky contact was performed by Zhang [64] who showed that the current density J for an Au-ZnO contact can be expressed as

$$J = J_{D0} \exp\left(\frac{qe_{33}s_{33}W_p}{2\varepsilon_s kT}\right) \left[\exp\left(\frac{qV}{kT}\right) - 1\right] \quad (1.26)$$

with the current density under forward bias

$$J_{D0} = \frac{q^2 D_n N_c}{kT} \sqrt{\frac{2qN_D(V_{bi0} - V)}{\varepsilon_s}} \exp\left(-\frac{q\Phi_{Bn0}}{kT}\right). \quad (1.27)$$

1.4.1 DISTINGUISHING PIEZOTRONICS AND PIEZORESISTIVITY

The piezotronic effect and the piezoresistive effect can show a similar response behavior which makes it difficult to determine the origin of a resistance change since both effects cause a change in the resistance of a sample when straining. Whereas the piezoresistive effect is present in all semiconducting materials the piezotronic effect only exists if a piezoelectric semiconductor has a single Schottky contact. This implies that every piezotronic sensor is also a piezoresistive sensor. The independent characterization of piezoresistivity and piezotronics in ZnO is therefore challenging and a main part of the characterization as described in *chapter III*. In contrast to the origin of the piezoresistive effect, the piezoelectric potential is typically present only for a short duration. Therefore a concept for the investigation of the piezoresistive effect in the absence of piezotronics could be the measurement of the current in statically strained samples.

1.5 ZINC OXIDE

ZnO is among the most studied semiconducting materials in the past 50 years. Even though Bunn [65] investigated the lattice parameters of ZnO already in 1935 and first optical studies were carried out by Mollwo [66] in 1954 the academic interest on ZnO is still high. There exist various applications of ZnO ranging from wall paints to medicine. Jin et al. showed that tetrapod shaped ZnO micro particles can be used as linker materials to increase the adhesion even of materials that are usually unjoinable [67]. Templates from ZnO can be used to create

Aerographite, a carbon based material with unique properties and one of the least dense materials [68]. It was also observed that ZnO is active against the herpes simplex virus [69].

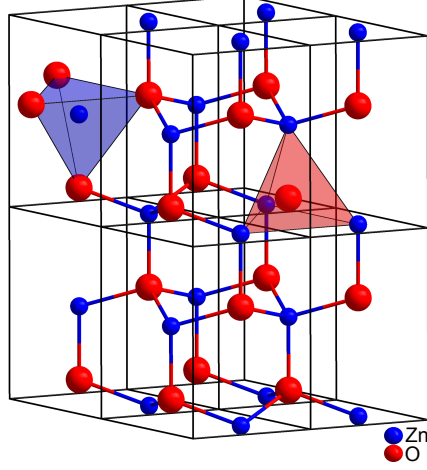


Figure 1.7: Unit cell of the ZnO wurzite structure represented by blue zinc and red oxygen atoms.

ZnO is an n-type semiconductor with a direct band gap in the near ultraviolet ($E_g \approx 3.3 \text{ eV}$ at 300 K) and a large exciton binding energy ($E_{EB} \approx 60 \text{ meV}$). The thermodynamically stable crystal structure at ambient conditions is wurzite. Other structures occur only if ZnO is grown on cubic substrates (zinc blende) or under high pressure (rocksalt). The unit cell of the wurzite structure shown in *Figure 1.7* refers to the space group $P6_3mc$. The reported lattice parameters investigated by x-ray diffraction are $a \approx 3.25 \text{ \AA}$ and $c \approx 5.21 \text{ \AA}$ [70–72]. The low symmetry results in a spontaneous polarization along the c axis. The piezoelectric tensor of ZnO is one of the highest among the tetrahedrally bonded semiconductors and comparable to GaN and AlN [34]. The polarization P_z along the c axis can be expressed as

$$P_z = e_{33}\epsilon_z + e_{31}S_{\perp} \quad (1.28)$$

with the strain along the c axis S_z and in the basal plane S_{\perp} , and the piezoelectric coefficients e_{33} and e_{31} [36]. The shear strain also has an independent influence on the polarization but its piezoelectric tensor e_{15} is usually neglected. Depending on the method of characterization or calculation the reported values for the piezoelectric coefficients vary as depicted in *Table 1.1*.

Various synthesis routes and a large number of different substrates are available for growing ZnO structures. **M**olecular **B**eam **E**pitaxy (MBE) [73–75], **P**ulsed

Laser **D**eposition (PLD) [76–78], hydrothermal growth [79–81] and chemical-vapor deposition methods [82–84] have been reported for the successful synthesis of ZnO. In this work **V**apor **L**iquid **S**olid (VLS) (compare chapter 4) as well as **F**lame **T**ransport **S**ynthesis (FTS) (*chapter 5*) routes have been used for the growth of ZnO.

The concentration of oxygen vacancies is one of the dominating factors which influence the properties of ZnO. E.g., the conductivity can change by orders of magnitude if the oxygen vacancy concentration is changing. The surface dipole moment is also directly influenced and allows ZnO to be either hydrophilic or hydrophobic [85].

1.6 WETTING

The interaction of liquid droplets with a solid surface can lead different effects. Whereas a superhydrophilic surface will cause a complete spreading of a water droplet, a superhydrophobic surface will create an almost spherical droplet which can move on the surface. The latter effect is known from the lotus leaves and thus referred as the lotus effect [86, 87]. The rolling water droplets usually pick up particles on the superhydrophobic surface leading to a cleaning effect which is already applied in bio-inspired superhydrophobic coatings [88–90]. The two dominating surface properties that determine the type of wetting are the dipole moment with the corresponding surface energy and the surface roughness. The oxygen vacancy concentration in ZnO can strongly influence the surface dipole moments and thus change the wetting. Additional variations in the structural sizes are easily obtained affecting surface roughness. These prerequisites make ZnO an interesting material in terms of wetting. The following introduction in the theory of wetting will provide the information that are necessary for further advanced concepts like the water jet reflection.

Young’s equation relates the wetting angle Θ_Y to the interface energies as

$$\cos(\Theta_Y) = \frac{\gamma_{SG} - \gamma_{SL}}{\gamma_{LG}} \quad (1.29)$$

with γ being the interfacial energy between solid-gas (SG), solid-liquid (SL) and liquid-gas (LG). It can be directly seen that the difference in γ_{SG} and γ_{SL} determines whether a surface is hydrophobic ($\Theta_Y > 90^\circ$) or hydrophilic ($\Theta_Y < 90^\circ$). Young’s equation does not contain any approach for the roughness of the surface

below the droplet. Wenzel [91] introduced a roughness r defined as the ratio of true surface area to projected surface area, and the contact angle for a rough surface Θ_W which is defined as

$$\cos(\Theta_W) = r \frac{\gamma_{SG} - \gamma_{SL}}{\gamma_{LG}}. \quad (1.30)$$

Since a high roughness is equivalent to a larger true surface area a high roughness pronounces the difference in the interface energies which is decreasing the contact angle on a hydrophilic surface and increasing it on a hydrophobic surface. This theory was further developed by Cassie and Baxter [92] by introducing the heterogeneous wetting which described the trapping of gas below the droplet and thus an incomplete wetting of a rough surface. The wetted fraction f is the ratio of wetted surface to non-wetted surface and the contact angle Θ_{CB} is defined as

$$\cos(\Theta_{CB}) = r f \frac{\gamma_{SG} - \gamma_{SL}}{\gamma_{LG}} + f - 1. \quad (1.31)$$

For a complete wetting ($f = 1$) the Cassie-Baxter equation is equal to the Wenzel equation leading to $\Theta_{CB} = \Theta_W$. *Figure 1.8* shows schematically for a hydrophobic material the wetting according to Young (1.8(a)), Wenzel (1.8(b)) and Cassie-Baxter (1.8(c), 1.8(d)). A unique property of the Cassie-Baxter theory is the fact that the contact angle can be the same for different roughnesses since the wetted fraction can change. This is a result of the under-determination of the Cassie-Baxter equation which allows infinite tuples of roughness and wetted fraction as solution. Accordingly the information gain from a contact angle experiment is limited and samples with different surface chemistry, different roughness and different wetted fraction can exhibit the same macroscopic contact angle even though the underlying wetting mechanisms differ.

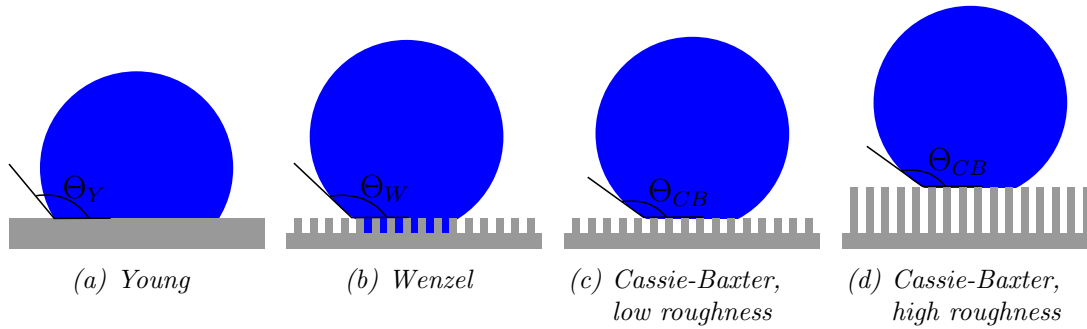


Figure 1.8: Typical contact angles on a hydrophobic surface corresponding to the different wetting models. The theoretical description involves a) a flat surface, b) a rough surface without trapped air below the droplet, c) a rough surface with trapped air, d) a very rough surface showing the same contact angle as c) due to the increase in trapped air.

2 MAGNETOSTRICTIVE MATERIALS

2.1 MAGNETOSTRICTION

When a solid material is exposed to an external magnetic field it changes its dimensions. This effect is called magnetostriction and was first observed by Joule [93] in 1842, when investigating the length change of an iron rod in a magnetic field. Since this lengthening is anisotropic this effect is called anisotropic or Joule magnetostriction. Besides there exists the isotropic volume or force magnetostriction which is usually small compared to Joule magnetostriction and only relevant at high magnetic fields [94]. In the following magnetostriction always refers to Joule magnetostriction.

The origin of magnetostriction is the spin-orbit interaction which leads to a coupling of the magnetic moment of an atom to its surrounding electron cloud. By applying an external magnetic field and thus changing the direction of the magnetization the minimum of the crystal's free energy changes leading to a new equilibrium bond length.

The atomic principle of the magnetostriction in a ferromagnetic material is shown in *Figure 2.1*. Above Curie temperature T_C the material is in a paramagnetic state and no magnetic order is present, leading to a length of l_P , as depicted in *Figure 2.1(a)*. When cooling down below T_C the ferromagnetic order leads to a spontaneous magnetostriction with a length change Δl_P and a new length l_F , compare *Figure 2.1(b)*.

$$\Delta l_P = l_F - l_P \quad (2.1)$$

When applying a magnetic field H the field induced magnetostriction is caused by a change in the magnetization direction, leading to a new length l_H with a length change Δl_F , compare *Figure 2.1(c)*.

$$\Delta l_F = l_H - l_F \quad (2.2)$$

For a solid body of length l which lengthens by Δl when applying a magnetic

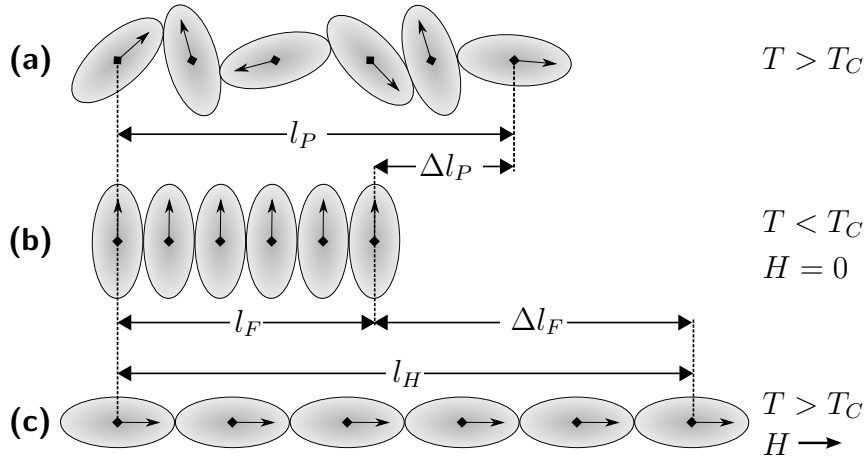


Figure 2.1: Principle of magnetostriction in ferromagnetic solids. Arrows indicate magnetic moments of atoms with elliptical electron clouds. a) Paramagnetic state above T_C . b) Spontaneous magnetostriction below T_C . c) Field-induced magnetostriction.

field, the longitudinal magnetostriction $\lambda_{||}$ is defined as

$$\lambda_{||} = \frac{\Delta l}{l}. \quad (2.3)$$

Regarding the direction of the effect *Equation (2.3)* defines a lengthening when applying a magnetic field as positive magnetostriction $\lambda_{||} > 0$ and a shortening as negative magnetostriction $\lambda_{||} < 0$. The lengthening in one direction of a solid is

usually accompanied by a reduction of thickness or diameter leading to a transverse magnetostriction λ_{\perp} . This can be described by Poisson's ratio ν

$$\nu = -\frac{\Delta t/t}{\Delta l/l} = -\frac{\lambda_{\perp}}{\lambda_{\parallel}} \quad (2.4)$$

with the change in thickness $\Delta t/t$ [95]. The change in volume $\Delta V/V$ can be expressed as [96]

$$\frac{\Delta V}{V} = (1 - 2\nu)\frac{\Delta l}{l}. \quad (2.5)$$

Since the volume for Joule magnetostriction is constant ($\Delta V = 0$), Poisson's ratio can be calculated as $\nu = -1/2$. If inserted in *Equation* (2.4) the transverse magnetostriction can be expressed as

$$\lambda_{\perp} = -\frac{1}{2}\lambda_{\parallel}. \quad (2.6)$$

This means that the absolute value of longitudinal magnetostriction is always higher and should be used for ME sensors as further explained in 12. In the following magnetostriction λ always refers to λ_{\parallel} unless otherwise stated. A schematic magnetostriction curve with a corresponding magnetization curve is depicted in *Figure 2.2*. The magnetostriction reaches its maximum λ_S at saturation field H_S . When the magnetization reaches zero at the coercive field H_C the magnetostriction vanishes. The mathematical description of magnetostriction is analogous to the piezoelectric effect, compare *chapter* 1.1. In addition to the magnetostrictive effect there exists the inverse magnetostrictive effect, discovered 1865 by Villari [97], which describes the change in magnetization when applying external mechanical stress. Following the direction convention, as introduced in *Figure 1.1(b)*, both effects can be expressed as

$$S_i = p_{ki}^m H_k + s_{ij}^H \sigma_j \quad (2.7)$$

$$B_m = p_{mj}^m \sigma_j + \mu_{mk}^{\sigma} H_k \quad (2.8)$$

using the same matrix convention as in equations 1.4 and 1.5. With the elastic compliance s^H at constant magnetic field H , the magnetic permeability μ^{σ} at a constant stress and the piezomagnetic coefficients p^m . The latter can be expressed as

$$p_{ki}^m = \frac{\partial S_i}{\partial H_k} = \frac{\partial \lambda}{\partial H_i}. \quad (2.9)$$

Typical values for the piezomagnetic coefficients are depicted in *Table 2.1*.

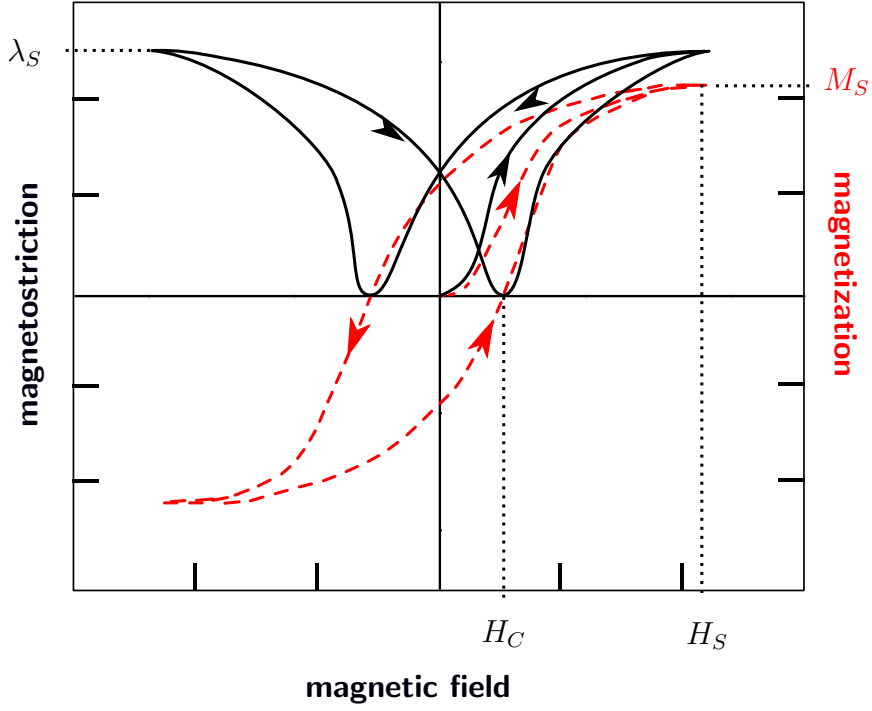


Figure 2.2: Generic magnetization curve with the corresponding magnetostriction.

Table 2.1: Magnetostrictive properties of commonly used materials, the data was extracted from [98].

Material	λ_S (ppm)	μ_r	d_m (ppm/mT)
Terfenol-D	2000	15	13
Galfenol	200	20	10
Metglas 2605SA1	40	40 000	40

2.2 MECHANICAL RESONANCE

A mechanical system is in resonance if the amplitude of the oscillation is increased when externally excited with a specific, so called, resonance frequency. Concerning a bar that is clamped on one side the oscillation can be torsional, transverse and longitudinal. The two latter are important for the mechanics of vibrating sensors as ME Sensors and will be described in the following.

For harmonic oscillations the frequency f (Hz) is commonly described by an angular frequency ω (rad/s) defined as

$$\omega = 2\pi f \quad (2.10)$$

Following Newton's second law the damped oscillation can be expressed as

$$\ddot{x} + 2\zeta\omega_0\dot{x} + \omega_0^2x = \frac{F(t)}{m} \quad (2.11)$$

with place x , damping constant $\zeta = c/(\sqrt{mk})$, damping coefficient c , eigenfrequency $\omega_0 = \sqrt{k/m}$, spring constant k and external driving force F . Using a periodic force $F = F_0 \sin(\omega t)$ with an amplitude F_0 and frequency ω the amplitude of the resonator can be described by

$$x_0 = \frac{F_0}{m\sqrt{(\omega_0^2 - \omega^2)^2 + (2\omega\omega_0\zeta)^2}}. \quad (2.12)$$

A resonance of the system is observed if excited with a resonance frequency

$$\omega_r = \omega_0\sqrt{1 - 2\zeta^2}. \quad (2.13)$$

The resonance peak shape is usually characterized by the quality factor

$$Q = \frac{1}{2\zeta} = \frac{\omega_r}{\omega_\Delta} \quad (2.14)$$

with the bandwidth ω_Δ being the width of the resonance curve at a level $1/\sqrt{2}$ of the maximum amplitude. *Figure 2.3* shows three generic resonance curves of oscillators with an eigenfrequency $f_0 = 1000 Hz$ for three different damping coefficients. For very low damping $\zeta \ll 1$ the system has a resonance frequency of $\omega_r \approx \omega_0$ and a high Q-factor. The height of the resonance peak decreases with increasing damping and the resonance peak shifts to lower frequencies.

The transverse eigenfrequency ω_{t0} of a cantilever depends on geometric factors, as thickness t and length l , and on material specific properties, as density ρ and Young's modulus Y . For a long thin cantilever ($t \ll l$ and $w \ll l$) the eigenfrequency is independent of the width w and can be expressed as [99]

$$\omega_{t0} = \frac{nt}{\sqrt{12}l^2} \sqrt{\frac{Y}{\rho}}, \quad n = \begin{cases} 1.875, & \text{for the first mode} \\ 4.694, & \text{for the second mode} \\ 7.855, & \text{for the third mode} \\ \vdots & \end{cases} \quad (2.15)$$

The longitudinal eigenfrequency ω_{l0} is independent of the thickness and described by

$$\omega_{l0} = \frac{(2n+1)\pi}{2L} \sqrt{\frac{Y}{\rho}}, \quad n = \begin{cases} 0, & \text{for the first mode} \\ 1, & \text{for the second mode} \\ 2, & \text{for the third mode} \\ \vdots & \end{cases} \quad (2.16)$$

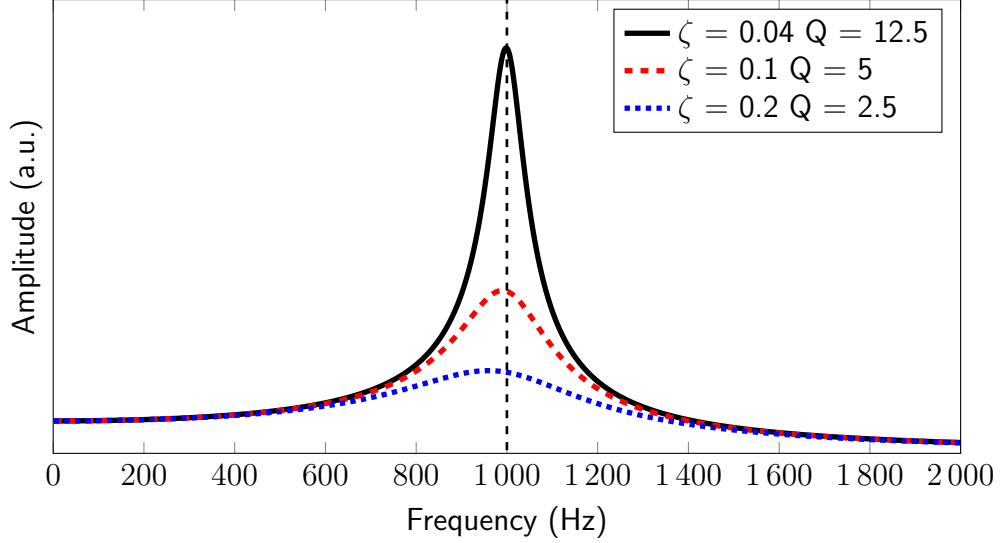


Figure 2.3: Generic resonance curves for oscillators with eigenfrequency $f_0 = 1000 \text{ Hz}$ and different damping. An increase in damping ζ is shifting the resonance frequency to lower values and reducing the quality factor Q of the oscillator.

2.3 FECOSIB

Metallic glasses, first developed in 1960 [100], are metallic alloys that lack a crystalline structure and therefore obey a unique combination of mechanical and magnetic properties. First metallic glasses were prepared by rapid cooling techniques which only allowed the production of thin films. Later, alloys were created which required relatively low cooling rates and thus bulk metallic glasses could be created [101–103]. The amorphous compound FeCoSiB is a metallic glass also known under its commercial name *Metglas*[®]. In the here presented work two different types of FeCoSiB have been used. Commercial *Metglas*[®] 2605SA1 foil with a thickness of $70 \mu\text{m}$ was used for the 2-1 ME Sensors as described in *chapter 12*.

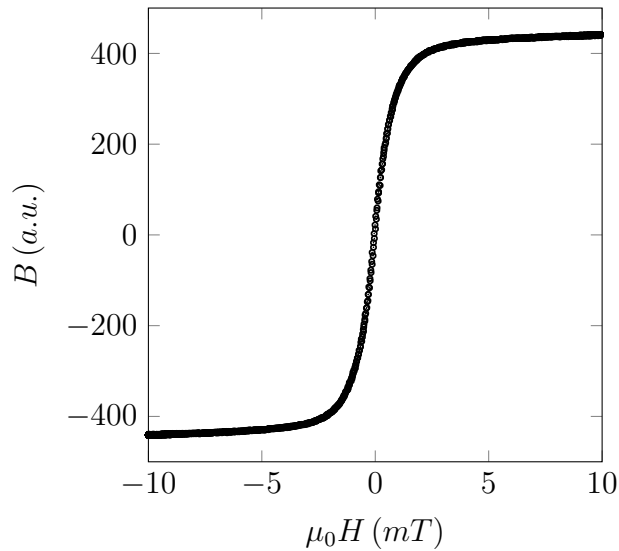


Figure 2.4: Magnetization curve of used metglas foil (measured by K. Meurisch).

Figure 2.4 shows a magnetization curve of a sample of *Metglas*[®] 2605SA1 (measured by Kerstin Meurisch). Sputter deposited films using a sputtering target (supplied by *EVO-CHEM Advanced Materials*) with a diameter of 50 mm and a thickness of 1.5 mm with a stoichiometry of $(\text{Fe}_{90}\text{Co}_{10})_{78}\text{Si}_{12}\text{B}_{10}$.

3 MAGNETO-ELECTRIC COMPOSITES

The occurrence of an electric polarization P when a magnetic field H is applied is called magnetoelectric (ME) effect. The effect was predicted for Cr_2O_3 by Dzyaloshinskii [104] in 1960 and proved experimentally by Astrov [105] only a few months later. The direct magnetoelectric effect was found for various materials and investigated intensively [106–113]. Since the magnitude of the effect was too small for applications the interest was only of a scientific point of view. In 1972 van Suchtelen [114] claimed that the combination of materials can lead to product properties as the indirect magnetoelectric effect. For this effect a magne-

tostrictive material is mechanically coupled to a piezoelectric material causing a magnetoelectric effect with the effective magnetoelectric coefficient

$$\alpha = \frac{\partial P}{\partial H} = \kappa \frac{\partial P}{\partial \sigma} \frac{\partial \sigma}{\partial \lambda} \frac{\partial \lambda}{\partial H} = \kappa d p^m \quad (3.1)$$

with mechanical coupling between the two phases κ , electric polarization P , magnetic field H , mechanical stress σ and magnetostriction λ . The piezoelectric and piezomagnetic coefficients are represented by d and p^m respectively. For magnetoelectric sensors it is common to give the magnetoelectric voltage coefficient α_{ME} as a figure of merit

$$\alpha_{ME} = \frac{\partial E}{\partial H} = \frac{d_{ij}}{\varepsilon_0 \varepsilon_{r,ij}} \kappa p_{kl}^m \quad (3.2)$$

with the relative permittivity ε_r . To realize a ME sensor consisting of a piezoelectric and a magnetostrictive phase various geometries are possible as depicted in *Figure 3.1*. The composites are typically named after the dimensionality of the individual phases. The 1-3 composites (*Figure 3.1(b)*), 2-1 composites (*Figure 3.1(d)*) and 1-1 composites (*Figure 3.1(e)*) contain at least one 1D phase and are promising candidates for ME sensor devices.

The 2-1 and 1-1 composites were investigated in the presented work. A single nano or micro scaled piezoelectric needle is necessary to realize these geometries. The preferred c-axis growth of ZnO combined with the large piezoelectric d_{33} coefficient makes it an excellent material for 2-1 and 1-1 ME sensors.

The 2-1 geometry is similar to the 2-2 geometry since both require a 1D piezoelectric phase but differ in crucial details. For both sensors the magnetostriction leads to a bending of the substrate causing an oscillation for alternating magnetic fields. The strain in the device is not homogeneous and depends on the position and clamping [115]. For single clamped sensors the strain is decreasing with the distance to the clamping. Sensors that are clamped on both sides have a maximum strain in the center between the two clampings. The advantage of the 2-1 geometry is that the position of the piezoelectric phase can be easily adjusted and positioned at the maximum strain position to increase sensitivity. This positioning also allows the use of higher resonance modes without any reverse effect as depicted in *Figure 3.2*. *Figure 3.2(a)* shows the side view of a 2-2 ME sensors in resonance in the first longitudinal mode. The strain distribution of the piezoelectric film is indicated by the color profile, showing a maximum strain in the center. Since the complete film is strained a piezoelectric potential builds and a voltage can be

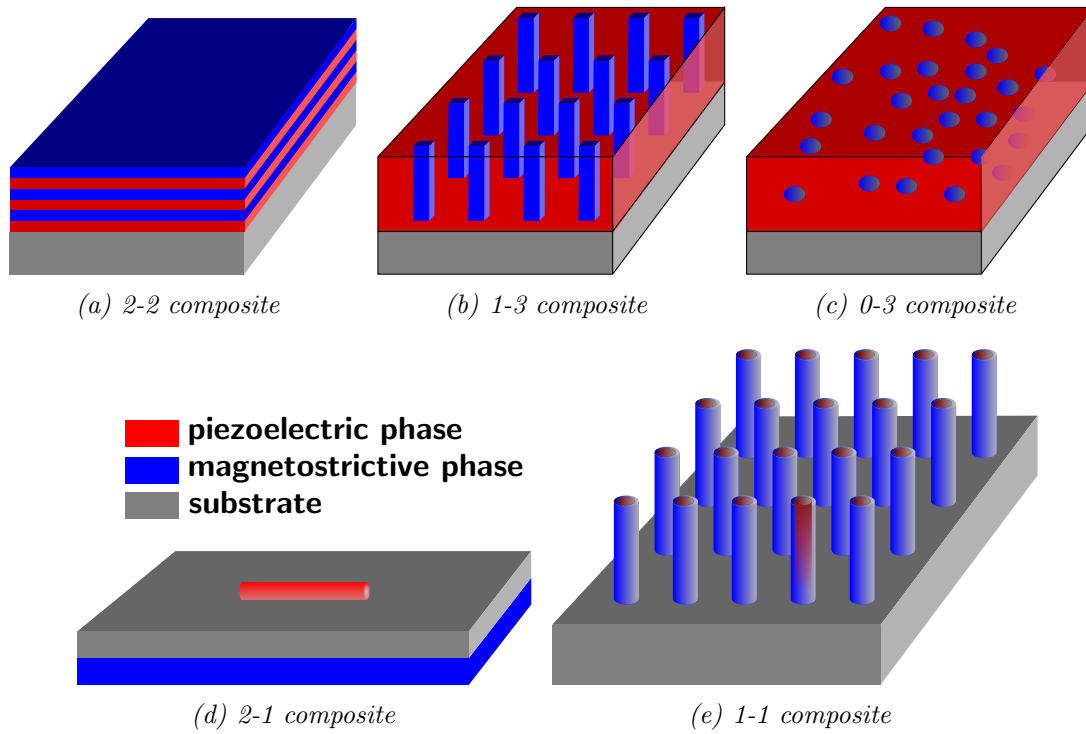


Figure 3.1: Dimensionality of two phase ME sensors. The geometries a)-c) are applied in other project involved in SFB 855 whereas the investigation of the geometries d) and e) is part of the presented work.

measured as indicated by the arrow. The second longitudinal mode, as shown in *Figure 3.2(b)*, results in a strained region (red) and a compressed region (blue). The resulting piezoelectric potentials are indicated by the arrows above, showing the same size but an opposing direction. Thus the resulting voltage is zero and the sensor will not create any useful signal in this mode. The third longitudinal mode, compare *Figure 3.2(c)*, creates two strained and one compressed region. This results in only a small total voltage since the compressed region reduces the created voltage.

Figure 3.2(d) shows a sensor that is only partially covered with a piezoelectric phase. If the piezoelectric material is positioned at the point of maximum strain in the center a piezoelectric potential builds, causing a voltage which can be measured as indicated by the arrow above. The same applies for higher longitudinal modes (*Figure 3.2(e)* & *Figure 3.2(f)*), where the piezoelectric phase is always at the position of maximum strain. Since the local strain is even higher when using higher modes, the sensitivity could possibly be increased when using higher modes.

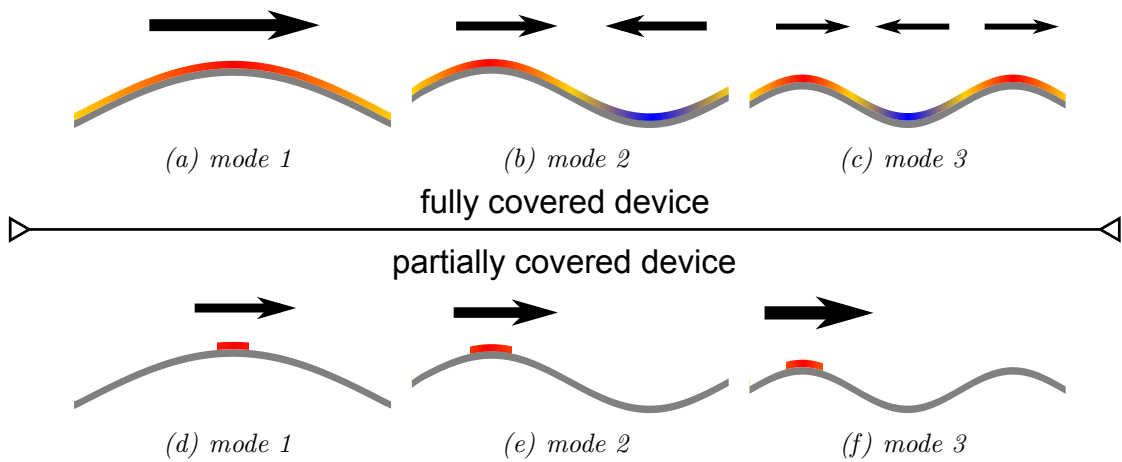


Figure 3.2: Longitudinal vibration modes of 2-2/2-1 sensor geometries that are fully covered with a piezoelectric phase a)-c) and partially covered with a piezoelectric phase d)-f). The substrate is indicated as gray, the piezoelectric phase is marked red under tension and blue under compression. The arrows qualitatively show the piezoelectric voltage.

Also it is possible to position the piezoelectric phase in the center of the device to allow the usage of all odd modes with the same device. The utilization of the 2-1 geometry with a piezoelectric ZnO needle is very promising for partially covered devices since the position for mounting can be easily selected.

PART II

SYNTHESIS

For the synthesis of metal oxide micro- and nanostructures a large variety of routes is available. Common examples are Magnetron sputtering [116, 117], chemical vapor deposition [118, 119], RF sputtering [120], molecular-beam epitaxy [121, 122], pulsed-laser deposition [123], metal-organic chemical-vapor deposition [124] and hydride or halide vapor-phase deposition [119, 125].

The development of various setups necessary for the preparation and characterization of samples was a major part of the presented work and divides in these main parts:

- **Conception:** In the planning phase of a new experimental setup it has to be decided which requirements have to be fulfilled. This holds for the whole setup as well as single components. A literature research provides information about the different possibilities to realize the setup. The final decision on the components is affected by available money, compatibility, security, support and availability. Electronic components should have computer interfaces and available software libraries (e.g. LabView VIs) to reduce the effort for the controlling. Whenever possible setups are designed in a modular way, since this makes it easier to modify the setup or reuse single modules in various setups.
- **Construction:** Since most setups consist of a large amount of individual parts the construction phase is necessary to investigate in which way the single components can be combined. The CAD software *Autodesk Inventor 2010* for the construction of mechanical components as well as the combination of several components was used. For electronic components the communication through the available interfaces has to be investigated. Analogue

interfaces or incompatibilities may require the use of additional devices for signal translation, e.g., AD-converters etc.

- **Machining:** Whenever suitable commercially available parts are chosen to reduce the workload. But since the individual requirements are often too specific the parts have to be machined individually. The machining is performed in person for simple geometries and easy machinable materials. Complex parts are usually machined by the workshop of the Technical Faculty. In certain cases it is necessary to assign specialized companies with the machining or assembly of individual parts.
- **Assembly:** When all parts of a setup are available the assembly of the setup can start. The parts have to be assembled in the correct sequence and with regard to their technical specifications.
- **Controlling:** The software for the setup has to be developed using *National Instruments LabView*. This allows automation and data acquisition of the process. By choosing an appropriate design the software can also prevent the user from damaging the setup by the creation of interlocks and an error detection system. Depending on the prerequisites the driver software has to be developed or can be directly obtained by the manufacturer.
- **Testing:** The testing should always be performed for all parts individually if possible. For many parts the individual testing is not possible and thus the testing routines become more complex and the detection of error sources may become difficult. If all parts function as required a calibration may be necessary to assure the required precision.
- **Further Development:** Some setups start as a very small and simple system and are improved, modified or combined with other setups. Often this requires again all steps starting from conception.

The systems which were developed include a sputter deposition system, a VLS synthesis setup, a ME characterization system, a piezoelectric characterization setup and various smaller electronic, mechanical and electromechanical characterization systems. The details of the individual systems are described in the corresponding chapters.

In the following three chapters different synthesis routes are described: the classical Vapor-Liquid-Solid method, the new developed flame transport synthesis and the sputter deposition.

4 VAPOR LIQUID SOLID

The VLS technique offers the possibility to grow a large variety of oxides. It was first described by Wagner and Ellis [126] in 1964. In this work the VLS process was used to obtain ZnO nano and micro crystals. The VLS developed system was also used for thermal and gas treatment of ZnO and with slight modifications for electrical characterization in a well defined atmosphere. *Figure 4.1* shows the concept for the classical VLS process for ZnO. A thin Au film is sputter deposited on a substrate. The heating of the substrate breaks the Au film in small droplets which are randomly distributed over the substrates surface. Classical lithography as well as self organized methods were already applied to achieve regular patterns of catalyst [127–132]. By providing an atmosphere of Zn vapor and O₂ the Au becomes enriched with Zn until a supersaturation leads to nucleation and growth below the Au droplet. Besides the VLS mechanism which leads to a growth [0001] direction a simultaneous VS mechanism causes a growth in $[2\bar{1}\bar{1}0]$ direction and thus an increase in diameter of rods grown ylong [0001] direction. Due to the large difference in growth kinetics the VLS mechanism is faster which results in structures with a relatively high aspect ratio. The conception and creation of the VLS setup, as schematically shown in *Figure 4.2*, was part of the presented work. The system was designed to control and log temperature, pressure and flow rates of oxygen and argon inside a quartz tube. The function of the individual components is as follows with the given numbers corresponding to the labels used in *Figure 4.2*.

A quartz tube (4) with an inner diameter of 40 mm is placed inside a tube furnace (3). The ends of the tube are bonded to custom made KF vacuum flanges using epoxy resin. To achieve a constant, low temperature at the flange water cooled fittings (2) are mounted on the vacuum flanges with a constant water temperature of 20°C. One end of the tube is connected to a rotary vane pump (12) whereas a gas inlet is mounted on the other side. Two gas flow controllers (6) define the

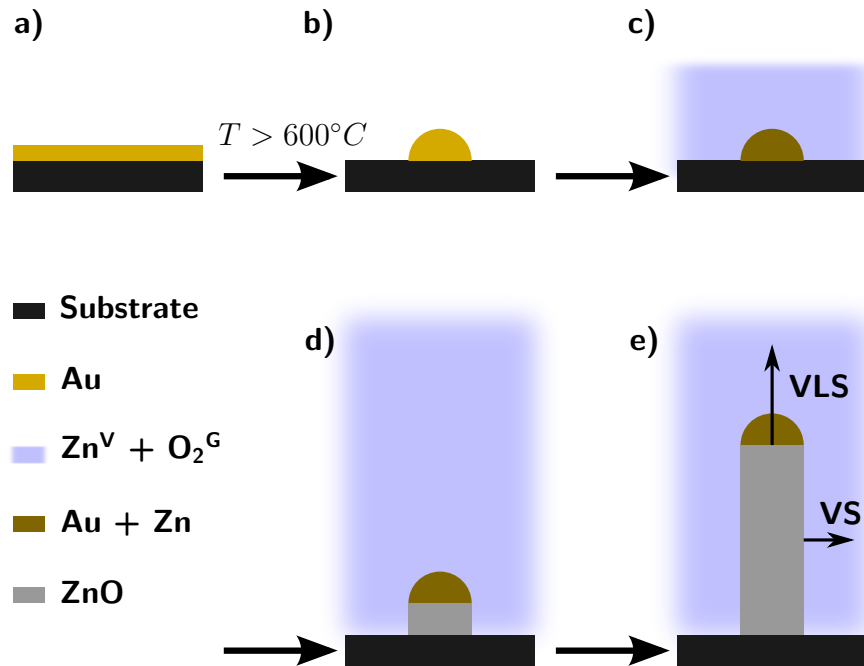


Figure 4.1: Schematic illustration of the VLS mechanism for ZnO using gold as a catalyst. a) A substrate covered with a thin catalytic Au film. b) The film contracts to small droplets upon heating. c) A vapor of Zn and O_2 is introduced to the reaction volume leading to the formation of Zn rich Au. d) With increasing Zn concentration the liquid Au gets supersaturated leading to the growth of ZnO below the liquid droplet. e) Simultaneous to the unidirectional VLS growth a Vapor Solid (VS) type of growth increases the thickness of the structures.

flow of argon and oxygen in the quartz tube. The communication to the gas flow controllers is established by a gas flow communication box (10). An electrically controlled valve (1) between the pump and the tube in combination with a Pirani gauge (5) allows the control of a defined pressure and therefore a defined flow of argon and oxygen through the quartz tube. A Pfeiffer RVC 300 was used to control the pressure in the system by monitoring the pressure and tuning the electrical valve using a PID controller. The temperature inside the tube is measured by two thermocouples (type K) as depicted in the cross sectional *Figure 4.3*. One thermocouple is positioned in the center of the furnace and connected to a PID Hengstler Grado 911 (11) to control the furnace power by switching a solid state relay. The second thermocouple is connected to a multimeter Voltcraft VC 820 to allow a temperature measurement at a second selectable position inside the tube. The gas flow communication box, the Voltcraft VC 820, the Pfeiffer RVC 300

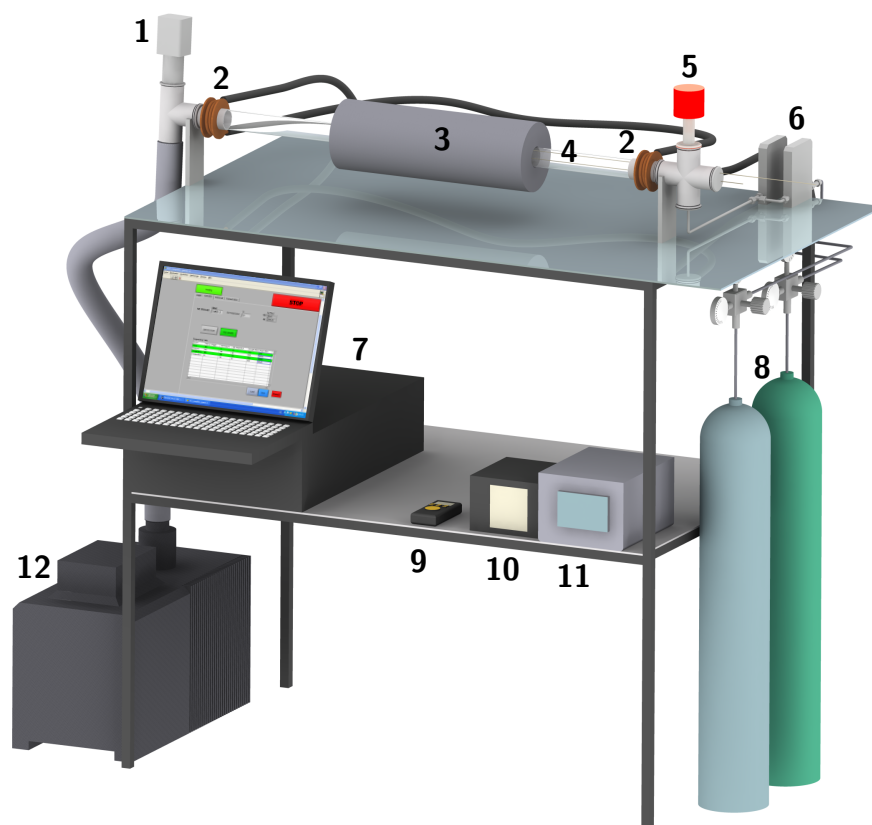


Figure 4.2: Conceptual view of the VLS synthesis system consisting of 1: electric gas valve, 2: water cooled copper fittings, 3: tube furnace, 4: quartz tube, 5: pressure gauge, 6: gas flow controllers, 7: controlling computer, 8: gas bottles with pressure reducers, 9: thermometer, 10: gas flow communication box, 11: temperature controller, 12: rotary vane pump.

and the *Hengstler Grado 911* are connected to a computer (7) using serial RS232 interfaces. A LabView based computer program was developed and written as part of this work. The program can be used to manually control each connected device, or to create parameter sets and automatically control a complete VLS run. During a synthesis run all process data are automatically recorded and written into a log file every second. The parameter data for each run is stored separately and can be loaded into the software again to guarantee a high reproducibility. A typical parameter set is shown in *Table 4.1*. Each row contains one complete parameter set that is transferred to the individual control units. The event trigger defines the conditions required to proceed with the parameter set of the next row. Time, pressure or temperature are allowed for triggering. A software routine defines the accuracy and stability necessary to accept a trigger as fulfilled. The recorded data

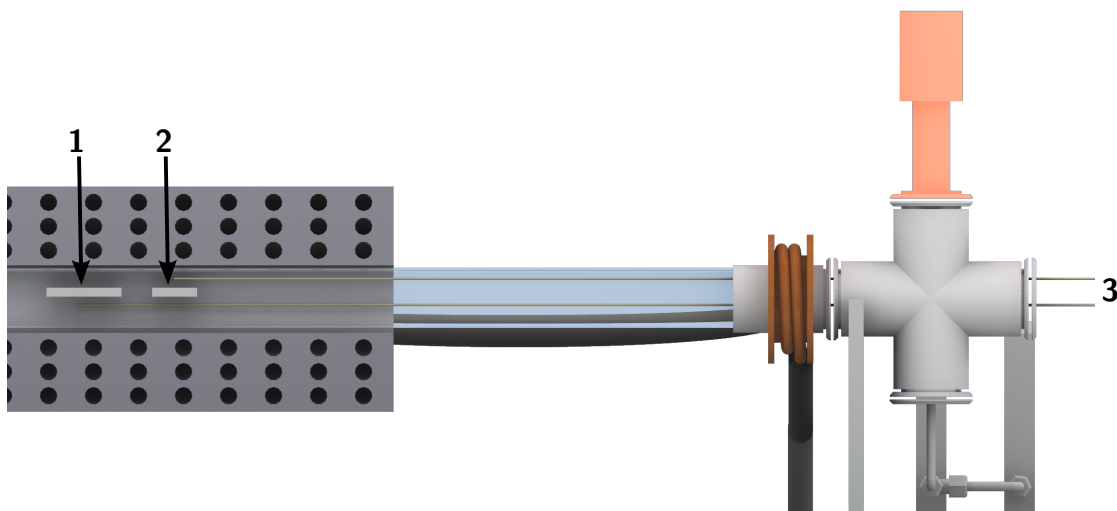


Figure 4.3: Cross sectional view of the VLS showing the positions of substrate (1), powder (2) and two thermocouples (3) measuring at the positions of (1) and (2).

of the run parameters shown in *Table 4.1* is shown in *Figure 4.4*. Details about the programming can be found in the appendix of this work, see *chapter C.1*.

4.1 STANDARD ROUTINE

In the following a typical run of the VLS setup is presented with the positions of powder and substrate as schematically depicted in *Figure 4.3*. A silicon substrate (1 cm x 1 cm) covered with a Au film, nominal film thickness 5 nm, is positioned 5 cm downwards from the furnace center. 0.9 g of a mixed ZnO/Graphite powder, weight ration 1, is inserted in the ceramic boat which is placed in the center of the furnace. The positions of the thermocouples are matching the positions of powder and substrate, with the furnace controlling thermocouple being positioned in the center of the furnace. Afterwards all flanges are fixed properly, the gas bottles are opened, the cooling system is checked and the vacuum pump is started. A *run-file* is created with the content shown in *Table 4.1* and saved on the computer. The functions of the individual lines are evacuating (1), Ar flushing (2), heating (3), VLS growth process (4) and cooling down (5). The latter is automatically inserted, giving an ambient pressure, room temperature and no gas flow. This is

Table 4.1: Work plan of a typical VLS experiment

#	Event	Trigger	Parameters			
			T ($^{\circ}$ C)	P (mbar)	O2 (sccm)	Ar (sccm)
1	Pressure	1 mbar	30	1	0	0
2	Pressure	1000 mbar	30	1000	0	100
3	Temperature	950 $^{\circ}$ C	950	1000	0	30
4	Time	1800 s	950	30	3	15
5	Temperature	30 $^{\circ}$ C	30	1000	0	0

also a security issue to force the system to stop heating and flows at the end of each process.

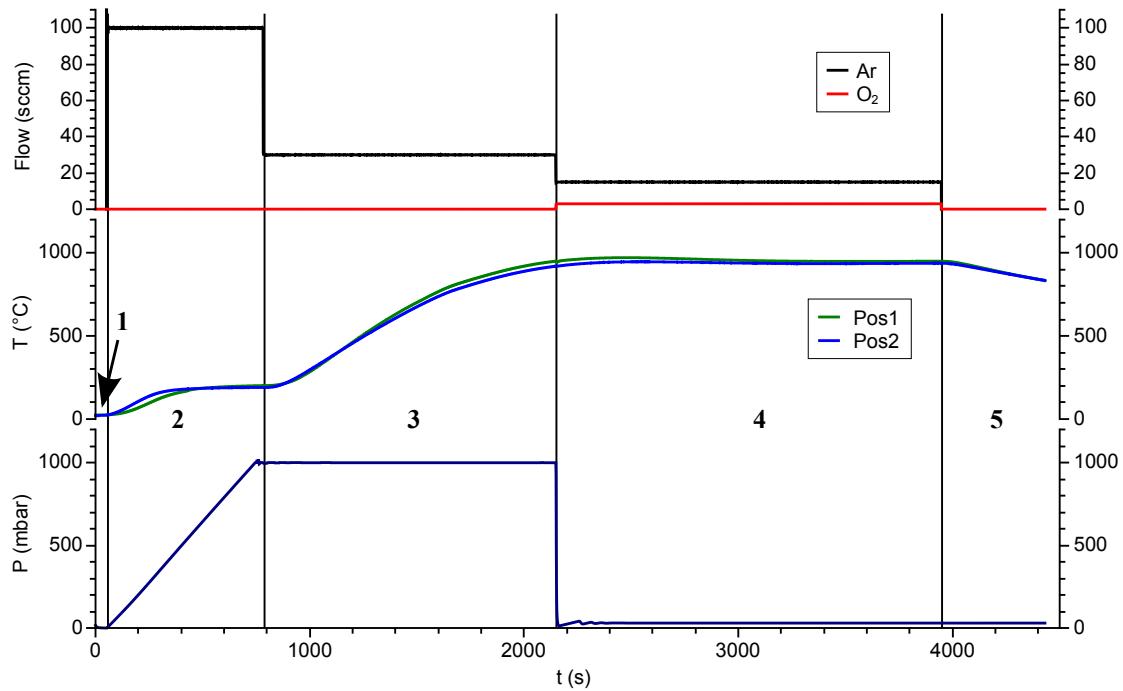


Figure 4.4: Logged data of a VLS run corresponding to the run file shown in table 4.1, with the numbers representing the run file line numbers. The temperatures belong to the positions of powder (Pos1) and substrate (Pos2).

When starting the process the parameters listed in line 1 are transferred to the individual control units. The software is monitoring all parameters every second and waiting for the trigger. In the presented case the software starts waiting for the pressure to reach 1 mbar, for a duration and precision defined by the software.

After reaching the desired pressure the parameters in line 2 are transferred and a new trigger is activated. This procedure repeats as long as there exist new lines. The logged data of the complete run are depicted in *Figure 4.4*. It can be clearly seen that all parameters are controlled precisely. Only the temperature is too high in the second zone. This is a result of the PID parameters of the *Hengstler Grado 911* which are optimized for high temperatures. Thus when performing experiments at low temperatures the PID parameters have to be modified in advance to allow a precise control without overshooting of the desired temperature. It can also be observed, that the temperature during the growth process (region 4) is stable and a small gradient between powder and substrate can be seen.

4.2 OBTAINED STRUCTURES

The parameters of the VLS were varied to investigate the influence of the growth process on the structural type. The structures were investigated using a *Zeiss Ultra Plus* SEM. A list of all investigated parameter sets can be found in the appendix, see *chapter A*. Repeated processes with the same parameters were carried out and a very good reproducibility was obtained proving the reliability of the setup.

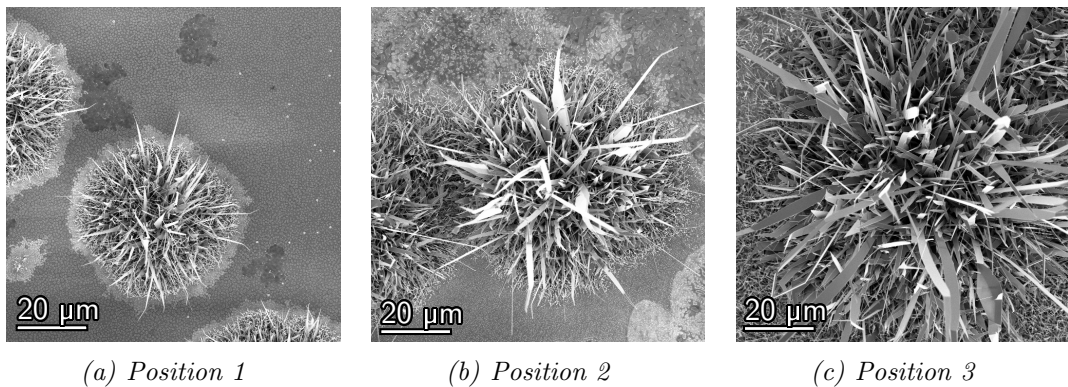


Figure 4.5: SEM images of VLS grown ZnO micro structures for varying substrate positions.

Figure 4.5 show SEM images for 3 samples which were all processed simultaneously at different distances to the ZnO powder. It can be seen that the amount of grown structures increases from position 1 over position 2 to position 3. The shape of the obtained structures is also affected by the position. Whereas most structures at position 1 have a pronounced 1D shape, the 2D shape can be ob-

served at position 2 and is even more expressed at position 3. This finding is a result of the temperature gradient inside the quartz tube and thus can be directly referred to the temperature at the position of the substrate. Since an investigation of the complete parameter space is not possible the focus on the synthesis was to investigate which different morphologies are producible and how the individual parameters affect the size and shape of the structures.

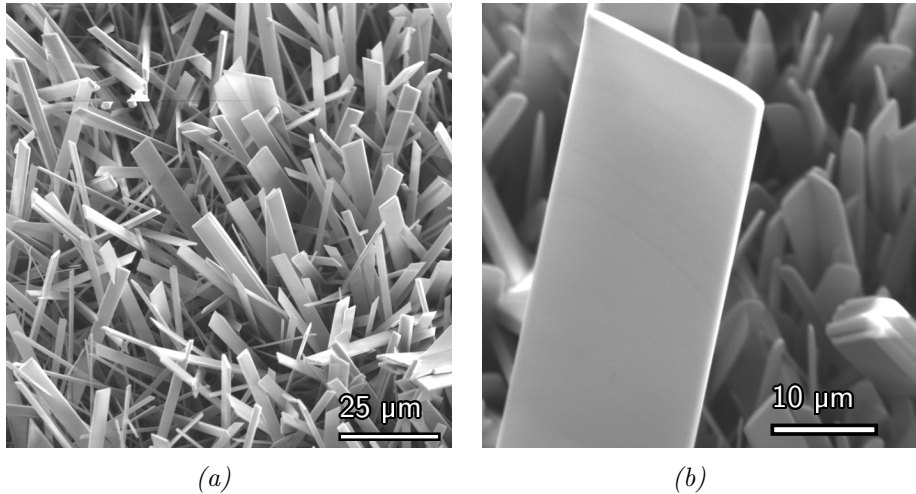


Figure 4.6: SEM images of 2D sheet like ZnO structures produced by VLS.

Figure 4.6 shows 2 dimensional ZnO structures grown by VLS. This structural type is a result of two different growth modes and was described by Zhang [133]. Already at 500°C growth in $[2\bar{1}\bar{1}0]$ direction is initiated which leads to a rod like structure. When holding at a temperature of 750°C growth in $[0001]$ direction occurs leading to a 2 dimensional sheet like single crystal.

Various types of network structures can be realized by VLS. Figure 4.7 shows four interconnected ZnO networks consisting of different basic building blocks. The networks homogeneously cover the substrates and show only a small extend perpendicular to the surface of the substrate.

VLS allows the production of ZnO single crystals with clearly pronounced hexagonal facets. Typical diameters of the hexagonal crystals are $1-10\ \mu\text{m}$, as illustrated in Figure 4.8.

The synthesis of rod like ZnO structures is shown in Figure 4.9. These structures can be obtained with hexagonal and rectangular cross section. Crystal lengths up to several $100\ \mu\text{m}$ could be achieved by VLS.

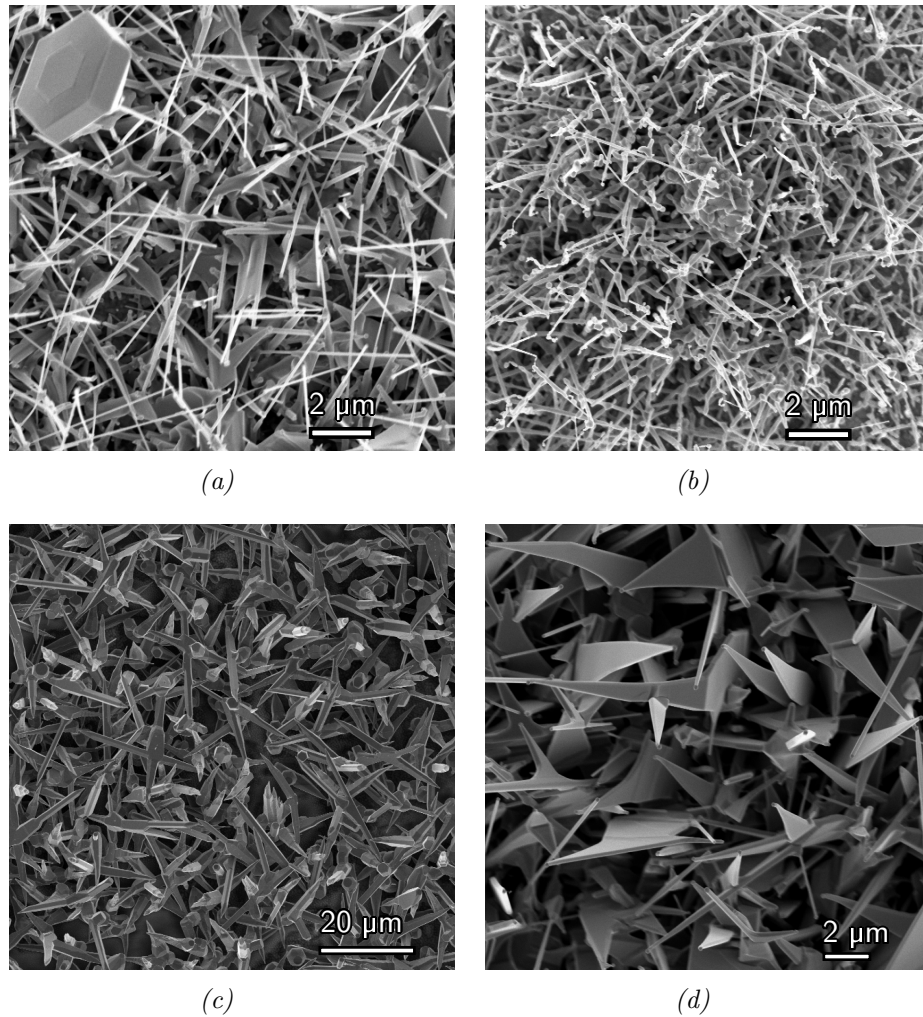


Figure 4.7: SEM images of ZnO network structures consisting of different basic building blocks.

Drawbacks of the used device is the small volume of structures that can be produced. The limiting factors are the diameter of the tube and therefore the maximum amount of powder which can be inserted, and the strong effect of the substrate positioning. Together with the relatively high heat capacity of the system and the resulting slow heating and especially cooling rates a maximum of 5 cm^2 substrate area can be coated homogeneously per day. Also the maximum size of individual structures is limited in VLS growth if compared to other methods. Overall it can be summarized that VLS is capable of producing a large variety of structures with an excellent reproducibility but strong size limitations.

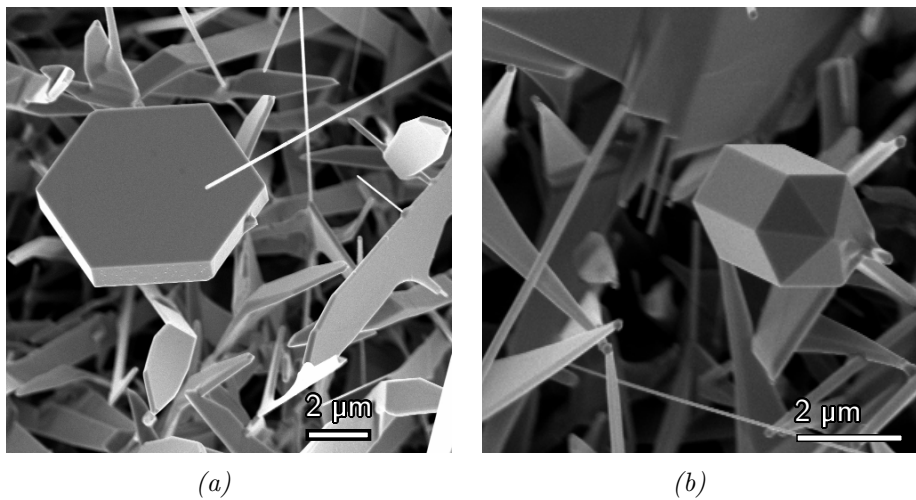


Figure 4.8: SEM images of ZnO structures with pronounced hexagonal facets.

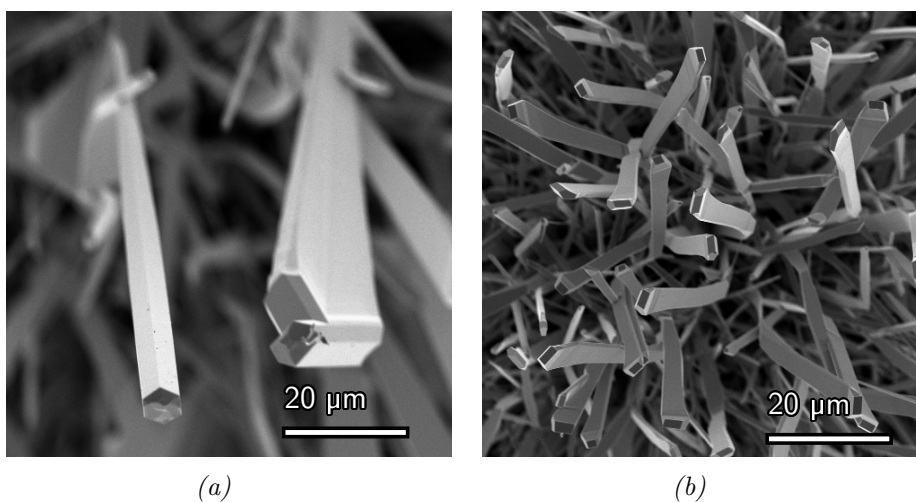


Figure 4.9: SEM images of high aspect ratio ZnO structures.

5 FLAME TRANSPORT

The flame transport synthesis (FTS) is a newly developed method for the synthesis of various metal oxide nano- and microstructures which offers a large number of possible geometrical configurations. The simplicity and cost effectiveness of

the FTS as well as the scalability and versatility are important advantages over conventional synthesis routes. The following detailed description of the different variants of FTS is partially excerpted from [134].

The fundamental idea of the FTS synthesis is a self controlled process in which metal precursor particles are mixed with the sacrificial polymer polyvinyl butyral (PVB) and ethanol. When heating above a certain critical temperature a spontaneous combustion ignites the mixture and the synthesis is controlled by the resulting flame. The size, shape and interconnections of the resulting structures are determined by the parameters of the FTS which are: amount and composition of the mixture, heating rate, geometry of the reactor and the position of substrates. To give an overview of the available synthesis three basic routes are described in the following. Different structures for different materials are shown with a focus on ZnO.

5.1 SYNTHESIS ROUTE 1: COATING

Metal micro particles in a mixture with PVB and ethanol form a highly viscous gel which is cast on the substrate, typically silicon, surface. When heating the substrate in a primitive muffle-type oven to temperatures above $800\text{ }^{\circ}\text{C}$ with heating rates higher than 100 K/min , the gel ignites and indicates the start of the synthesis process. During the synthesis the burning of the ethanol and PVB causes a stable temperature and low oxygen partial pressure inside the flame. A metal oxide shell is encapsulating an inner metal core and the transport from the core to the surface is dominated by the diffusion at grain boundaries. Thus metal oxide needles start to grow on the surface at the positions of the grain boundaries. *Figure 5.1(a)* illustrates this growth process for a single core spike particle. The investigation of individual spikes with TEM revealed that the spikes have a twin boundary which is most likely effecting the growth mechanism and determines the shape of the spikes [135] as further described in *chapter 8.2*.

By investigating the overall amount of created core spike particles it can be seen that the PVB, besides its role of consuming the oxygen, also helps separating the individual particles at the beginning of the process. The result is an interconnected network of metal oxide core spike particles, where the interconnection is established by interpenetration and interlocking of individual spikes, compare *Figure 5.2(a)*.

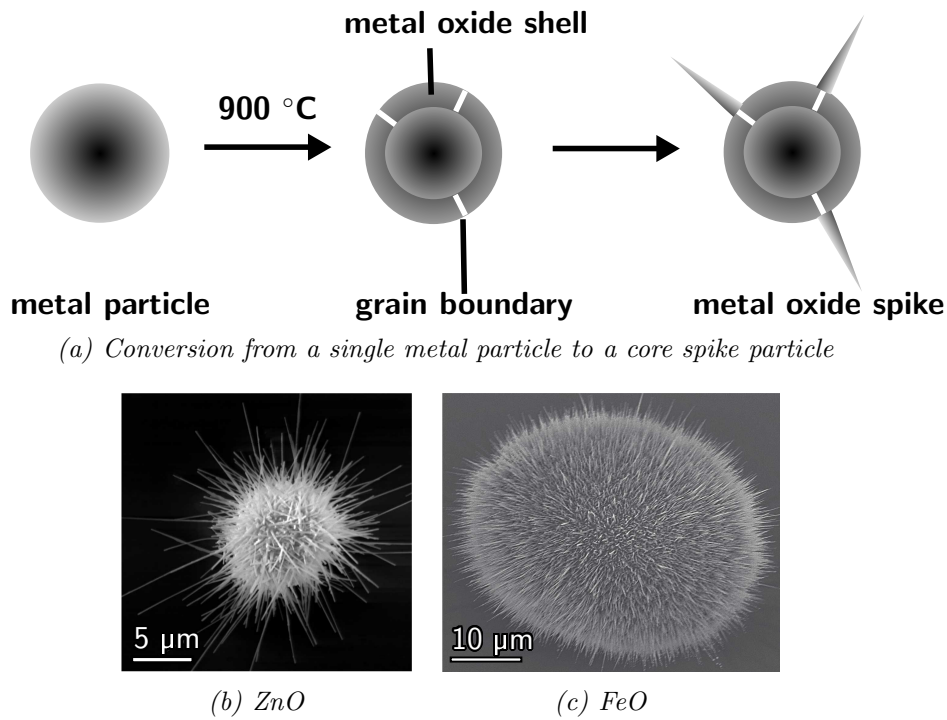


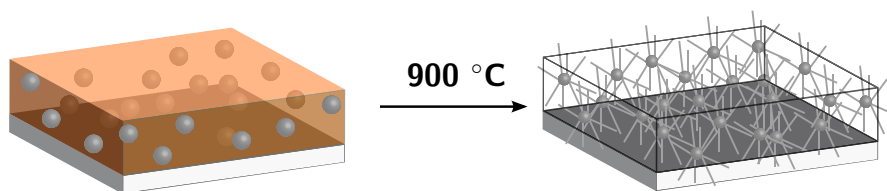
Figure 5.1: Core spike particle evaluation as a schematic (a) and SEM images of ZnO (b) and FeO (c) particles.

Figure 5.2 further shows successfully grown metal oxide networks with Bi (b), Al (c), Fe (d) and Zn (e)–(h) as a precursor material.

The formation of an interconnected network with metal oxide building blocks has some great advantages over conventional materials. The combination of high temperature stability, chemical inertness and mechanical flexibility is typically not possible for conventional materials. Whereas metals are often reactive or tend to oxidize, ceramics are brittle and even high temperature polymers like Polyimide cannot withstand temperatures above 400 °C [136]. Therefore the basic idea was to add flexibility to a ceramic by using a microstructured network.

The reduction of the feature size is a common tool to increase the flexibility of a material as commonly observed if comparing the flexibility of a window glass and a thin glass fiber. The mechanism behind this mechanical improvement can be easily described by calculating the shear stress of a beam for varying diameters. Jourawski's formula [137] shows that the shear stress τ is inverse proportional to the material thickness t perpendicular to the shear

$$\tau \propto \frac{1}{t} \quad (5.1)$$



(a) Schematic of separated metal particles forming an interconnected network.

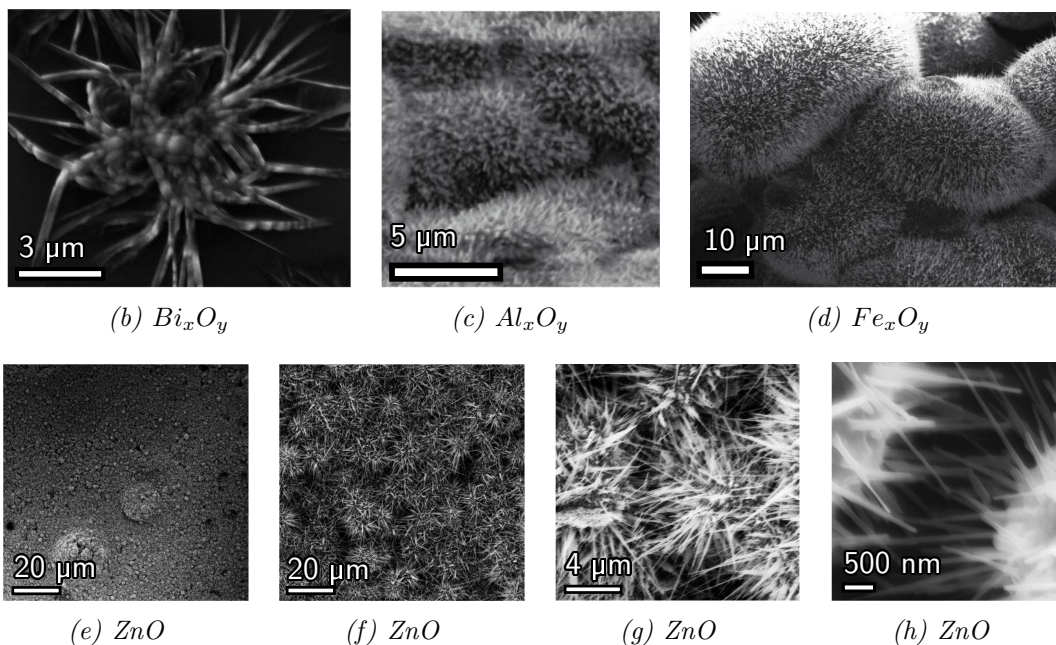


Figure 5.2: Core spike particle evaluation as a schematic (a) and SEM images of different metal oxide networks (b)–(h).

The challenge for achieving a flexible ceramic is to create basic building blocks which have a small feature size and interconnect them to build a macroscopic material. This goal was achieved using the FTS on a surface and a patent was granted for the synthesis route [138].

5.2 SYNTHESIS ROUTE 2: CRUCIBLE

As an alternative synthesis approach the mixture of metallic zinc powder, PVB and ethanol can be filled in a ceramic crucible which is placed inside a furnace. During heating the mixture ignites and the resulting flame is providing the high temperatures and the oxygen poor atmosphere for the growth of metal oxide nano- and microparticles. Besides, the flame is also acting as a transport medium, and

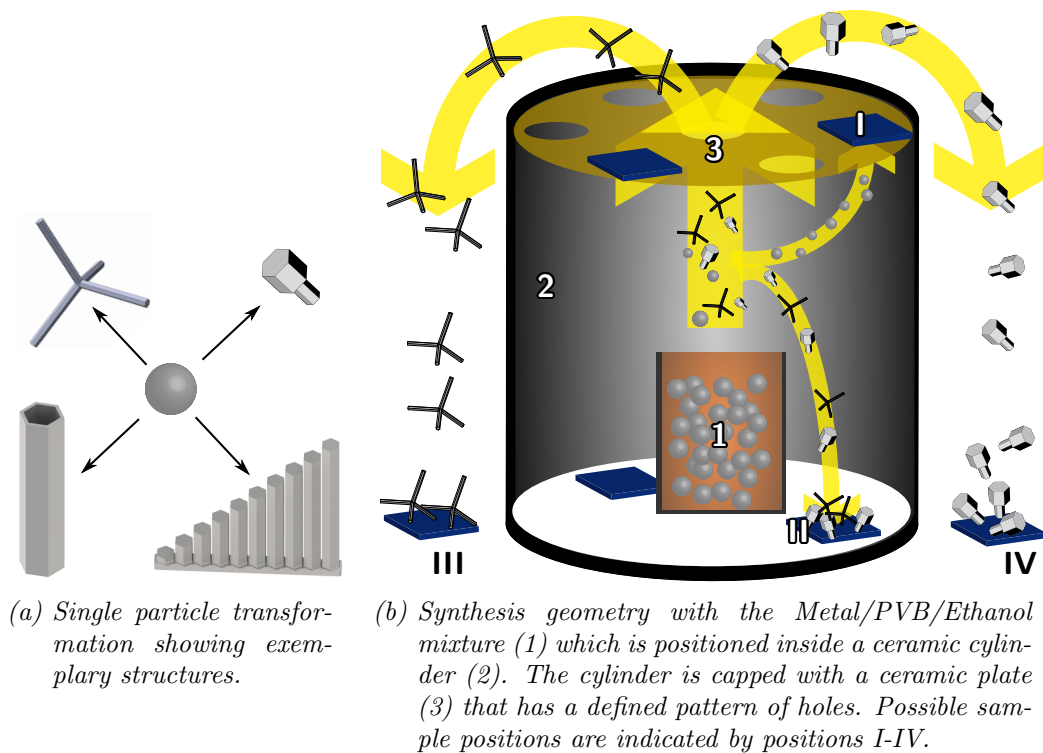


Figure 5.3: Schematic of the new developed flame transport synthesis showing a) possible particle transformations and b) a schematic of the used synthesis geometry.

carrying the grown structures to the substrate surface. The growth of a large variety of different structures on a desired substrate or as a powder is possible. The amount of the mixture, the temperature profile and the geometry of the setup are the dominating parameters that determine the growth of the structures. *Figure 5.3(b)* depicts schematically the geometry of the used setup.

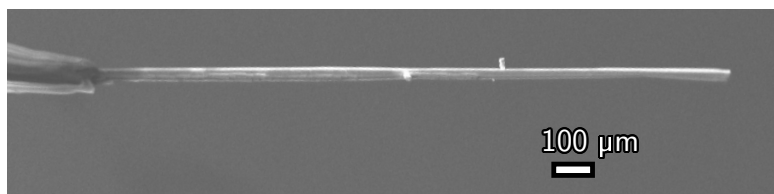


Figure 5.4: SEM image of a single ZnO rod created using the flame transport synthesis. The rod is mounted on a glass capillary as seen on the left side.

Two fundamental different growth types of structures exist: growth inside the flame and growth on the surface. The growth in the flame yields individual structures which may interconnect during growth and get deposited on a substrate as an interconnected network. Various building blocks for these networks are possible as illustrated in *Figure 5.3(a)*. *Figure 5.5* shows a network consisting of ZnO tetrapods whereas *Figure 5.6* shows another ZnO network with hammer shaped building blocks. The SEM images in *Figure 5.7* show a network consisting of hollow ZnO tetrapods. As obvious from these images the shape of the building blocks can be selected by the synthesis parameters and only one type of structure will form.

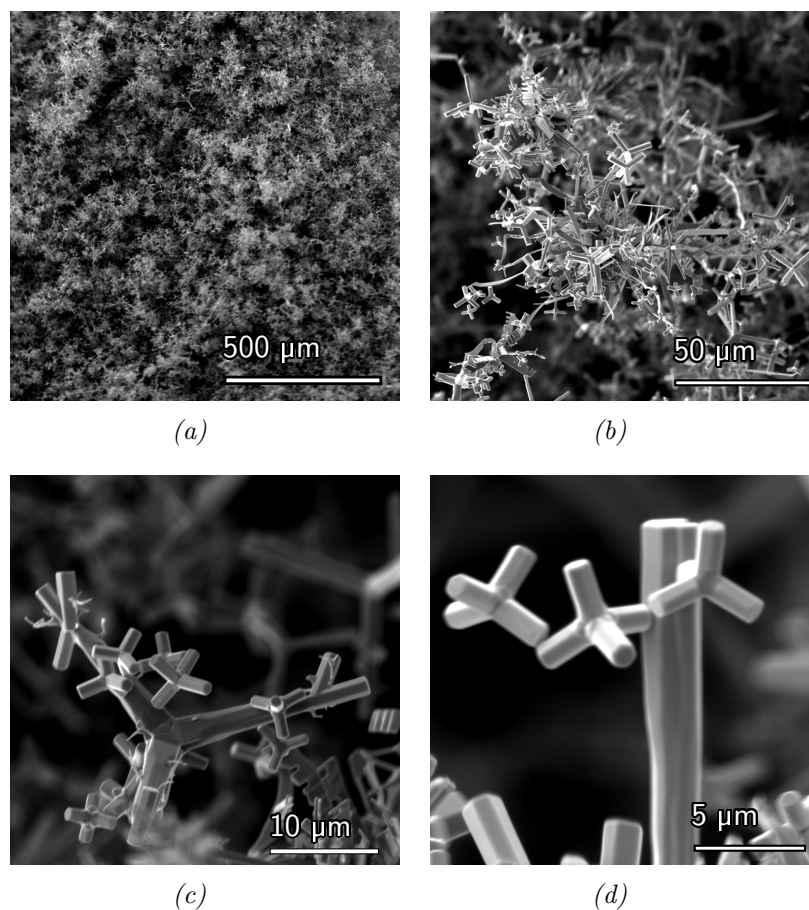


Figure 5.5: SEM zoom series of a ZnO network consisting of interconnected tetrapod shaped building blocks.

The structural variations arise from the different growth conditions during the flight to the substrate. The temperature, oxygen and zinc vapor concentrations as

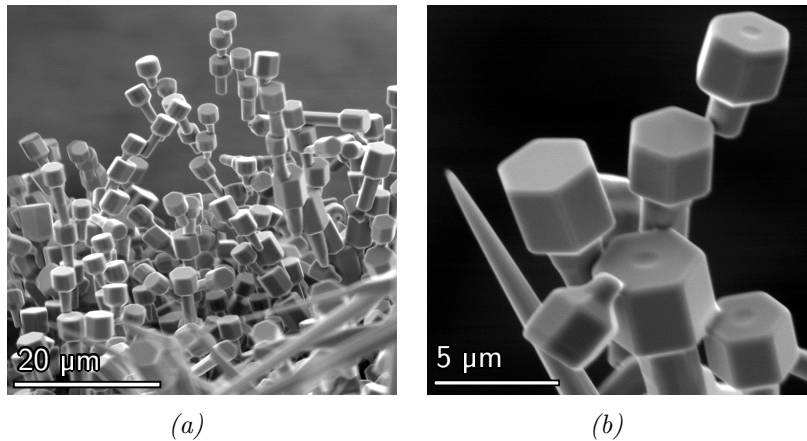


Figure 5.6: SEM images showing an interconnecting ZnO network consisting of hammer shaped building blocks.

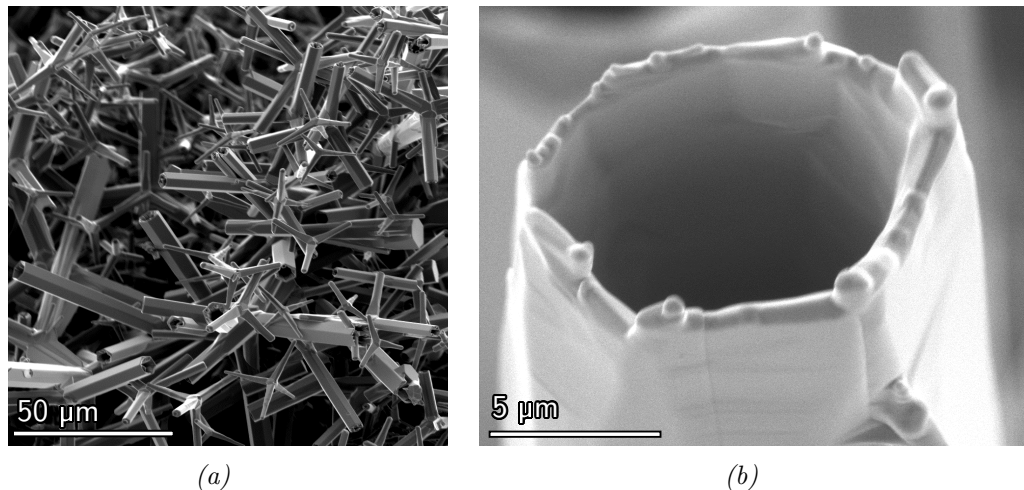


Figure 5.7: SEM images showing (a) a network of hollow ZnO tetrapods and (b) a magnification of an individual hollow rods.

well as the growth times vary depending on the substrate position. Structures that get deposited close to each other are likely to have similar trajectories and thus similar growth conditions. Therefore the structural variations of adjacent building blocks is only small and the resulting structures are independent from the used substrate. The dominating growth mechanism for this type of synthesis is the VS growth.

The second type of growth mode, growth directly on the surface, is not creating networks of individual building blocks, but a regular, aligned coverage of a sub-

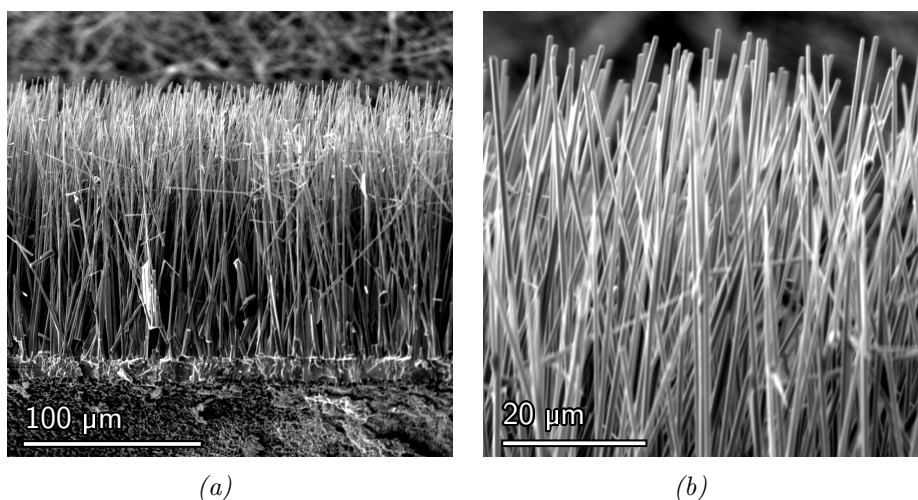


Figure 5.8: Cross sectional SEM view of parallel ZnO rods with high aspect ratio perpendicularly grown on a Si substrate.

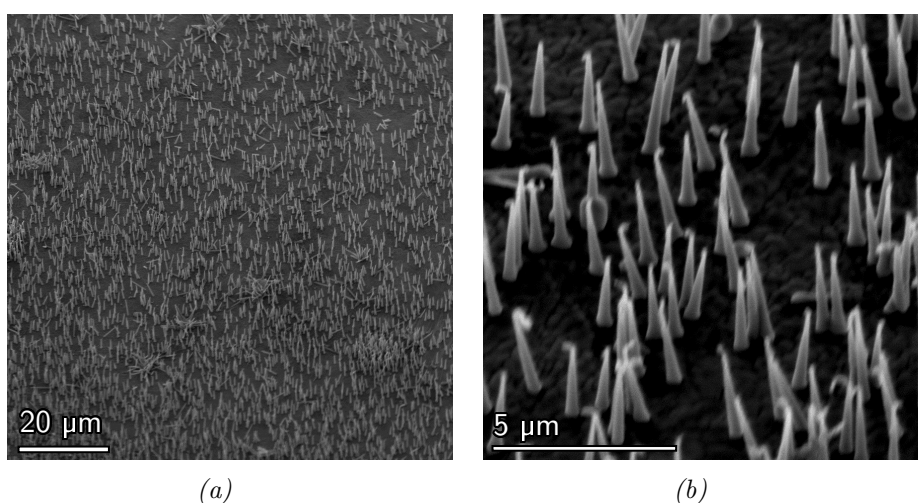


Figure 5.9: SEM image showing a homogeneously coverage of a Si substrate with perpendicular oriented ZnO rods with a relatively low aspect ratio.

strate with a single structural type. Depending on the position of the substrate various types of structures can be grown, examples are parallel rods with high (*Figure 5.8*) and low (*Figure 5.9*) aspect ratio, large microrods (*Figure 5.4*), columnar growth (*Figure 5.10*) and nail shaped structures (*Figure 5.11*). Analogous to the growth in flame adjacent structure exhibits a similar structure which is a result of the same growth conditions. The regular alignment of the structures, which cannot be observed for the growth in flame, is dominated by the temperature gradient,

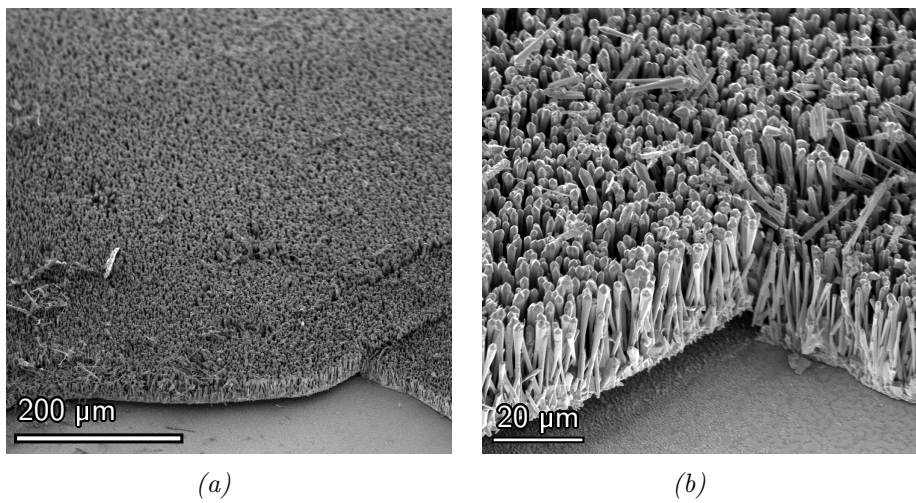


Figure 5.10: SEM images of columnar grown ZnO microrods.

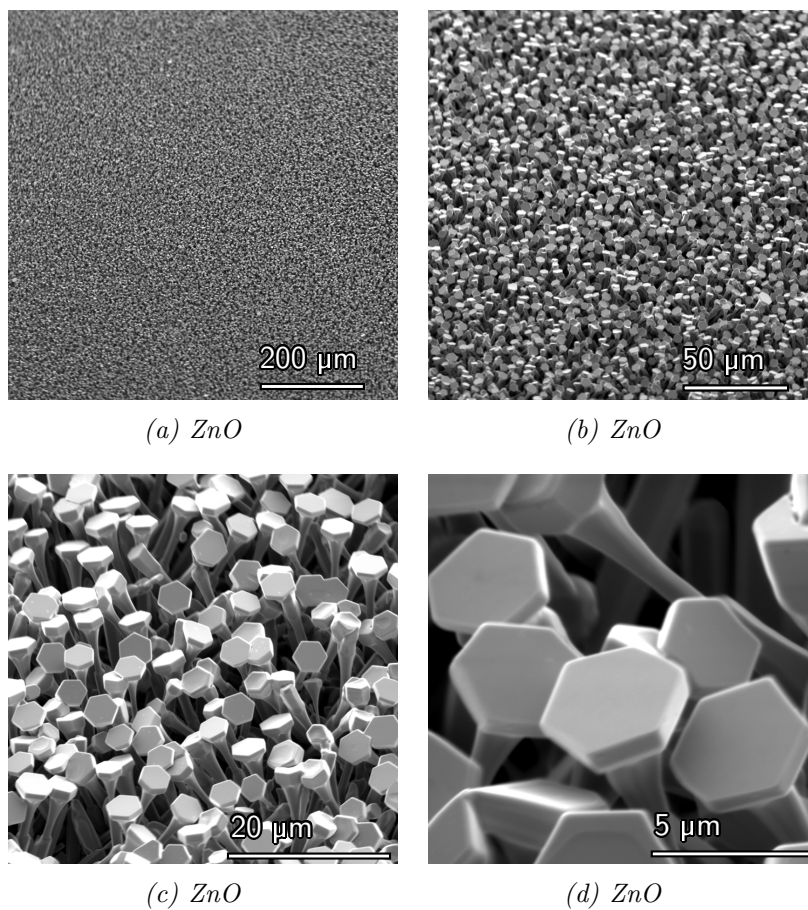


Figure 5.11: SEM zoom series of nail shaped ZnO micro structures created using FTS.

the concentration gradient and the choice of substrate. The substrate's influence to ZnO growth is well known and described e.g., for Si [139], SiC [140], GaAs [141] and CaF₂ [142]. Additionally mechanism of growth can be affected by using a catalyst to enforce VLS types of growth as described in *chapter 4*. Under certain conditions and in the absence of an additional catalyst the self catalyzed growth can be observed [143].

5.3 SYNTHESIS ROUTE 3: FLAME SPRAYING

The third variant of the FTS is the utilization of the metal precursor powder in a spray gun as shown in *Figure 5.12*. Analogue to conventional coating techniques the metal powder is filled in a reservoir of the spray gun. Upon use of the spray gun the Venturi principle [144] is applied to constantly feed the gaseous stream with metal particles. Using a gas mixture of propane and oxygen a stable flame is generated and the metal particles are transformed inside the flame causing a constant particle stream. Like conventional spraying techniques the particle stream can be easily adjusted and directed towards a desired substrate surface.

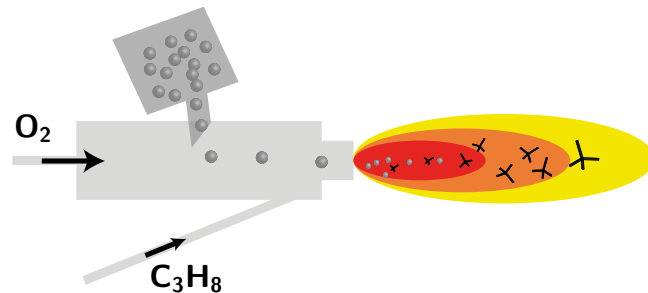


Figure 5.12: Schematic representation of the flame spraying variant of FTS.

The growth times inside the flame are short compared to the other FTS variants being in the order of milliseconds. Thus the structural variation is smaller compared to the other variants. The growth time or time inside the flame is the dominating synthesis parameter and strongly affects the resulting structures as depicted in *Figure 5.13*. The growth time can be calculated using the distance between substrate and spray gun and the velocity of the particles in the flame which is assumed to be constant during their flight. It can be observed that short growth times of less than 1 ms (*Figure 5.13(a)*) will form a covering metal oxide

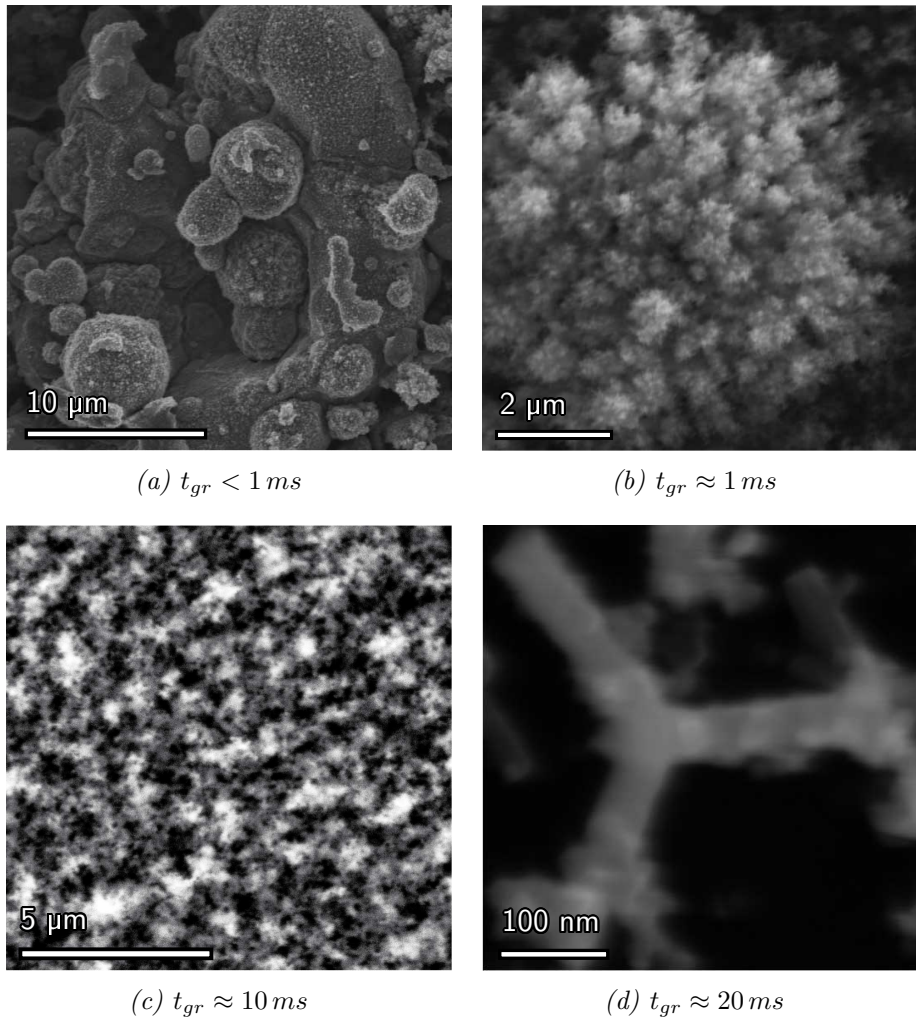


Figure 5.13: SEM images of structures grown by spray synthesis for different growth times t_{gr} .

layer on the substrate surface. For growth times from $1 - 10 \text{ ms}$ (Figure 5.13(b), Figure 5.13(c)) a porous network is synthesized with a higher porosity for larger growth times. A growth time of 20 ms is sufficient to grow networks consisting of tetrapod shaped building blocks, as shown in Figure 5.13(d).

It can be concluded that FTS offers new routes to synthesize various types of nano- microstructures using a simple and therefore cheap concept. Individual structures as well as interconnected networks can be created leading to a large amount of possible applications. Since the number of different structures is larger compared to the classical VLS approach, the FTS turned out to be superior and was selected for the production of ZnO structures for further processing.

6 SPUTTER DEPOSITION

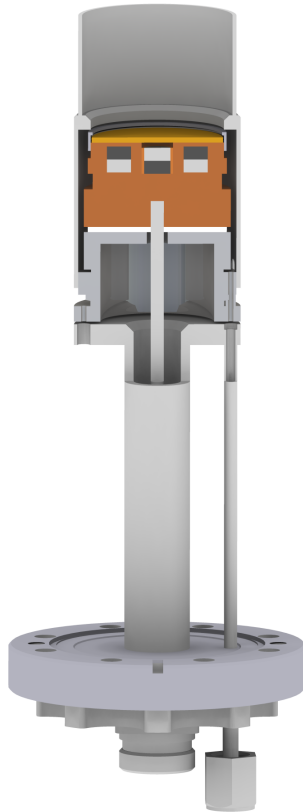
The deposition of a metal film opposite to the cathode of a DC glow discharge was first observed by Grove in 1852 [145]. Problems were the relatively small deposition rates and the process restriction to metallic target materials. The development of magnetron sputtering starting in the 1960s strongly increased the deposition rates and additionally allowed sputtering of various materials as ceramics and polymers.

The common planar balanced magnetron geometry is shown in *Figure 6.1*. An arc shaped magnetic field B is present above the target material caused by permanent magnets in the magnetron head. Under application of a voltage $V \approx -10^2 V$, causing an electrical field \mathcal{E} between anode shield and target, and the introduction of a sputtering gas a glow discharge is initiated. The electrons in the plasma are affected by the Lorentz Force

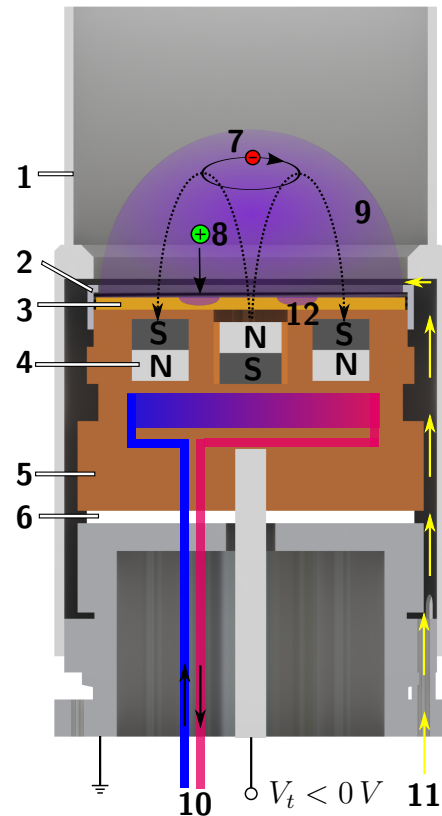
$$\vec{F}_e = -q_e(\vec{\mathcal{E}} + \vec{v} \times \vec{B}) \quad (6.1)$$

with electron charge q_e , the velocity of the electron v . This forces the electrons to move in a closed loop, the electron race track. In this loop the ionization efficiency is increasing and allows an operation at lower pressures compared to a simple glow discharge geometry. The generated ions are accelerated towards the target surface and gain kinetic energy depending on the applied voltage V . Upon impact the ions transfer their kinetic energy to the target surface causing a vaporization of target material which will be deposited opposite to the target. The highest erosion occurs directly below the electron race track, causing sputter trenches as depicted in *Figure 6.1(b)*. The used magnetron has a target diameter of 50 mm and is mounted on a CF63 flange as illustrated in *Figure 6.1(a)*. The magnetron is elongated to reduce the distance between target and substrate.

For the controlled deposition of thin films a sputter deposition chamber was constructed. With the developed setup a large variety of materials ranging from ferromagnetic metals to ceramics can be deposited using substrates with a diameter of 50 mm . The system is partially automated with a self made software allowing sophisticated processing, e.g. the deposition of alternating multilayer under a defined angle of incidence at a precisely controlled rotation of the substrate.



(a) Elongated magnetron for 2 inch targets mounted on a CF63 flange.



(b) 1: Anode shield, 2: target clamp, 3: target, 4: magnet system, 5: copper body, 6: electrical isolation, 7: electron race track, 8: impinging ion, 9: plasma, 10: water cooling, 11: gas inlet, 12: sputtering trench

Figure 6.1: Schematic of the magnetron used in this work. a) complete magnetron b) detailed cross section of the magnetron head showing the sputtering principle above the target surface.

The logging of the process data and automation of interlocks allow a very stable processing over long time periods without conceding any compromises to the lab safety. The following chapter describes the sputter deposition chamber and its individual parts in details and gives an example of a typical deposition routine.

The conception and construction of the sputter deposition chamber was part of the presented work. The system, as shown in *Figure 6.2*, contains three main parts, a chamber for the deposition process, a second load lock chamber which is separately pumped, and a controlling unit. A UHV gate valve allows the separation

of the chambers. This gives the system the flexibility to mount samples without breaking the vacuum of the deposition chamber and allows fast sample entry. The cooling of the magnetrons is established by an *ProfiCool Primus* chiller. The functions of the individual components are described in the following.

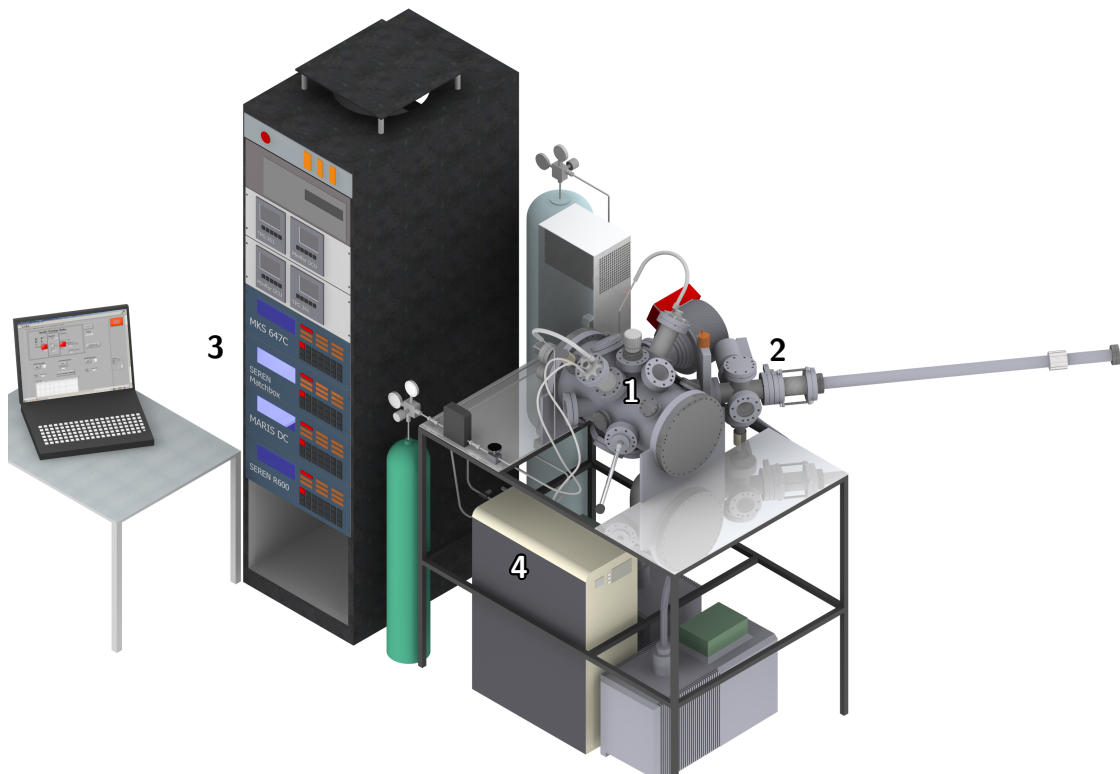


Figure 6.2: Schematic drawing of the sputter deposition setup consisting of a processing chamber (1), a load lock chamber (2), a powering and controlling unit (3) and a cooling system (4).

6.1 DEPOSITION CHAMBER

Figure 6.3 shows a schematic of the deposition chamber. The cylindrical recipient, designed by Stefan Rehders, has two large DN250 CF flanges at its ends, one DN160 CF flange, 12 DN63 CF flanges and 8 DN40 CF flanges to allow a large variety of processes and geometric configurations. The deposition chamber is evacuated by a *Pfeiffer HiPace 400* turbomolecular pump and a *Varian SH-110* scroll pump to a base pressure of $1 \cdot 10^{-8}$ mbar. The pressure during sputtering is typically between $3 \cdot 10^{-3}$ mbar and $6 \cdot 10^{-3}$ mbar. The scroll pump is switched

by a relay that is controlled by the turbomolecular pump controller to ensure both pumps start and stop simultaneously. The venting of the deposition chamber is performed by an automatic venting valve which flushes nitrogen through the turbomolecular pump in the chamber.

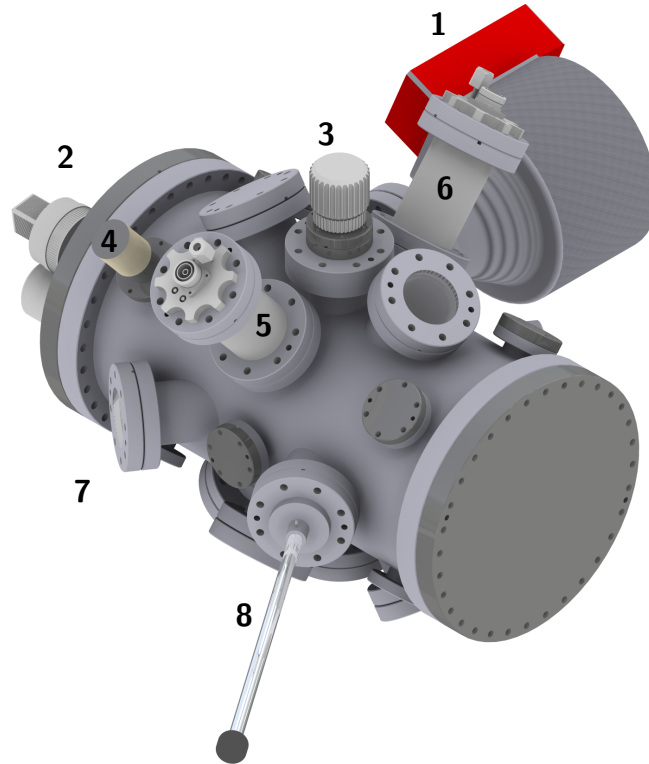


Figure 6.3: Geometry of the processing chamber with turbomolecular pump (1), sample holder (2), rotary shutter (3), vacuum gauge (4), DC magnetron (5), RF magnetron (6), window (7) and push-to-pull shutter (8).

The sputtering gas inlet is controlled by a *MKS 647C* gas flow system using argon with a purity of 99.9999%. The gas is guided inside the magnetron, thus the highest pressure is directly in front of the sputter target. The used magnetrons (*ION'X-2UHV_9152* built by Thin Film Consulting) are custom made for cylindrical sputtering targets with a diameter of 50 mm. To modify the magnetic flux near the target surface the center magnet can be removed. This allows the sputtering of ferromagnetic targets with a thickness up to 1.5 mm. The powering for the sputtering process is realized by a 500 W DC power supply *Maris DC* and a 600 W RF power supply *Seren R601* in combination with a *AT6/500* matching network box.

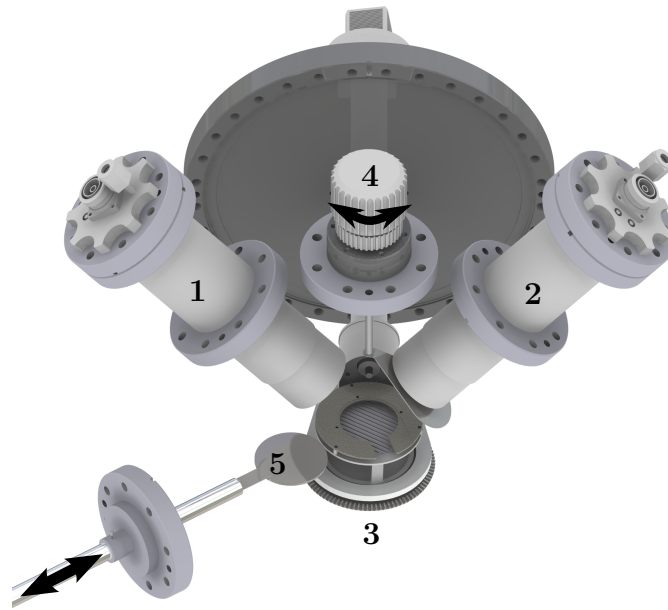


Figure 6.4: Schematic image of the used sputtering geometry. The positions of the magnetrons (1, 2) are fixed to an angle of 40° to the non-tilted sample holder (3). A rotary shutter (4) and a push-to-pull shutter (5) are available.

The samples are mounted on a custom built sample holder *Epicentre 282*, as shown in *Figure 6.5*. The sample supply base can be tilted to modify the angle of incidence for the sputtered ions from glancing incidence to perpendicular sputtering. In the standard position the angle of incidence regarding both magnetrons is 50° . The angle between the axes of the magnetrons is 80° and in combination with the metal chimneys of the magnetrons a contamination of the non-active target material is minimized. A stepper engine *Trinamic PD42-3-1140* can provide an azimuthal rotation of the sample at a defined rotation velocity. The stepper engine supplies a resolution of 51200 micro steps per rotation and can read back the angular position by an integrated 100 step encoder. This allows the exact angular positioning which is necessary, e.g. for sample transfer. A graphite heating element that can heat the samples up to 600°C as well as a type K thermocouple is also located in the sample holder. Two shutters are available to be put between the magnetrons and the substrate. The rotary shutter (see (4) in *Figure 6.4*) can be moved close to the magnetron to prevent the non-active target from being contaminated when sputtering with the other magnetron. The push-to-pull shutter (see (5) in *Figure 6.4*) can cover the whole substrate if the sample holder is non-tilted.

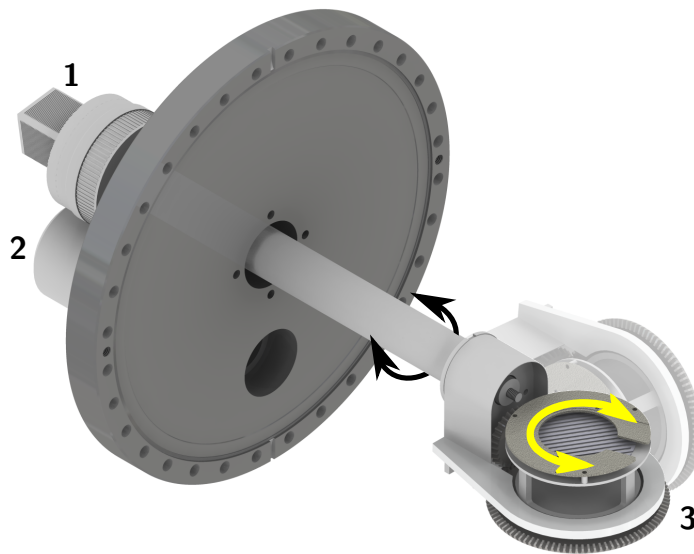


Figure 6.5: Sample holder consisting of a stepper engine (1) for azimuthal rotation (yellow arrow), a connection box (2) for thermocouple and heating element connections and the sample holder head (3), which can be tilted manually (black arrow) from outside.

6.2 LOAD LOCK CHAMBER AND TRANSFER SYSTEM

The load lock chamber was designed for fast entry of the samples. Since the volume of the load lock chamber is very small the pump down procedure takes less than 5 minutes. Compared to the venting of the deposition chamber this saves much time and also increases the quality of the deposited films, since no vacuum break in the deposition chamber is necessary when mounting samples. The load lock chamber is pumped by a Pfeiffer TMU 071 turbomolecular pump and a Pfeiffer PK-D62-712 rotary vane pump to a base pressure of $8 \cdot 10^{-8}$ mbar. The scroll pump is switched by a relay that is controlled by the turbomolecular pump controller to ensure both pumps start and stop simultaneously. For sample entry the chamber can be flushed with nitrogen through an automatic venting valve in the turbomolecular pump. The load lock chamber can be opened at the hinge flange as depicted in *Figure 6.6(a)* to allow the mounting of samples. Sample transfer is performed at pressures below $2 \cdot 10^{-5}$ mbar. After opening the gate valve a magnetically coupled transfer rod was used to transfer the samples in the deposition chamber. For exact alignment a flexible metal bellow could be used for

precise tilting of the transfer axis to perfectly match the position of the sample holder in the deposition chamber. The sample exchange system was developed and assembled by Stefan Rehders and allows fast and stable transfer of the samples, see *Figure 6.6(b)*.

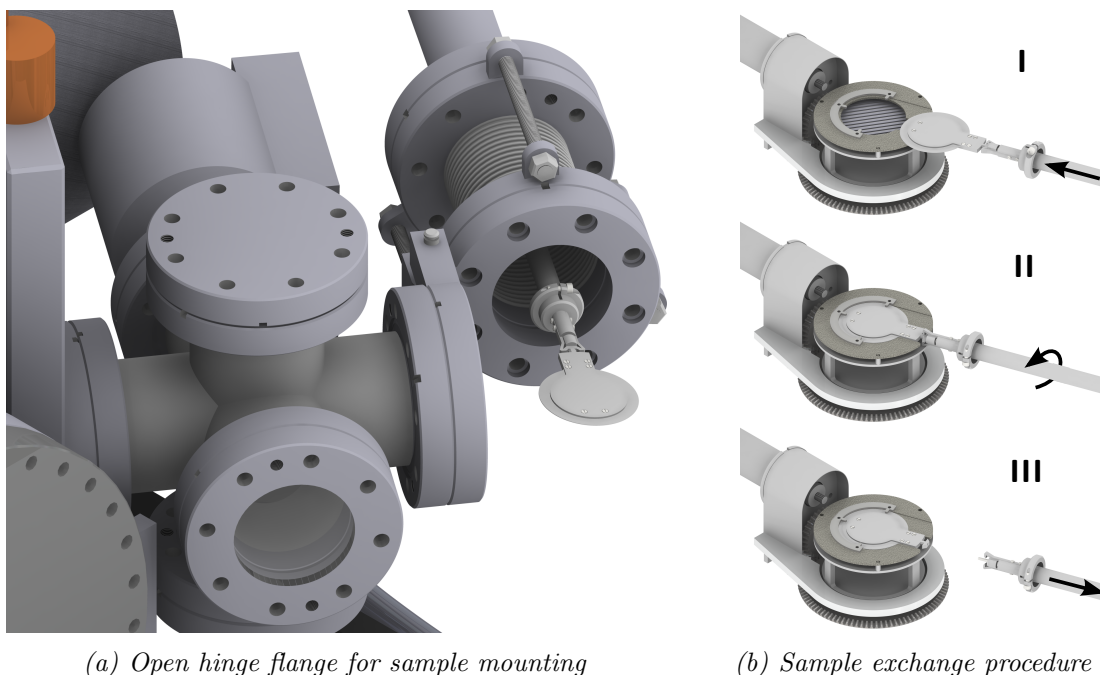


Figure 6.6: Sample mounting procedure. The sample is mounted by opening the hinge flange (a). After evacuating the sample is transferred to the sample holder and exchanged (b). The exchange is performed by pushing (I), rotation by 90° (II) and retraction (III) of the transfer rod.

6.3 CONTROL UNIT

The control unit was designed with the aim to minimize any possible malfunctions and to increase the reproducibility of the process. The former was achieved by the use of interlocks. Some interlocks were realized by direct wiring, e.g., water flow detectors are directly connected to the power supplies of the magnetrons and prohibit any switch on if the water flow is not sufficient. Other interlocks were realized in the controlling *LabView* software.

A LabView based software was developed to control the deposition process via a central computer, details about the software can be found the appendix *chap-*

ter C.2. The computer is connected to the gas flow controller, the RF power supply, the matching network controller and the vacuum gauge via a *rs 232* serial interfaces. The DC power supply is interfaced through an analogue interface which is controlled by an 8-channel relay card and an A/D converter *National Instruments 6008*. The stepper engine for the sample rotation is connected with a *rs 485* serial adapter. Through these interfaces the computer can acquire information about pressure, gas flow, sample position and power supply parameters like DC voltage, DC current, RF forward and reflected power.

For processing the software allows the creation of work plans with any amount of work steps. In each step the gas flows, the sputtering powers, the sample position and the sample rotation can be modified. During processing all information about flow, pressure and power supply status is recorded to increase the transparency of the processing. Due to the work plan the user is able to program any kind of single or multiple layer sputtering system with defined rotation. The angle of incidence and the shuttering have to be manipulated manually, but the system is prepared for additional stepper engines that would allow their computer controlled motion.

6.4 STANDARD SPUTTERING PROCEDURE

The following describes a typical sputtering run of the system. Before venting the load lock chamber can start the transfer rod has to be pulled out of the deposition chamber and the gate valve is closed. The venting is started from the control unit which will switch off both turbomolecular pump and rotary vane pump before flushing the load lock chamber with nitrogen. After reaching atmospheric pressure the hinge flange is opened. The sample plate carrying the sample is mounted on the head connector of the transfer rod and the hinge flange is closed again. The pumps are started and the chamber is evacuated to a pressure in the magnitude of $1 \cdot 10^{-5}$ mbar within 3 minutes. The gate valve is opened and the sample is transferred towards the sample holder. For exchange of the samples the sample holder is tilted to the standard position and the transfer angle is selected in the control software which will cause a precise rotation by the stepper engine. The sample is exchanged by pushing it in the clamps of the sample holder, rotating the transfer rod by 90° and retracting the transfer rod completely, as shown in *Figure 6.6(b)*. The gate valve is closed and separates the chambers.

To allow pressures of $3 \cdot 10^{-3} \text{ mbar}$ in the deposition chamber the pump speed of the turbomolecular pump has to be reduced by setting the revolution to 33% being 273 Hz . The rotary shutter is moved in front of the first magnetron and a sputtering process is started with this magnetron to clean the target surface from impurities. The same is performed for the second magnetron. A sputtering work plan is created as depicted in *Table 6.1*. The process is started by selecting *start*

Table 6.1: Typical sputtering work plan consisting of 5 processing steps for the subsequent sputtering from both magnetrons.

#	Time (s)	Flow 1 (sccm)	DC Power (W)	Flow 2 (sccm)	RF Power (W)	Position (degree)	Rotation (Rot./min)
1	10	15	0	0	0	0	0
2	180	15	50	0	0	0	6
3	10	0	0	0	0	180	0
4	10	0	0	200	0	0	0
5	240	0	0	20	50	0	0

from 1st work plan position in the software. The parameters in line number 1 of *Table 6.1* are transferred to the corresponding components causing a pressure increase to $3 \cdot 10^{-3} \text{ mbar}$. After 10 seconds the parameters in line number 2 are loaded and a sputtering process with a DC Power of 50 W is started at a sample revolution of 6 rotations per minute for 180 seconds. Then the sputtering is stopped and the sample is rotated by another 180° as defined in line 3. The pressure is then increased to $6 \cdot 10^{-2} \text{ mbar}$ to allow the ignition of the RF plasma. The plasma ignition is performed with a power of 50 W and at the same second the pressure is reduced to $4 \cdot 10^{-3} \text{ mbar}$. After 240 seconds the process is finished and all gas flows, rotations and magnetron powering are stopped.

The sample holder is moved to the angular position for sample exchange, the gate valve is opened and the sample is picked up using the transfer rod analogue to the procedure described above. The sample is transferred to the load lock chamber the gate valve is closed and the load lock chamber is vented.

7 SUMMARY OF THE SYNTHESIS

Two different synthesis routes have been investigated: the classical VLS approach and the new introduced FTS. It was observed that both methods can be used to create ZnO nano- microstructures in various geometries. The FTS method has some advantages over the VLS as it is faster and allows the fabrication of very long ZnO microrods. Thus FTS is selected for the synthesis of ZnO microstructures which are used for characterization and the realization of ME sensors.

For the coating of these ZnO structures and other surfaces a sputter deposition setup was developed. The setup is extremely variable and allows the deposition from two sources on a substrate which can be rotated and tilted in order to fit the requirements. The developed software can handle the deposition of multilayers and records the instrument data during sputtering. This leads to a very high reproducibility of the processing and a long time stability which allows e.g., overnight deposition.

PART III

CHARACTERIZATION

The characterization of individual ZnO microrods with a diameter below $100\ \mu\text{m}$ is a challenging task since it requires small probes and thus high technical effort. Depending on the applied method various types of information can be gathered and usually several methods are combined to get a maximum of information about the sample. Methods already applied for the investigation of ZnO needles include **S**low **P**ositron **I**mplantation **S**pectroscopy (SPIS) [146], **A**tomical **F**orce **M**icroscopy (AFM) [146], **P**iezoelectric **F**orce **M**icroscopy (PFM) [147], **S**canning **E**lectron **M**icroscopy (SEM) [146] [148], **X**-**R**ay **D**iffraction (XRD) [146, 148, 149], **N**uclear **R**eaction **A**nalysis (NRA) [146], **P**hoto **L**uminescence **A**nalysis (PL) [148, 149], **T**ransmission **E**lectron **M**icroscopy (TEM) [149], Raman [150] and more. Thus a large amount of theoretical models and precise descriptions of various effects can be found in recent literature.

The focus in the presented work was set on the characterization of electrical and mechanical properties of the ZnO microrods to investigate the possible application in ME sensors. Especially the piezotronic effect which is rarely discussed in literature is investigated to allow a comparison to classical piezoelectric devices. The following chapters describe the characterization of ZnO microrods and are divided in individual parts for crystalline, electromechanical and piezoelectric properties.

8 CRYSTALLINE PROPERTIES

The knowledge of the crystalline quality of the obtained ZnO needles is substantial for further investigation and application since it determines the electric and piezoelectric properties. In this chapter the investigation of ZnO single crystals is described using sophisticated methods which allow an extremely high spatial resolution. The experiments were carried out by partners of the collaborative research center *SFB 855*.

8.1 X-RAY NANO BEAM DIFFRACTION

Conventional XRD systems require minimum sample volumes of several mm^3 to obtain enough intensity within a reasonable time. In contrast a synchrotron is providing enough intensity to investigate much smaller volumes. This allows the investigation of X-ray interaction at different positions of a ZnO micro needle. By looking at the shift of the Bragg peaks for the different positions, variations of the lattice parameters can be detected. To investigate the influence of a magnetostrictive coating, uncoated and FeCoSiB coated ZnO rods are compared. This part is partially excerpted from [151], the experiments were mainly carried out by S. Hrkac.

The measurement principle is schematically illustrated in *Figure 8.1*. A monochromatic X-ray beam with an energy of 12.8 keV , provided by the high resolution nanofocus endstation of the *MiNaXS-Beamline P03* at *PETRA III* [152], was focused on different locations of a ZnO rod as schematically shown in *Figure 8.1(a)*. A beam cross section of $400\text{ nm} \times 800\text{ nm}$ was realized using focusing mirror optics. The incidenting beam, indicated by its reciprocal wave vector k_i , was diffracted by the sample as shown in *Figure 8.1(b)* leading to an intense Bragg reflection peak in the detector if fulfilling Bragg's law. The angle θ could be tuned by rotation of the sample using a Huber goniometer head in combination with a motor to allow rotation around the c -axis. A *2D Dectris 300 k Pilatus Pixel detector* with a pixel size of $172 \times 172\ \mu\text{m}^2$ was mounted at a distance of 185 mm with respect to the sample. The *European Synchrotron Radiation Facility* software was used to analyze the ob-

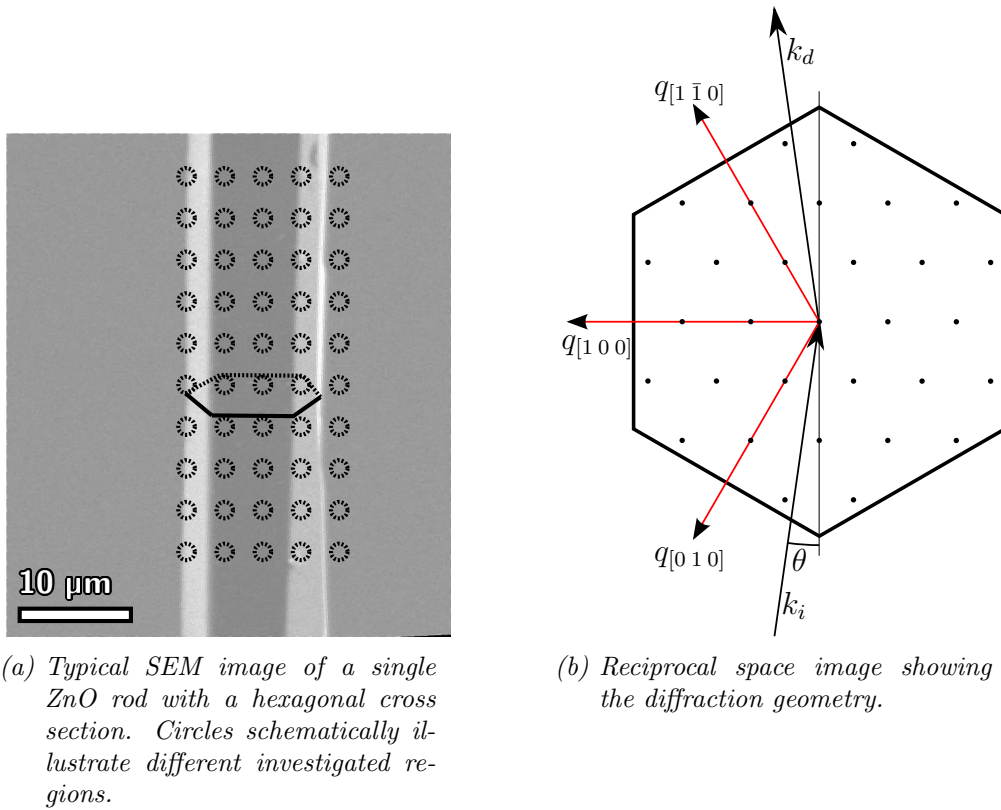


Figure 8.1: Schematic illustrations showing the X-ray nanofocus diffraction experiments.

tained diffraction patterns [153]. The high intensity of the (100) Bragg reflection confirmed the homogeneity of the crystal and its single crystalline nature. The lattice spacings for the (100) planes was found to be ($d_{100} = 2.8159 \pm 0.0001 \text{ \AA}$) for an uncoated ZnO rod, indicating the absence of intrinsic strain across the whole rod.

The FeCoSiB coated ZnO rods showed a growth induced compressive strain which is defined as

$$S_{100}(c) = \frac{q_{100}(uc)}{q_{100}(c)} - 1. \quad (8.1)$$

The average strain was found to be $S_{100}(c) = -55 \cdot 10^{-5}$ with a variation of $\Delta S_{100}(c) = \pm 20 \cdot 10^{-5}$ close to the edges of the samples. The strain is a result of the deposition process and has been observed for similar systems [154]. *Figure 8.2a* illustrates the strain in a ZnO microrod. It can be seen that the strain decays strongly within the first $5 \mu\text{m}$ in the crystal whereas only a residual strain is remaining over the rest of the crystal. Strain variations along the z-axis of the

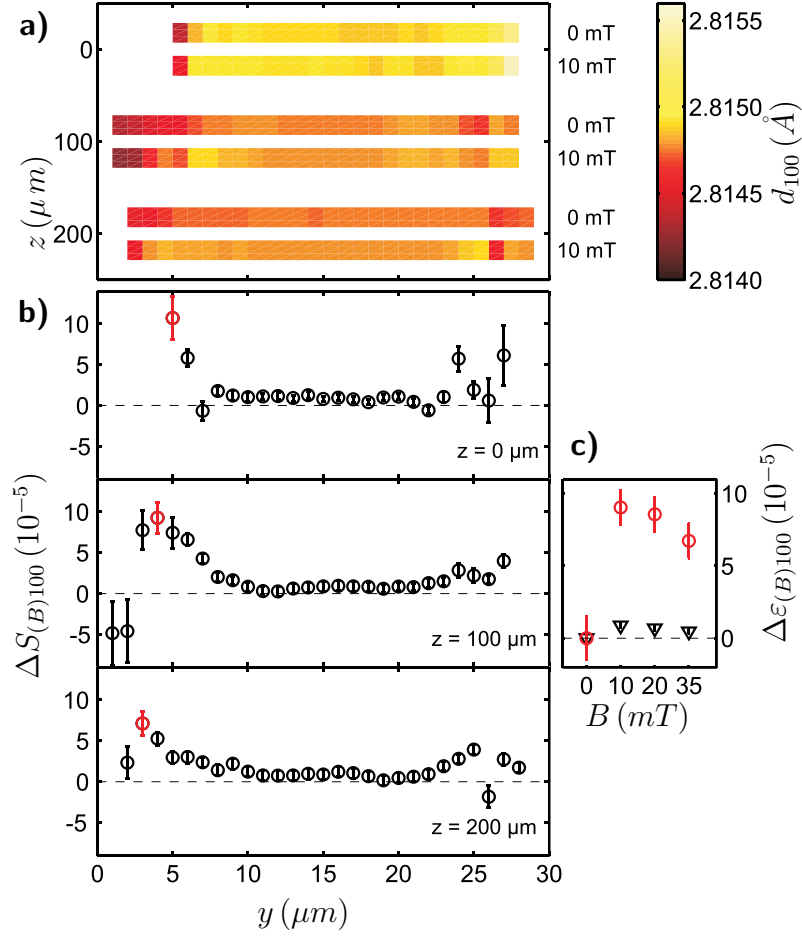


Figure 8.2: Results of the nano beam investigations. a) d_{100} spacings at 3 positions with and without an applied magnetic field. b) corresponding local strain profiles. c) comparison of the average field induced strain to the local maxima shown in Figure 17.2c. Original image by S. Hrkac, reproduced with permission from [151].

needle were observed and are possibly caused by the inhomogeneity of the coated FeCoSiB thin film.

$$\Delta S_{(B)100} = S_{(B)100} - S_{(B=0)100} \quad (8.2)$$

It can be seen that the strain in the center of the rod is almost independent of the applied magnetic field with an average of $\Delta S_{(B)100} = (1 \pm 1) \cdot 10^{-5}$. The strongest effect is obtained near surface. Constant magnetic fields were applied to the microrod and the strain of the ZnO was investigated. Figure 8.2a shows the

d_{100} spacings for a magnetic field of $B = 10 \text{ mT}$ compared to the strain without the application of a magnetic field. The corresponding local strain profiles are depicted in *Figure 8.2b*. A comparison of the average field induced strain to the local maxima at the edge is shown in *Figure 8.2c*. The magnetic field induced strain is described by the edges of the rod with local maxima up to $\Delta S_{(B)100} = (10 \pm 2) \cdot 10^{-5}$. The strain decay is similar to the strain induced by the coating. Comparing the field induced strain to the strain induced by the coating it can be found that the field induced strain is a relaxation of the compressive strain which is caused by the coating. The high local strain exceeded the calculated values of $4 \cdot 10^{-5}$ [155] which is $3/2\lambda_S$ with λ_S being the saturation magnetostriction for bulk FeCoSiB [156]. This enhancement of the effect could be caused either by an overlap of the strain fields, or by the relaxation process which occurs due to the existing pre-stress after deposition.

Summarized it could be demonstrated that the synthesized ZnO needles have excellent crystalline properties and do not show intrinsic strain. The deposition of a FeCoSiB film on the needles causes a compressive strain inside the needle which is highest at the edges of the sample. By application of a magnetic field the compressive strain is slightly relaxed. This demonstrates that the fundamental basics for building ME composites with individual needles are fulfilled since it is possible to change the lattice spacings of a single crystalline ZnO needle by application of a magnetic field.

8.2 MORPHOLOGIC INVESTIGATIONS OF ZNO NANOSPIKES

The following part is partially excerpted from [135], the experiments were mainly performed by V. Hrkac. To investigate the morphology of an individual nanoscopic ZnO spike TEM experiments were carried out. The ZnO nanospikes were synthesized using the FTS synthesis route as described in *chapter 5* using Zn powder with a diameter of $10 \mu\text{m}$ (supplied by *Goodfellow, UK*). **P**oly **V**inyl **B**utyrac (PVB) (supplied by *Kuraray GmbH, Germany*) was mixed with ethanol and Zn powder in a ratio of 1:2:6 (Zn:PVB:ethanol) and coated on a silicon substrate ($1 \times 1 \text{ cm}^2$) using a slip casting device. The substrate was then heated to a temperature of 873 K using a heating rate of 100 K/min for *1 hour*.

A SEM image showing a typical ZnO core spike particle is depicted in *Figure 8.3*. The core particles have a typical diameter of $10\ \mu\text{m}$. The rods are usually connected to the core under an angle close to 90° and show triangular flat geometry with a thickness of several nanometers and a width below $1\ \mu\text{m}$. The spikes narrow towards their ends and obey a typical length of several micrometers. The long axis of each nanospike was found to be parallel to the $(1\bar{1}0\bar{1})$ edge. The preferred viewing direction in TEM for this morphology is $[2\bar{1}\bar{1}3]$ [157]. The domain boundary $(2\bar{1}\bar{1}1)$ propagates almost parallel to the growth direction and the angle between the preferred viewing direction and the normal of the domain boundary is 47.5° . This leads to a superposition of the domains and a characteristic fringe contrast. The superposition structure was simulated by V. Hrkac using a supercell

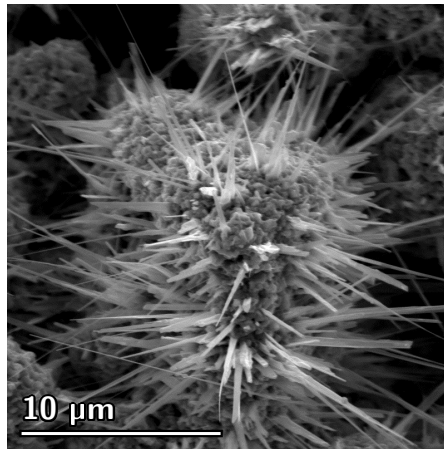


Figure 8.3: SEM image of a typical ZnO core spike particle.

approach. Using this approach all experimental results could be simulated. A further, more detailed description of the simulation the experimental results can be found elsewhere [158].

9 ELECTROMECHANICAL CHARACTERIZATION

The characterization of the electromechanical properties of ZnO microrods is important for possible applications, e.g. as ME-sensors. The intrinsic properties of the needle have to be investigated separately from effects which may occur due to imperfect sample preparation. The mechanical pre-stress is a typical example for an additional effect which arises during mounting and will be discussed in details. Electrical artifacts which can be the result of bad electrical contacts are also investigated and presented in the following chapter.

9.1 ELECTRIC CONTACT

The establishment of a reliable electric contact is an important step and necessary for most applications. As depicted in *chapter 1.3* the contacting of semiconductors with metals can be rather complex. Depending on the planned application it is important to control the type of contact formation and create ohmic or Schottky contacts depending on the desired application. Small contact resistances and thus ohmic contacts are needed for investigations of the intrinsic conductivity of a material whereas Schottky contacts are necessary when applying the piezotronic effect. Noble metals usually form Schottky contacts to ZnO, e.g. Au [159–161], Pt [162, 163], Pd [164, 165] or Ag [159, 161] whereas only few metals, e.g. Al [166] can be used to get ohmic contacts.

9.1.1 SAMPLE PREPARATION

A single ZnO microrod was contacted with Al/Au on one end and Ag on the other end as depicted in *Figure 9.1*. The polyimide substrate is partially covered by a mask of Al foil and introduced to the load lock chamber. After transferring to the deposition chamber a layer of Au with a nominal thickness of 125 nm is sputter deposited. The sample is transferred back to the load lock chamber and locked out. After mask lift off a single ZnO microrod is positioned in the center of the

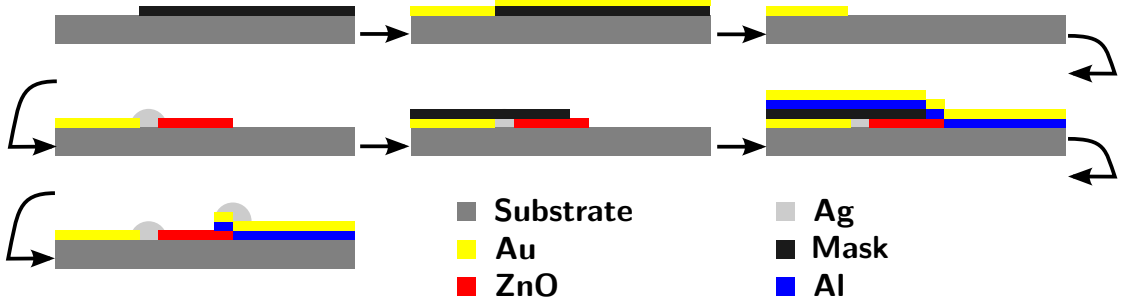


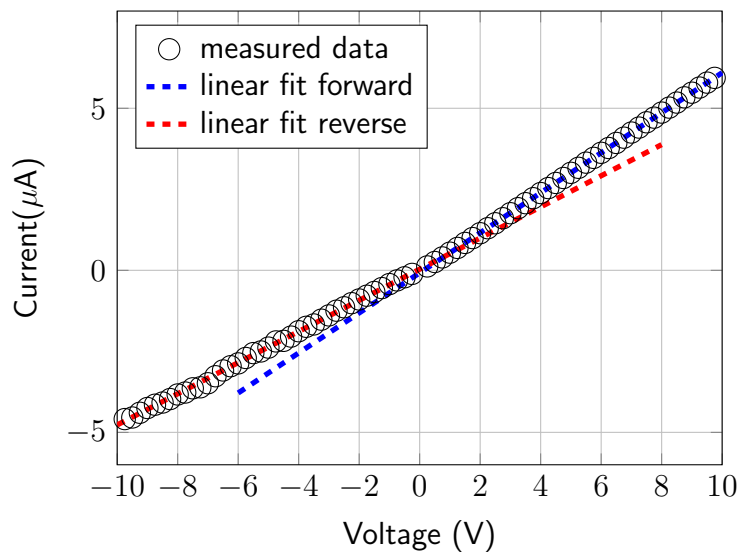
Figure 9.1: Processing steps for a single ZnO needle with Ag-ZnO-Al contact.

substrate and fixed with Ag-glue *Acheson Silver DAG 1415 M* to establish the first contact. A second mask from Al foil is positioned on the substrate leaving the unfixed end uncovered. The sample is introduced to the load lock chamber and transferred to the deposition chamber. A layer of Al (75 nm) followed by a layer of Au (125 nm) is sputter deposited. After transferring back to the load lock chamber the sample is taken out and the mask is removed. A small amount of Ag-glue *Acheson Silver DAG 1415 M* is used to fix the microrod end to the substrate.

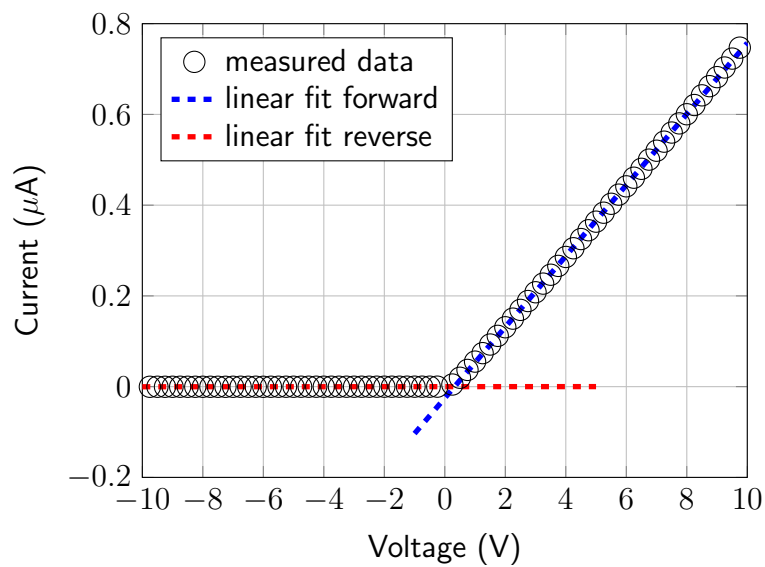
Figure 9.2 shows the characteristic IV-curves for the resulting sample at ambient conditions under day light exposure (*Figure 9.2(a)*) and when blocking light for 24 h in a light shielded environment (*Figure 9.2(b)*). A positive voltage in this case is defined as a positive voltage on the Ag contact with respect to the Al contact. The IV-characteristics change completely from an ohmic type if exposed to daylight to a single Schottky type in the dark environment. Least square fits were performed for both polarities as shown in *Figure 9.2(a)* with the red line being the fit for negative voltages and the blue line being the fit for positive voltages. The results of the fitting routine are shown in *Table 9.1* where the current is defined as

$$I = I_0 + G \cdot U \quad (9.1)$$

with the current at zero volts I_0 and the electrical conductance G . The fitting accuracy is described using the coefficient of determination R^2 [167]. The IV behavior of the illuminated sample can be explained as follows. Even though the forward and reverse current characteristics are linear they show a slightly different steepness. This indicates that the current limiting mechanisms differ and depend on the polarity. When following the theoretical model (see *chapter 1.3*)



(a) Under day light.



(b) In dark box.

Figure 9.2: Influence of light on IV-Curves for a single ZnO microrod with Ag-ZnO-Al type contact.

the Ag is expected to build a Schottky contact to the ZnO whereas the Al-ZnO contact should obey an ohmic behavior. Additional resistance arises from intrinsic resistance of the ZnO. The electrical resistance of the metal-metal contacts (e.g. Al-Au), wiring and the internal resistances of the measurement equipment are relatively small and can be neglected. When applying a positive voltage, the

Table 9.1: Results of least square fit for Figure 9.2

Light	Polarity	G ($\mu\text{A}/\text{V}$)	I_0 (μA)	R^2
yes	+	0.62	-0.08	0.99996
yes	-	0.48	0.03	0.99830
no	+	0.08	-0.03	0.99978
no	-	$2.4 \cdot 10^{-5}$	$-1.9 \cdot 10^{-5}$	0.79656

Ag-ZnO Schottky contact forward current would increase exponentially (compare *Equation* (1.19)) but is limited by the intrinsic resistance of ZnO, thus showing a linear IV-curve. The high coefficient of determination for the linear fit supports this hypothesis. When applying a negative voltage the IV-curve does not show a low current flow as expected for the reverse current of a Schottky contact but a similar increase as compared to the forward current. The daylight causes a photo-excitation of electrons in the metal which allows them to pass the energy barrier as described in *chapter* 1.3.1.

The IV characteristic of the sample in the absence of light is as expected and can be explained by the standard Schottky theory, see *chapter* 1.3.1. The only difference to the standard model is the linear increase of the current in forward direction where an exponential increase is the standard case. Similar to the illuminated sample the current through the Schottky contact would increase exponentially but is limited by the high ohmic resistance of the ZnO microrod. The large difference in the forward current when illuminating the sample is related to photo-excitation of electrons in the semiconductor.

The external light changes the conductivity by two different mechanisms: a direct influence where a single photon affects a single electron and an indirect effect where the oxygen vacancy concentration is affected. In the case of a direct influence a photon can increase the conductivity by creating an electron-hole pair or by photo-excitation of single electrons which results in a fast response time of the current. It was observed that the conductance of the sample changes immediately when exposing to light or blocking light but reaching a stable state takes a relatively long time. The reason for the slow drift is the second, indirect influence of external photons which leads to a change in the oxygen vacancy concentration. The diffusion limited healing of these oxygen vacancies in the absence of light is further described in *chapter* 12.2.3.

The IV measurements show clearly that it is possible to tune the contact type from Schottky to ohmic by sputtering either Au or Al. Incidenting photons have a strong effect on the current flow even when their energy is insufficient to supply enough energy to an electron in the valence band to reach the conduction band. Therefore it is necessary to block incident light to a ZnO based sensor device.

9.2 PIEZOELECTRICITY AND PIEZOTRONICS

Once reliable contacts are established to a ZnO microrod its piezoelectric properties can be investigated. For a further development of ZnO based ME-sensors it is important to characterize the piezoelectric phase individually without the presence of a magnetic field. Therefore a mechanical deformation setup was developed to deform the piezoelectric ZnO and detect the sensor response. Besides the piezoelectric properties the piezotronic effect was investigated and the results are discussed.

9.2.1 TEST SETUP

The piezo bending setup was developed to investigate the piezoelectric and piezotronic effect by direct mechanical deformation as schematically shown in *Figure 9.3*. The system was designed by Stefan Rehders to measure rectangular samples with dimensions of $10\text{ mm} \times 50\text{ mm}$. The mechanical stability and electric contacting is performed using clamps at the sample ends which are on a floating potential. For bending of the sample an indenter tip is positioned above the center of the sample in a fixed height. The vertical position of the sample can be modified using a precision vertical stage. The indenter can be controlled by a *P-602 PiezoMove Flexure* piezoelectric actuator with a maximum distance of $200\text{ }\mu\text{m}$. The actuator is driven by a *NI E-660* voltage source which is controlled over an *Meilhaus MERedLab*. The shielding of the system contains two main parts: the electrical shielding and the light shielding. The electrical shielding is connected to ground potential and can be closed above the sample. A hole for the indenter tip allows mechanical deformation of the sample without any electrical influence from the indenter electronics to the measurement. To shield the samples from light influence the whole system is placed inside a black ABS (Acrylonitrile butadiene styrene) box.

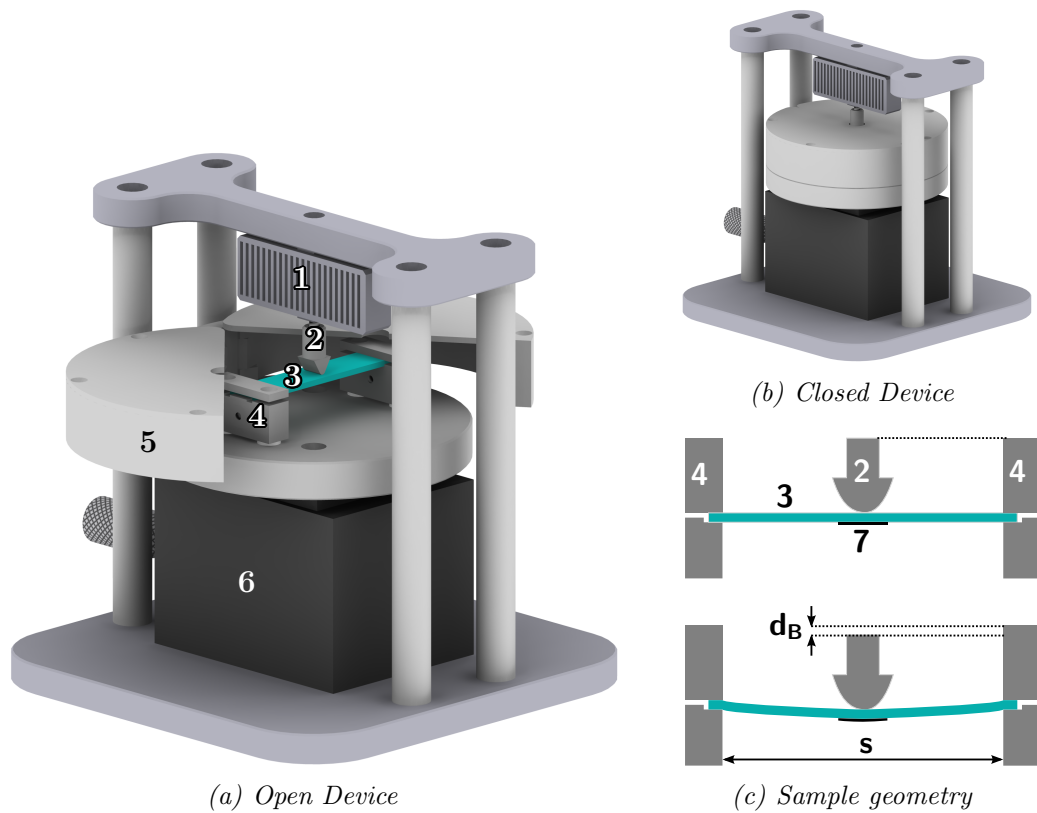


Figure 9.3: Piezo bending device. (a) A piezoelectric actuator (1) moves an indenter (2) downwards and bends the sample (3) which is clamped at both ends (4). The shielding (5) can be opened for sample mounting and height positioning of the sample with a precision vertical stage (6). (b) Closed shielding during measurements. (c) Schematic illustration of the geometry during bending. Electrical contacts are established by the mechanical clamps (4). The ZnO microrod is mounted on the underside of the substrate (7). The setup was design by Stefan Rehders.

A quantitative analysis of the piezoelectric and piezotronic response when bending or straining a piezoelectric material demands a precise description of the geometry. The piezoelectric material will be positioned on the underside of the sample as depicted in *Figure 9.3(c)* to avoid a direct contact of the indenter. Since the thickness of the piezoelectric material is always small compared to the substrate thickness the strain in the piezoelectric material can be described by the strain in the undersurface of the substrate. The path of the piezoelectric actuator d_B

as illustrated in *Figure 9.3(c)*, called *bending distance* in the following, is directly related to the strain in the surface of the sample. The strain ϵ is defined as

$$\epsilon = \frac{\arctan\left(\frac{2d_B}{s}\right)(4d_B^2 + s^2)s}{2d_B} - 1 \quad (9.2)$$

with s being the distance between the sample clampings and the bending distance d_B , compare 9.3(c). *Figure 9.4* illustrates the strain over the bending distance for clamping distances of 5 mm, 50 mm and 500 mm. For typical bending distances

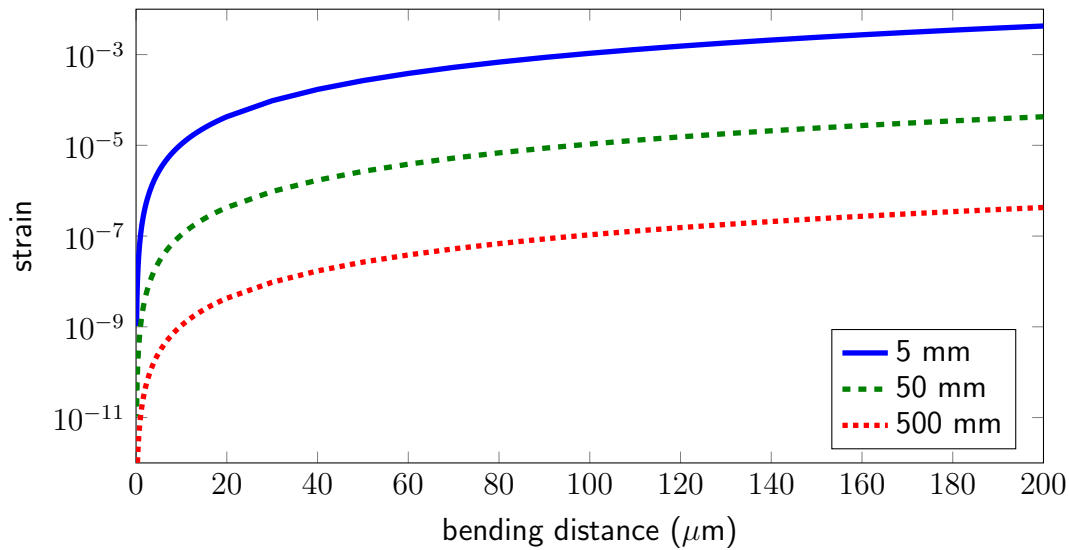


Figure 9.4: Calculated strain for clamping distances of 5 mm, 50 mm and 500 mm

up to 200 μm a clamping distance of 50 mm creates strains comparable to the strain generated by high magnetostrictive materials. Thus a substrate length of 5 mm was selected as a standard size which corresponds to a clamping distance of 40 mm. The piezo bending system is controlled with a variety of programs using *National Instruments Labview*. All programs have in common that the bending states of the samples can be changed by defining the positions of the indenter. The amount and size of the individual steps, the time interval between steps and the number of measurement cycles can be defined. The used programs and their principles are explained in the following paragraphs.

9.2.2 MEASUREMENT MODES

Piezoelectric Charge To directly measure the piezoelectric effect of individual samples a charge meter *Kistler 5015a* is connected to the samples. A maximum sample rate of $\approx 80 \text{ s}^{-1}$ can be used to measure the charge when bending the sample. A typical measurement is shown in *Figure 9.5*. The response to a deformation

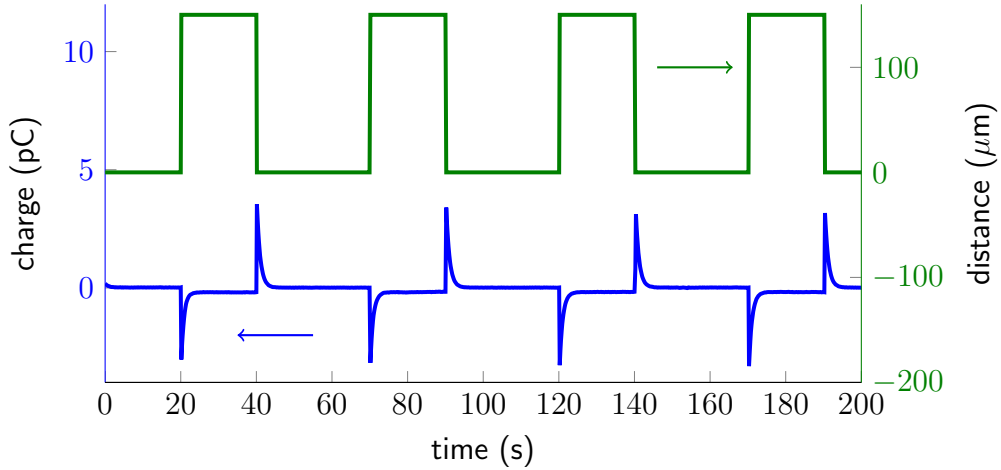


Figure 9.5: Typical charge response of a device which is periodically deformed.

is a spontaneous peak in the charge signal followed by an exponential decay of the signal. Upon relaxation a similar signal with opposed sign can be observed. Since the sample rate of the Kistler 5015A is low compared to the duration of the decay, every characteristic step is measured several times. A *Matlab* script is used to average the data and remove the background noise before the data is fitted by an exponential function which describes the charge decay as

$$Q(t) = Q_0 e^{-t/\tau} \quad (9.3)$$

with the charge peak Q_0 and time constant τ defined as

$$\tau = R_{total} C_{total} \quad (9.4)$$

using total resistance $R_{total} = \frac{R_s R_g}{R_s + R_g}$ and the overall capacity $C_{total} = C_s + C_g$ as described by the equivalent circuit in *Figure 9.6*. Since the electric properties of the charge meter are not changing ($R_g, C_g = const.$) and the capacity of the

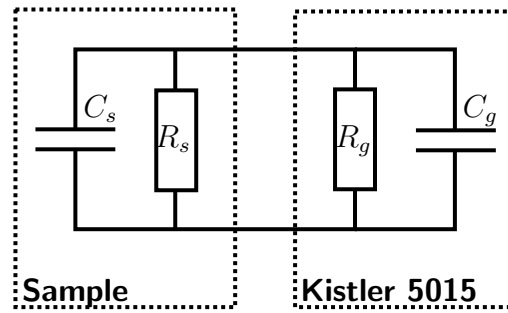


Figure 9.6: Equivalent circuit for charge measurements.

sensors are low ($C_S \ll C_g$) a change in τ is caused by a change in R_s . The complete Matlab calculation and fitting routine can be found in the appendix, see *chapter B.6*.

Multiple IV-Curves To enable the measurement of complete IV-curves a *Keithley Sourcemeter 2400* is connected to the sample. A complete IV-curve in a defined voltage range is recorded for every bending state. The delay between sample bending and the start of the IV-measurement can be defined to distinguish between static effects and dynamical effects that only occur directly after bending. The program allows the recording of multiple cycles and the resulting data can be averaged or investigated using *Matlab chapter B.1*. An exemplar 3D plot of a multiple IV measurement is shown in *Figure 9.7*.

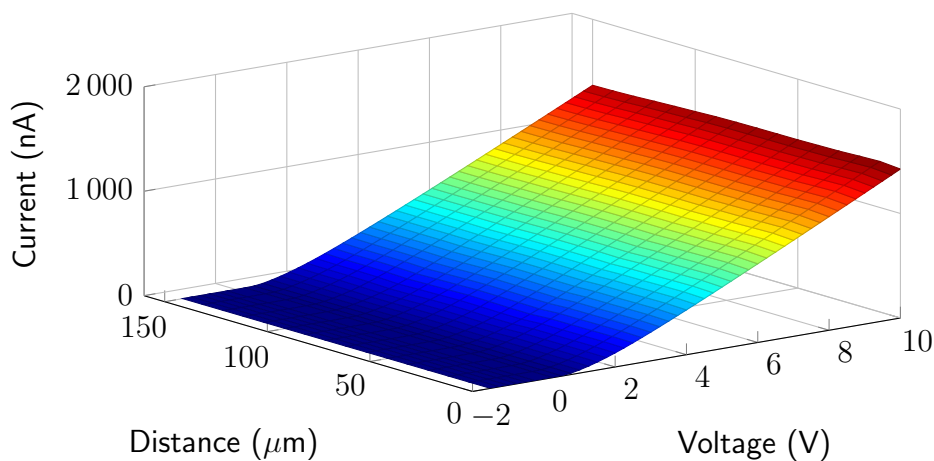


Figure 9.7: Typical plot of IV-curves for different deformation states

9.2.3 MEASUREMENT OF ZNO MICRORODS

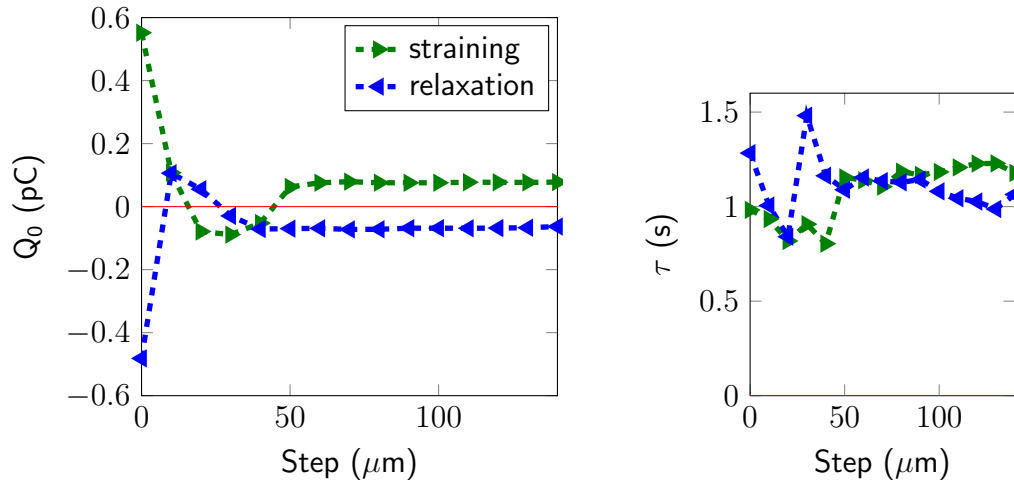
Three samples C1, C2 and C3 were prepared as described in section 9.1 using ohmic contacts on both ends of the ZnO microrods. The Al sputtering was performed at 50 W using RF magnetron sputtering for 300 s followed by the sputtering of Au at 50 W DC for 150 s at a pressure of $3.5 \cdot 10^{-3} \text{ mbar}$. The nominal layer thicknesses are 75 nm and 125 nm respectively. The piezoelectric charge response the IV-characteristics of the samples under strain is discussed in the following. The individual samples are prepared using the same preparation routine, therefore any differences can be addressed to the variations of the individual ZnO microrods or pre-stress which may occur during mounting.

9.2.3.1 Charge Response Measurements

The response of the samples to a stepwise increasing strain followed by a stepwise relaxation was measured and is discussed in the following paragraphs.

Sample C1 To investigate the influence of the used step size sample C1 was measured using two different step sizes of $2 \mu\text{m}$ and $10 \mu\text{m}$ and a maximum deformation of $150 \mu\text{m}$. *Figure 9.8(a)* shows the charge maxima Q_0 as described in *Equation (9.3)* with a step size of $10 \mu\text{m}$ for straining and relaxation of the sample. To exclude the measurement of artifacts and sensor drift a typical amount of 100 cycles was measured and averaged. The interval between the individual steps was at least 15 s to allow the detection of large time constants. The abscissa values always correspond the lower value of a step, e.g., $40 \mu\text{m}$ is either the straining step $40 - 50 \mu\text{m}$ or the relaxation step $50 - 40 \mu\text{m}$. The graph shows a complex charge response behavior for low strain, starting at a relatively large response at $0 \mu\text{m}$ followed by an exceptional negated charge signal for strain up to $40 \mu\text{m}$. The Q_0 values for strain above $40 \mu\text{m}$ are constant and the relaxation values match the straining values very good since they show the negated values almost perfectly over the measured region with a small shift for lower strain values. The mismatch at these low strains can be explained by the used measurement geometry. Since the indenter is not mechanically connected to the sample it is not possible to pull the sample to a defined position whereas pushing is possible. This means that the relaxation velocity is determined by the elastic behavior of the sample

whereas the straining velocity is defined by the piezoelectric actuator which moves of the indenter. Therefore the relaxation velocity should be always lower than the straining velocity leading to less pronounced piezoelectric effects when relaxing. Since the restoring force increases with deformation, the difference in straining and relaxing is highest for a non-deformed sample and becomes neglectable for large deformations.



(a) Measured charge response using a step width of $10 \mu\text{m}$.

(b) Calculated time constants.

Figure 9.8: Measurement of sample C1 showing a) charge response and b) time constants. Dashed lines are for guiding the eye.

Thus pre-stress in the sample which occurs during mounting of the sample is highly relevant since it affects the relaxation process. The pre-stress is defined when using the precise height adjustment of the sample table and can only be investigated by a piezoelectric response measurement. Another pre-stress effect is the intrinsic stress which may occur during preparation of the sample or variations in temperature. Additionally a small tilt in the indenter tip relative to the surface of the sample may induce a torsional stress in the sample leading to either compressive or tensional stress for low deformations. This can cause the single piezoelectric ZnO needle to be compressed for low deformations and strained for larger deformation which could be the case in sample C1 since it would explain the non intuitive polarity change for low deformations.

For the measurement shown in *Figure 9.8(a)* it can be suggested, that an intrinsic stress is affecting the measurement for low deformations. Strains above $50 \mu\text{m}$ are

sufficient to dominate over the intrinsic stress and allow a stable measurement. The

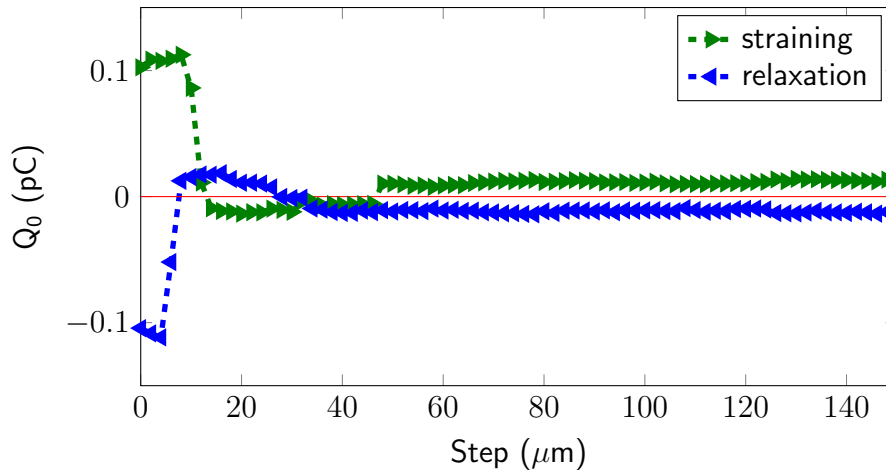


Figure 9.9: Measured charge response of sample C1 using a step width of $2\ \mu\text{m}$. Dashed lines are for guiding the eye.

calculated time constants τ depicted in *Figure 9.8(b)* show a relatively constant level of $1.1\ \text{s}$ throughout the whole bending distance. Thus no important influence originating from a change in the sample resistance is expected.

To further investigate this intrinsic stress observation and the effect of the used step size the measurement was repeated with the same parameters but a step size of $2\ \mu\text{m}$. The results of the measurement are shown in *Figure 9.9*. The obtained charge responses for the $2\ \mu\text{m}$ stepped measurement show the same characteristics as compared to the measurement using a step size of $10\ \mu\text{m}$ but a smaller amplitude. To further investigate the effect of the step size the data was used to recalculate a step size of $10\ \mu\text{m}$ by summing up the corresponding data of the $2\ \mu\text{m}$ step measurement. The resulting data is shown in *Figure 9.10* and matches the $10\ \mu\text{m}$ step measurement very well. The shape and the amplitude are almost the same, but the noise in the summed up data has increased. This can be clearly seen when comparing the regions between a strain of $60 - 150\ \mu\text{m}$. Whereas the measurement using a step size of $10\ \mu\text{m}$ shows a constant Q_0 level the $2\ \mu\text{m}$ shows constant but noisy behavior. This noise is transferred to a calculated data with a step size of $10\ \mu\text{m}$ by summing up the individual data points. The origin of the noise is charge fluctuation in the input of *Kistler 5015A* due to the triboelectric effect or imperfect shielding. Since the amplitude of the noise is independent from the measured charges it becomes more prominent for smaller charges.

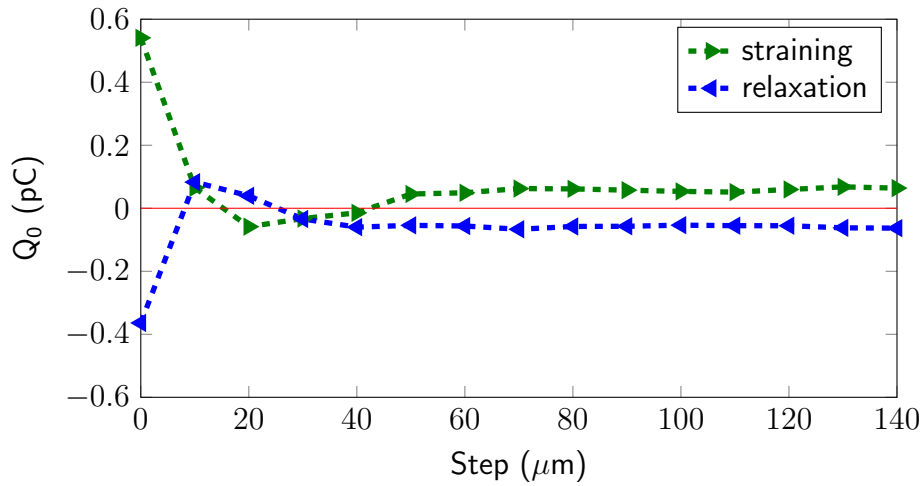


Figure 9.10: Calculated charge response of sample C1 for a step width of $10\ \mu\text{m}$ using the measurement data from Figure 9.9 with a step width of $2\ \mu\text{m}$. Dashed lines are for guiding the eye.

The same calculation was performed to visualize the characteristics of the charge responses for a step width of $50\ \mu\text{m}$, see Figure 9.11. The plot shows an almost constant charge response behavior for the measurement and is missing the exceptional polarization change features of the plots with a smaller step size.

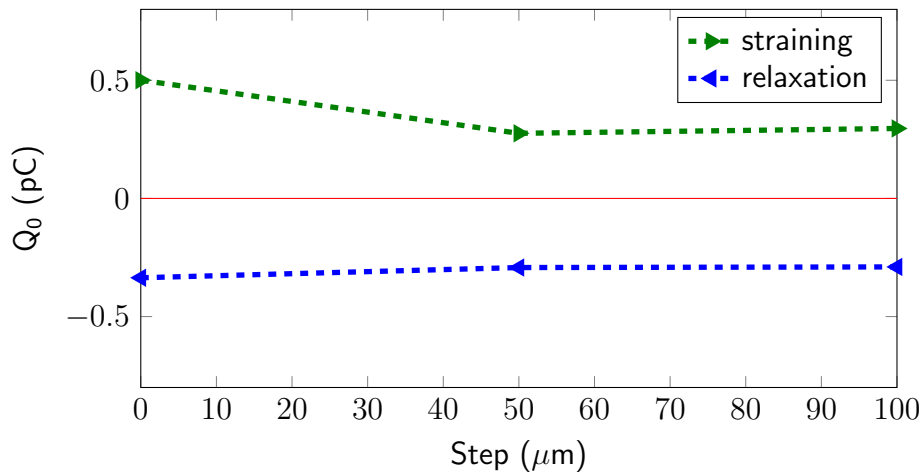
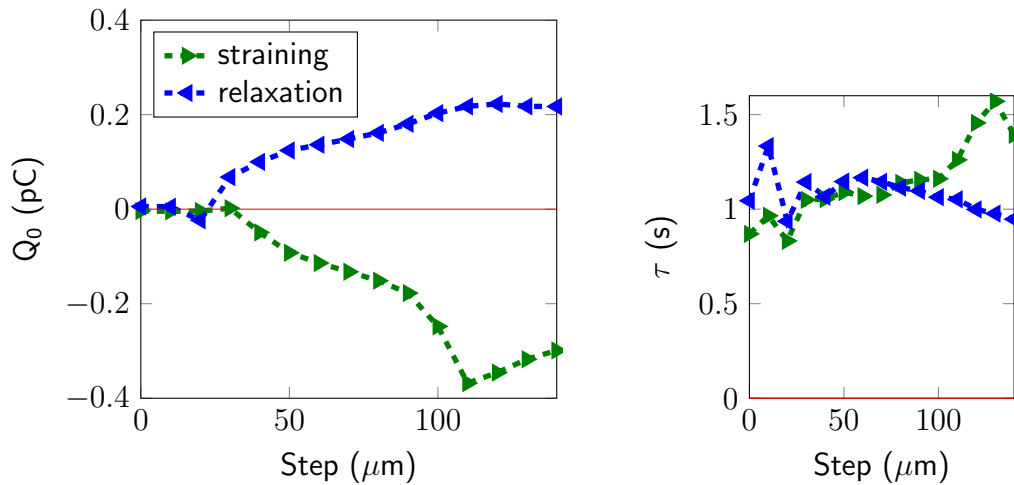


Figure 9.11: Calculated charge response of sample C1 for a step width of $50\ \mu\text{m}$ using the measurement data from Figure 9.9 with a step width of $2\ \mu\text{m}$. Dashed lines are for guiding the eye.

Comparing the measurements for the different step sizes, the consequence of these observations is to choose a step size which is large enough to have a negligible

noise contribution and small enough to see exceptional features like a polarization change. Therefore a step size of $10 \mu m$ was used for all further investigations.

The investigated sample C1 shows nearly constant piezoelectric response for strain above $50 \mu m$ which is expected (compare *Figure 9.4*). The magnitude of the charge signal upon relaxation equals the corresponding strain signal with an inverted polarization which also perfectly matches the theory. The polarity change in the charge characteristics for low strain is reproducible and indicates a complex pre-stress in the sample.



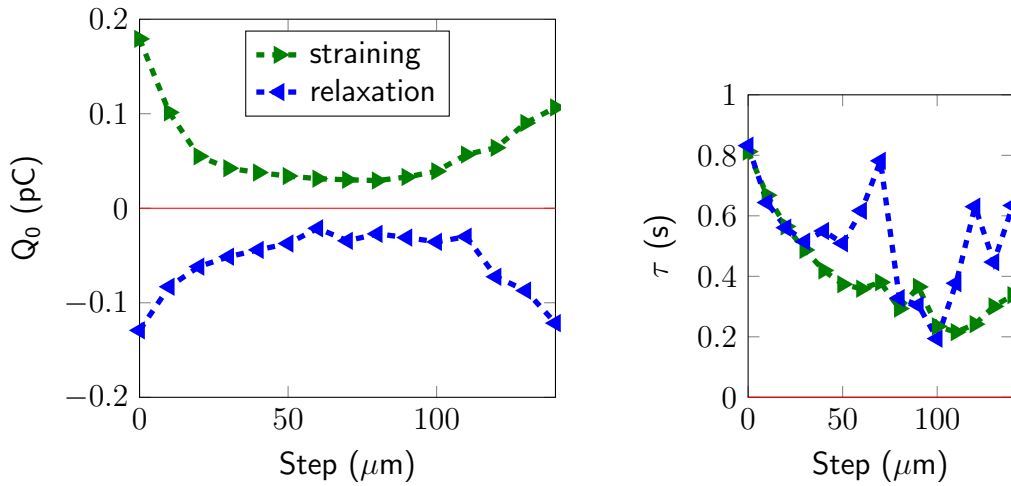
(a) Measured charge response using a step width of $10 \mu m$.

(b) Calculated time constants.

Figure 9.12: Measurement of sample C2 showing a) charge response and b) time constants. Dashed lines are for guiding the eye.

Sample C2 The charge response measurement of sample C2, as illustrated in *Figure 9.12(a)*, shows a negative charge signal when strained. The sample shows no piezoelectric response for strains below $30 \mu m$ and an increasing response for strains above. The charge signals for straining and relaxation show the same characteristics but a slightly larger effect for the strained case. The polarization of the signal is inverse to sample C1 showing a negative charge under strain. The time constant τ is relatively constant throughout the whole investigated region at a level of $1.1 s$, as shown in *Figure 9.12(b)*.

Sample C3 The measured charge response for sample C3, as depicted in *Figure 9.13(a)*, shows a positive charge signal when strained. The sample shows a



(a) Measured charge response using a step width of $10 \mu\text{m}$.

(b) Calculated time constants.

Figure 9.13: Measurement of sample C3 showing a) charge response and b) time constants. Dashed lines are for guiding the eye.

piezoelectric response over the whole measured region starting with a relatively large charge signal for small strains followed by a smaller almost constant effect for strains between $30 \mu\text{m}$ and $100 \mu\text{m}$, and a further increase for higher strains. The charge magnitude for straining is slightly above charge magnitude for the relaxation. The time constant τ is 0.8 s for a strain of $0 \mu\text{m}$ and decreasing with larger distances. This change in τ can be addressed to a change in the resistance of the sensor.

When comparing the charge response measurements for the samples C1, C2 and C3 it can be seen that the pre-strain strongly affects the charge response. This pre-strain can be induced when fixing the ZnO microrod on the substrate and additionally when mounting the sample in the setup. Thus the charge measurements show a charge response which may indicate the type of pre-stress. But even with the existence of a pre-stress the measurements allow to identify the c-axis direction which defines the polarity of the measured charge signal.

9.2.3.2 IV-Characteristics

The influence of static strain on the IV-characteristics for the samples C1, C2 and C3 is presented in the following paragraphs. All samples show single Schottky type IV-curves (compare *Figure 1.5(a)*) in the non-strained case. The samples

were strained up to $150\ \mu\text{m}$ with a step size of $2\ \mu\text{m}$ for sample C1 and $10\ \mu\text{m}$ for samples C2 and C3. The electrical current was measured for applied voltages from $-10\ \text{V}$ to $10\ \text{V}$ for every step. No effect to the reverse current of the samples was detected. Therefore, to clearly represent the important changes, the figures do not show the complete measured IV-curves but mainly the forward current.

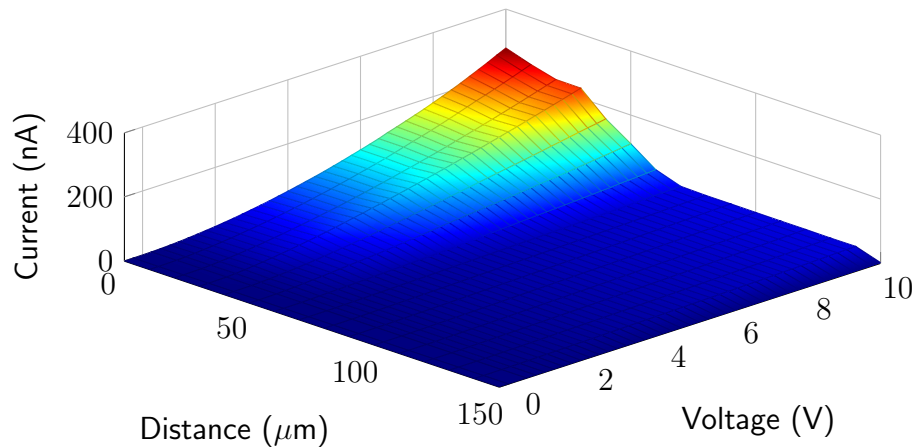


Figure 9.14: 3D representation of the measured IV curves of sample C1 upon mechanical deformation.

Sample C1 Figure 9.14 shows the change in IV-characteristics of sample C1 when straining. The conductance strongly decreases when straining up to $60\ \mu\text{m}$ and remains almost constant when straining further.

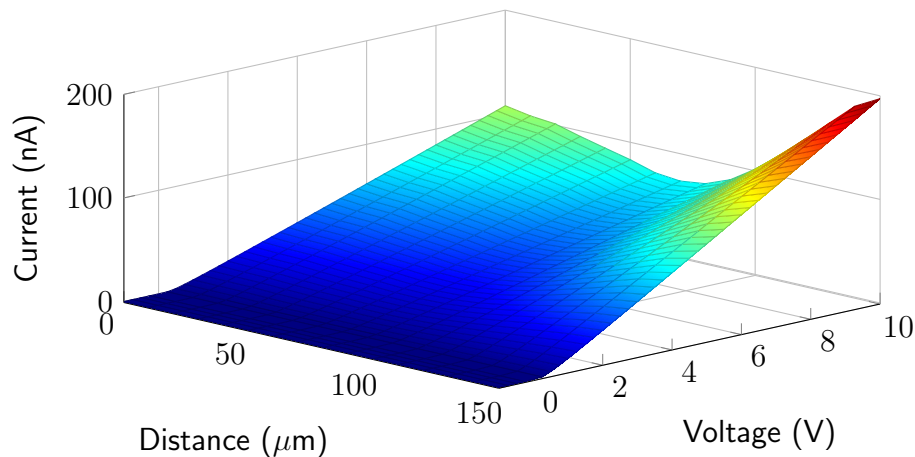


Figure 9.15: 3D representation of the measured IV curves of sample C2 upon mechanical deformation.

Sample C2 The measured change in the IV-characteristics of sample C2 under strain is depicted in *Figure 9.15*. The conductivity slightly decreases when straining up to $70\ \mu\text{m}$ and increases when straining further. The conductivity at a strain of $150\ \mu\text{m}$ is almost twice the conductivity of the non-strained sample.

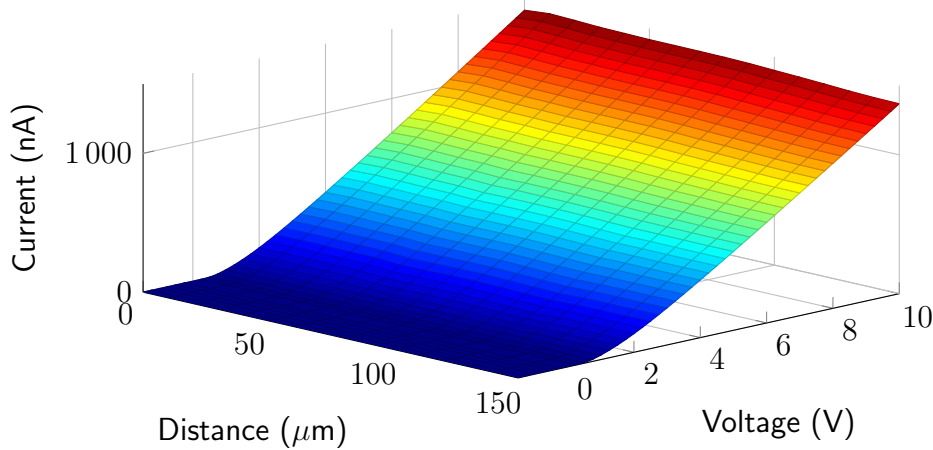


Figure 9.16: 3D representation of the measured IV curves of sample C3 upon mechanical deformation.

Sample C3 The measured change in the IV-characteristics of sample C3 under strain is depicted in *Figure 9.16*. It can be seen that the conductivity stays almost constant when straining the sample.

9.2.3.3 Relation of Piezoelectric Response and IV-Characteristics

With the combination of piezoelectric response measurements and the investigation of IV-characteristics changes under strain single piezoelectric ZnO needles can be characterized. It is possible to investigate the piezoelectric behavior, existing pre-stress and the change in band structure which causes a change in conductivity. Even though every sample showed a reproducible characteristics for the piezoelectric response and the IV-characteristics and all samples are prepared using the same concept and parameters, the effects of the individual samples vary which indicates either pre-stress in the sample or variations in the crystallinity and defect concentration. The piezotronic response can be separated from the conductivity change caused by the variations in the band structure under strain. This can be clearly seen for sample C3 which shows a change in τ , and thus in resistance in the

charge measurements, but no change in resistance when statically strained. The maximum sample rates of the measurement devices of the setup are limiting the information gain regarding the piezotronic effect. A periodic excitation of the single ZnO needle in combination with a lock-in amplifier could be an improvement of the sample rate which allows faster measurement and thus a better separation of the piezotronic effect and the band structural change. This idea was already realized in the setup described in *chapter 9.3* which allows the characterization of single needle based magnetoelectric sensors for various frequencies.

9.3 SEM IN-SITU PUSH PULL

The combined measurement of mechanical, piezoelectric and electric properties for individual ZnO microrods is a challenging task due to the small size and thus small forces. In cooperation with Sanjit Bhowmick from Hysitron an **E**lectronic **P**ush-**T**o-**P**ull (E-PTP) device was used inside a SEM to investigate the properties of a single ZnO microrod. Individual ZnO microrods with diameters of 300 nm to 400 nm and lengths of $l \approx 20\mu\text{m}$ were picked up using a nanomanipulator and positioned on the E-PTP inside a dual beam SEM-FIB. *Figure 9.17* shows SEM images with different magnifications of the used device. A Pt-based gas injection system was used for welding and contact establishment of four probing points, see *Figure 9.17(d)*. The formation of ohmic contact to the ZnO was observed for all microrods which agrees to the theoretical model as described in *chapter 1.3*. The straining of the ZnO microrods was obtained using a *PI 85* in situ nanomechanical testing instrument (*Hysitron, Inc., Minneapolis MN*). The length and diameter of the microrod was measured in situ from video frames of the SEM and directly correlated with the mechanical response.

A typical measurement for the load with respect to the displacement is depicted in *Figure 9.18*, showing several load cycles with increased maximum displacement. Additionally a load displacement measurement for a broken ZnO microrod is shown which allows the calculation of the true load as

$$F_{true} = F_m - F_i \quad (9.5)$$

where F_m is the measured force and F_i is the intrinsic force. The E-PTP device stiffness is the origin of F_i and was found to be $k = 320 \text{ N/m}$.

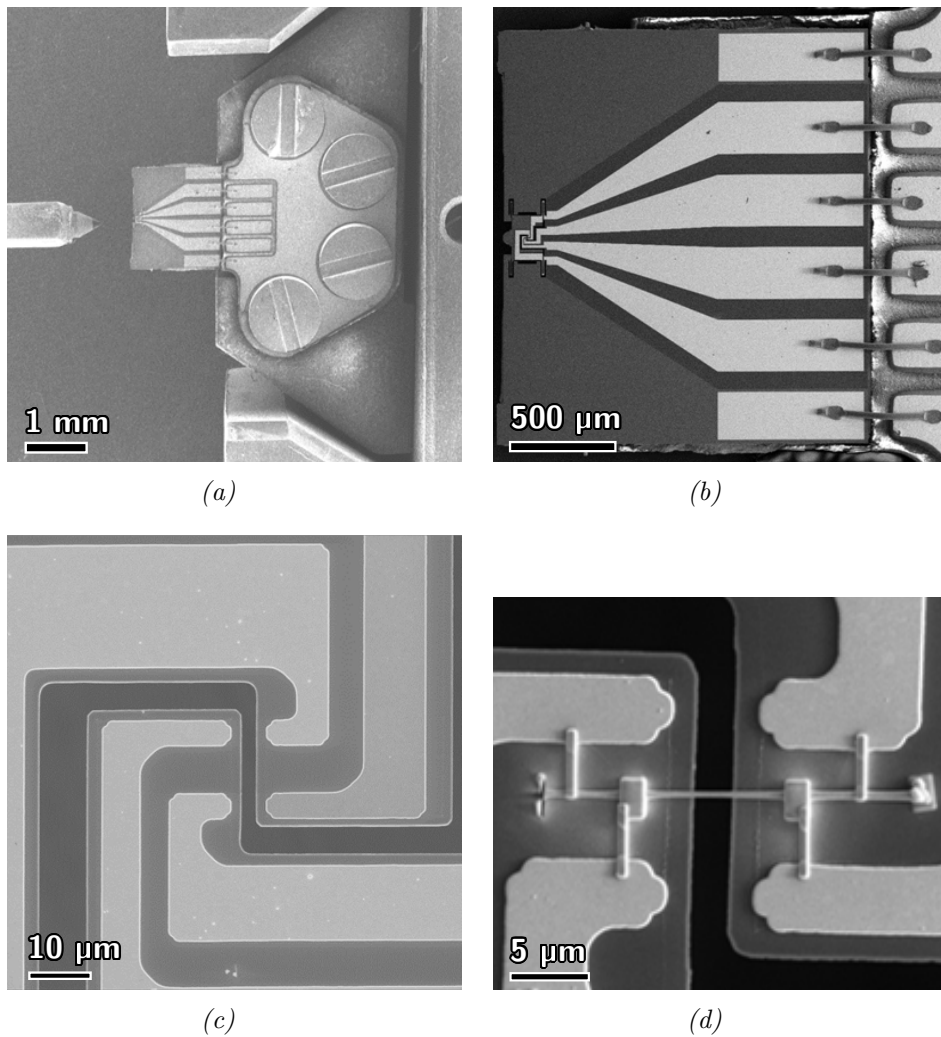


Figure 9.17: SEM images of the used E-PTP device in different magnifications. a) Low magnification image showing the indenter on the left side. b) Image showing the 4 contacts on the right side and the elastic mounting device on the left side. c) Magnified view of the sample mounting position without sample. d) Same view as c) with an already attached ZnO microrod. SEM images recorded by S. Bhowmick.

A typical stress strain curve with corresponding electrical resistance is shown in *Figure 9.19(a)*. It can be seen that the stress increases non-linearly and the microrod's elastic modulus increases slightly with increasing strain. The elastic modulus of ZnO was calculated to be $Y \approx 88 \text{ GPa}$ from a separate set of experiments where no voltage was applied. The resistance is decreasing with increasing strain resulting in an average piezoresistive gauge factors of $G \approx -1.4$. Upon

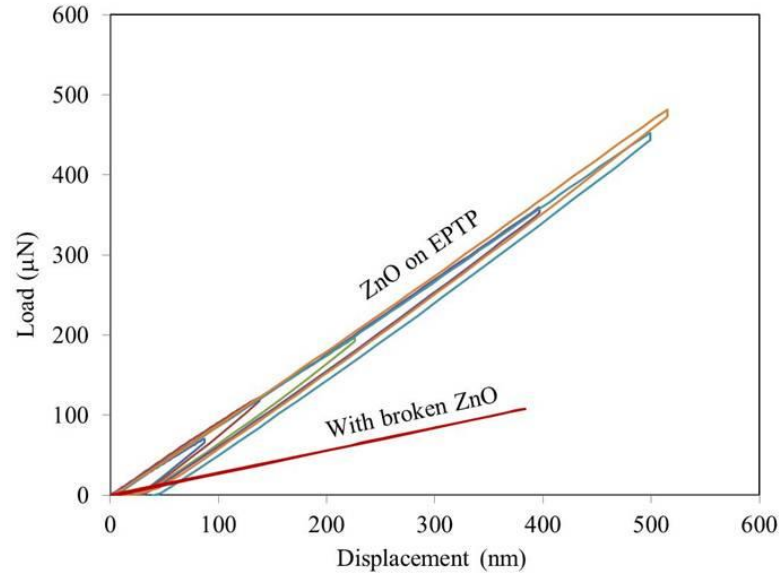


Figure 9.18: Load-displacement measurement of the E-PTP device with attached microrod and with broken microrod. Measurement performed by S. Bhowmick.

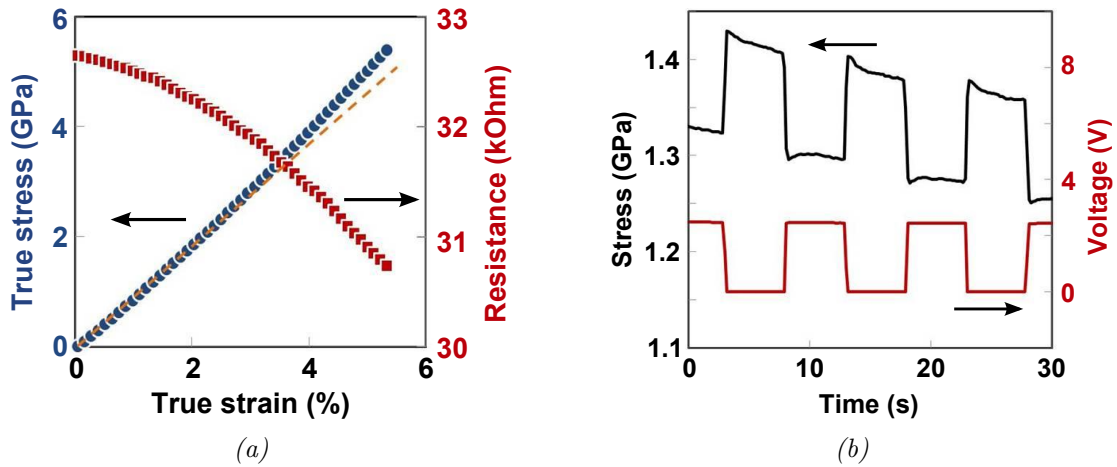


Figure 9.19: Electromechanical measurements of a single ZnO microrod. a) Stress-strain curve with the corresponding resistance strain measurement. b) Stress generation for a microrod pre-strained to 2.2% due to an applied voltage. Measurement performed by S. Bhowmick.

application of an external voltage the resulting force was measured when keeping the strain constant at 2.2%, as shown in *Figure 9.19(b)*. The measurement shows a reproducible change in stress of $\Delta\sigma \approx 0.1 \text{ GPa}$ when applying a voltage of $V = 2.45 \text{ V}$. The influence of a pre-strain to the stress change is depicted in

Figure 9.20. The measurement shows three voltage sweeps from -1.5 V to 1.5 V for existing pre-strains of 1.1%, 2.2% and 3.3%. It can be seen that the maximum stress change for the 1.1% pre-strain is only half of the size of the maximum stress change for the pre-strain of 3.3%. Thus it can be stated that the pre-strain in the measured ZnO microrod strongly affects the piezoelectric properties.

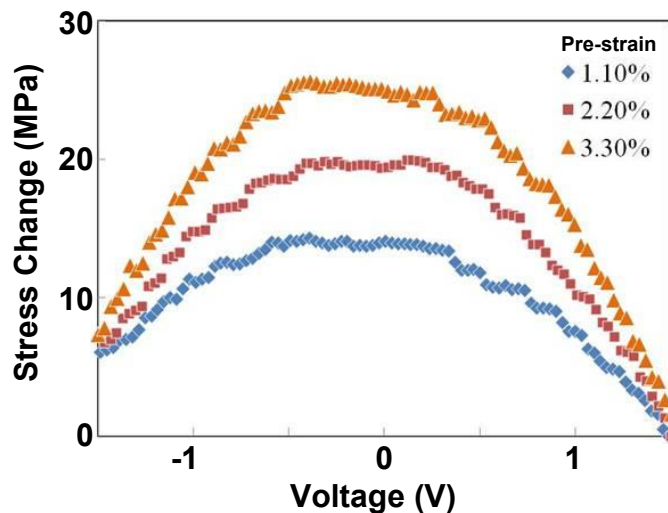


Figure 9.20: Measurement of the stress change of a single ZnO microrod for different pre-strains. The applied voltage was swept from -1.5 V to 1.5 V . Measurement performed by S. Bhowmick.

9.4 COMPARISON OF THE USED METHODS

Comparing the different methods of electromechanical characterization it was demonstrated that the mechanical connection to the substrate and the substrate itself can play a dominant role. Whereas the mounting on large polymer substrates represents a geometry similar to the application, e.g. as ME sensors as depicted in *chapter 12*, the measurement using the EPTP device is more suitable to investigate the intrinsic properties of the ZnO microrods. It was observed that the pre-stress can be dominant when using conventional gluing techniques. The piezobending device allows the characterization of this pre-stress and therefore presents an excellent way of directly investigating the electromechanical properties of a composite which contains a ZnO microrod as piezoelectric phase. To avoid pre-strain in the piezoelectric ZnO microrods thin substrates should be used when building multi phase sensors, e.g. ME-sensors.

The measurements using the EPTP device show that the intrinsic properties of ZnO microrods in the absence of pre-stress can be measured precisely in SEM using a four contact geometry with ohmic contacts. This allows the determination of the piezoresistive gauge factor. These results are important to understand the underlying mechanisms for piezotronic sensors as further discussed in *chapter 12*.

10 SUMMARY OF THE CHARACTERIZATION

The characterization of individual ZnO microrods synthesized by FTS revealed several interesting properties. Even though the individual crystals are relatively large they are single crystalline and lack any intrinsic strain, as measured by X-ray nano beam diffraction. The individual nanospikes of ZnO core spike particles have a twin boundary as a main structural feature, as measured using TEM. The electromechanical investigation of single ZnO microrods was performed using ohmic contact which were established by sputtering of Al. The electromechanical measurement of microrods attached to polymer substrates revealed the presence of pre-strain for a mechanically dominating substrate. The comparison of piezoelectric measurements with the IV-characteristics under strain indicates the presence of a non-permanent resistance change which could be related to the piezotronic effect. The piezoresistive effect could be measured precisely for an individual ZnO microrod using an EPTP device in SEM. To further distinguish piezoresistive effects from piezotronics a faster measurement concept is required which is introduced in *chapter 12*.

The properties of ZnO are strongly affected by incident light which changes the concentration of oxygen vacancies. Besides the electric properties the surface dipole moment and thus the wetting is strongly influenced. A new concept for the investigation of rough hydrophobic surface is introduced in the following chapter.

PART IV

EFFECTS AND APPLICATIONS

When investigating a new material its controlled synthesis and an exact characterization are necessary to use the properties in an application. As mentioned in *chapter 1.5* ZnO offers a large number of interesting properties which allow the realization of many applications. E.g., the different surface dipole moments of ZnO and the rough surface morphology can lead to either complete wetting or superhydrophobic surfaces depending on the oxygen vacancy concentration. The description of the wetting on such surface is usually described using the theory of heterogeneous wetting [92], as introduced in *chapter 1.6*. This theory is often insufficient when trying to understand the underlying mechanisms of wetting. Therefore an extended model was developed which allows a better understanding of superhydrophobic surfaces.

Additionally the application of the piezotronic effect in magnetic field sensors is described and compared to the conventional piezoelectric effect, commonly used in ME-sensors. The information gained from these sensors together with the results of the ZnO characterization, as mentioned in *chapter III* help to further understand the piezotronic effect and to distinguish between piezotronics and the piezoelectric effect.

11 WATER JET REFLECTION AS PROBE FOR SUPERHYDROPHOBIC SURFACES

The non-wetting of superhydrophobic surfaces is a useful phenomenon starting from the feathers of a duck ranging over functional outdoor clothes to self cleaning surfaces. Even though a general theoretical description was provided by Wenzel [91] already in 1936 and expanded by Cassie and Baxter (CB) [92] in 1945 the experimental characterization of the wetting of such surfaces is a difficult task. In the case of heterogeneous wetting as described by CB it is impossible to determine the roughness r and the wetted fraction f of the surface, compare *chapter* 1.6. Thus two samples with a different surface chemistry, a different roughness and a different wetted fraction can exhibit the same contact angle even though the underlying mechanisms of wetting differ. Therefore a contact angle measurement alone is not providing enough information to understand the wetting without further investigation. In this chapter a theory is introduced which expands the theory of CB and makes use of a dynamic wetting phenomenon water jet reflection to improve the characterization quality of wetting experiments. Further it offers the possibility to distinguish between the wetting of two different samples which obey the same contact angle. Hydrophobic materials with a certain roughness on a micrometer scale can exhibit contact angles larger than 160° . Wenzel [91] described the wetting of surfaces with a certain roughness and Cassie and Baxter [92] introduced the term of heterogeneous wetting which implies that not the complete solid below a droplet is wetted but only a fraction. By measuring the contact angle infinite tuples of f and r can be found since the equation describing the heterogeneous wetting theory is under-determined. The combination of the high surface energy of water and the non wetting properties of superhydrophobic surfaces causes several interesting effects. Whereas a lateral movement of water droplets results in the lotus effect [168], [169] a drop falling onto the surface can start bouncing [170]. Recently Chiarot [171] showed that a sequence of ink droplets can be deflected when shot on a superhydrophobic surface. For jets of liquids with a high surface tension there also exist some interesting phenomena such as the Kaye effect [172] and the deflection of mercury jets [173]. Scharnberg [174] observed that a water

jet that impacts a superhydrophobic surface can split, contract and subsequently lift off and thus the water jet seems to be reflected by the surface. *Figure 11.1* schematically shows the water jet reflection on a superhydrophobic surface. A water jet impinging a surface under an angle of α_{in} spreads on the surface up to a maximum width b , contracts and subsequently lifts off after a total flow length l_f under an angle of α_{out} . The energetic terms in *Figure 11.2* sketch the individual

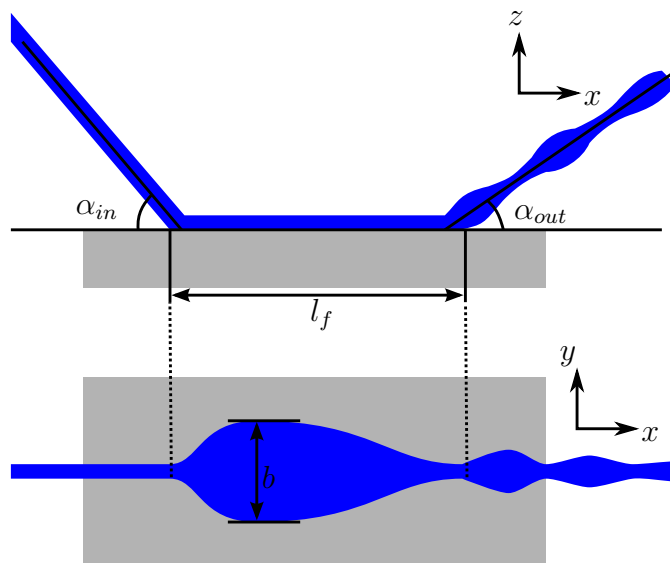


Figure 11.1: General description of a water jet coming from the left, flowing on the surface and then lifting off the surface, as shown from two viewpoints. The side view shows the angle of incidence α_{in} and reflected jet α_{out} . The flow length l_f is the distance between impact and lift off. The topview shows the broadening of the water jet on to surface to a maximum width b .

energetic contributions throughout the reflection. The total energy E_{total} must be preserved and is constant through the whole process. The kinetic energy E_{kin} is transferred in interfacial energy indicated by the liquid-gas interface (E_{LG}), the solid-gas interface (E_{SG}) and the solid-liquid interface (E_{SL}) when spreading and back to kinetic energy when contracting. In certain cases an ellipsoid cross section of the jet after lift off occurs which can be described by the oscillation in E_{kin} and E_{LG} as depicted after lift off. The water jet reflection depends on parameters like surface geometry, jet velocity and angle of incidence which affects the reflection in terms of angle of the reflected jet, flow length, spreading etc. In contrast to the reflection of light the underlying mechanism has a complex hydrodynamic na-

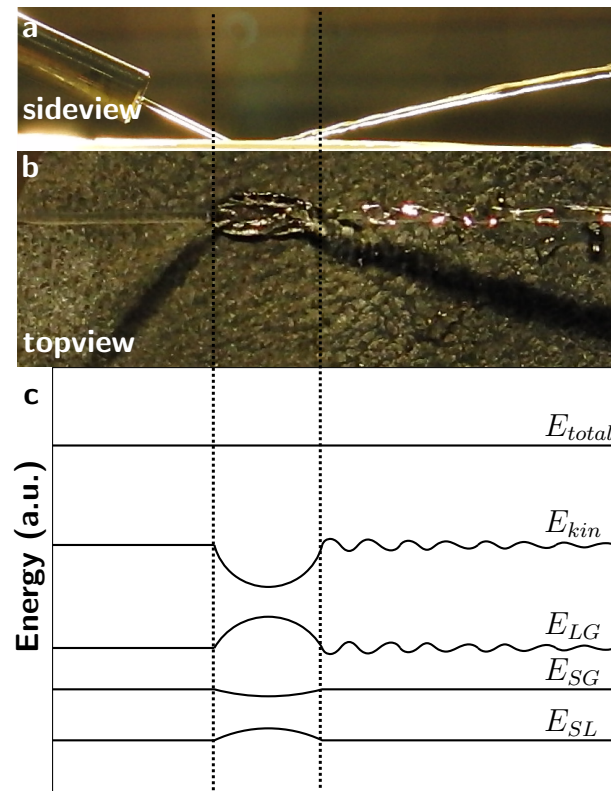


Figure 11.2: Water jet reflection on a super hydrophobic surface. a) Sideview of a typical reflection with a water jet coming from the left. b) Top view showing a water jet reflection. c) Qualitative description of the variations in the energetic terms during a complete reflection. The energetic terms split in kinetic energy (E_{kin}), and interface energies in liquid-gas (LG), solid-gas (SG) and solid-liquid (SL) interface.

ture and has not been fully described yet. Celestini [175] developed a basic model which explains the fundamentals of the water jet reflection. The kinetic energy in the surface perpendicular velocity component of the water jet is transferred in surface energy thus the water jet is spreading on the superhydrophobic surface. The spreading stops when the perpendicular velocity component becomes zero. Afterwards the surface energy is transferred back into the perpendicular velocity component with a directional shift of 180° and the jet lifts off the surface.

The artificial surfaces were formed by coating single crystalline Re fiber arrays with a thin hydrophobic polytetrafluoroethylen (PTFE) film [176]. A single crystal was grown from a eutectic NiAl-1.5 at.% Re alloy by directional solidification in a Bridgman-type growth facility. Due to the strongly asymmetric composition of the eutectic alloy and the simultaneous solidification of both phases the minor phase

(hexagonal Re) forms mechanical tough nanofibers in the major phase (B2-NiAl) [173], [177], [178]. Temperature gradient and solidification speed can be used to control the resulting structure e.g. wire diameter and spacing [179] These nanofibers are all oriented in the same crystallographic orientation (isooriented) [180] which was proven by XRD and EBSD [181]. The major phase is removed by selective etching using a (HCl (32%) : H_2O_2 (30%) : H_2O , 10 : 10 : 80) solution. The Re-nanofibers are not etched, yielding a sample with nanofibers standing upright on the alloy surface. By variation of the etching time, the fiber length can be precisely controlled. In order to obtain an artificial superhydrophobic surface, a PTFE thin film with a nominal thickness of 75 nm was deposited by sputtering [182].

The water jet was generated using a nozzle with an inner diameter of $600 \mu m$ which was connected to a closed water reservoir. The velocity of the water jet was varied using different air pressures to generate a constant pressure inside the water container. The measurement of the maximum spreading width was obtained by extraction from photographs taken from above the surface, whereas side view photographs were taken to determine the angle of incidence. A very short exposure time of typically 5 ms was obtained using a *Casio Exilim F1* digital camera. The contact time data was extracted from photographs taken from the side view which allows direct measurement of flow length l_f and the angle of incidence. Each data point represents the average of typically 10 individual measurements.

As part of the presented work a theoretical model was developed which bases on the conservation of energy during the reflection by comparing the energetic terms at two different well defined moments of the reflection: before hitting the surface and at the broadest point on the surface. The model is parameter free, directly derived from first principles and showing excellent agreement with experimental data. In order to expand common wetting theory all energies in solid-liquid and solid-gas interfaces were calculated with regard to the well established model by CB [92], which introduces the heterogeneous wetting of a surface with a roughness and a wetted fraction below the droplet (see *chapter 1.6*). The energy of the water jet before hitting the surface E_0 is the sum of the water surface energy E_{S0} and the kinetic energy E_{K0} of the jet

$$E_0 = E_{S0} + E_{K0}. \quad (11.1)$$

The surface energy of a water-air interface with area A_0 can be expressed as

$$E_{S0} = A_0 \gamma_{LG} \quad (11.2)$$

with the surface tension of water γ_{LG} . For a cylindrical jet with diameter d and

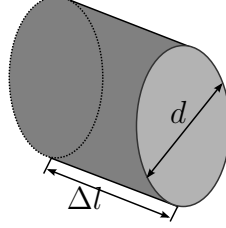


Figure 11.3: Schematic of a water jet with a circular cross section, diameter d and length Δl .

length Δl as depicted in *Figure 11.3*, the area is

$$A_0 = \pi d \Delta l. \quad (11.3)$$

This leads to a surface energy of

$$E_{S0} = \pi d \Delta l \gamma_{LG}. \quad (11.4)$$

The kinetic energy of a mass m moving with velocity v is defined as

$$E_{K0} = \frac{1}{2} m v^2. \quad (11.5)$$

The mass can be expressed as $m = \rho V$ with volume V and density ρ . The cylindrical jet volume is

$$V = \pi \left(\frac{d}{2} \right)^2 \Delta l. \quad (11.6)$$

Accordingly the kinetic energy is

$$E_{K0} = \frac{1}{8} \rho \pi d^2 \Delta l v^2. \quad (11.7)$$

Thus a jet with the velocity v and the diameter d has total energy per unit length Δl of

$$\frac{E_0}{\Delta l} = \frac{1}{8} \rho \pi d^2 v^2 + \gamma_{LG} \pi d. \quad (11.8)$$

with ρ being the density of the water. Other energetic terms as the potential energy and the viscoelastic energy can be neglected since the water jet reflection is only

stable for small jet radii and non-turbulent water jets (in all experiments Reynolds number < 1000). E.g. for the used radius of $300 \mu\text{m}$ and a jet velocity of 1 m/s the potential energy is as low as 1% of the kinetic energy. For a negligible contribution of the viscosity the energy of maximum width can be calculated from the jet velocity and the interface energy since the energy must be conserved. Following the theory of bouncing droplets [183] the viscosity of the water only plays a minor

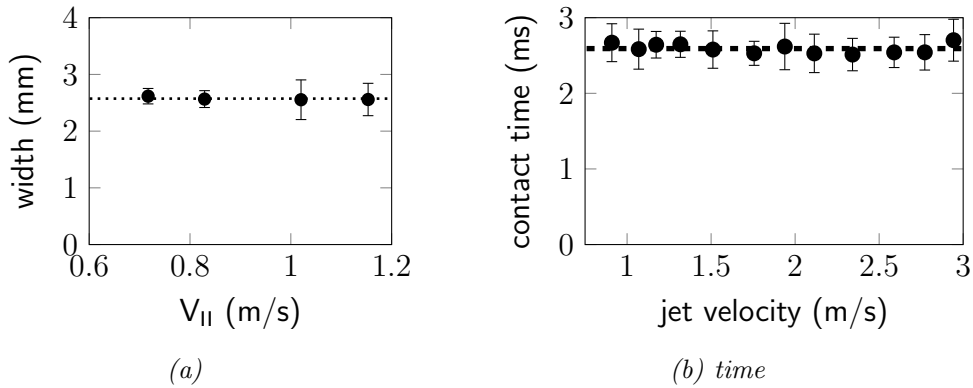


Figure 11.4: Experimental results of four different jet velocities. *a)* Measured width of the water for different surface parallel jet velocities ($V_{||}$). *b)* Measured contact time of the water for different total jet velocities.

role and can be neglected, if the contact time does not depend on the velocity of the droplet. The contact time of a water jet hitting a superhydrophobic surface was measured using a jet with a radius of $300 \mu\text{m}$ and an angle of incidence of 26.6° with respect to the surface plane. *Figure 11.4(a)* shows the maximum width for surface parallel jet velocities ranging from 0.7 m/s to 1.2 m/s and a constant perpendicular velocity. It can be clearly seen that the maximum width is not changing for a varying parallel velocity component. Therefore it can be stated that the kinetic energy in the parallel velocity component does not contribute to the spreading of the waterjet on the surface and is constant throughout the complete process. Following this finding the flow length l_f (distance impact to lift off) is a direct measure for the contact time t_c , defined as

$$t_c = \frac{l_f}{v_{||}}. \quad (11.9)$$

Figure 11.4(b) shows the contact time for jet velocities ranging from 0.9 m/s to 2.9 m/s corresponding to perpendicular Weber numbers of 1.7 and 5.4 respectively.

It can be seen that the contact time is constant over the whole measured region. This observation also agrees with the measurements performed by Celestini [175] for small perpendicular Weber numbers. Now, neglecting the viscosity of the water, a model of the water jet reflection can be developed which only bases on the principle of energy conservation. During the flow over the surface the kinetic energy is transferred into surface expansion. At the broadest point the perpendicular velocity component becomes zero and only the parallel velocity component is remaining. If the parallel component of the jet velocity is constant for the reflection, there is no influence on the maximum width and therefore the parallel velocity component does not play an important role for the reflection mechanism and can be neglected. By neglecting the parallel velocity component the kinetic energy at the point of the maximum width is zero, whereas the sum of the surface energies reaches its maximum. The total energy per unit length can be described as:

$$\frac{E_b}{\Delta l} = dA_{SL}\gamma_{SL} + dA_{LG}\gamma_{LG} + dA_{SG}\gamma_{SG} \quad (11.10)$$

With dA_x being the area per unit length. Following the theory of CB and using a wetting width b and a roughness of the liquid gas interface R_{LG} equation 11.10 can be expressed as:

$$dA_{SL} = brf \quad (11.11)$$

$$dA_{LG} = bR_{LG} \quad (11.12)$$

$$dA_{SG} = -brf \quad (11.13)$$

$$\frac{E_b}{\Delta l} = brf\gamma_{SL} + bR_{LG}\gamma_{LG} - brf\gamma_{SG} \quad (11.14)$$

$$\frac{E_b}{\Delta l} = b(rf(\gamma_{SL} - \gamma_{SG}) + R_{LG}\gamma_{LG}) \quad (11.15)$$

By applying $v = v_{\perp}$ to equation 11.8 and the conservation of energy $E_0 = E_b$ the maximum width can be written as

$$b = \pi d \frac{1/(8\gamma_{LG})\rho v_{\perp}^2 + 1}{\cos(\Theta_{CB}) - f + 1 - R_{LG}}. \quad (11.16)$$

The mathematical details can be found in the appendix (see *chapter D*). The wetted fraction can be expressed as

$$f = \cos(\Theta_{CB}) + 1 - R_{LG} + \frac{\pi d}{b} \left(\frac{1}{8\gamma_{LG}} \rho v_{\perp}^2 + 1 \right). \quad (11.17)$$

The shape of the liquid-gas interface R_{LG} is the only parameter which cannot be directly derived from common wetting theory. As an approximation the upper surface area of the water can be assumed to be flat, compare *Figure 11.5*. The curvature of the water-air interface is related to the pressure inside the water by the Laplace equation [183] leading to the same curvature on the undersurface [171]. Since the undersurface and the upper surface have the same area the roughness of the liquid-gas interface can be expressed as $R_{LG} = 2$. To check the validity of

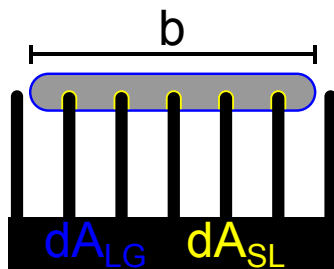


Figure 11.5: Schematic illustrating the wetting of a rough surface during the water jet reflection. Liquid-gas interface is marked blue whereas solid-liquid interface is marked yellow.

the theory two different samples with a similar contact angle were selected. The experiments were carried out using artificial surfaces made from Re fiber arrays and natural ones made of leaves of the nasturtium. The surfaces exhibited contact angles of 140.8° for the natural surfaces and 141.6° for the Re fibers. Water jet reflection experiments were carried out for both surfaces and the maximum spreading width was measured for the nasturtium leaves and for the artificial Re needles. By applying equation 11.17 the wetted fraction was calculated. Using a least square fit the calculated wetting fraction was found to be $f = 0.950$ for the nasturtium leaves. It was observed that the theory agrees with the measurement over the whole measured region, see *Figure 11.6*, and the calculated wetted fraction is reasonable. Whereas the nasturtium leaves show an almost complete wetting the Re needles obey almost no wetting ($f = 0.014$). This result perfectly fits the expectations since the Re needles have a very high aspect ratio and the wetting was expected to happen only at their tips leading to a low wetting fraction. Furthermore this result shows the superiority of nature, since it shows that a natural surface which was evolutionary optimized is perfectly suitable for water repellency without having mechanical instabilities. A wetted fraction of $f \approx 1$ presents an ideal surface in terms of super hydrophobicity since it obeys enough roughness to show a heterogeneous wetting with a high contact angle but is still

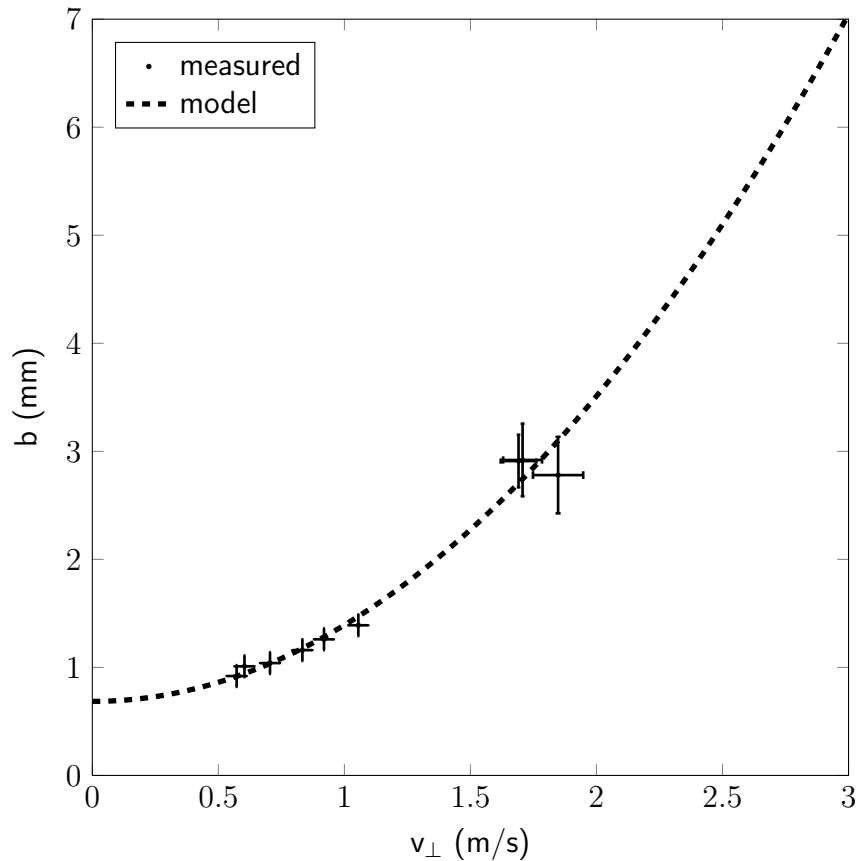


Figure 11.6: Comparison of the measured with b to the developed theoretical model.

flat enough to be mechanically stable. As shown in this work, artificial surfaces can obey similar contact angles but are not optimized for a high wetted fraction. This means that these surfaces contain a roughness which is unnecessary for a further improvement in terms of wetting but which mechanically destabilizes the surface. In our experiments it was observed that the artificial surfaces are easily destroyed mechanically whereas the nasturtium leaves are extremely stable. In conclusion it can be stated that superhydrophobic surfaces or coatings should be optimized for a high wetted fraction which can be analyzed using the presented water jet reflection approach, which allows to determine f and r in the CB model only by wetting experiments for the first time.

For the development of artificial surfaces made from, e.g. ZnO this theory can improve the understanding of the wetting and help to create better superhydrophobic surfaces.

12 MAGNETIC FIELD SENSORS

The development of magnetoelectric sensors was a central part in the project *SFB 855*. The individual project parts focused on various concepts to allow a reliable measurement of magnetic fields with a small magnitude. Theoretical descriptions, e.g., of the interfaces, integrated MEMS sensors and self biased sensors are some examples for the different aspects of sensor optimization. In the presented work the main focus is set on the investigation of individual ZnO microrods as a possible piezoelectric phase. Additionally the concept of piezotronic measurements in ME sensors is introduced and compared to the conventional measurement.

12.1 MAGNETO-ELECTRIC TEST SETUP

The ME test setup was designed to allow a characterization of magnetoelectric sensors. For this purpose a defined, static magnetic field is generated and the response of the sensor to a second, periodical magnetic field is detected. To allow the detection of small magnetic fields the shielding of the setup as well as the precise generation of a magnetic field were the main challenges. *Figure 12.1* shows the schematic of the ME test setup consisting of shielding, coils with power supplies, sensor holder and the data acquisition and controlling unit. The details of the individual parts are described in the following.

12.1.1 SHIELDING

The shielding of the setup consists of several individual shielding parts to reduce the influence of external noise to the sensor.

- aluminum shielding cylinder: The inner shield, as depicted in *Figure 12.2*, is made from aluminum to prevent any electric coupling from an external noise source to the sensor. The ends of the cylinder are closed using aluminum caps. Even though the inner shielding is designed to shield electric noise, there is an additional magnetic shielding effect invoked by eddy currents which cause a shielding of magnetic AC fields. This shielding effect depends

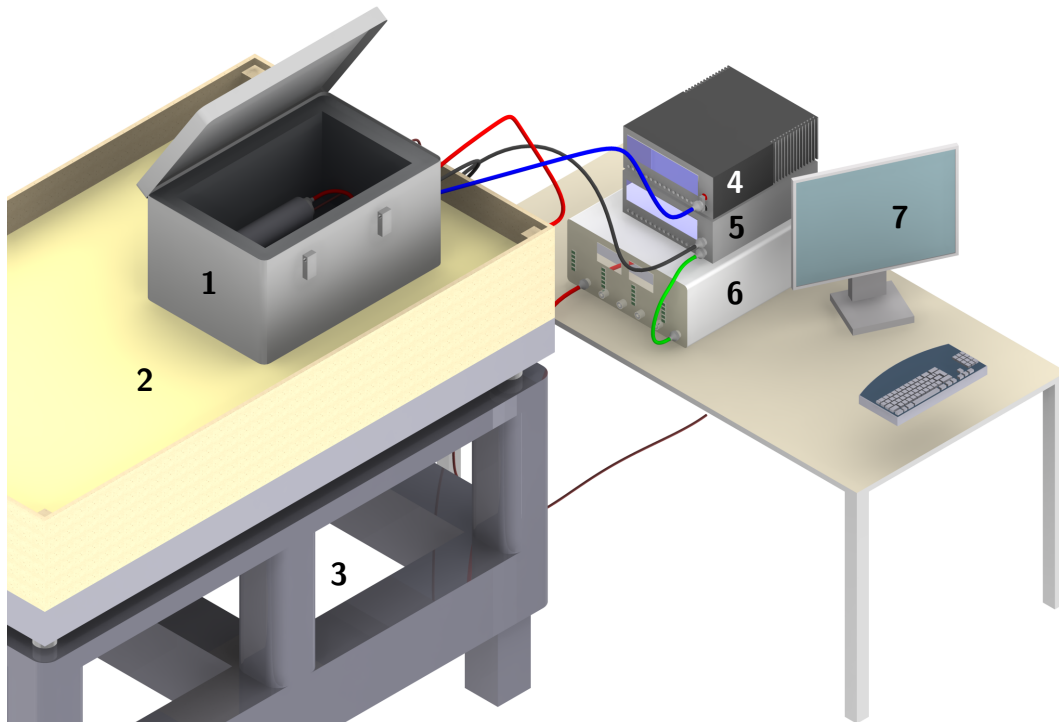


Figure 12.1: ME characterization device. The measurement box (1) is placed on a sand bed (2) which acts as the counter top for an air damped table (3). The AC power supply (4), DC power supply (5), Lock-in amplifier (6) and the controlling computer are separated from the damped table.

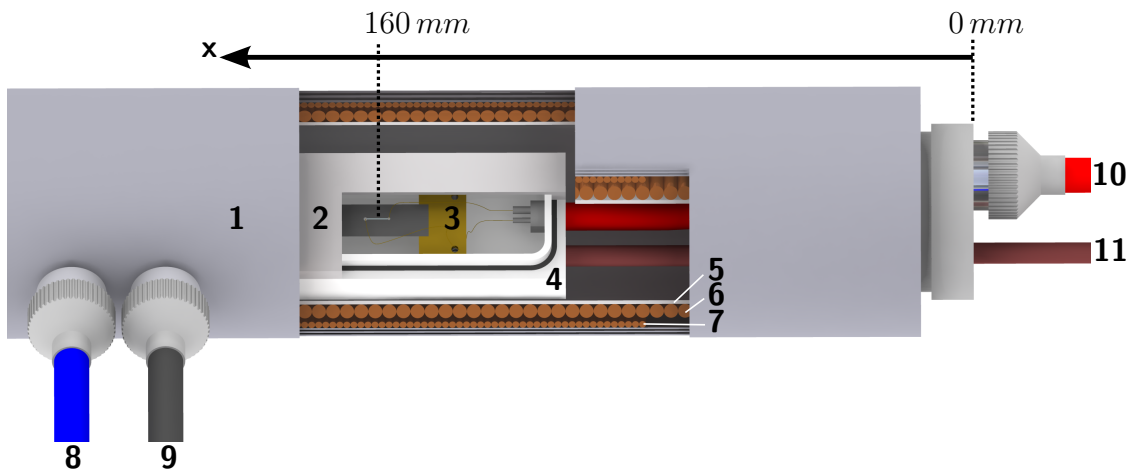


Figure 12.2: Magnetolectric measurement device consisting of a magnetic shielding (1) two pairs of coils (6 and 7) with the corresponding coaxial connectors (8 and 9) and an electrical shielding cylinder (5). The magnetolectric sensor (3) is mounted inside a ABS box (4) which can be closed with a cap (2) to allow evacuation of the box through a flexible hose (11). The sensor signal can be measured at a coaxial connector (10).

on the frequency of the magnetic field. For a thin sheet it can be described as

$$P = \frac{\pi^2 B_p^2 d^2 f^2}{6\rho D}, \quad (12.1)$$

with the lost power per unit mass P , the peak magnetic field B_p , the thickness of the sheet d , the frequency f , the resistivity ρ and density D [184]. This frequency dependency of the shielding demands a calibration of the magnetic AC coils in a broad frequency range to allow precise tuning of the magnetic field inside the aluminum cylinder, as further described in *chapter* 12.1.4.

- permalloy sheets: To shield the sensor from external magnetic fields ten layers of 70 μm thick permalloy sheets are wrapped around the cylinder containing coils and aluminum cylinder. The individual layers are electrically separated, as shown in *Figure 12.2*.
- aluminum box: The magnetic shielding cylinder with coils and sensor is placed inside an aluminum box for vibrational, light and electrical shielding. A polymer foam is fitted inside of the box to reduce external vibrations and block photons. The shielded coaxial cables for driving the coils are split to individual wires and connected to the coils inside the aluminum box. Thus no electrical noise coupling to the wires can influence the generated magnetic fields.
- Damped table: The aluminum box is placed on a vibration damped table consisting of a mass (250 Kg) made from sand in wooden surrounding and an air damped table with automatic height adjustment.

12.1.2 COILS AND POWER SUPPLIES

For generation of the magnetic fields two coils were wrapped around the inner aluminum shield. The current for the coils is generated using *Keithley Sourcemeter 2400* or a battery array for DC currents and a *Keithley current source 6221* for AC currents.

12.1.3 SENSOR HOLDER

The sensors are mounted in a polymer carrier box made from POM as depicted in *Figure 12.2*. The sensors are clamped on one side and contacted to the sensor

cable using standard connectors. The box can be closed with a top cover and is sealed with an O-ring. When closed the box can be evacuated to a pressure of 10 mbar using a vacuum suction nozzle.

12.1.4 MAGNETIC FIELD CALIBRATION

To achieve a defined magnetic field inside the shielding at the position of the sensor coil calibration measurements were performed. Both AC and DC coils were tested using a set of different constant currents supplied by the *Keithley Sourcemeeter*

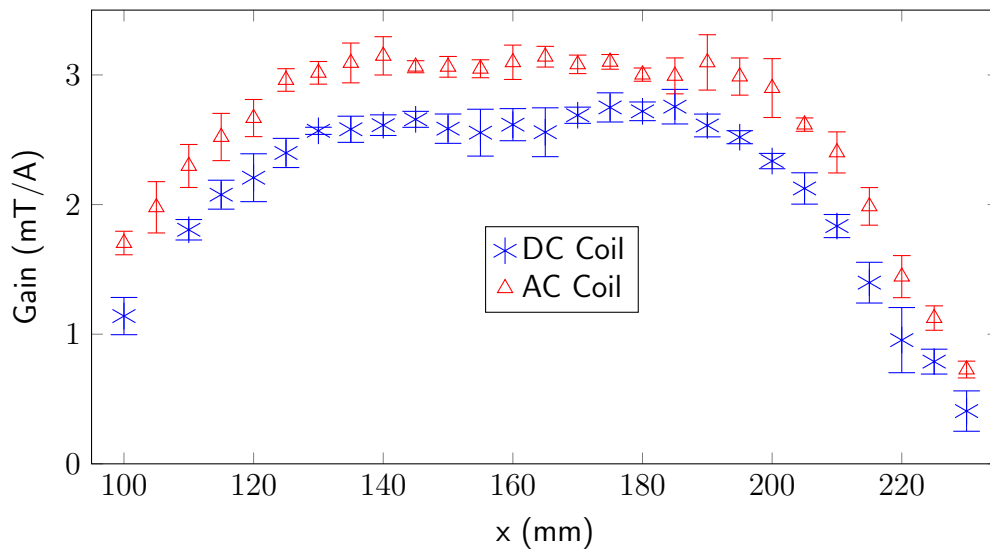


Figure 12.3: Calibration curves for the DC and AC coils of the ME Setup. The gain factor was measured at different positions inside the shielding relative to the end of the shielding cylinder.

2400. The resulting magnetic fields were detected by a Hall sensor at different positions inside the shielding. *Figure 12.3* shows the gain factors, magnetic field per current, for both coils at different positions. It can be seen that there exists a stable plateau at a position ranging from 135 mm to 185 mm relative to the end of the shielding cylinder. All measurements with ME sensors are performed within these 5 cm to guarantee a precise characterization of the sensors.

The calibration of the magnetic AC field requires a calibration measurement for all applied frequencies. A flux gate magnetic field sensor *Fluxmaster* was used to measure the magnetic AC field for frequencies from 1 Hz to 1 kHz as shown by the black line in *Figure 12.4*. By considering the bandwidth of the flux gate the gain factors can be calculated as indicated by the blue line. All measurements used the

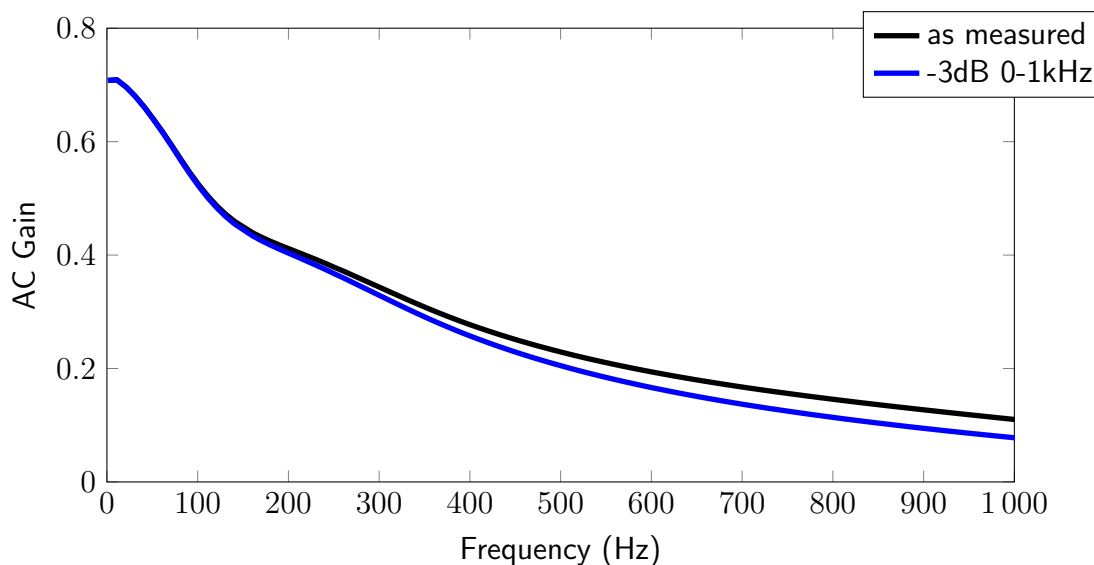


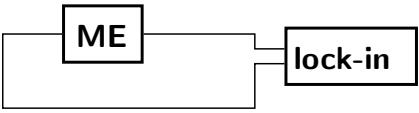
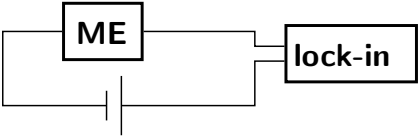
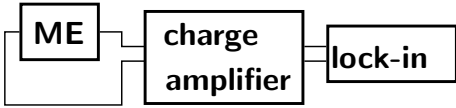
Figure 12.4: AC calibration curves showing an increase in shielding for increasing frequencies.

gain factors of *Figure 12.3* within the *Labview* software. A *Matlab* script was used afterwards to calculate the real AC fields, see *chapter B.2*.

12.1.5 MEASUREMENT AND CONTROLLING UNIT

All devices of the setup are controlled by a LabView program on a central computer. Typically a constant magnetic bias field in addition with a sinusoidal measurement field is applied to the ME sensor. The frequency and phase information of the periodic field is directly connected to a lock-in amplifier *Stanford Research Systems SR 830* via a trigger link cable. The lock-in amplifier detects phase and amplitude of the sensor signal. These values are read back by the computer software if certain prerequisites are met, e.g. best measurement range, waiting time after frequency change etc. The recorded data is stored in an ASCII file containing information about the sample, the measurement configuration (lock-in filter configuration, integration time constants) and the applied condition (magnetic fields, frequency). Various programs exist to characterize the sensors. The measurement can be varied in terms of the measurand allowing the measurement of current, voltage or charge, as shown in *Table 12.1*.

Table 12.1: Connection types for the different measurands of the ME setup.

Measurand	Connection Schematic	Description
Voltage (V)		Direct connection of the lock-in amplifier to the sensor.
Current (A)		Battery array supplying voltage from -27 V to 27 V in steps of 1.5 V . Lock-in amplifier is detecting the current.
Charge (C)		Sensor is connected to charge amplifier. Proportional output is connected to lock-in amplifier which detects the voltage.

12.1.6 BIAS MEASUREMENT

The bias measurement allows the investigation of the influence of an applied magnetic bias field to the sensor signal. A periodic magnetic field and with a fixed frequency is applied to the sensor. The magnetic bias field is varied and the response signal of the sensor to different bias fields is detected. *Figure 12.5* illustrates a typical bias field measurement showing the low sensor signal if no bias field is applied whereas a local maximum is observed at 0.6 mT . The bias field measurement is a prerequisite for other measurement routines since it allows to define the optimum working bias field for each sensor and therefore increases sensors' signal and sensitivity. Details about the developed software can be found in the supplementary information (*chapter C.6*).

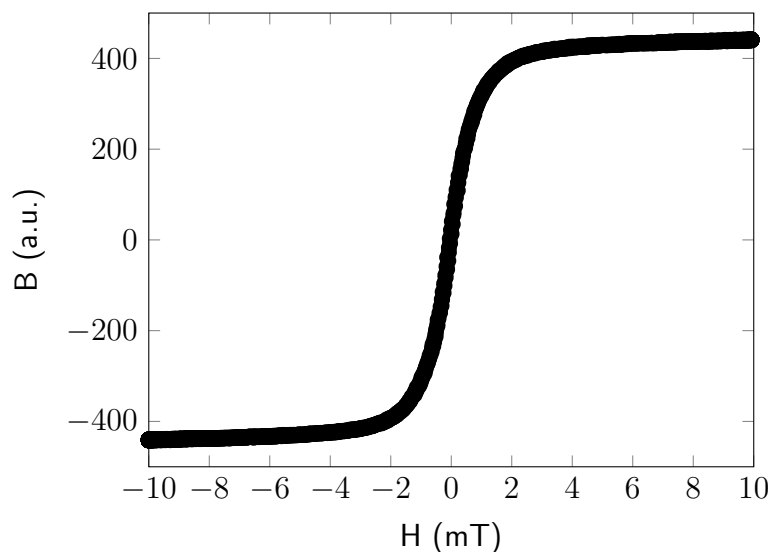


Figure 12.5: Typical bias field measurement showing a vanishing effect in the absence of a magnetic bias field and local maxima at ± 0.6 mT.

12.1.7 FREQUENCY MEASUREMENT

The frequency measurement allows the characterization of the sensor's frequency dependency and help finding features optimum working frequencies like the resonance frequency of the sensor. The measurement is performed by applying a constant magnetic bias field and a periodic magnetic field with a constant amplitude. The frequency of the periodic field is varied throughout the measurement and the sensor response is recorded. *Figure 12.6* shows a typical frequency measurement with a resonance peak at 187 Hz. The Q-factor, the bandwidth and the position of the resonance peak can be determined using a Matlab script, compare *chapter B.4*. Details about the developed software can be found in the supplementary information C.7.

12.1.8 FREQUENCY BIAS MAPPING

A combination of the two measurements mentioned above is the frequency bias mapping measurement. The electric response of a sensor is measured when varying the frequency and magnetic bias field. The resulting data gives information about the position, Q-factor and height of the resonance peak with respect to the applied magnetic bias field. *Figure 12.7* shows a measured example of a sample which has

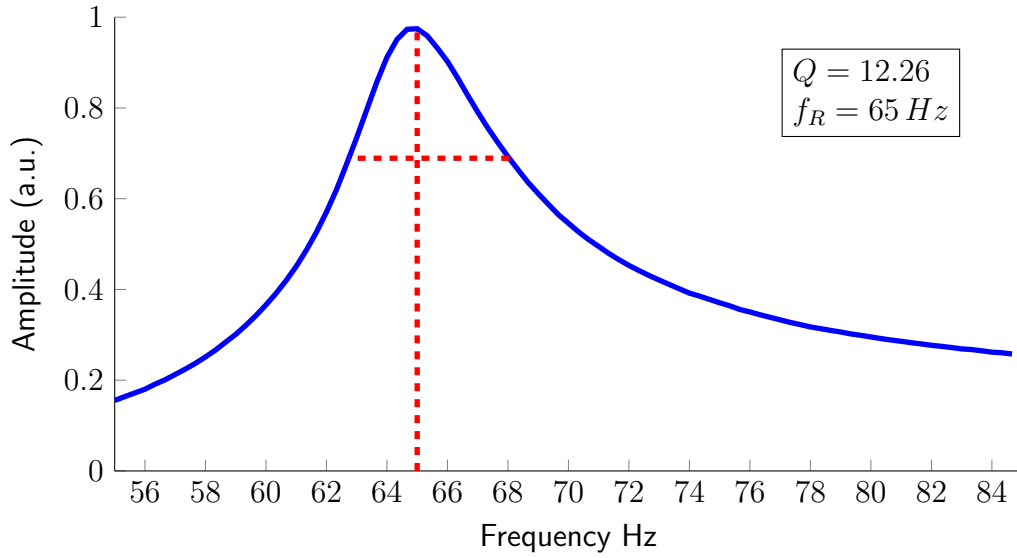


Figure 12.6: Typical frequency measurement showing a resonance peak at $f_R = 65 \text{ Hz}$ and a Q -factor of $Q = 12.26$.

a resonance peak around 80 Hz . The position of the optimum response with the resonance frequency f_R and the corresponding Q -factor Q at a magnetic bias field B_{Bias} can be extracted from the measurement. The influence of the orientation of the magnetic bias field can be expressed as the ratio of the average signals for positive and negative bias field

$$SR_{\pm} = \frac{\bar{X}(B_{Bias} > 0)}{\bar{X}(B_{Bias} < 0)} \quad (12.2)$$

Details about the developed software can be found in the supplementary information C.8.

12.1.9 LINEARITY MEASUREMENT

The sensitivity measurement is used to characterize the sensor in terms of linearity and limit of detection. To maximize the ME effect the bias field is set to the optimum value as detected by the bias map measurement. For resonant sensors the frequency of the magnetic measurement field is typically set to the resonance frequency of the sensor. For non-resonant sensors any frequency can be selected. *Figure 12.8* shows a typical sensitivity measurement. The sensor has a linear characteristic for large magnetic fields and shows constant noise for low magnetic

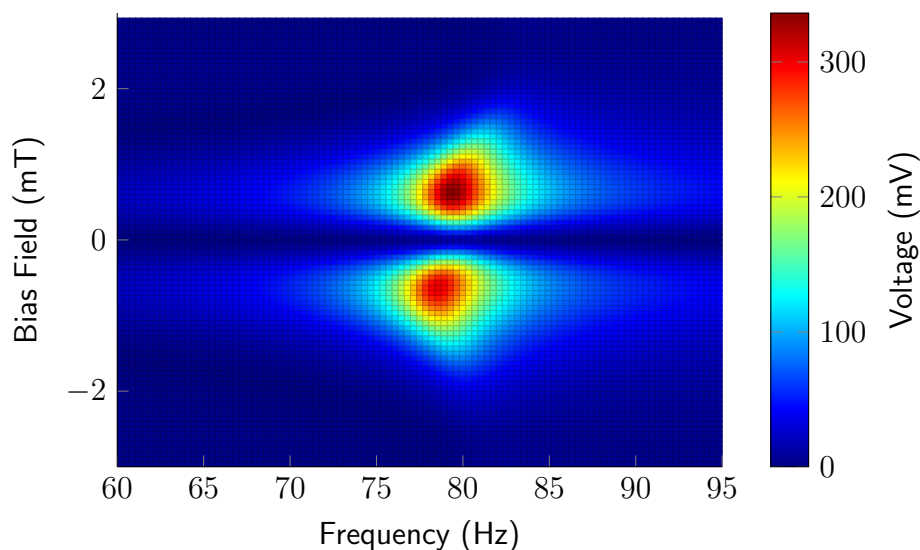


Figure 12.7: Example for a frequency bias mapping measurement with resonant peaks at 79 Hz.

fields. The limit of detection (LoD) can be calculated by fitting the linear response for large fields and the noise level. The intersection of these linear fits determines the limit of detection. Details about the developed software can be found in the supplementary information C.9.

12.1.10 RESONANCE SHIFT SENSITIVITY

The resonance shift measurement can be used to characterize the delta-E effect of a resonant sensor [185]. For this type of measurement the sensor is excited with a frequency close to the resonance frequency and the response of the sensor is measured. By application of a magnetic DC field the resonance peak shifts leading to a detectable response of the sensor. *Figure 12.9* shows the principle of a resonance shift measurement, using a piezoelectric oscillator for excitation, with the resonance peak shifting to higher frequencies for an increasing magnetic field. The excitation with a fixed frequency would lead to a sensor signal which depends on the applied magnetic DC field. A high slope of the signal close to the resonance frequency is desirable and can be achieved using a large excitation of the sensor which will cause an anharmonic resonance curve as shown in *Figure 12.9*.

The resonance shift measurements with the ME setup are restricted to the available hardware and therefore do not allow ideal measurements. The excitation of the sensor can be either performed mechanically using an unshielded piezoelectric

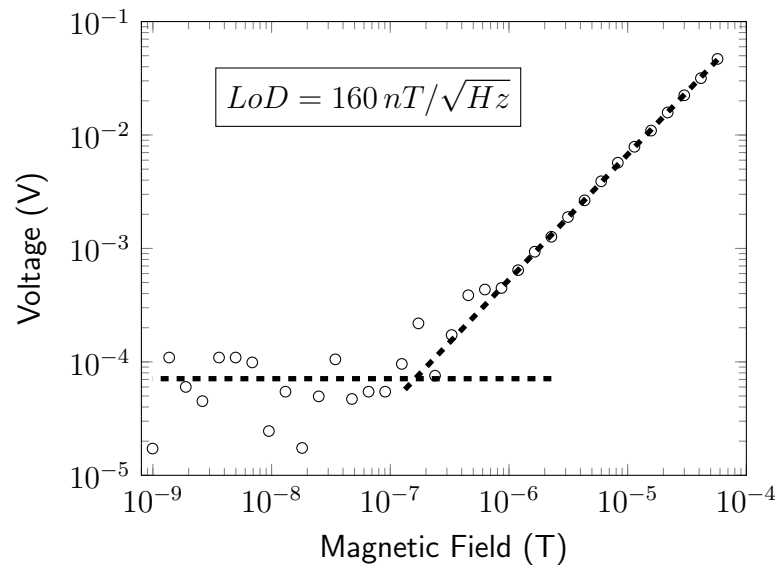


Figure 12.8: Typical linearity measurement measuring the voltage created by the sensor for magnetic AC fields with a varying amplitude. The limit of detection (LoD) is the intersection of the two dashed lines which represent the noise level and the linear response for large fields.

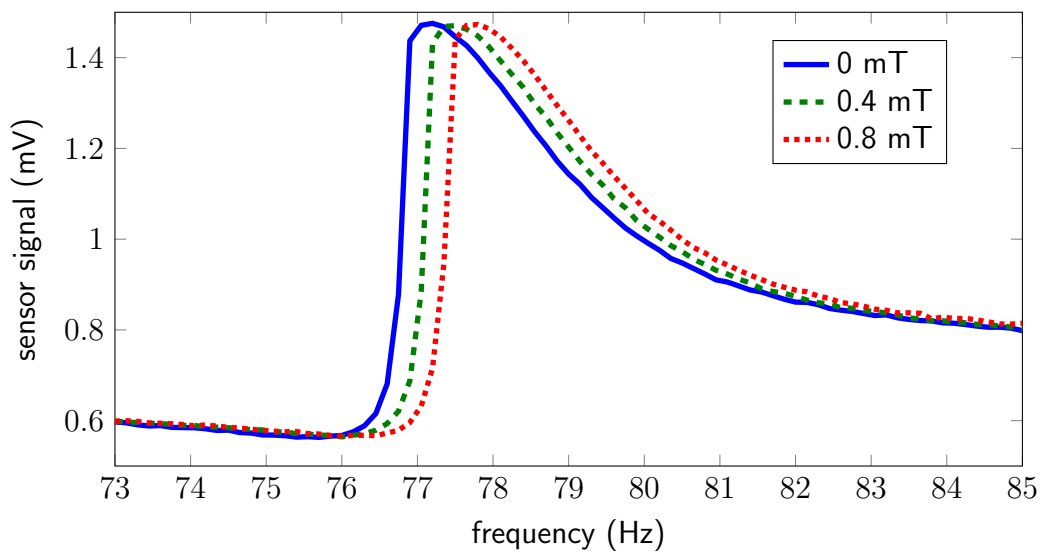


Figure 12.9: Typical measurement of a mechanically driven sensor showing the shift in resonance frequency for different applied magnetic fields.

actuator or magnetostrictively using a magnetic AC field. Whereas the mechanical excitation introduces a large noise in the measurement signal and thus limits the detection of small signals, the magnetostrictive excitation is limited by the com-

bination of current source and used coils which do not allow large excitations. To enable high resonance signals as magnetic bias field is required. Since the setup consists of only two separate coils the magnetic bias field and magnetic DC measurement field have to be generated superposed by a single DC current source. Due to technical limitations this allows either the application of an ideal bias field superposed with large measurement fields or no bias field and small measurement fields. These technical issues could be solved by a new setup that contains three coils and optimized current sources. Due to these existing limitations the resonance shift measurements are not further discussed for the individual samples. *Figure 12.10* shows an example for a resonance shift sensitivity measurement at a frequency of 68 Hz using a magnetic AC field of 0.2 mT . The measurement shows

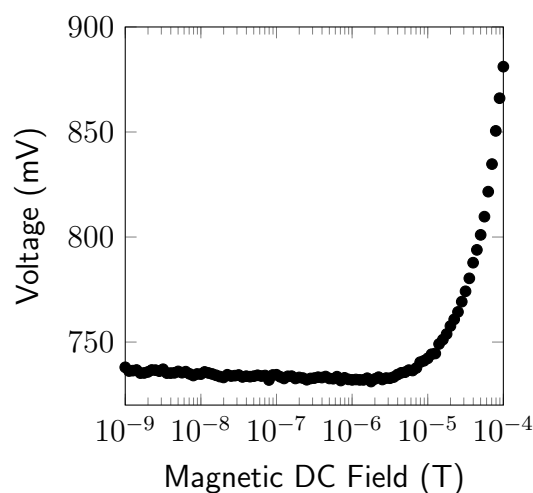


Figure 12.10: Measurement of the signal decrease due to the Delta-E effect.

a non-linear response to the applied magnetic DC field. The measured sensor voltage decreases with the decreasing magnetic field and approaches a constant level for magnetic fields below $2\text{ }\mu\text{T}$. This example shows that measurements which detect the shift in resonance are applicable for the presented ME sensors but are limited by the measurement setup at the time of writing.

12.2 2-1 ME COMPOSITES

The preparation of the 2-1 ME composites is analogous to the devices used in the piezoelectric bending system as described in *chapter 9.1*. FeCoSiB (*Metglas 2605SA1*) was used as magnetostrictive substrate material and is separated from the piezoelectric ZnO needle by *Kapton* tape. The investigation of the ME sensors is divided in three parts describing the basic sensor, the geometric effects and the application of piezotronics in a ME device.

12.2.1 BASIC SENSOR

The sensor ME1 was prepared using a FeCoSiB foil substrate with dimensions of $22.7\text{ mm} \times 8.9\text{ mm}$. The selected ZnO needle ($d = 242\text{ }\mu\text{m}$, $l = 730\text{ }\mu\text{m}$) was positioned as shown in *Figure 12.11*. Both electrical contacts were established using

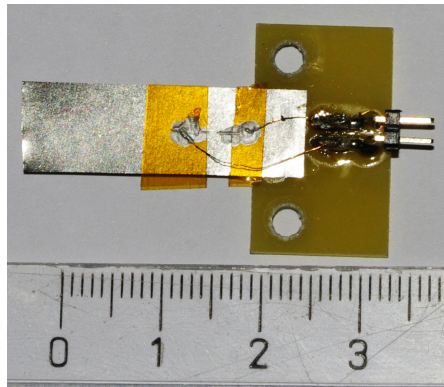


Figure 12.11: Geometry of Sensor ME1

Acheson Silver DAG 1415 M silver glue. *Figure 12.12* shows the IV-characteristics of the sample directly after introducing to the setup (*Figure 12.12(a)*) and after 50 hours (*Figure 12.12(b)*). The IV curve directly after inserting the sample shows a characteristic similar to a classical diode with a small current for negative voltages and an exponentially increasing current for positive voltages. Regarding the theoretical models described in *chapter 1.3* the Ag should form Schottky type contacts to the ZnO leading to a symmetric IV curve with a high resistivity. Necessary for a symmetric IV curve is the presence of 2 diodes with the same characteristics that are poled contrary. Thus independent from the applied voltage one of the diodes is always reverse biased and limiting the current.

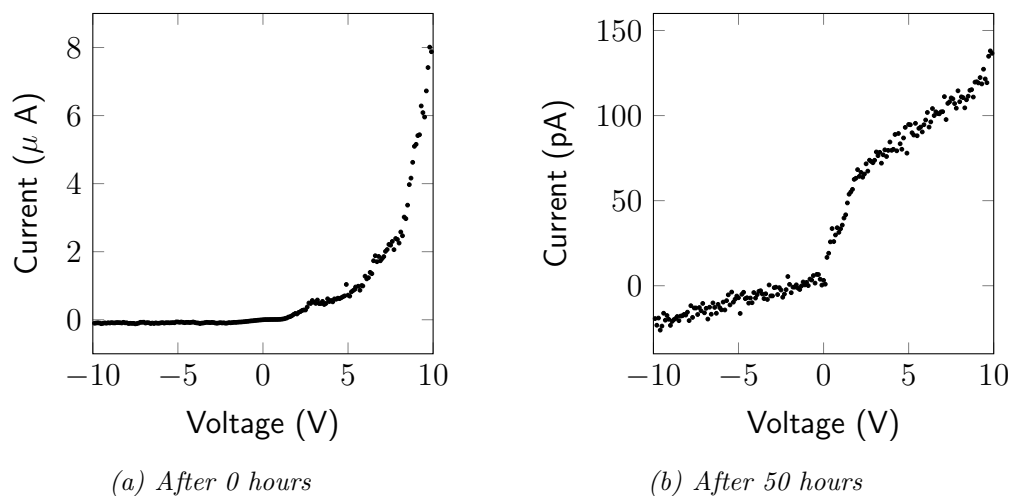


Figure 12.12: Light influence on the IV-characteristics of Sensor ME1.

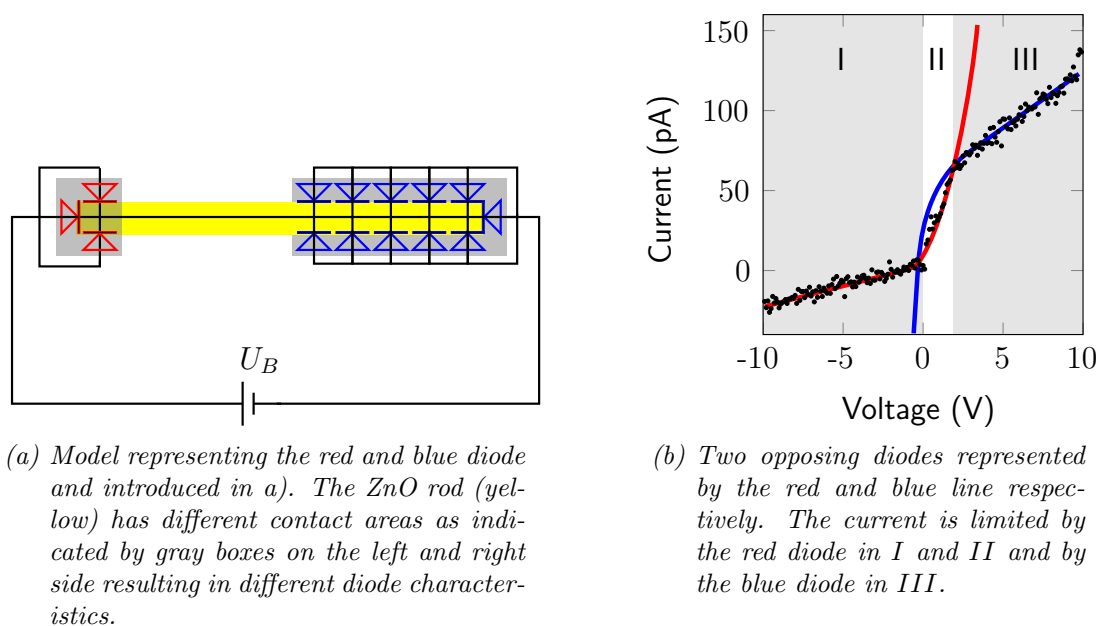


Figure 12.13: Theoretical model which could explain the measured IV characteristics as shown in Figure 12.12(b).

The observed IV characteristic is a result from 2 contrary poled diodes which have a strongly different IV characteristic. Therefore the diode with the higher resistivity is limiting the current flow for any applied voltage making the second diode invisible in the overall IV-characteristic. Since the forward current of a diode is increasing exponentially with the applied voltage whereas the reverse current is

only increasing linearly, it is expected that the current becomes dominated by the second diode for large applied voltages. This effect is observed for the sample after 50 hours. *Figure 12.13(b)* qualitatively explains the current by dividing the graph in 3 parts and showing the characteristics of both individual diodes, as indicated by the blue and red lines. For negative voltages (region I) the reverse current of the red diode is limiting the overall current leading to a small total current flow. For small positive voltages (region II) the red diode is still dominating leading to an exponential increase of the current. For large positive voltages (region III) the reverse current of the blue diode is limiting the overall current flow leading to a higher resistivity.

Following this explanation the two Ag-ZnO contacts must have a strongly different IV characteristic. One possible explanation could be a difference in the contact area as schematically shown in *Figure 12.13(a)*. The red diode symbols indicate the contact to the ZnO microrod (yellow) on the left side whereas the larger amount of blue diode symbols indicate the interface area on the right side. This would result in a non-symmetric IV-characteristic as shown by the red and blue curve in *Figure 12.13(b)*. Other possible explanations for the difference in the two Schottky diodes are local variations of the oxygen vacancy concentration which may lead to different built in potentials [186]. It was also observed that Schottky contacts to Ag may change after some time [187], which could explain the observed behavior.

ME Sensing To investigate the response of the sensor to a magnetic AC field a bias mapping measurement was performed using a magnetic AC field with an amplitude of 0.02 mT , see *Figure 12.14*. The measurement shows a symmetric response with respect to the magnetic bias field with the largest signal response for 0.87 mT having a resonance peak at 63 Hz with a Q-factor of $Q = 8.5$. When comparing the absolute signal values a slightly higher signal, is found for positive bias fields ($SR_{\pm} = 1.34$). This signal difference is a result of sensor drift which is caused by the variations of the oxygen vacancy concentration. A linearity measurement was performed, using a frequency of 63 Hz and a magnetic bias field of 0.87 mT , as shown in *Figure 12.15*. The sensor response was linear ($\alpha_{ME} = 7.8\text{ V/A}$) and limit of detection was found to be $15\text{ nT}/\sqrt{\text{Hz}}$. To investigate the higher resonance modes a scanning map ranging from 210 Hz to 290 Hz was recorded, as shown in *Figure 12.16*. The measurement shows two resonance peaks which are partially overlapping. For the higher peak an optimum bias field of 0.73 mT at

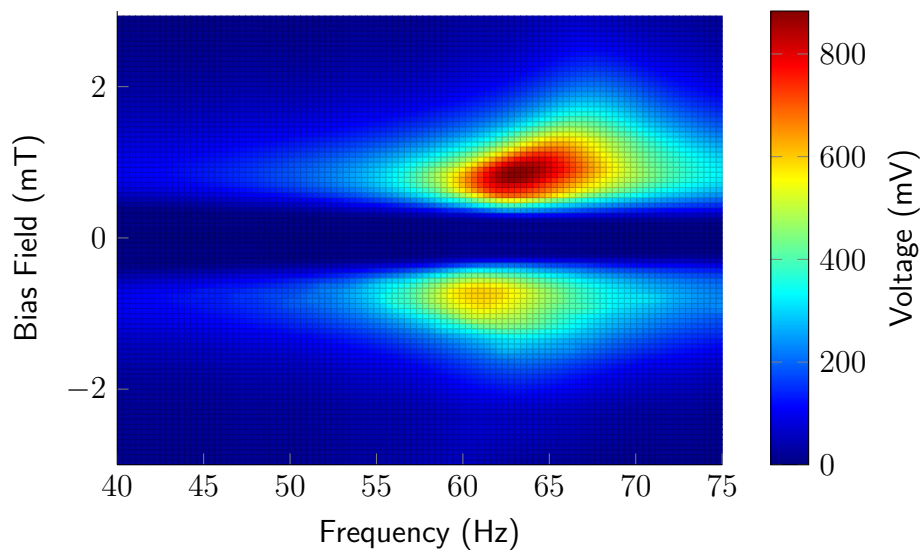


Figure 12.14: Scanning map of sensor ME1 showing a resonance peak at 63 Hz for an optimum bias field of 0.87 mT.

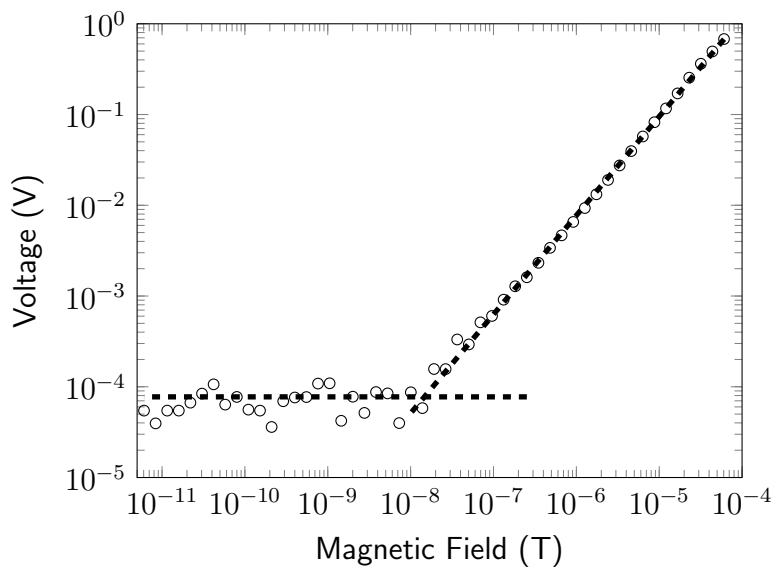


Figure 12.15: Linearity measurement of sensor ME1 measured at 63 Hz using a magnetic bias of 0.87 mT yielding a limit of detection of $15 \text{ nT}/\sqrt{\text{Hz}}$

a frequency of 245.6 Hz was found, resulting in a Q-factor of 15.5. The sensor response is symmetric with respect to the applied magnetic bias field ($SR_{\pm} = 1.1$) The linearity measurement at this resonance peak is depicted in *Figure 12.17* and shows a limit of detection of $20 \text{ nT}/\sqrt{\text{Hz}}$. When comparing the results to the first resonance mode it can be seen that the limit of detection is slightly higher even

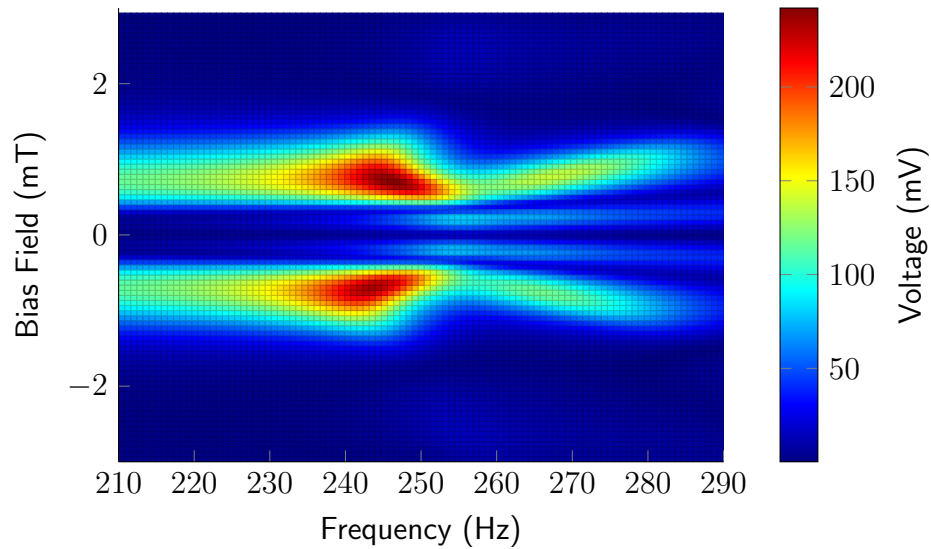


Figure 12.16: Scanning map of the higher resonance modes of sample ME1 showing a resonance at 245.6 Hz for a bias field of 0.73 mT.

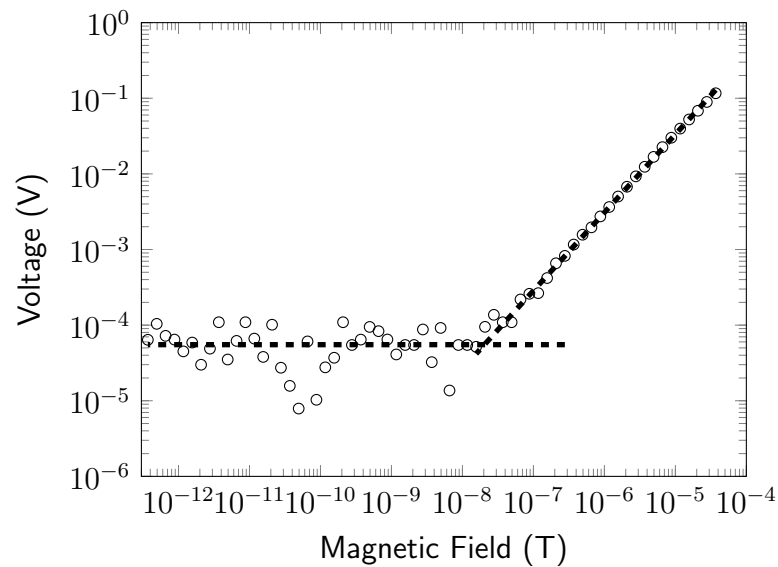


Figure 12.17: Linearity measurement of sensor ME1 measured at 245.6 Hz using a magnetic bias of 0.73 mT yielding a limit of detection of $20 \text{ nT}/\sqrt{\text{Hz}}$

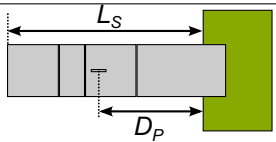
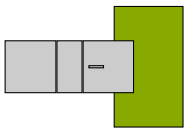
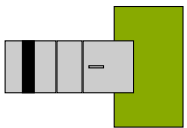
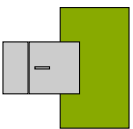
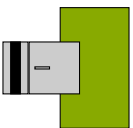
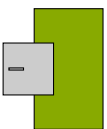
though the Q-factor of the resonator is higher at the second resonance mode. This is a result of the same noise level of $80 \mu\text{V}/\sqrt{\text{Hz}}$ and the different ME coefficients. Accordingly a high Q-factor together with a large ME coefficient is beneficial for a ME sensor. One major problem is the relatively high noise level which is a result

of the low capacity of the sensor. A workaround is the utilization of an intrinsic voltage to current transducer as presented in *chapter 12.2.3*. The bias maps are a good measure for the quality of the sensor and can be used to easily compare sensor modifications. The influence of the sensor geometry is further discussed in the following chapter.

12.2.2 SENSOR GEOMETRY

The resonance frequency depends strongly on the geometry of an oscillating sensor, as mentioned in *chapter 2.2*. The geometric parameters that can be varied when building 2-1 ME sensors are the size of the substrate material, position of *Kapton*

Table 12.2: Overview of the used geometrical configurations of sensor ME2. The sketch illustrates the geometry of the sensor with length L_S and distance of the ZnO microrod to the clamping D_P .

Sample	Sketch	Geometry	Comment
ME2.1		$L_S = 37 \text{ mm}$ $D_P = 20 \text{ mm}$	
ME2.2		$L_S = 20 \text{ mm}$ $D_P = 3.5 \text{ mm}$	
ME2.3		$L_S = 20 \text{ mm}$ $D_P = 3.5 \text{ mm}$	mass (43 mg) attached as indicated by thick black line (17 mm from clamping)
ME2.4		$L_S = 11 \text{ mm}$ $D_P = 3.5 \text{ mm}$	
ME2.5		$L_S = 11 \text{ mm}$ $D_P = 3.5 \text{ mm}$	mass (107 mg) attached as indicated by thick black line (9 mm from clamping)
ME2.6		$L_S = 6 \text{ mm}$ $D_P = 3.5 \text{ mm}$	

tape and position of the ZnO needle. In addition to these parameters the influence of an applied mass on the sensor was investigated. By modifying a sensor and subsequently measuring a bias map using an AC amplitude of 0.2 mT the influence of the individual modification steps is clarified. The sensor ME2 was prepared using a FeCoSiB substrate completely covered with Kapton tape. A single ZnO microrod ($d = 101\ \mu\text{m}$, $l = 2.6\text{ mm}$) was positioned on the sensor and contacted using silver glue. The IV-characterization revealed a conductivity similar to sensor ME1. 6 modifications (ME2.1, ME2.2, ME2.3, ME2.4, ME2.5 and ME2.6) of this sensors were investigated with the details of each geometry described in *Table 12.2*.

ME2.1 The frequency bias map of the sample modification ME2.1 is shown in *Figure 12.18*. The measurement shows a symmetric response with respect to the applied magnetic bias field with only a slightly stronger signal ($SR_{\pm} = 0.78$) when applying negative bias fields. The highest resonance peak is observed for a bias field of $B_{Bias} = -0.75\text{ mT}$ at $f_R = 218.2\text{ Hz}$ having a Q-factor of $Q = 30.8$ and a ME-coefficient of $\alpha_{ME} = 0.76\text{ V/A}$.

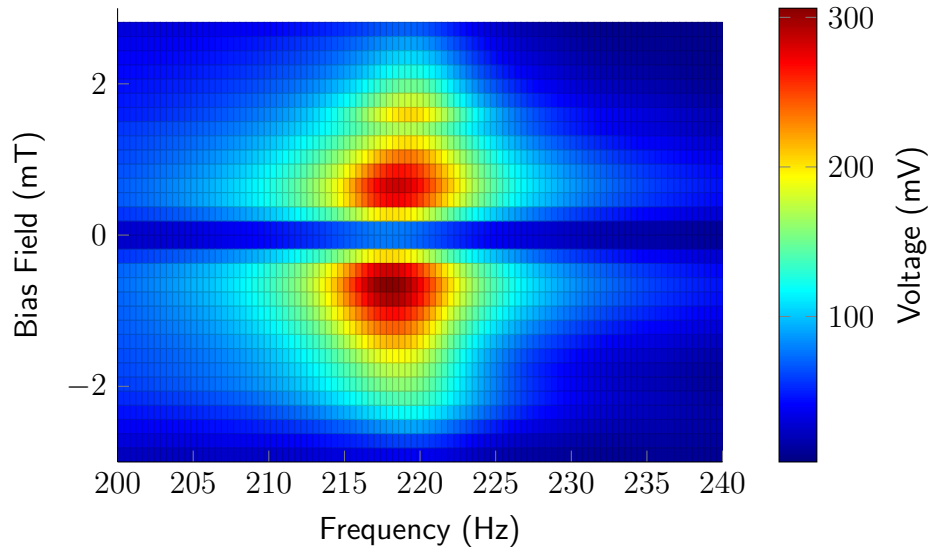


Figure 12.18: Scanning map of sample ME2.1 showing a resonance at 218.2 Hz .

ME2.2 *Figure 12.20* shows the frequency bias map for the sample modification ME2.2. The measurement is symmetric with respect to the applied magnetic bias field ($SR_{\pm} = 1.03$) and has the highest resonant response for a bias field of

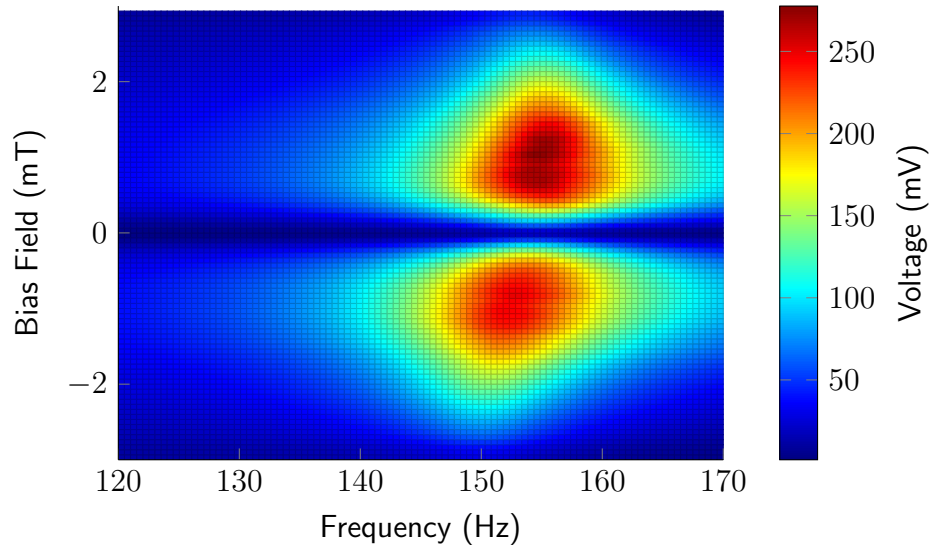


Figure 12.19: Scanning map of sample ME2.2 showing a resonance at 154.8 Hz

$B_{Bias} = 1 \text{ mT}$ at $f_R = 154.8 \text{ Hz}$ with a Q-factor of $Q = 15.3$ and a ME-coefficient of $\alpha_{ME} = 0.61 \text{ V/A}$.

ME2.3 A mass was applied to the modification ME2.2 and a frequency bias map was recorded for the new modification ME2.3 as depicted in *Figure 12.20*. The measurement shows the largest signal in resonance at $f_R = 94.8 \text{ Hz}$ when applying a bias field of $B_{Bias} = 0.8 \text{ mT}$. The Q-factor at this resonance is $Q = 13.7$ and the corresponding ME-coefficient is $\alpha_{ME} = 0.78 \text{ V/A}$. The average signal for a positive magnetic bias field is larger than the average signal for negative bias fields ($SR_{\pm} = 1.35$).

ME2.4 The sample ME2.4 shows a resonance peak at $f_R \approx 500 \text{ Hz}$ as shown in *Figure 12.21*. The measurement shows an abnormal signal at 500 Hz which may be a result of the power line coupling. Thus the exact shape of the resonance peak including the determination of the Q-factor cannot be obtained for this sensor modification and no further measurements were performed.

ME2.5 The frequency bias map for the sample ME2.5 is shown in *Figure 12.22*. The measurement shows a strong variation for positive and negative bias fields ($SR_{\pm} = 1.45$). The highest signal can be observed at a resonance frequency of

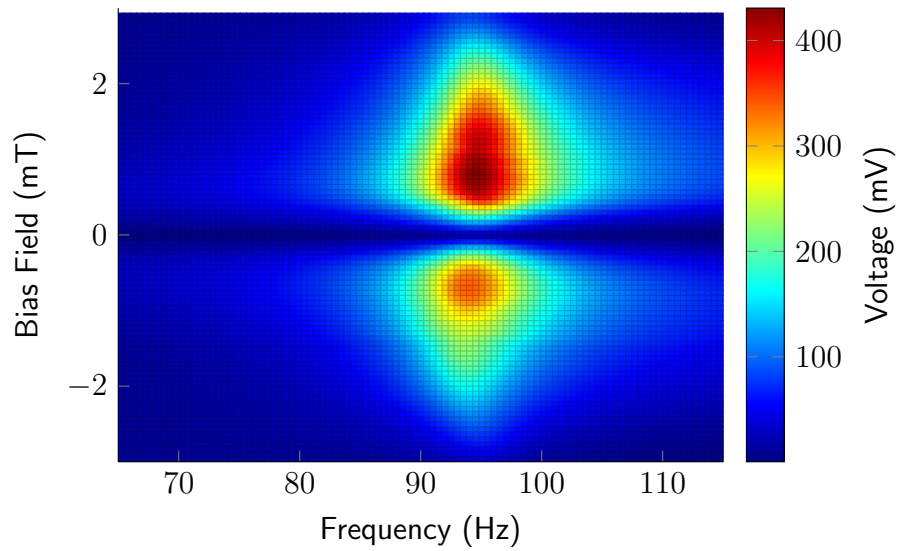


Figure 12.20: Scanning map of sample ME2.3 showing a resonance at 94.8 Hz

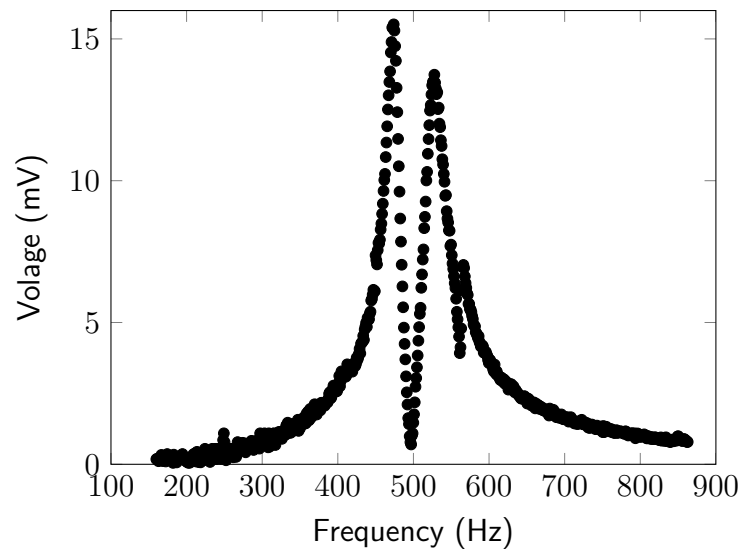


Figure 12.21: Frequency scan of sample ME2.4 showing a resonance at approximately 500 Hz which is strongly disturbed by noise caused by the 50 Hz power line.

$f_R = 200.9 \text{ Hz}$ for a magnetic bias field of $B_{Bias} = 2.3 \text{ mT}$ with a Q-factor of $Q = 10.5$ and a ME-coefficient of $\alpha_{ME} = 0.37 \text{ V/A}$.

ME2.6 The frequency bias map for the sample ME2.6 is shown in *Figure 12.23*. The signal response is symmetric with respect to the applied bias field ($SR_{\pm} =$

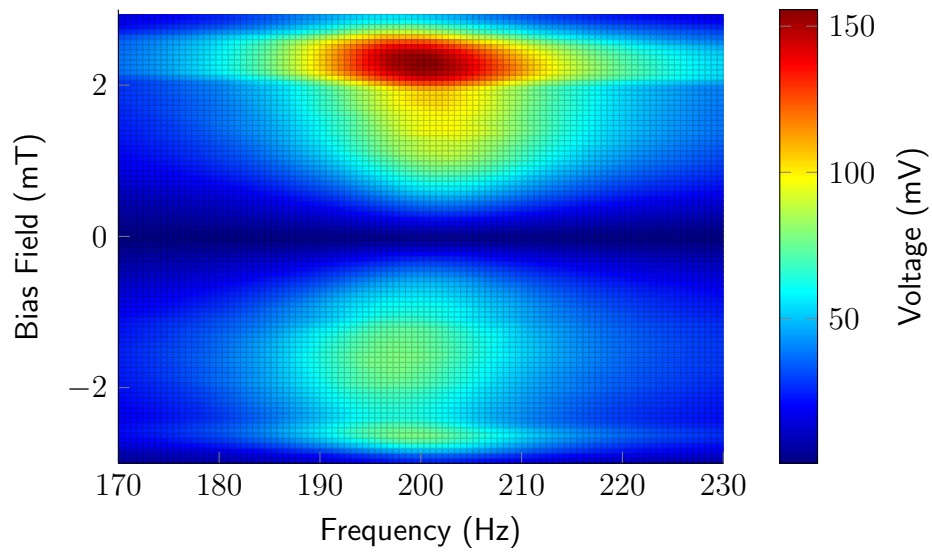


Figure 12.22: Scanning map of sample ME2.5 showing a resonance at 200.9 Hz.

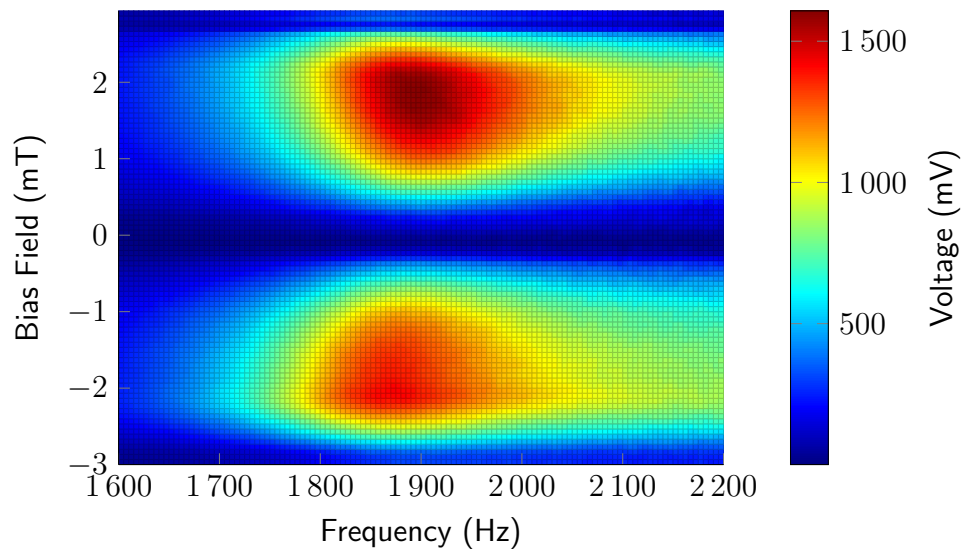


Figure 12.23: Scanning map of sample ME2.6 showing a resonance at 1870 Hz.

1.03). The largest response is observed at a resonance frequency of $f_R = 1870 \text{ Hz}$ for an applied magnetic bias field of $B_{Bias} = 1.9 \text{ mT}$ with a Q-factor of $Q = 9.8$ and a ME-coefficient of $\alpha_{ME} = 1.55 \text{ V/A}$.

Discussion The measurements of the different sample modifications clearly show the influence of the sample geometry independent from the used ZnO microrod. The resonance frequency is strongly affected by the sample length giving lower values for longer sensors. This observation agrees with the theoretical model described in *chapter 1.3*. An exception is the sample modification ME2.1 which obeys a relatively high resonance frequency. This effect may be attributed to the position of the ZnO microrod on the sensor. Sample ME2.1 is the only sensor with the microrod located in the center of the free oscillating substrate. Therefore the measured resonance frequency is probably not related to the first mechanical resonance mode, but a higher mode which is more expressed because it causes a higher local strain at the position of the ZnO microrod.

Equation (2.15) shows that the resonance frequency depends on the material properties density ρ , Young's modulus Y and thickness of the sample t . For oscillators consisting of more than one phase the determination of these material properties is not trivial and an exact fitting of all values is impossible since the system is underdetermined. By substitution the sensor property G_{res} can be defined as

$$G_{res} = t \sqrt{\frac{Y}{\rho}}. \quad (12.3)$$

The resulting eigenfrequency is given as

$$\omega_0 = \frac{n G_{res}}{\sqrt{12} l^2} \quad (12.4)$$

Considering the damping as described in *Equation (2.14)* and *Equation (2.13)* the difference in resonance frequency ω_r and eigenfrequency ω_0 is defined as

$$\omega_r = \omega_0 \sqrt{1 - \frac{1}{2Q^2}}. \quad (12.5)$$

For the obtained Q-factors Q a ratio for eigenfrequency and resonance frequency of $\frac{\omega_r}{\omega_0} > 0.99$ can be found. Therefore the damping effect to the resonance frequency can be neglected and the resonance frequency can be directly calculated as

$$f_R = \frac{n G_{res}}{2\pi \sqrt{12} l^2} \quad (12.6)$$

Figure 12.24 shows the measured resonance frequencies for the samples ME2.1, ME2.2, ME2.4, and ME2.6 and calculated resonance frequencies for the first three

modes by applying the sensor factor $G_{res} = 5340 \frac{m^2}{s}$. It can be clearly seen that the measured values for the sensors ME2.2, ME2.4, and ME2.6 match the calculation for the first resonance mode. The measured resonance frequency for sensor ME2.1 fits the calculated data for mode 3 which confirms the above made hypothesis and proves that higher resonance modes can be used if the ZnO microrod is positioned in the center of the oscillator. The measurement also shows a decay in the Q-factor

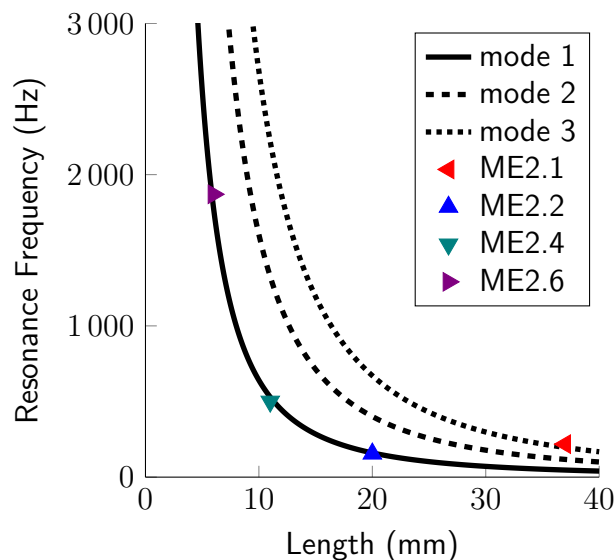


Figure 12.24: Resonance frequencies for the different modifications of sensor ME2. The measured values (marked by triangles) are compared to the calculated resonance frequencies as described by Equation (12.6).

with a decreasing sensor length. This observation may be addressed to the sensor clamping which affects the mechanical properties of the oscillator close to the clamping point. This effect is more expressed for short sensors since the average distance to the clamping is decreased which leads to a decrease in the Q-factor. The effect has already been observed for single-clamped oscillators [188, 189].

The optimum bias field for the long sensors ME2.1, ME2.2, and ME2.3 varies slightly between absolute values of $0.75 - 1 \text{ mT}$ which is expected for *Metglas*. Shorter sensors (ME2.5 and ME2.6) require higher fields of $1.9 - 2.3 \text{ mT}$. This observation may be addressed to the shape anisotropy in long sensors which can cause a shift in the magnetic field which leads to the maximum magnetostriction. The strong asymmetry of the applied bias field which is most pronounced for the samples with an additional mass (ME2.3 and ME2.5) and may be an indicator of pre-stress in the sensor which can cause a drift during the measurement.

The measurements of a sensor with a varying geometry showed that the resonance frequency could be tuned from $f_R \approx 100 \text{ Hz}$ to $f_R \approx 2 \text{ kHz}$. The positions of the resonance frequencies can be described using common oscillator theory and thus allows a precise tuning of the resonance frequency to match a desired frequency. Additional masses on the resonator can be used to reduce the resonance frequency of the sensor. But since the Q-factor will decrease and pre-stress in the sensor will strongly affect the response to a magnetic field the tuning of the resonance frequency should preferentially be done by changing the length of the sensor. It was also shown that changing the position of the ZnO microrod can be performed to allow the use of higher resonance modes which would increase the Q-factor compared to a shorter sensor with the same resonance frequency. A possible improvement of the signal to noise ratio can be obtained if the voltage is transformed to a current inside the ZnO microrod. This piezotronic measurement principle is further described in the following chapter.

12.2.3 PIEZOTRONIC SENSOR

The relatively high noise level of the piezoelectric ME sensors which base on a single ZnO microrod require an improvement of the measurement principle, e.g., by directly measuring the current. To investigate the piezotronic effect as a potential candidate for the enhancement of ME sensors sensor ME3 was prepared analogous to the classical sensors (ME1 and ME2) but with a ZnO/Al contact on one end of the ZnO microrod. Together with the established silver glue contact on the other end of the ZnO microrod a Schottky-ohmic IV characteristic as introduced in *chapter 1.3* should be observed. The sensor was prepared using a *Metglas* foil substrate with dimensions of $20 \text{ mm} \times 10 \text{ mm}$, *Kapton* tape was used as a separator between the electric contact and the substrate. The used microrod has a diameter of $d = 42 \mu\text{m}$ and a length of $l = 2.6 \text{ mm}$. A bias map measurement was performed using a magnetic AC field of $200 \mu\text{T}$, the result is shown in *Figure 12.25*. The measurement shows a symmetric resonance peak with respect to the applied magnetic bias field with the highest resonance for a magnetic bias field of $B = 0.6 \text{ mT}$, $f_R = 79.4 \text{ Hz}$ with a Q-factor of $Q = 23.6$ and a ME coefficient of $\alpha_{ME} = 0.16 \text{ V/A}$. A linearity measurement at this resonance was recorded, and is presented in *Figure 12.26*. The sensor shows a linear response to the applied magnetic field and a limit of detection of $120 \text{ nT}/\sqrt{\text{Hz}}$.

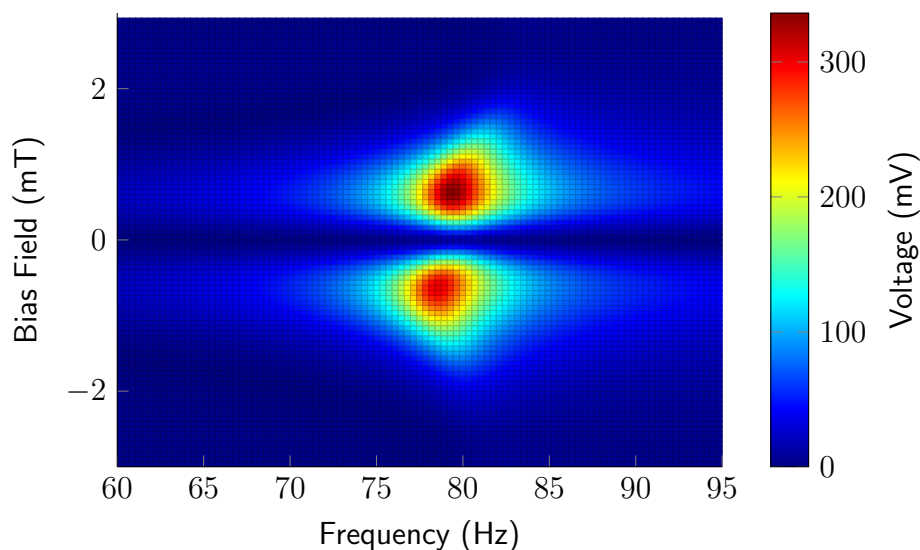


Figure 12.25: Bias map of sample ME3 showing a resonance peak at 79.4 Hz.

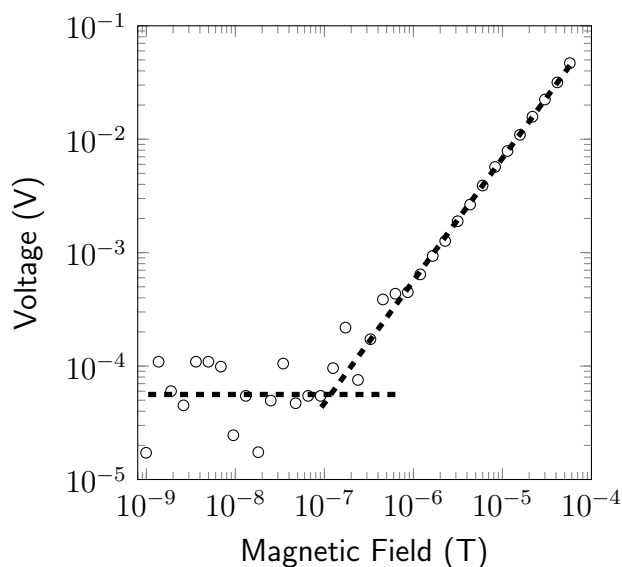


Figure 12.26: Linearity measurement of sensor ME3 at 79.4 Hz and a magnetic bias field of 0.6 mT showing a limit of detection of $120 \text{ nT}/\sqrt{\text{Hz}}$

To investigate the piezotronic response of the sensor the bias map measurement was repeated with an applied voltage of 27 V and the current signal was detected by the lock-in amplifier. The measurement was performed 48 hours after inserting the sample in the shielded measurement setup and is depicted in *Figure 12.27*. The sample shows a current signal response characteristic which exactly matches

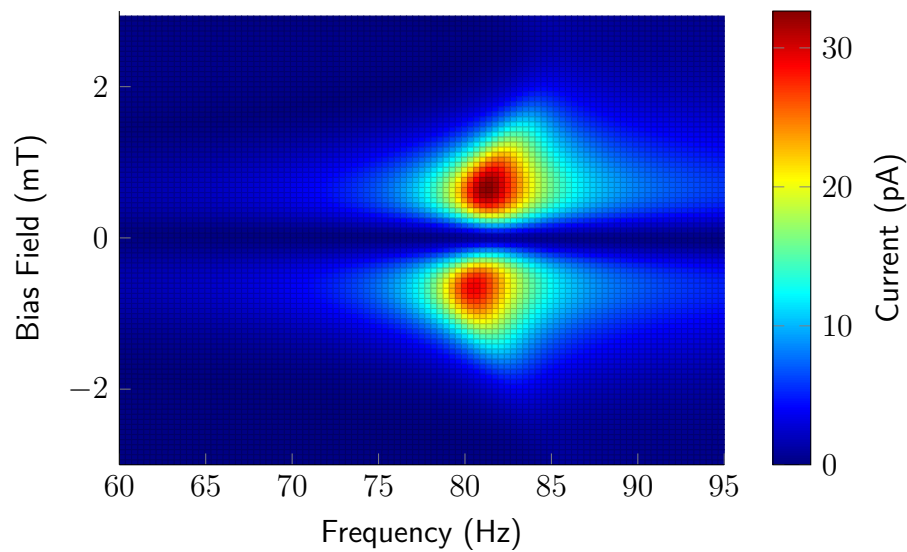


Figure 12.27: Piezotronic bias map of sensor ME3 which almost perfectly matches the bias map shown in Figure 12.25.

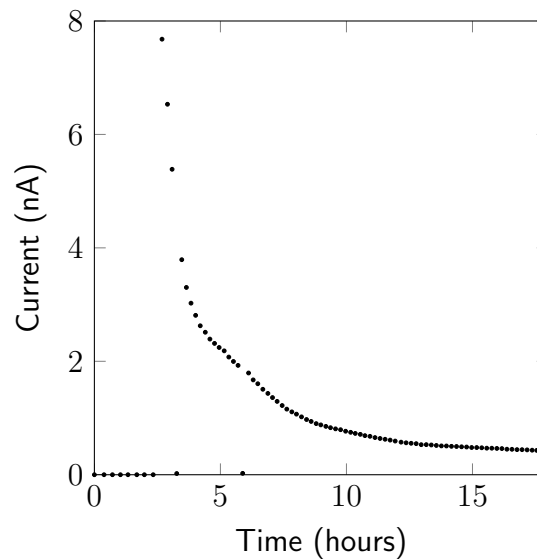
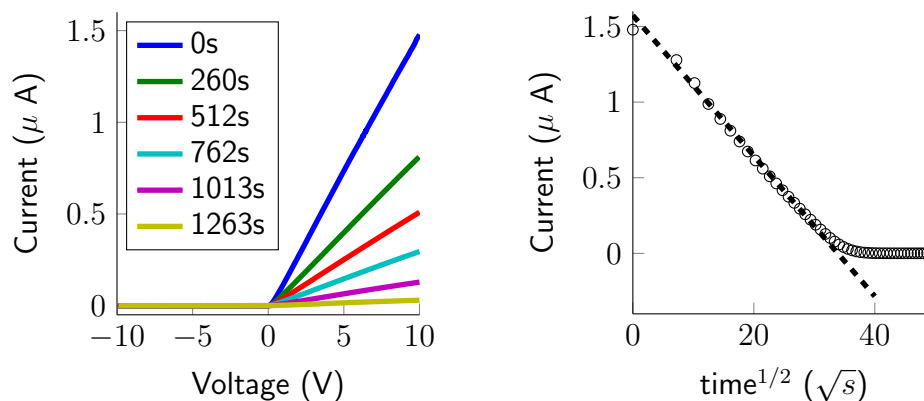


Figure 12.28: Measurement of the piezotronic sensor response over time using a constant magnetic AC field of 0.1 mT.

the classical approach as shown in Figure 12.25. This shows that the type of measurement is not influencing the mechanical resonator and large AC fields can be detected by using the piezotronic effect.

To investigate the sensor drift a large magnetic AC field of 0.1 mT was applied to the sensor and the response was measured repeatedly after insertion, as shown



(a) Measured IV curves of sensor ME3 after inserting in the sensor. 0s refers to the time directly after insertion.

(b) Measured current for $U = 10\text{V}$, extracted from a), plotted against $\sqrt{\text{time}}$.

Figure 12.29: Change in IV characteristics of sensor ME3 after introducing into the measurement setup.

in *Figure 12.28*. It can be clearly seen there is no useful sensor signal directly after insertion. After three hours a sudden increase in the signal occurs which is followed by a steady decrease in the signal.

Time dependent measurements of the IV-characteristics after inserting the sample in the setup were performed and show a strong decrease in the conductivity with respect to time, as depicted in *Figure 12.29(a)*. Diffusion of oxygen is well known for modifying the conductivity of ZnO [186, 190]. The charge transport of individual ZnO nanowires was described by Lord et al. [191], using a model developed for Si [192]. The model is qualitatively depicted in *Figure 12.30* showing the cross section of a ZnO nanowire with the radius r . The negative charges on the ZnO surface create a space charge region with the width W and thus a bending in valence band and conduction band of the ZnO towards the surface. This results in a conducting channel with a diameter of D_{cc} in the center of the nanowire which can be calculated as

$$D_{cc} = 2 \left(r^2 - \frac{2r\Psi_0 N_{ss}}{N_d \left(1 + \frac{qrN_{ss}}{2\varepsilon_r \varepsilon_0} \right)} \right)^{1/2}, \quad (12.7)$$

where N_{ss} denotes the surface state density, Ψ_0 is the electrostatic potential at the surface and N_d is the doping concentration. A diffusion of oxygen in the space charge region will cause a change in the doping concentration and thus in the diameter of the conducting channel. According to Fick's 2nd law [193] the

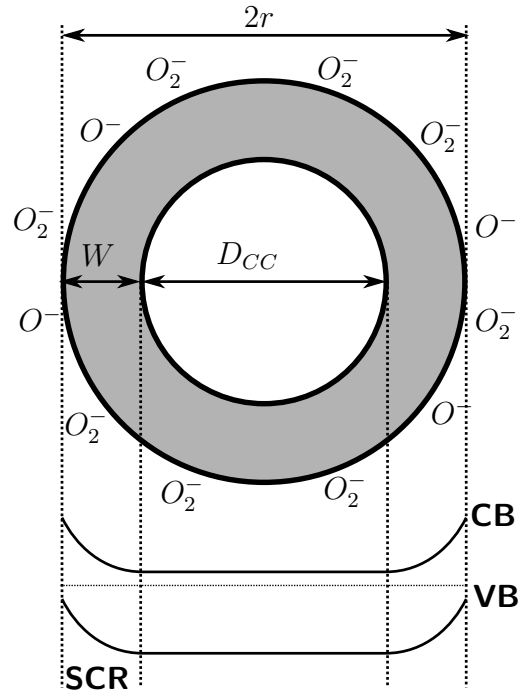


Figure 12.30: Schematic cross section of a ZnO nanowire showing the presence of a conducting channel with the diameter D_{cc} in the center. A space charge region (SCR) with width W and a bending in conduction band and valence band is created by the negatively charged surface of the nanowire.

diffusion length x depend on the time

$$x \propto \sqrt{t}. \quad (12.8)$$

By plotting the current values for supply voltages 10 V against \sqrt{t} , see *Figure 12.29(b)*, a linear dependency can be found in the first $\approx 1000\text{ s}$ of the measurement which proves that diffusion limited processes are the main reason for the change in conductivity. For longer time spans the change in current becomes zero.

To distinguish between piezoresistivity and piezotronics a model can be developed to describe the piezotronic current flow. This validity of the model can be checked by comparing the results of the piezoresistive characterization (as mentioned in *chapter 9.3*) and the piezotronic measurements of the ME sensors.

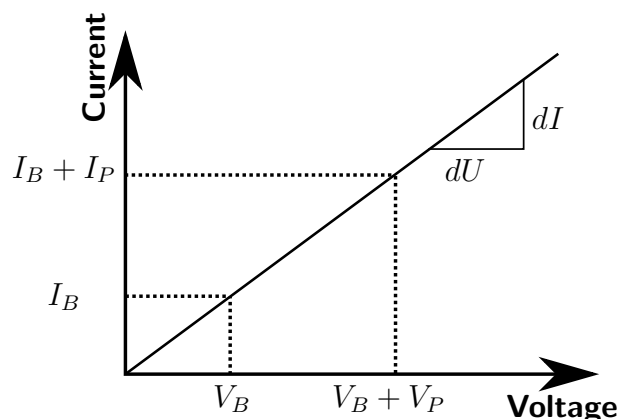


Figure 12.31: Model showing the piezotronic effect following the theory for piezoresistivity simplified for an ohmic IV curve. A bias voltage V_B causes a current flow I_B . An additional piezoelectric potential V_P increases the current by I_P .

To understand the influence of the conductivity of the ZnO microrod on the piezotronic effect the forward direction of the IV characteristics can be simplified as an ohmic resistor, see *Figure 12.31*. In the case of an ohmic resistor the resistivity R_F is defined as

$$R_F = \frac{dU}{dI}. \quad (12.9)$$

If a bias voltage V_B is applied to the device a corresponding current flow of I_B can be obtained. The periodic piezoelectric potential of an oscillating ME sensor acts like an additional supply voltage and the resulting current can be described as

$$I(t) = \underbrace{\frac{V_B}{R_F}}_{\text{DC component}} + \underbrace{\frac{V_p(t)}{R_F}}_{\text{AC component}}. \quad (12.10)$$

By using a lock-in amplifier to detect the current flow the DC component is cut off and the measured current I_p directly depends on the piezoelectric potential and the resistance of the ZnO microrod.

$$I_p(t) = \frac{V_p(t)}{R_F} \quad (12.11)$$

Therefore a high conductivity of the ZnO microrod will cause a relatively large ME signal response. The theoretical approach directly explains the decay of the current signal as shown in *Figure 12.28* and proofs its relation to the change in conductivity. The absence of a signal directly after inserting the sample can be

also attributed to the high conductivity of the microrod. A very high conductivity of a piezoelectric material will provide enough charge carriers to short circuit the piezoelectric potential which will destroy the piezotronic effect.

To investigate the influence of the pressure to the sensor drift another measurement with a constant AC field was performed at a pressure of $p_{meas} \approx 10 \text{ mbar}$, as shown in *Figure 12.32*. The characteristic is similar to the drift measurement at ambient pressure meaning that the limiting factor does not depend on the oxygen partial pressure in the atmosphere. This supports the above mentioned hypothesis where the bulk diffusion of oxygen vacancies are affecting the conductivity of the ZnO microrod. The time constant of this effect therefore directly depends on the diameter of the microrod. Due to the relatively large diameter of $d = 42 \mu\text{m}$ the response to light is relatively slow which agrees with the observations for slow UV sensors using ZnO microrods [194]. Accordingly we could demonstrate that small ZnO structures grown by FTS can be successfully used as very fast UV sensors, as shown by Gedamu [195], having a time constant of 32 ms . To check

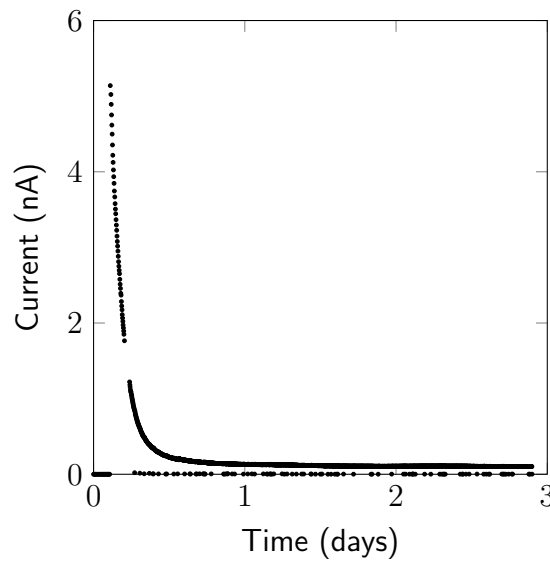


Figure 12.32: Measurement of the piezotronic sensor response over time at a pressure of 10 mbar using a constant magnetic AC field of 0.1 mT.

for the linearity of the piezotronic ME sensor a measurement with decreasing AC field was performed, using a supply voltage of 36 V, as depicted in *Figure 12.33*. A linear response of the sensor was observed resulting in a limit of detection of 3 nT . Additionally a second linear response was observed for fields smaller than $10 \text{ nT}/\sqrt{\text{Hz}}$. By considering both linear responses the limit of detection was found

to be $380 \text{ pT}/\sqrt{\text{Hz}}$. The observed sensor response shows that it is possible to use

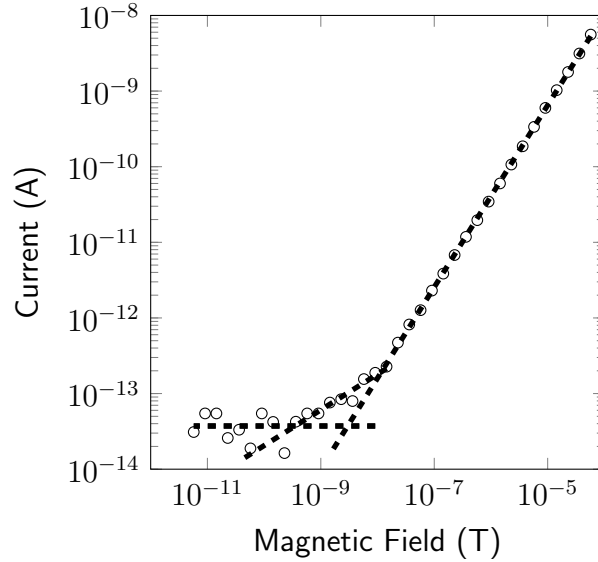


Figure 12.33: *ME3 piezotronic linearity measurement leading to a limit of detection of $380 \text{ pT}/\sqrt{\text{Hz}}$.*

single ZnO microrods as a voltage to current transducer which allows the measurement of a current as a response to the applied magnetic field with a lower limit of detection. As mentioned in *chapter 1.4.1* both the piezotronic and the piezoresistive effect cause an effect where straining leads to a change in resistance. The gauge factor of the piezotronic measurements can be calculated using the results of the charge measurement and the piezotronic measurement. The sensor charge signal can be calculated using the amplification factor $G_{Kistler}$ of the charge amplifier

$$Q_{Sensor} = U_{Meas} G_{Kistler}. \quad (12.12)$$

The sensor voltage can be calculated with the sensor capacity C_{Sensor} .

$$U_{Sensor} = \frac{Q_{Sensor}}{C_{Sensor}} \quad (12.13)$$

The change in length of a piezoelectric material can be calculated using the literature values for the piezoelectric coefficient d_{33} as

$$\Delta l = d_{33} U_{sensor}. \quad (12.14)$$

Table 12.3: Parameters for sensor ME3

Name	Value
l	2.6 mm
U_{Bias}	36 V
C_{sensor}	5 pF
d_{33}	12.4 pm/V [196]
I_{sensor}	$3.3 \cdot 10^{-9} A @ 10^{-5} T$
R	1 GΩ
U_{meas}	6,8 mV @ $10^{-5} T$
$G_{Kistler}$	0.2 pC/V

The gauge factor for piezoresistive materials is defined as

$$G = \frac{\frac{\Delta R}{R}}{\frac{\Delta l}{l}}. \quad (12.15)$$

The resistance of the sensor can be extracted from the IV curves whereas the resistance change ΔR is measured in the piezotronic measurement as

$$\Delta R = R - \frac{U_{sensor}}{I_{sensor}}. \quad (12.16)$$

The resulting gauge factor is

$$G = \frac{l}{d_{33}} \left(\frac{C_{Sensor}}{U_{Meas} G_{Kistler}} - \frac{1}{I_{Sensor} R} \right). \quad (12.17)$$

The individual values which are necessary for the calculation of the gauge factor can be obtained from the different measurements of the sensor ME3. *Table 12.3* lists all extracted values. The resulting gauge factor is $G = 7.7 \cdot 10^{11}$. Since the data was extracted from different measurements it cannot be excluded that all parameters were stable for all the obtained measurements, and especially the resistance strongly varies with time, as mentioned before. Thus the obtained value should not be considered as precise measurement of the gauge factor but as reasonable estimation. Compared to the gauge factor determined using the EPTP device as mentioned in *chapter 9.3* of $G = -1.4$ an increase of almost 12 orders of magnitude is observed. This large difference in gauge factors proves that

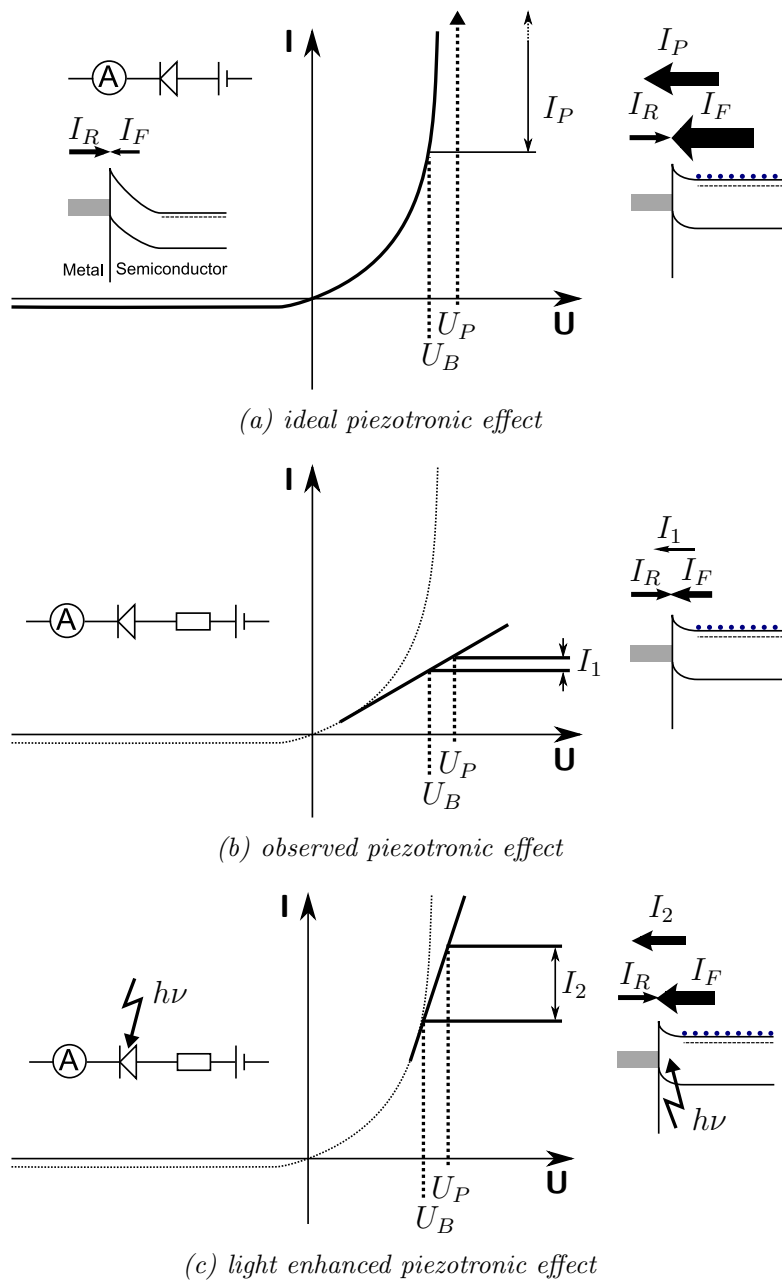


Figure 12.34: Qualitative model showing the current of piezotronic effect when applying a forward bias voltage U_B and a piezoelectric voltage U_P . The left insets illustrate the equivalent circuits for each case. The right insets show the energy band diagrams with the corresponding forward (I_F) and reverse (I_R) currents, with the respective arrow size representing the magnitude of the current.

the origin of the current signal in the ME measurements is not the piezoresistive effect, but the piezotronic effect.

With the presented measurements the theoretical model, as introduced in *Figure 12.31* can be extended. *Figure 12.34* illustrates a qualitative model showing the currents of the piezotronic effect when applying a forward bias voltage U_B and a piezoelectric voltage U_P . In an ideal piezotronic device, compare *Figure 12.34(a)*, the equivalent circuit consists only of a Schottky diode and a voltage source. Due to the exponential current increase in forward direction the piezoelectric voltage U_P will create a large current increase of I_P .

The observed piezotronic effect is limited by the intrinsic resistance of the piezoelectric ZnO microrod, as depicted in *Figure 12.34(b)*, with the resistor in the equivalent circuit representing the ZnO microrod. This limits the current flow and only a relative small current increase I_1 is measured.

An improved piezotronic effect, shown in *Figure 12.34(c)*, could be realized by induction of additional charge carriers in the space charge region of the Schottky contact by illumination with light. The piezotronic current I_2 would increase because additional charge carriers can contribute to the total current flow.

When comparing the classical sensor approach using a charge amplifier to the new developed piezotronic ME sensor a strong increase in the signal to noise ratio can be observed. The limit of detection is improved by a factor of 40 when using the classical single linear fitting routine and by a factor of 315 when using a two line fitting routine. The size of the piezotronic effect is defined by the resistivity of the microrod. To enhance the effect additional charge carriers must be available close to the Schottky contact. This could be achieved by illuminating a spot of the microrod close to the contact area using UV light to generate electron hole pairs. Another possibility can be the measurement of the capacity change of the Schottky contact. The piezotronic effect is not limited to ZnO and should be observable in every piezoelectric material that can form a Schottky contact. The challenge for all these materials will be to obtain a large amount of charge carriers for a large effect but preventing the charge carriers from short circuiting the device.

12.2.4 CONCLUSION

It could be demonstrated that ME sensors can be obtained by using a 2-1 geometry with a magnetostrictive foil and a piezoelectric ZnO microrod. The resonance frequency is low compared to MEMS based ME sensor devices [115] and can be

tuned by the length of the sensor to fit the desired needs. Thus the sensors are capable to measure periodic magnetic fields for frequencies of several kHz down to frequencies below $100 Hz$. For the classical approach which involves a charge amplifier the best sensor has a limit of detection of $6 nT/\sqrt{Hz}$.

It could be shown that higher resonance modes can be used by precise positioning of the ZnO microrod on the magnetostrictive substrate. Due to the higher local strain the magnetoelectric effect may be more pronounced if compared to 2-2 sensor geometries where the piezoelectric phase is completely covering the magnetostrictive substrate. Further investigations with different lengths and positions of ZnO microrods have to be performed to fully understand the underlying mechanisms.

The investigations of the piezotronic effect revealed that the limit of detection can be improved by a factor of 315 if compared the the conventional piezoelectric measurement.

In this work the focus was set on the optimization of the piezoelectric phase of a ME sensor. Especially the Q-factors of the obtained sensors are two orders of magnitude lower compared to the Q-factors of other ME sensors [197]. Thus the optimization of the magnetostrictive phase and the oscillator towards a higher Q-factor will boost the signal by two orders. Accordingly the limit of detection will be reduced by two orders of magnitude. Additionally, K. Meurisch¹ showed that the limit of detection using the same magnetostrictive phase can be improved by a factor of 18 by field annealing. Transferring these results to the presented sensors and combining them with the piezotronic measurement a limit of detection below $1 pT/\sqrt{Hz}$ is realistic for a ZnO microrod based sensor.

¹personal communication

PART V

SUMMARY AND OUTLOOK

In the presented work a complete discussion for 1D micro- and nanostructures is presented which includes the synthesis, the characterization and the application in a piezotronic ME sensor. The development of the different methods and setups was a major part of the presented work. The developed setups include a VLS synthesis system, the new introduced FTS setup, an automated sputter deposition vacuum chamber, a piezoelectric characterization system and a setup for the characterization of ME sensors. The material focus was set on ZnO based structures since they obey a unique combination of properties which make them promising candidates for various uses.

Beside the well established VLS synthesis method the new developed FTS [138] was used to create a large variety of micro- and nanostructures. Single crystalline 1D ZnO microrods could be created with lengths up to several millimeters using FTS. Sophisticated analysis methods revealed interesting crystalline properties like twin boundaries in the spikes of core spike particles [135] and a high crystal quality and the absence of intrinsic strain in the ZnO microrods [151]. The electromechanical characterization revealed a complex pre-stress in the microrods if attached to a macroscopic substrate. In situ SEM investigations using an EPTP device allowed a characterization of the piezoresistive gauge factor in the absence of pre-stress.

Incident light has a strong influence on the conductivity and surface dipole moment of ZnO microrods. An outstanding result was presented when investigating the wetting of rough micro- and nanostructured surfaces. It was shown that the water jet reflection on superhydrophobic surfaces can be utilized as a surface probe to reveal the details of heterogeneous wetting. This is a big advance in understanding superhydrophobicity since it can be used to distinguish surfaces with the same contact angle and revealed that a wetted fraction of almost 1, as found for the

leaves of nasturtium, shows ideal water repellent properties of superhydrophobic surfaces.

Magnetic field sensors were realized using ZnO microrods in combination with a magnetostrictive foil. It could be shown that besides the classical approach using the piezoelectric effect, the piezotronic effect can be utilized to detect the magnetic

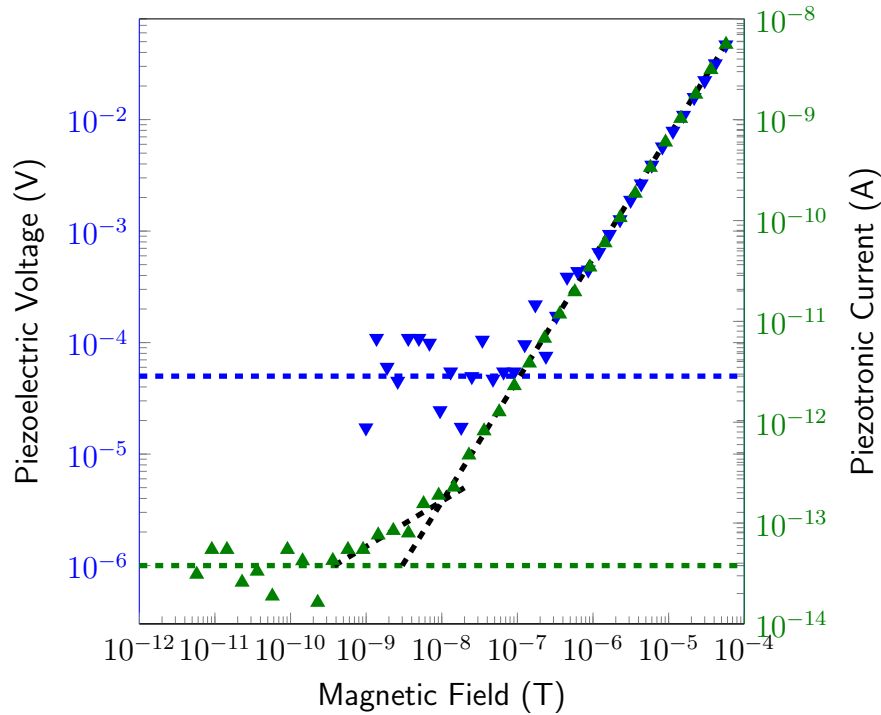


Figure 12.35: Comparison of the piezoelectric and piezotronic measurement of the same ME sensor.

field. The piezotronic measurement showed a lower limit of detection compared to the classical measurement and a less complex measurement equipment. The example in *Figure 12.35* shows a limit of detection of $120 \text{ nT}/\sqrt{\text{Hz}}$ for the piezoelectric measurement and $380 \text{ pT}/\sqrt{\text{Hz}}$ for the piezotronic measurement of the identical sensor. This immense increase of almost three orders of magnitude clearly shows the advantage of piezotronics over classical piezoelectric measurements. This lower complexity is a result of the intrinsic voltage to current transducer which allows the direct measurement of the current as a sensor signal which is an excellent property for a further integration of this measurement principle. It could be demonstrated that the resonance frequency of the sensor can be easily tuned to allow an optimization of the sensor for the exact needs.

A further optimization of the piezotronic ME sensor, using the findings of other projects in *SFB 855*, a limit of detection below $1 \text{ pT}/\sqrt{\text{Hz}}$ is realistic. Especially the optimization of the oscillator in terms of a higher Q-factor and the field annealing of the magnetostrictive phase will cause an increase in the sensor quality allowing the detection of lower magnetic fields.

The piezotronic measurements revealed a strong influence of the conductivity of the ZnO microrod on the magnitude of the signal. The optimization of the conductivity towards an improved device is the proper trade-off between piezoelectric properties, which require a low conductivity to avoid short circuiting, and available charge carriers for passing the Schottky barrier. A possible alternative would be the injection of additional charge carriers in the space charge region of the Schottky contact by light.

LIST OF PUBLICATIONS

- F. N. Sayed, O. Jayakumar, R. Sasikala, R. Kadam, S. R. Bharadwaj, L. Kienle, U. Schürmann, S. Kaps, R. Adelung, J. Mittal et al., *The Journal of Physical Chemistry C* 116(23), **2012**, 12462–12467
- S. Kaps, Y. Mishra, V. Hrkac, H. Greve, L. Kienle, E. Quandt und R. Adelung, *MRS Online Proceedings Library* 1398(1), **2012**
- M. Mecklenburg, A. Schuchardt, Y. K. Mishra, S. Kaps, R. Adelung, A. Lotnyk, L. Kienle und K. Schulte, *Advanced Materials* 24(26), **2012**, 3486–3490
- S. Bhowmick, D. Stauffer, H. Guo, S. Kaps, Y. Mishra, V. Hrkac, O. Warren, R. Adelung, A. Minor und L. Kienle, *Microscopy and Microanalysis* 19(S2), **2013**, 434–435
- S. Hrkac, M. Abes, C. Koops, C. Krywka, M. Muller, S. Kaps, R. Adelung, J. McCord, E. Lage, E. Quandt et al., *Applied Physics Letters* 103(12), **2013**, 123111–123111
- Y. K. Mishra, S. Kaps, A. Schuchardt, I. Paulowicz, X. Jin, D. Gedamu, S. Freitag, M. Claus, S. Wille, A. Kovalev et al., *Particle & Particle Systems Characterization* **2013**
- V. Hrkac, L. Kienle, S. Kaps, A. Lotnyk, Y. K. Mishra, U. Schürmann, V. Duppel, B. V. Lotsch und R. Adelung, *Journal of Applied Crystallography* 46(2), **2013**, 0–0
- D. Gedamu, I. Paulowicz, S. Kaps, O. Lupan, S. Wille, G. Haidarschin, Y. K. Mishra und R. Adelung, *Advanced Materials* 26(10), **2014**, 1541–1550
- T. Reimer, I. Paulowicz, R. Röder, S. Kaps, O. Lupan, S. Chemnitz, W. Bencke, C. Ronning, R. Adelung und Y. K. Mishra, *ACS applied materials & interfaces* **2014**
- O. Lupan, V. Cretu, M. Deng, D. Gedamu, I. Paulowicz, S. Kaps, Y. K. Mishra, O. Polonskyi, C. Zamponi, L. Kienle et al., *The Journal of Physical Chemistry C* 118(27), **2014**, 15068–15078

- Y. K. Mishra, S. Kaps, A. Schuchardt, I. Paulowicz, X. Jin, D. Gedamu, S. Wille, O. Lupan und R. Adelung, *KONA Powder and Particle Journal* 31(0), **2014**, 92–110

LIST OF PATENTS

- R. Adelung, S. Kaps, Y. Mishra, M. Claus, T. Preusse und C. Wolpert, *German Patent PCT/DE2011/000282, WO2011116751-A3* **2011**

SUPERVISED THESISES

Master Thesis

- Arnim Schuchardt - **2010**
"Elektrische und piezoelektrische Charakterisierung von durch Flammensynthese hergestellten Zinkoxid-Strukturen"
- Akash Bhatnagar - **2010**
"Synthesis and Study of ZnO micro-nanostructures"
- Melike Baytekin - **2012**
"Interlocking hydroxyapatite film on Ti substrate"

Bachelor Thesis

- Charline Wolpert - **2009**
"Massenhafte Synthese und Benetzungseigenschaften von ZnO-Kern-Nanostachel-Systemen"
- Christian Ohrt - **2009**
"Charakterisierung ultrahydrophober Oberflächen mittels Wasserstrahlreflexion"
- Jorit Gröttrup - **2011**
"Herstellung und Vergleich von ZnO-Nanostrukturen unter Anwendung des VLS-Mechanismus und der Flammentransportsynthese"
- Stefanie Schlüter - **2010**
"Kontrollierte Synthese von Nanostrukturen auf Eisenpartikeln"
- Robert Veith - **2013**
"Optimierung von 2-1 magnetoelektrischen Sensoren"
- Mathis Lohmann - **2013**
"Optimierung von 1-1 ME-Sensoren im Rahmen des Sonderforschungsbereiches 855"

BIBLIOGRAPHY

1. <http://www.intel.com/content/www/us/en/silicon-innovations/intel-22nm-technology.html>, **2014**
2. G. E. Moore et al., “Cramming more components onto integrated circuits”, **1965**
3. P. Mulvaney, *Langmuir* *12*(3), **1996**, 788–800
4. C. Bean und J. Livingston, *Journal of Applied Physics* *30*(4), **1959**, S120–S129
5. P. Bondavalli, P. Legagneux und D. Pribat, *Sensors and Actuators B: Chemical* *140*(1), **2009**, 304–318
6. B. Ding, M. Wang, J. Yu und G. Sun, *Sensors* *9*(3), **2009**, 1609–1624
7. J. Huang und Q. Wan, *Sensors* *9*(12), **2009**, 9903–9924
8. Y. Wang und J. T. Yeow, *Journal of Sensors* *2009*, **2009**
9. Z.-M. Huang, Y.-Z. Zhang, M. Kotaki und S. Ramakrishna, *Composites science and technology* *63*(15), **2003**, 2223–2253
10. E. Tan und C. Lim, *Composites Science and Technology* *66*(9), **2006**, 1102–1111
11. G. G. Tibbetts, M. L. Lake, K. L. Strong und B. P. Rice, *Composites Science and Technology* *67*(7), **2007**, 1709–1718
12. Ü. Özgür, Y. I. Alivov, C. Liu, A. Teke, M. Reshchikov, S. Doğan, V. Avrutin, S.-J. Cho und H. Morkoc, *Journal of applied physics* *98*(4), **2005**, 041301
13. T. Eguchi, T. Shike und N. Yamazaki, “Safety device for piezoelectric gas lighter”, **1992**, uS Patent 5,145,358
14. A. Shirinov und W. Schomburg, *Sensors and Actuators A: Physical* *142*(1), **2008**, 48–55
15. A. Kuoni, R. Holzherr, M. Boillat und N. F. de Rooij, *Journal of Micromechanics and Microengineering* *13*(4), **2003**, S103
16. X. Wang, X. Wang, J. Zhou, J. Song, J. Liu, N. Xu und Z. L. Wang, *Nano letters* *6*(12), **2006**, 2768–2772
17. E. S. Kim und R. S. Muller, *Electron Device Letters, IEEE* *8*(10), **1987**, 467–468
18. S. C. Ko, Y. C. Kim, S. S. Lee, S. H. Choi und S. R. Kim, *Sensors and Actuators A: Physical* *103*(1), **2003**, 130–134
19. R. P. Ried, E. S. Kim, D. M. Hong und R. S. Muller, *Microelectromechanical Systems, Journal of* *2*(3), **1993**, 111–120
20. M. H. Hallmann, G. O. Huntzinger und Y. P. Peng, “Piezoelectric knock sensor”, **1983**, uS Patent 4,371,804
21. D. U. Johnston und G. A. Shinkle, “Piezoelectric knock sensor”, **1983**, uS Patent 4,393,688
22. Y. P. Peng, “Piezoelectric knock sensor”, **1988**, uS Patent 4,727,279
23. M. Alexe, S. Senz, M. A. Schubert, D. Hesse und U. Gösele, *Advanced Materials* *20*(21), **2008**, 4021–4026

24. Y. Qin, X. Wang und Z. L. Wang, *Nature* 451(7180), **2008**, 809–813
25. S. Sarkar, A. Makhil, K. Lakshman, T. Bora, J. Dutta und S. Kumar Pal, *The Journal of Physical Chemistry C* 116(27), **2012**, 14248–14256
26. J. Song, J. Zhou und Z. L. Wang, *Nano letters* 6(8), **2006**, 1656–1662
27. C. Sun, J. Shi und X. Wang, *Journal of Applied Physics* 108(3), **2010**, 034309
28. J. Curie und P. Curie, *Comptes Rendus* 91, **1880**, 291–5
29. R. C. Buchanan, *Ceramic materials for electronics*, Bd. 25, CRC Press I Llc, **2004**
30. M. Lippmann, *Taylor & Friends* **1881**
31. J. Curie und P. Curie, *Comptes-rendus de l'Académie des Sciences* 93, **1881**, 1137–1140
32. I. Kobiakov, *Solid State Communications* 35(3), **1980**, 305–310
33. G. Carlotti, G. Socino, A. Petri und E. Verona, *Applied physics letters* 51(23), **1987**, 1889–1891
34. A. Dal Corso, M. Posternak, R. Resta und A. Baldereschi, *Physical Review B* 50(15), **1994**, 10715
35. Y. Noel, C. Zicovich-Wilson, B. Civalieri, P. D'arco und R. Dovesi, *Physical Review B* 65(1), **2001**, 014111
36. F. Bernardini, V. Fiorentini und D. Vanderbilt, *Physical Review B* 56(16), **1997**, R10024
37. M. Catti, Y. Noel und R. Dovesi, *Journal of physics and chemistry of solids* 64(11), **2003**, 2183–2190
38. N. A. Hill und U. Waghmare, *Physical Review B* 62(13), **2000**, 8802
39. R. L. Aagard, “Piezoresistive pressure sensor”, **1987**, uS Patent 4,651,120
40. C. Cabuz, E. I. Cabuz und T.-Y. Wang, “Piezoresistive pressure sensor”, **2009**, uS Patent 7,546,772
41. F. Paoletti, M.-A. Gretillat und N. de Rooij, in “Micro Electro Mechanical Systems, 1996, MEMS'96, Proceedings. An Investigation of Micro Structures, Sensors, Actuators, Machines and Systems. IEEE, The Ninth Annual International Workshop on”, IEEE, **1996**, S. 162–167
42. R. Voss, K. Bauer, W. Ficker, T. Gleissner, W. Kupke, M. Rose, S. Sassen, J. Schalk, H. Seidel und E. Stenzel, in “Solid State Sensors and Actuators, 1997. TRANSDUCERS'97 Chicago., 1997 International Conference on”, IEEE, **1997**, Bd. 2, S. 879–882
43. X. Li, M. Bao, H. Yang, S. Shen und D. Lu, *Sensors and Actuators A: Physical* 72(3), **1999**, 217–223
44. R. Gunter, W. Delinger, K. Manygoats, A. Kooser und T. Porter, *Sensors and Actuators A: Physical* 107(3), **2003**, 219–224
45. N. V. Lavrik, M. J. Sepaniak und P. G. Datskos, *Review of scientific instruments* 75(7), **2004**, 2229–2253
46. K. W. Wee, G. Y. Kang, J. Park, J. Y. Kang, D. S. Yoon, J. H. Park und T. S. Kim, *Biosensors and Bioelectronics* 20(10), **2005**, 1932–1938
47. N. Nguyen, *Flow measurement and Instrumentation* 8(1), **1997**, 7–16

48. D.-K. Kim, S.-G. Kang, J.-H. Sim, J.-K. Shin, P. Choi und J.-H. Lee, *Japanese Journal of Applied Physics* 39(12S), **2000**, 7134
49. Z. Fan, J. Chen, J. Zou, D. Bullen, C. Liu und F. Delcomyn, *Journal of Micromechanics and Microengineering* 12(5), **2002**, 655
50. A. Wisitsoraat, V. Patthanasetakul, T. Lomas und A. Tuantranont, *Sensors and Actuators A: Physical* 139(1), **2007**, 17–22
51. R. Bogue, *Sensor Review* 27(1), **2007**, 7–13
52. X. Liu, M. Mwangi, X. Li, M. O'Brien und G. M. Whitesides, *Lab on a Chip* 11(13), **2011**, 2189–2196
53. F. Geyling und J. Forst, *Bell System Technical Journal* 39(3), **1960**, 705–731
54. K. Yamada, M. Nishihara, S. Shimada, M. Tanabe, M. Shimazoe und Y. Matsuoka, *Electron Devices, IEEE Transactions on* 29(1), **1982**, 71–77
55. O. Tufte und E. Stelzer, *Journal of Applied Physics* 34(2), **1963**, 313–318
56. Y. Kanda, *Sensors and Actuators A: Physical* 28(2), **1991**, 83–91
57. L. Chang, *Foundation of MEMS.*, Pearson Education Limited, **2011**
58. Q. Chen, Y. Sun, Y. Wang, H. Cheng und Q.-M. Wang, *Sensors and Actuators A: Physical* 190, **2013**, 161–167
59. Y. Yang, W. Guo, J. Qi und Y. Zhang, *Applied Physics Letters* 97(22), **2010**, 223107
60. W. Schottky, *Zeitschrift fuer Physik A Hadrons and Nuclei* 118(9), **1942**, 539–592
61. J. Kim, J. Moon, H. Lee, W. Han, H. Cho, J. Lee und H. Kim, *Materials Science and Engineering: B* 165(1), **2009**, 77–79
62. H. Sheng, N. Emanetoglu, S. Muthukumar, S. Feng und Y. Lu, *Journal of electronic materials* 31(7), **2002**, 811–814
63. Z. L. Wang, *Advanced Materials* 19(6), **2007**, 889–892
64. Y. Zhang, Y. Liu und Z. L. Wang, *Advanced Materials* 23(27), **2011**, 3004–3013
65. C. Bunn, *Proceedings of the Physical Society* 47(5), **1935**, 835
66. E. Mollwo, *Z. angew. Phys* 6, **1954**, 257
67. X. Jin, J. Strueben, L. Heepe, A. Kovalev, Y. K. Mishra, R. Adelung, S. N. Gorb und A. Staubitz, *Advanced Materials* **2012**
68. M. Mecklenburg, A. Schuchardt, Y. K. Mishra, S. Kaps, R. Adelung, A. Lotnyk, L. Kienle und K. Schulte, *Advanced Materials* 24(26), **2012**, 3486–3490
69. T. Antoine, Y. K. Mishra, J. Trigilio, V. Tiwari, R. Adelung und D. Shukla, *Antiviral research* **2012**
70. H. Karzel, W. Potzel, M. Köfferlein, W. Schiessl, M. Steiner, U. Hiller, G. Kalvius, D. Mitchell, T. Das, P. Blaha et al., *Physical Review B* 53(17), **1996**, 11425
71. E. H. Kisi und M. M. Elcombe, *Acta Crystallographica Section C: Crystal Structure Communications* 45(12), **1989**, 1867–1870
72. L. Gerward und J. S. Olsen, *Journal of Synchrotron radiation* 2(5), **1995**, 233–235
73. N. Izyumskaya, V. Avrutin, W. Schoch, A. El-Shaer, F. Reuss, T. Gruber und A. Waag, *Journal of crystal growth* 269(2), **2004**, 356–361

74. K. Ogata, K. Sakurai, S. Fujita, S. Fujita und K. Matsushige, *Journal of crystal growth* 214, **2000**, 312–315
75. Y. Segawa, A. Ohtomo, M. Kawasaki, H. Koinuma, Z. Tang, P. Yu und G. Wong, *physica status solidi (b)* 202(2), **1997**, 669–672
76. X. Fan, J. Lian, Z. Guo und H. Lu, *Applied Surface Science* 239(2), **2005**, 176–181
77. E. S. Shim, H. S. Kang, J. S. Kang, J. H. Kim und S. Y. Lee, *Applied Surface Science* 186(1), **2002**, 474–476
78. J.-L. Zhao, X.-M. Li, J.-M. Bian, W.-D. Yu und X.-D. Gao, *Journal of crystal growth* 276(3), **2005**, 507–512
79. R. Laudise und A. Ballman, *The Journal of Physical Chemistry* 64(5), **1960**, 688–691
80. R. Laudise, E. Kolb und A. Caporaso, *Journal of the American Ceramic Society* 47(1), **1964**, 9–12
81. B. Liu und H. C. Zeng, *Journal of the American Chemical Society* 125(15), **2003**, 4430–4431
82. P.-C. Chang, Z. Fan, D. Wang, W.-Y. Tseng, W.-A. Chiou, J. Hong und J. G. Lu, *Chemistry of materials* 16(24), **2004**, 5133–5137
83. S. Faÿ, L. Feitknecht, R. Schlüchter, U. Kroll, E. Vallat-Sauvain und A. Shah, *Solar Energy Materials and Solar Cells* 90(18), **2006**, 2960–2967
84. S. Lautenschlaeger, S. Eisermann, B. K. Meyer, G. Callison, M. R. Wagner und A. Hoffmann, *physica status solidi (RRL)-Rapid Research Letters* 3(1), **2009**, 16–18
85. X. Feng, L. Feng, M. Jin, J. Zhai, L. Jiang und D. Zhu, *Journal of the American Chemical Society* 126(1), **2004**, 62–63
86. A. Marmur, *Langmuir* 20(9), **2004**, 3517–3519
87. L. Gao und T. J. McCarthy, *Langmuir* 22(7), **2006**, 2966–2967
88. Z. Luo, Z. Zhang, L. Hu, W. Liu, Z. Guo, H. Zhang und W. Wang, *Advanced Materials* 20(5), **2008**, 970–974
89. K. Tadanaga, K. Kitamuro, A. Matsuda und T. Minami, *Journal of sol-gel science and technology* 26(1-3), **2003**, 705–708
90. N. Zhao, J. Xu, Q. Xie, L. Weng, X. Guo, X. Zhang und L. Shi, *Macromolecular rapid communications* 26(13), **2005**, 1075–1080
91. R. Wenzel, *Ind. Eng. Chem.* 28(8), **1936**, 988–994
92. A. B. D. Cassie und S. Baxter, *Nature* 155(3923), **1945**, 21–22, ua001 Times Cited:43 Cited References Count:4
93. J. Joule, *Ann. Electr. Magn. Chem* 8(1842), **1842**, 219–224
94. M. Ibarra und P. Algarabel, *Physical Review B* 50(6), **1994**, 4196
95. S.-D. Poisson, *Mémoire sur l'équilibre et mouvement des corps élastiques*, L'Académie des sciences, **1828**
96. C. Gerthsen und D. Meschede, *Gerthsen physik*, Springer DE, **2010**
97. E. Villari, *Ann. Phys. Chem* 126, **1865**, 87–122

98. J. Zhai, Z. Xing, S. Dong, J. Li und D. Viehland, *Journal of the American Ceramic Society* 91(2), **2008**, 351–358
99. S. R. Singiresu, *Reading, MA: Addison-Wesley* **1995**
100. W. Klement, R. Willens und P. Duwez, *Nature* **1960**
101. W.-H. Wang, C. Dong und C. Shek, *Materials Science and Engineering: R: Reports* 44(2), **2004**, 45–89
102. A. Drehman, A. Greer und D. Turnbull, *Applied Physics Letters* 41(8), **1982**, 716–717
103. H. Chen, *Acta Metallurgica* 22(12), **1974**, 1505–1511
104. I. Dzyaloshinskii, *Zh. Eksp. Teor. Fiz* 37, **1960**, 881–882
105. D. Astrov, *Sov. Phys. JETP* 13(4), **1961**, 729–733
106. B. Krichevstov, V. Pavlov, R. Pisarev und A. Selitsky, *Ferroelectrics* 161(1), **1994**, 65–71
107. J.-P. Rivera, *Ferroelectrics* 161(1), **1994**, 147–164
108. B. Alshin und D. N. Astrov, *Soviet Physics JETP-USSR* 17(4), **1963**, 809–811
109. G. T. Rado, *Physical Review Letters* 13(10), **1964**, 335
110. E. Ascher und H. Rieder, *J. Appl. Phys.* 1966, **1966**, 37
111. R. Santoro, D. Segal und R. Newnham, *Journal of Physics and Chemistry of Solids* 27(6), **1966**, 1192–1193
112. T. Watanabe und K. Kohn, *Phase Transitions: A Multinational Journal* 15(1), **1989**, 57–68
113. T. O'dell, *Philosophical Magazine* 16(141), **1967**, 487–494
114. J. Van Suchtelen, *Philips Res. Rep* 27(1), **1972**, 28–37
115. S. Marauska, *Hochempfindliche mikromechanische magnetoelektrische Magnetfeldsensoren*, Dissertation, Kiel, Christian-Albrechts-Universität, Diss., 2013, **2013**
116. A. Hachigo, H. Nakahata, K. Higaki, S. Fujii und S. Shikata, *Applied Physics Letters* 65(20), **1994**, 2556–2558
117. J. G. E. Gardeniers, Z. M. Rittersma und G. J. Burger, *Journal of Applied Physics* 83(12), **1998**, 7844–7854
118. S. K. Tiku, C. K. Lau und K. M. Lakin, *Applied Physics Letters* 36(4), **1980**, 318–320
119. M. Kasuga und M. Mochizuki, *Journal of Crystal Growth* 54(2), **1981**, 185–194
120. K. K. Kim, J. H. Song, H. J. Jung, W. K. Choi, S. J. Park und J. H. Song, *Journal of Applied Physics* 87(7), **2000**, 3573–3575
121. P. Fons, K. Iwata, S. Niki, A. Yamada und K. Matsubara, *Journal of Crystal Growth* 201, **1999**, 627–632
122. Y. F. Chen, D. M. Bagnall, H. J. Koh, K. T. Park, K. Hiraga, Z. Q. Zhu und T. Yao, *Journal of Applied Physics* 84(7), **1998**, 3912–3918
123. R. D. Vispute, V. Talyansky, S. Choopun, R. P. Sharma, T. Venkatesan, M. He, X. Tang, J. B. Halpern, M. G. Spencer, Y. X. Li, L. G. Salamanca-Riba, A. A. Iliadis und K. A. Jones, *Applied Physics Letters* 73(3), **1998**, 348–350

124. Y. Liu, C. R. Gorla, S. Liang, N. Emanetoglu, Y. Lu, H. Shen und M. Wraback, *Journal of Electronic Materials* 29(1), **2000**, 69–74
125. N. Takahashi, K. Kaiya, T. Nakamura, Y. Momose und H. Yamamoto, *Japanese Journal of Applied Physics Part 2-letters* 38(4B), **1999**, L454–L456
126. R. Wagner und W. Ellis, *Applied Physics Letters* 4(5), **1964**, 89–90
127. J. Rybczynski, D. Banerjee, A. Kosiorek, M. Giersig und Z. Ren, *Nano Letters* 4(10), **2004**, 2037–2040
128. H. J. Fan, B. Fuhrmann, R. Scholz, F. Syrowatka, A. Dadgar, A. Krost und M. Zacharias, *Journal of crystal growth* 287(1), **2006**, 34–38
129. H. T. Ng, J. Han, T. Yamada, P. Nguyen, Y. P. Chen und M. Meyyappan, *Nano Letters* 4(7), **2004**, 1247–1252
130. E. C. Greyson, Y. Babayan und T. W. Odom, *Advanced Materials* 16(15), **2004**, 1348–1352
131. H. Chik, J. Liang, S. Cloutier, N. Kouklin und J. Xu, *Applied physics letters* 84(17), **2004**, 3376–3378
132. X. Wang, X. Wang, C. J. Summers und Z. L. Wang, *Nano Letters* 4(3), **2004**, 423–426
133. J. Zhang, X. Zhang, L. Chen, J. Xu, L. You, H. Ye und D. Yu, *Applied physics letters* 90(23), **2007**, 233104
134. Y. K. Mishra, S. Kaps, A. Schuchardt, I. Paulowicz, X. Jin, D. Gedamu, S. Freitag, M. Claus, S. Wille, A. Kovalev et al., *Particle & Particle Systems Characterization* **2013**
135. V. Hrkac, L. Kienle, S. Kaps, A. Lotnyk, Y. K. Mishra, U. Schürmann, V. Duppel, B. V. Lotsch und R. Adelung, *Journal of Applied Crystallography* 46(2), **2013**, 0–0
136. T. Agag, T. Koga und T. Takeichi, *Polymer* 42(8), **2001**, 3399 – 3408
137. G. Maier, *Meccanica* 33(1), **1998**, 108–108
138. R. Adelung, S. Kaps, Y. Mishra, M. Claus, T. Preusse und C. Wolpert, *German Patent PCT/DE2011/000282, WO2011116751–A3* **2011**
139. R. Lad, P. D. Funkenbusch und C. Aita, *Journal of Vacuum Science and Technology* 17(4), **1980**, 808–811
140. M. A. L. Johnson, S. Fujita, W. H. Rowland, W. C. Hughes, J. W. Cook und J. F. Schetzina, *Journal of Electronic Materials* 25(5), **1996**, 855–862
141. W. C. Shih und M. S. Wu, *Journal of Crystal Growth* 137(3-4), **1994**, 319–325
142. H. J. Ko, Y. F. Chen, Z. Zhu, T. Hanada und T. Yao, *Journal of Crystal Growth* 208(1-4), **2000**, 389–394
143. J. Shi, H. Hong, Y. Ding, Y. Yang, F. Wang, W. Cai und X. Wang, *J. Mater. Chem.* 21, **2011**, 9000–9008
144. B. Eck, *Einführung in die technische Strömungslehre*, Springer, **1936**
145. W. R. Grove, *Philosophical Transactions of the Royal Society of London* 142, **1852**, 87–101
146. G. Brauer, W. Anwand, D. Grambole, W. Skorupa, Y. Hou, A. Andreev, C. Teichert, K. Tam und A. Djurišić, *Nanotechnology* 18(19), **2007**, 195301

147. M.-H. Zhao, Z.-L. Wang und S. X. Mao, *Nano Letters* 4(4), **2004**, 587–590
148. J. B. Baxter, A. Walker, K. Van Ommering und E. Aydil, *Nanotechnology* 17(11), **2006**, S304
149. Y.-K. Tseng, C.-J. Huang, H.-M. Cheng, I.-N. Lin, K.-S. Liu und I.-C. Chen, *Advanced Functional Materials* 13(10), **2003**, 811–814
150. J.-J. Wu und S.-C. Liu, *The Journal of Physical Chemistry B* 106(37), **2002**, 9546–9551
151. S. Hrkac, M. Abes, C. Koops, C. Krywka, M. Muller, S. Kaps, R. Adelung, J. McCord, E. Lage, E. Quandt et al., *Applied Physics Letters* 103(12), **2013**, 123111–123111
152. C. Krywka, H. Neubauer, M. Priebe, T. Salditt, J. Keckes, A. Buffet, S. V. Roth, R. Doehrmann und M. Mueller, *Journal of Applied Crystallography* 45(1), **2011**, 85–92
153. A. Hammersley, S. Svensson, M. Hanfland, A. Fitch und D. Hausermann, *International Journal of High Pressure Research* 14(4-6), **1996**, 235–248
154. M. Abes, C. Koops, S. Hrkac, E. Quandt, L. Bouchenoire, B. Murphy und O. Magnussen, *Journal of Applied Physics* 113(12), **2013**, 124303
155. M. Abes, C. Koops, S. Hrkac, H. Greve, E. Quandt, S. Collins, B. Murphy und O. Magnussen, *Applied Physics Letters* 102(1), **2013**, 011601
156. E. d. T. de Lacheisserie, M. Cyrot, M. Décorps, B. Dieny, O. Geoffroy, D. Gignoux, C. Lacroix, J. Laforest, P. Lethuillier, P. Molho et al., *Presses Universitaires de Grenoble* **1999**
157. B.-H. Huang, S.-Y. Chen und P. Shen, *The Journal of Physical Chemistry C* 112(4), **2008**, 1064–1071
158. V. Hrkac, *Nanocharacterization of materials for biomagnetic sensing using TEM*, Dissertation, University Kiel, **2014**
159. N. Ohashi, J. Tanaka, T. Ohgaki, H. Haneda, M. Ozawa und T. Tsurumi, *Journal of Materials Research* 17(06), **2002**, 1529–1535
160. F. D. Auret, S. A. Goodman, M. Hayes, M. J. Legodi, H. A. van Laarhoven und D. C. Look, *Applied Physics Letters* 79(19), **2001**, 3074
161. A. Y. Polyakov, N. B. Smirnov, E. A. Kozhukhova, V. I. Vdovin, K. Ip, Y. W. Heo, D. P. Norton und S. J. Pearton, *Applied Physics Letters* 83(8), **2003**, 1575
162. S.-H. Kim, H.-K. Kim und T.-Y. Seong, *Applied Physics Letters* 86(11), **2005**, 112101
163. K. Ip, Y. W. Heo, K. H. Baik, D. P. Norton, S. J. Pearton, S. Kim, J. R. LaRoche und F. Ren, *Applied Physics Letters* 84(15), **2004**, 2835
164. R. C. Neville, *Journal of Applied Physics* 41(9), **1970**, 3795
165. S. V. Slobodchikov, K. M. Salikhov, E. V. Russu und Y. G. Malinin, *Semiconductors* 35(4), **2001**, 464–467
166. H.-K. Kim, K.-K. Kim, S.-J. Park, T.-Y. Seong und I. Adesida, *Journal of Applied Physics* 94(6), **2003**, 4225
167. G. Yule, *Journal of the Royal Statistical Society* 62, **1897**, 249–295
168. B. Bhushan, Y. C. Jung und K. Koch, *Langmuir* 25(5), **2009**, 3240–3248, 413CP Times Cited:38 Cited References Count:41

169. S. J. Lee, B. G. Paik, G. B. Kim und Y. G. Jang, *Japanese Journal of Applied Physics Part 1-Regular Papers Brief Communications & Review Papers* 45(2A), **2006**, 912–918, 017KI Times Cited:7 Cited References Count:13
170. D. Richard, C. Clanet und D. Quere, *Nature* 417(6891), **2002**, 811–811, 563YM Times Cited:121 Cited References Count:10
171. P. R. Chiarot und T. B. Jones, *Journal of Micromechanics and Microengineering* 19(12), **2009**, 524RY Times Cited:1 Cited References Count:18
172. A. Kaye, *Nature* 197(487), **1963**, 1001, 8807B Times Cited:10 Cited References Count:1
173. W. Baker, *Proceedings of the Physical Society* 40(1), **1927**, 181–185
174. M. Scharnberg, *Functional organic thin films*, University Kiel, **2007**
175. F. Celestini, R. Kofman, X. Noblin und M. Pellegrin, *Soft Matter* 6(23), **2010**, 5872–5876
176. A. W. Hassel, S. Milenkovic, U. Schürmann, H. Greve, V. Zaporozhchenko, R. Adelung und F. Faupel, *Langmuir* 23(4), **2007**, 2091–2094, 133CW Times Cited:14 Cited References Count:28
177. K. A. Jackson und J. D. Hunt, *Transactions of the Metallurgical Society of Aime* 236(8), **1966**, 1129, 81375 Times Cited:1025 Cited References Count:25
178. L. Philippe, I. Peyrot, J. Michler, A. W. Hassel und S. Milenkovic, *Applied Physics Letters* 91(11), **2007**, 210RT Times Cited:7 Cited References Count:10
179. S. Milenkovic, A. W. Hassel und A. Schneider, *Nano Letters* 6(4), **2006**, 794–799, 034GE Times Cited:21 Cited References Count:20
180. A. Hellawell und W. Beere, *Metal Science* 10(7), **1976**, 260
181. V. Cimalla, C. C. Rohlig, J. Pezoldt, M. Niebelschutz, O. Ambacher, K. Bruckner, M. Hein, J. Weber, S. Milenkovic, A. J. Smith und A. W. Hassel, *Journal of Nanomaterials 2008*, **2008**, 299UR Times Cited:10 Cited References Count:31
182. U. Schuermann, W. Hartung, H. Takele, V. Zaporozhchenko und F. Faupel, *Nanotechnology* 16(8), **2005**, 1078–1082, 957YX Times Cited:45 Cited References Count:22
183. A. W. Adamson, A. P. Gast et al., *Physical chemistry of surfaces*, Bd. 4, Wiley New York, **1990**
184. D. Djukic, *International Journal of Intelligent Systems Technologies and Applications* 7(1), **2009**, 92
185. B. Gojdka, R. Jahns, K. Meurisch, H. Greve, R. Adelung, E. Quandt, R. Knöchel und F. Faupel, *Applied Physics Letters* 99(22), **2011**, 223502
186. M. Allen und S. Durbin, *Applied Physics Letters* 92(12), **2008**, 122110
187. M. Allen, M. Alkaisi und S. Durbin, *Applied physics letters* 89(10), **2006**, 103520–103520
188. S. Schmid und C. Hierold, *Journal of Applied Physics* 104(9), **2008**, 093516
189. K. Y. Yasumura, T. D. Stowe, E. M. Chow, T. Pfafman, T. W. Kenny, B. C. Stipe und D. Rugar, *Microelectromechanical Systems, Journal of* 9(1), **2000**, 117–125
190. S. A. Ansari, M. M. Khan, S. Kalathil, A. N. Khan, J. Lee und M. H. Cho, *Nanoscale* **2013**
191. A. M. Lord, T. G. Maffei, A. S. Walton, D. M. Kepaptsoglou, Q. M. Ramasse, M. B. Ward, J. Köble und S. P. Wilks, *Nanotechnology* 24(43), **2013**, 435706

192. V. Schmidt, S. Senz und U. Gösele, *Applied Physics A* 86(2), **2007**, 187–191
193. A. Fick, *The London, Edinburgh, and Dublin Philosophical Magazine and Journal of Science* 10(63), **1855**, 30–39
194. J. Dai, C. Xu, X. Xu, J. Guo, J. Li, G. Zhu und Y. Lin, *ACS applied materials & interfaces* 5(19), **2013**, 9344–9348
195. D. Gedamu, I. Paulowicz, S. Kaps, O. Lupan, S. Wille, G. Haidarschin, Y. K. Mishra und R. Adelung, *Advanced Materials* 26(10), **2014**, 1541–1550
196. J. Christman, H. Maiwa, S.-H. Kim, A. Kingon und R. Nemanich, in “MRS Proceedings”, Cambridge Univ Press, **1998**, Bd. 541, S. 617
197. C. Kirchhof, M. Krantz, I. Teliban, R. Jahns, S. Marauska, B. Wagner, R. Knöchel, M. Gerken, D. Meyners und E. Quandt, *Applied Physics Letters* 102(23), **2013**, 232905
198. F. N. Sayed, O. Jayakumar, R. Sasikala, R. Kadam, S. R. Bharadwaj, L. Kienle, U. Schürmann, S. Kaps, R. Adelung, J. Mittal et al., *The Journal of Physical Chemistry C* 116(23), **2012**, 12462–12467
199. S. Kaps, Y. Mishra, V. Hrkac, H. Greve, L. Kienle, E. Quandt und R. Adelung, *MRS Online Proceedings Library* 1398(1), **2012**
200. S. Bhowmick, D. Stauffer, H. Guo, S. Kaps, Y. Mishra, V. Hrkac, O. Warren, R. Adelung, A. Minor und L. Kienle, *Microscopy and Microanalysis* 19(S2), **2013**, 434–435
201. T. Reimer, I. Paulowicz, R. Röder, S. Kaps, O. Lupan, S. Chemnitz, W. Benecke, C. Ronning, R. Adelung und Y. K. Mishra, *ACS applied materials & interfaces* **2014**
202. O. Lupan, V. Cretu, M. Deng, D. Gedamu, I. Paulowicz, S. Kaps, Y. K. Mishra, O. Polonskyi, C. Zamponi, L. Kienle et al., *The Journal of Physical Chemistry C* 118(27), **2014**, 15068–15078
203. Y. K. Mishra, S. Kaps, A. Schuchardt, I. Paulowicz, X. Jin, D. Gedamu, S. Wille, O. Lupan und R. Adelung, *KONA Powder and Particle Journal* 31(0), **2014**, 92–110

PART VI

SUPPLEMENTARY INFORMATION

A VLS PARAMETERS

Used parameters for the VLS synthesis. Every run was performed using 3-4 substrates which were placed with a distance of 1 *cm* gap.

Temperature	O2 Flow	Ar Flow	Pressure
1150	1	30	600
1150	2	30	600
1150	3	30	600
1150	4	30	600
1150	1	50	600
1150	2	50	600
1150	3	50	600
1150	4	50	600
1150	1	30	700
1150	2	30	700
1150	3	30	700
1150	4	30	700
1150	1	50	700
1150	2	50	700

continued ...

... continued

Temperature	O2 Flow	Ar Flow	Pressure
1150	3	50	700
1150	4	50	700
1150	1	30	800
1150	2	30	800
1150	3	30	800
1150	4	30	800
1150	1	50	800
1150	2	50	800
1150	3	50	800
1150	4	50	800
1175	1	30	600
1175	2	30	600
1175	3	30	600
1175	4	30	600
1175	1	50	600
1175	2	50	600
1175	3	50	600
1175	4	50	600
1175	1	30	700
1175	2	30	700
1175	3	30	700
1175	4	30	700
1175	1	50	700
1175	2	50	700
1175	3	50	700
1175	4	50	700
1175	1	30	800
1175	2	30	800
1175	3	30	800
1175	4	30	800
1175	1	50	800

continued ...

... continued

Temperature	O2 Flow	Ar Flow	Pressure
1175	2	50	800
1175	3	50	800
1175	4	50	800
1200	1	30	600
1200	2	30	600
1200	3	30	600
1200	4	30	600
1200	1	50	600
1200	2	50	600
1200	3	50	600
1200	4	50	600
1200	1	30	700
1200	2	30	700
1200	3	30	700
1200	4	30	700
1200	1	50	700
1200	2	50	700
1200	3	50	700
1200	4	50	700
1200	1	30	800
1200	2	30	800
1200	3	30	800
1200	4	30	800
1200	1	50	800
1200	2	50	800
1200	3	50	800
1200	4	50	800

B MATLAB FUNCTIONS

B.1 CALCULATE AVERAGE MULTI IV CURVES

This script automatically detects the different bending positions and calculates average IV-curves for each bending step.

```
1 clear all
2 close all
3
4 ordnername = 'Path/To/Folder';
5 %create list of all files in folder
6 liste = dir(ordnername);
7 files = {liste.name};
8
9 %initialize variables
10 c = [];
11 x = [];
12 y = [];
13 z = [];
14 z1 = [];
15 cz = [];
16
17 %loop to read data from all files
18 for i=3:(numel(files));
19     fid = fopen(fullfile(ordnername, files{i}));
20     A2 = textscan(fid,'%f',1,'delimiter','\n');
21     A = textscan(fid,'%f %f','delimiter','tab','headerlines',6);
22     h = A2{1} * ones(length(A{1}),1);
23     y = [y A{1}];
24     x = [x A{2}];
25     z = [z h];
26     z1 = [z1; A2{1}];
27     fclose('all');
28 end
29
30 diffc = transpose(unique(z));
31 xm = [];
32 ym = [];
```

```

33 xym = [];
34 voltage_array = [];
35 current_aray = [];
36 distance_array = [];
37 stdy = [];
38 %loop to calculate average
39 for i = diffc;
40     steplist = find(z(1,:) == i);
41     for i2 = steplist;
42         xm = [xm x(:,i2)];
43         ym = [ym y(:,i2)];
44     end
45     voltage_array = [voltage_array mean(xm,2)];
46     dy = ym;
47     stdy = [stdy transpose(std(transpose(ym)))];
48     current_aray = [current_aray mean(ym,2)];
49     distance_array = [distance_array i * ones(size(voltage_array,1),1)];
50     xm = [];
51     ym = [];
52
53 end
54
55 %plot data
56 name = 'piezobending_multiUI_example';
57 xlimits = [-10 10];
58 ylimits = [0 160];
59 zlimits = [-1 400];
60 xlabel = 'Voltage (V)';
61 ylabel = 'Distance (\mum)';
62 zlabel = 'Current (nA)';
63
64 surface_plot_for_thesis(voltage_array,distance_array,current_aray.*1000000000,
65 xlabel,yaxislabel,zaxislabel,xlimits,ylimits,zlimits)

```

B.2 GET CALIBRATION FACTOR

This script is used to correct the magnetic AC fields when working with the ME setup. A calibration reference is loaded and the correction factor for the desired frequency is determined by interpolation.

```

1 function [ d_interp ] = return_calibrated_ac_field( f_interp )
2     load('calibration_ME_AC_Coil');
3     d_interp = pchip(frequency,calibration_factor,f_interp);

```

```
4 end
```

B.3 PROCESS ME BIAS MAP

This *Matlab* script imports the measured data for a complete bias map. The data is processed and plotted. The Q-factors, positions of the resonance peak, the optimum bias field and SR_{\pm} is calculated.

```

1 clear all
2 close all
3 fclose('all')
4
5 ordnername = 'Folder/T0/analyze';
6 liste = dir(ordnername);
7 dirIndex = [liste.isdir];
8 S = liste(~dirIndex);
9 liste = S;
10
11 S = [liste(:).datenum];
12 [S,S] = sort(S);
13 S = {liste(S).name};
14 files = S;
15
16 datasets = numel(files);
17 Bias_array = zeros(datasets,100);
18 Bias_array(:, :) = NaN;
19 Frequency_array = zeros(datasets,100);
20 R_array = zeros(datasets,100);
21 Amplitude_array = zeros(datasets,100);
22 qfactors = zeros(datasets,1);
23 ResPeak = zeros(datasets,1);
24 Bias = zeros(datasets,1);
25 maxR = zeros(datasets,1);
26
27 %Schleife zum auslesen der einzelnen Messdateien
28 for i=1:(numel(files))
29     [R,Theta,Frequency,Bias_Field,AC_Amplitude] = ME_FS(ordnername, files{i});
30     l = numel(R);
31     Frequency_array(i,1:l) = Frequency;
32     R_array(i,1:l) = R;
33     Bias_array(i,1:l) = Bias_Field;
34     [qfac a1 a2 Res] = qfactor(Frequency, R);
35     qfactors(i) = qfac;

```

```
36     ResPeak(i) = Res;
37     Bias(i) = Bias_Field;
38     maxR(i) = max(R);
39 end
40
41 %Korrektur der Frequenzabhngigkeit des AC Feldes
42 corr_d = return_calibrated_ac_field(Frequency_array);
43 R_array = R_array./corr_d;
44
45 %Abbildung erstellen
46 f=figure
47 a=axes
48 surface(Frequency_array,Bias_array.*1000,R_array.*1000)
49 c=colorbar
50 ylabel(c,'Voltage (mV)')
51 %ylabel(c,'Current (pA)')
52 xlabel(a, 'Frequency (Hz)')
53 ylabel(a, 'Bias Field (mT)')
54
55 %Abbildung der Resonanzpeakposition
56 f = figure
57 plot(Bias,ResPeak)
58 %Abbildung der Maximalwerte
59 f = figure
60 plot(Bias, maxR)
61 %Abbildung der Q-Faktoren
62 f = figure
63 plot(Bias,qfactors)
64
65 %Vergleich der Mittelwerte fr positives und negatives Bias Feld
66 neg_bias = find(Bias < 0);
67 pos_bias = find(Bias > 0);
68 R_per_Bias = mean(transpose(R_array));
69 u = mean(R_per_Bias(neg_bias));
70 o = mean(R_per_Bias(pos_bias));
71 ration_pm = o/u;
```

B.4 GET Q-FACTOR

This script is a further development of an original script written by Patrick Egan (2006). It calculates the Q-factor, the bandwidth and the position of the resonance peak.

```

1 function [qfac, ttrail_x, tlead_x, peak_x] = qfactor(x,y)
2 %
3 % modified Version using a template by written by Patrick Egan (2006)
4 %
5 y = y / max(y);
6 N = length(y);
7 lev50 = 1/(sqrt(2));
8 if y(1) < lev50;           % find index of center (max or min) of pulse
9     [garbage,centerindex]=max(y);
10    Pol = +1;
11 else
12     [garbage,centerindex]=min(y);
13    Pol = -1;
14 end
15 if (centerindex == numel(y))
16    qfac = NaN;
17    ttrail_x = NaN;
18    tlead_x = NaN;
19    peak_x = NaN;
20    return
21 end
22 i = 2;
23 while ((sign(y(i)-lev50) == sign(y(i-1)-lev50)) && (i <= N-1));
24    i = i+1;
25 end                               %first crossing is between v(i-1) & v(i)
26 interp = (lev50-y(i-1)) / (y(i)-y(i-1));
27 tlead_x = x(i-1) + interp*(x(i)-x(i-1));
28 i = centerindex+1; %start search for next crossing at center
29 while ((sign(y(i)-lev50) == sign(y(i-1)-lev50)) && (i <= N-1));
30    i = i+1;
31 end
32 if i ~= N;
33    Ptype = 1;
34    interp = (lev50-y(i-1)) / (y(i)-y(i-1));
35    ttrail_x = x(i-1) + interp*(x(i)-x(i-1));
36    width = ttrail_x - tlead_x;
37 else
38    Ptype = 2;

```

```
39     ttrail_x = NaN;
40     width = NaN;
41 end
42 qfac = x(centerindex)/width;
43 peak_x = x(centerindex);
```

B.5 CALCULATE AVERAGE CHARGE PEAK AREA

This *Matlab* script imports the data from a charge measurement. The number and positions of the bending steps are automatically detected. In a further processing every step is averaged individually.

```
1 close all
2 clear all
3
4 fid = fopen('Path/To/File');
5 A = textscan(fid,'%f %f %f','delimiter','tab','headerlines',6);
6
7 % inc beschreibt den aktuellen Schritt
8 inc=[[A{2};0]-[0;A{2}]];
9 % uniA listet die gemessenen Stufen auf
10 uniA = unique(A{2});
11 %completedataset = [];
12 % ff liste auf in welchen Zeilen die Daten zu einer spezifischen Stufe
13 % stehen.
14 number_of_steps = numel(find(inc ~= 0));
15 number_of_measurement_points = numel(A{1});
16 %Mittlere Anzahl der Messpunkte pro Stufe berechnen. 90% davon als
17 %steplength definieren.
18 stepwidth = round((number_of_measurement_points*0.9)/number_of_steps);
19 %steplength ist die Zeitspanne einer tufe
20 steplength = floor(max(A{1})/number_of_steps)-1;
21
22 charge=[];
23 maxpeak = [];
24 maxpeakerr = [];
25
26 %integrations Zeitintervall
27 t_int = 0.5;
28 %Zeitintervall fr EXP fit
29 t_exp = 0.5;
30 area1 = [];
31 area2 = [];
```

```

32
33 for i4=2:numel(uniA);
34     ff = find(A{2} == uniA(i4));
35     newA = [A{1}(ff) A{2}(ff) A{3}(ff) inc(ff)];
36     findstep = find(newA(:,4) > 0);
37     completecharge = [];
38     completetime = [];
39     for i=2:(numel(findstep)-1);
40         onetimesection = newA(findstep(i):findstep(i)+stepwidth,1);
41         if max(onetimesection)-min(onetimesection) <= 30
42             charge = transpose(newA(findstep(i):findstep(i)+stepwidth,3));
43             completecharge = [completecharge charge];
44             time = transpose(onetimesection-(min(onetimesection)));
45             completetime = [completetime time];
46         end
47     end
48     meancharge = [];
49     meantime = [];
50     for i6=0:t_int:steplength
51         %Datenpunkte finden die in dem Intervall liegen
52         block = find(completetime >= i6 & completetime <= i6 + t_int);
53         %Kein Datenpaar erstellen, falls block keine Elemente enthlit
54         if ~isempty(block);
55             meancharge = [meancharge mean(completecharge(block))];
56             meantime = [meantime i6];
57         end
58     end
59     midcounter = round(numel(meancharge)/2);
60     offset = mean(meancharge(midcounter:end-1));
61     meancharge = meancharge - offset;
62
63     %area1 = [area1 sum(meancharge)*t_int];
64     area1 = [area1 min(meancharge)];
65
66
67 end
68
69
70 for i4=1:numel(uniA)-1;
71     ff = find(A{2} == uniA(i4));
72     newA = [A{1}(ff) A{2}(ff) A{3}(ff) inc(ff)];
73     findstep = find(newA(:,4) < 0);
74     completecharge = [];

```



```

75   completetime = [];
76   for i=2:(numel(findstep)-1);
77       onetimesection = newA(findstep(i):findstep(i)+stepwidth,1);
78       if max(onetimesection)-min(onetimesection) <= 30
79           charge = transpose(newA(findstep(i):findstep(i)+stepwidth,3));
80           completecharge = [completecharge charge];
81           time = transpose(onetimesection-(min(onetimesection)));
82           completetime = [completetime time];
83       end
84   end
85   meancharge = [];
86   meantime = [];
87   for i6=0:t_int:steplength
88       %Datenpunkte finden die in dem Intervall liegen
89       block = find(completetime >= i6 & completetime <= i6 + t_int);
90       %Kein Datenpaar erstellen, falls block keine Elemente enthlt
91       if ~isempty(block);
92           meancharge = [meancharge mean(completecharge(block))];
93           meantime = [meantime i6];
94       end
95   end
96   midcounter = round(numel(meancharge)/2);
97   offset = mean(meancharge(midcounter:end-1));
98   meancharge = meancharge - offset;
99
100  %area2 = [area2 sum(meancharge)*t_int];
101  area2 = [area2 max(meancharge)];
102 end
103
104 createfiguretest(transpose(uniA(2:end))-max(inc),
105 area1,transpose(uniA(1:end-1)),area2)

```

B.6 CALCULATE TIME CONSTANTS

This script can calculate the individual time constants for the charge measurements. The averaged data sets for every bending step are fitted by an exponential decay function.

```

1  fid = fopen('PATH/TO/FILE');
2  A = textscan(fid,'%f %f %f','delimiter','tab','headerlines',6);
3
4  % inc beschreibt den aktuellen Schritt
5  inc=[[A{2};0]-[0;A{2}]];
6  % uniA listet die gemessenen Stufen auf

```

```

7 uniA = unique(A{2});
8 %completedataset = [];
9 % ff liste auf in welchen Zeilen die Daten zu einer spezifischen Stufe
10 % stehen.
11 number_of_steps = numel(find(inc ~= 0));
12 number_of_measurement_points = numel(A{1});
13 %Mittlere Anzahl der Messpunkte pro Stufe berechnen. 90% davon als
14 %steplength definieren.
15 stepwidth = round((number_of_measurement_points*0.9)/number_of_steps);
16 %steplength ist die Zeitspanne einer tufe
17 steplength = floor(max(A{1})/number_of_steps)-1;
18
19 charge=[];
20 maxpeak = [];
21 maxpeakerr = [];
22
23 %integrations Zeitintervall
24 t_int = 0.01;
25 %Zeitintervall fr EXP fit
26 t_exp = 1;
27
28 for i4=1:numel(uniA);
29     ff = find(A{2} == uniA(i4));
30     newA = [A{1}(ff) A{2}(ff) A{3}(ff) inc(ff)];
31     findstep = find(newA(:,4) > 0);
32     completecharge = [];
33     completetime = [];
34     for i=2:(numel(findstep)-1);
35         onetimesection = newA(findstep(i):findstep(i)+stepwidth,1);
36         if max(onetimesection)-min(onetimesection) <= 30
37             charge = transpose(newA(findstep(i):findstep(i)+stepwidth,3));
38             completecharge = [completecharge charge];
39             time = transpose(onetimesection-(min(onetimesection)));
40             completetime = [completetime time];
41         end
42     end
43     meancharge = [];
44     meantime = [];
45     for i6=0:t_int:steplength
46         %Datenpunkte finden die in dem Intervall liegen
47         block = find(completetime >= i6 & completetime <= i6 + t_int);
48         %Kein Datenpaar erstellen, falls block keine Elemente enthlt
49         if ~isempty(block);

```

```

50         meancharge = [meancharge mean(completecharge(block))];
51         meantime = [meantime i6];
52     end
53 end
54 midcounter = round(numel(meancharge)/4);
55 offset = mean(meancharge(midcounter:end-1));
56 meancharge = meancharge - offset;
57 if mean(meancharge) < 0
58     x = -1;
59 else
60     x = 1;
61 end
62 fitregion = find(meantime < t_exp);
63 if ~isempty(fitregion)
64     p = polyfit(meantime(fitregion),log(abs(meancharge(fitregion))),1);
65     rsq = rsq_for_linfit(meantime(fitregion),log(x*(meancharge(fitregion))));
66     maxpeak = [maxpeak -1/p(1)];
67     %maxpeakerr = [maxpeakerr (1-rsq)];
68 else
69     maxpeak = [maxpeak NaN];
70     %maxpeakerr = [maxpeakerr NaN];
71 end
72 end
73 end
74
75 minpeak = [];
76
77 for i4=1:numel(uniA);
78     ff = find(A{2} == uniA(i4));
79     newA = [A{1}(ff) A{2}(ff) A{3}(ff) inc(ff)];
80     findstep = find(newA(:,4) < 0);
81     completecharge = [];
82     completetime = [];
83     for i=2:(numel(findstep)-1);
84         onetimesection = newA(findstep(i):findstep(i)+stepwidth,1);
85         if max(onetimesection)-min(onetimesection) <= 30
86             charge = transpose(newA(findstep(i):findstep(i)+stepwidth,3));
87             completecharge = [completecharge charge];
88             time = transpose(onetimesection-(min(onetimesection)));
89             completetime = [completetime time];
90         end
91     end
92     meancharge = [];

```

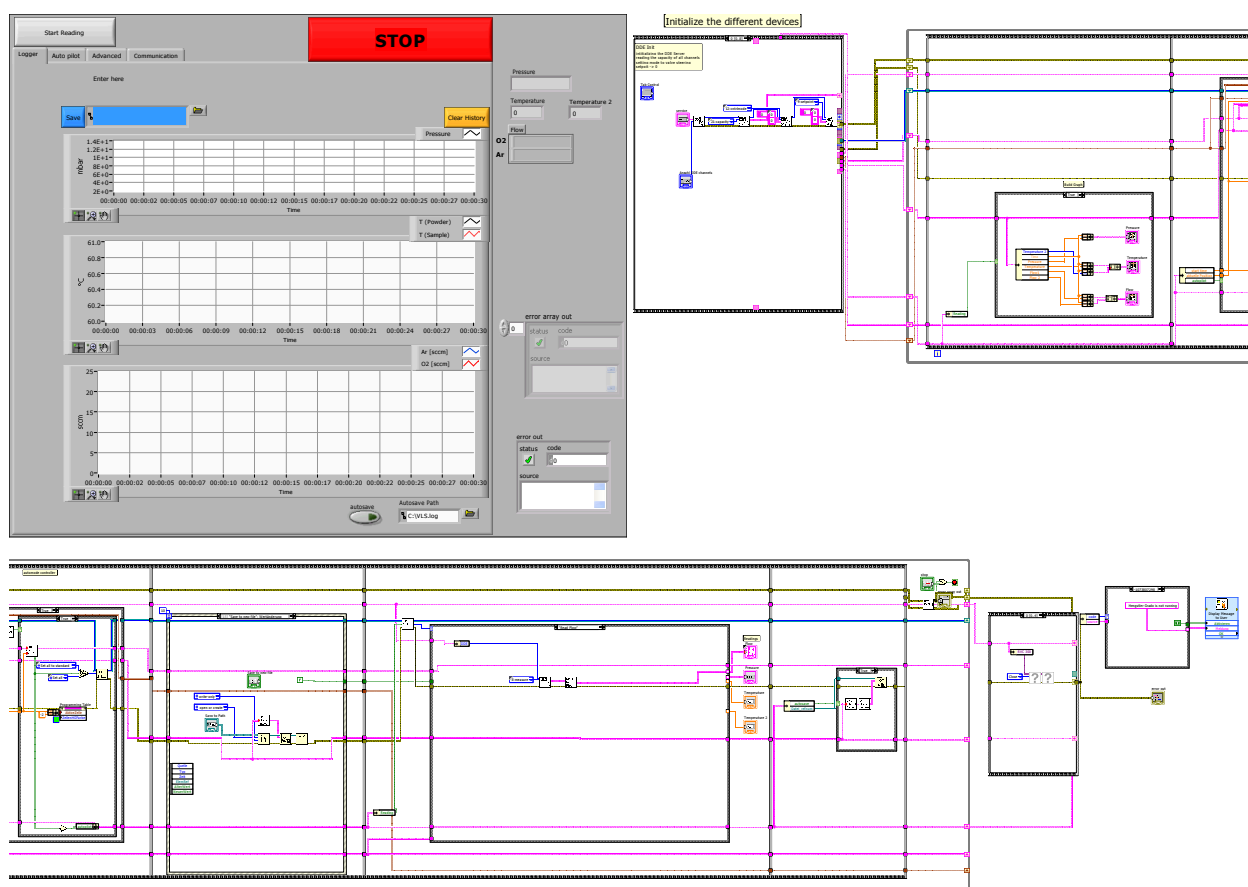
```
93 meantime = [];  
94 for i6=0:t_int:steplength  
95     %Datenpunkte finden die in dem Intervall liegen  
96     block = find(completetime >= i6 & completetime <= i6 + t_int);  
97     %Kein Datenpaar erstellen, falls block keine Elemente enthl  
98     if ~isempty(block);  
99         meancharge = [meancharge mean(completecharge(block))];  
100        meantime = [meantime i6];  
101    end  
102 end  
103 midcounter = round(numel(meancharge)/4);  
104 offset = mean(meancharge(midcounter:end-1));  
105 meancharge = meancharge - offset;  
106 if mean(meancharge) < 0  
107     x = -1;  
108 else  
109     x = 1;  
110 end  
111 fitregion = find(meantime < t_exp);  
112 if ~isempty(fitregion)  
113     [p,S] = polyfit(meantime(fitregion),log(abs(meancharge(fitregion))),1);  
114     %rsq = rsq_for_linfit(meantime(fitregion),log(x*(meancharge(fitregion))));  
115     [y,err] = polyval(p,meantime(fitregion),S);  
116     minpeak = [minpeak -1/p(1)];  
117     maxpeakerr = [maxpeakerr mean(err)];  
118 else  
119     minpeak = [minpeak NaN];  
120     maxpeakerr = [maxpeakerr NaN];  
121 end  
122  
123 end
```

C LABVIEW

On the following pages the *Labview* programs are shown which were developed to control different setups. Due to the high complexity of the programs only overviews of the *Front-panel* and *Backpanel* are depicted. The principle of each program is briefly mentioned. All programs were developed from scratch. Software libraries for the individual devices used were available. The creation/modification of the device libraries was usually the first part when realizing a new setup. All programs have in common that the measurement data are automatically exported in ASCII compatible files to allow a further processing, e.g., with *Matlab*.

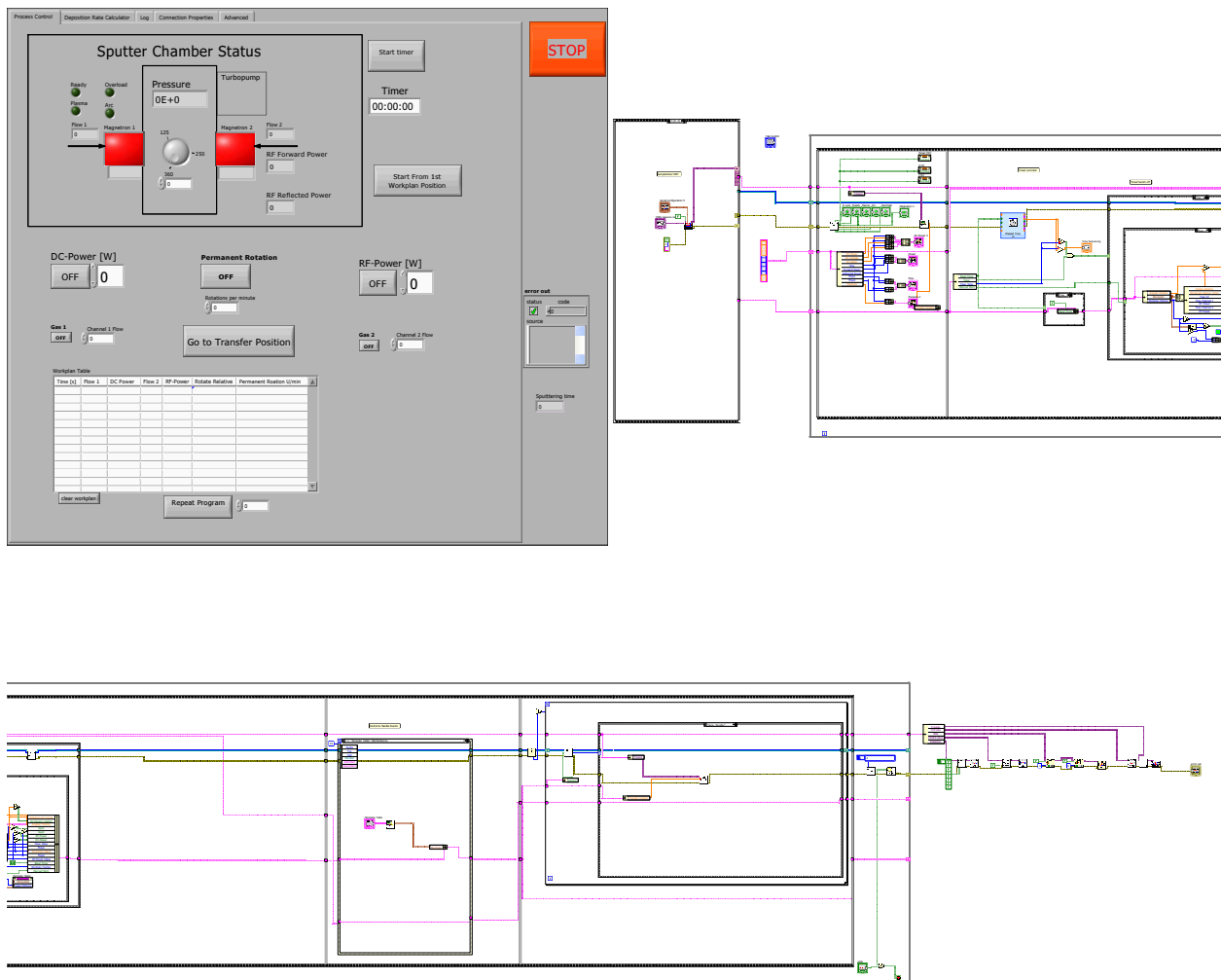
C.1 VAPOR LIQUID SOLID

This software was designed to generate a controlled atmosphere and allow the definition of temperature, pressure and gas flow of 2 gases independently, inside a quartz tube. Each parameter is controlled by a PID. The software allows the creation of a work plan which represents a list of parameter sets. The validity of the recent parameter set is automated by using break criteria. This allows automatic processes which are required e.g., for the use of the setup for a synthesis. The work plans can be saved and loaded. The logged data (time, temperature, pressure, gas flows) is written to a file to guarantee a high traceability of the synthesis.



C.2 SPUTTER CONTROL

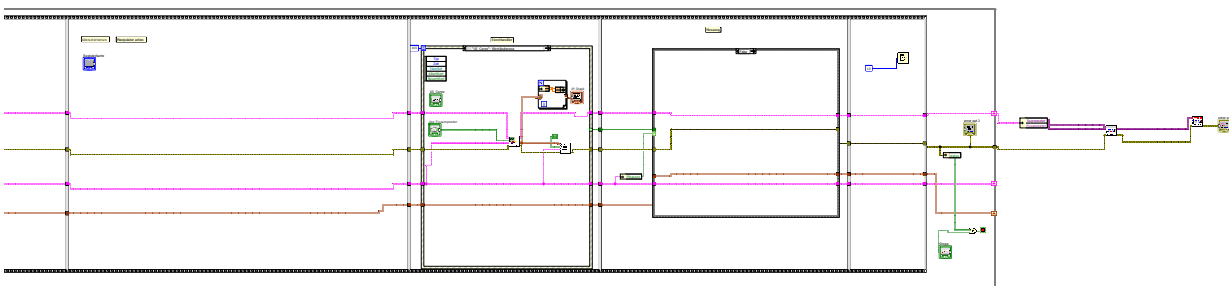
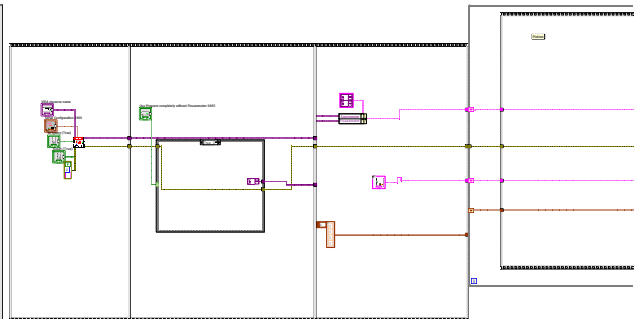
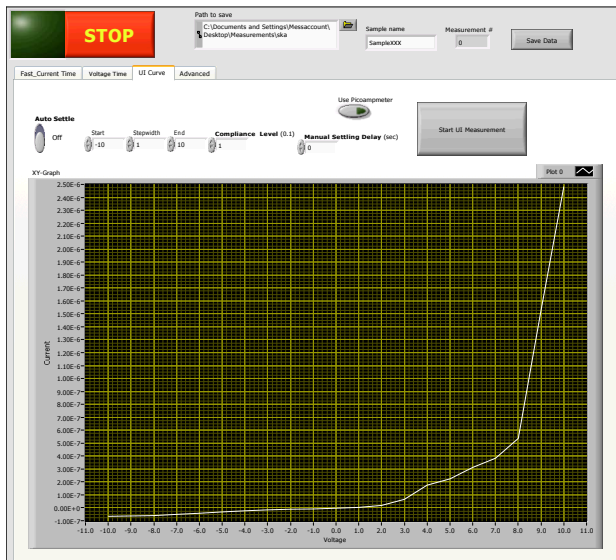
This software was designed to control the sputter deposition setup as described in *chapter 6*. The main window in the program depicts the status of the system showing pressure, gas flows, sample position and magnetron details. The software allows a manual operation mode to directly transfer parameters to the individual components and an automatic workplan mode which is capable of performing sophisticated sputtering routines. The implemented functions are: control of sample rotation, control of sample orientation, gas flow management, magnetron power management, pressure sensing and multilayer sputtering. The logging of the available data allows a good tracking of the process which is required e.g., if sputtering over night. Usually the program runs non-stop on the sputter deposition system for several months.



C.3 COMPLETE IV

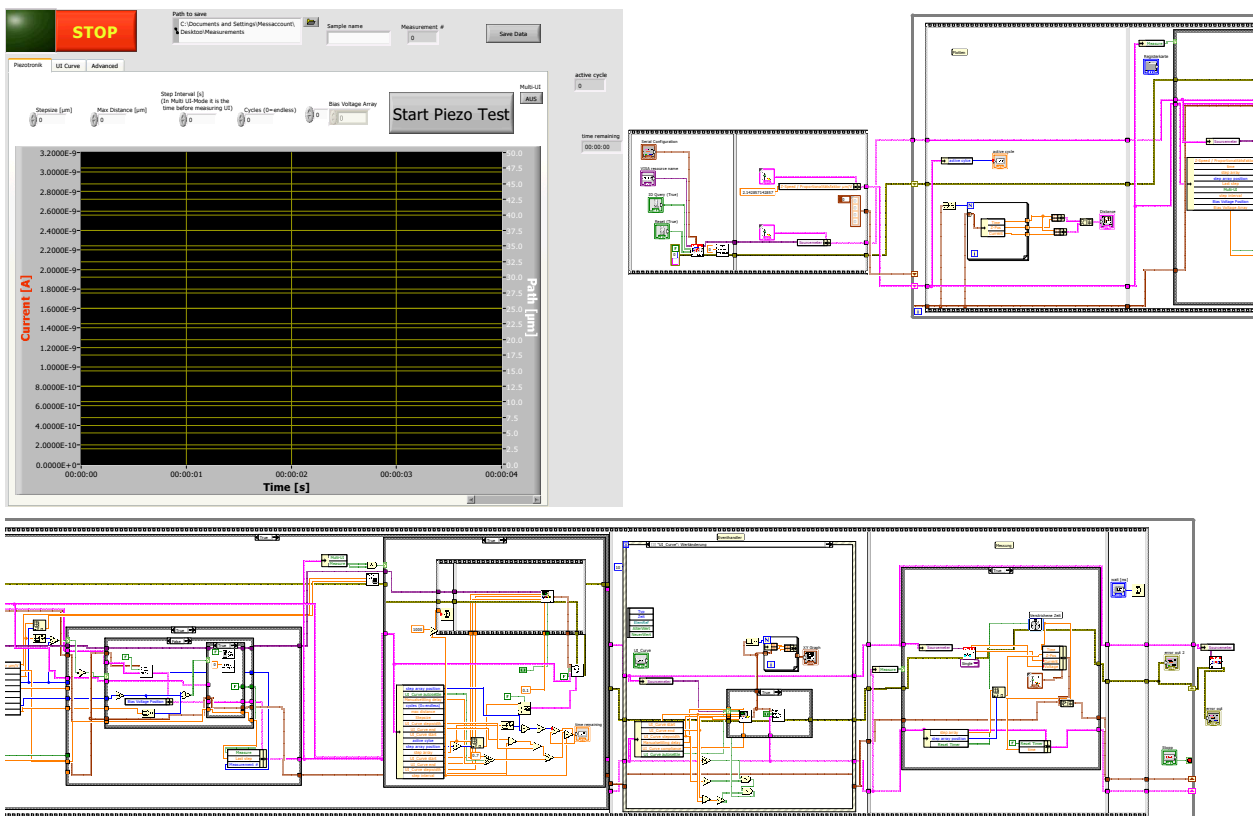
This software is used to investigate the IV-characteristics of any sample. The *Keithley Sourcemeter 2400* is used as a combined current/voltage source/measurement device. Optionally a *Keithley Picoammeter 6485* can be used for a higher precision. Possible measurement modes are:

- IV-curves
- current vs. time for a fixed voltage
- voltage vs. time for a fixed current



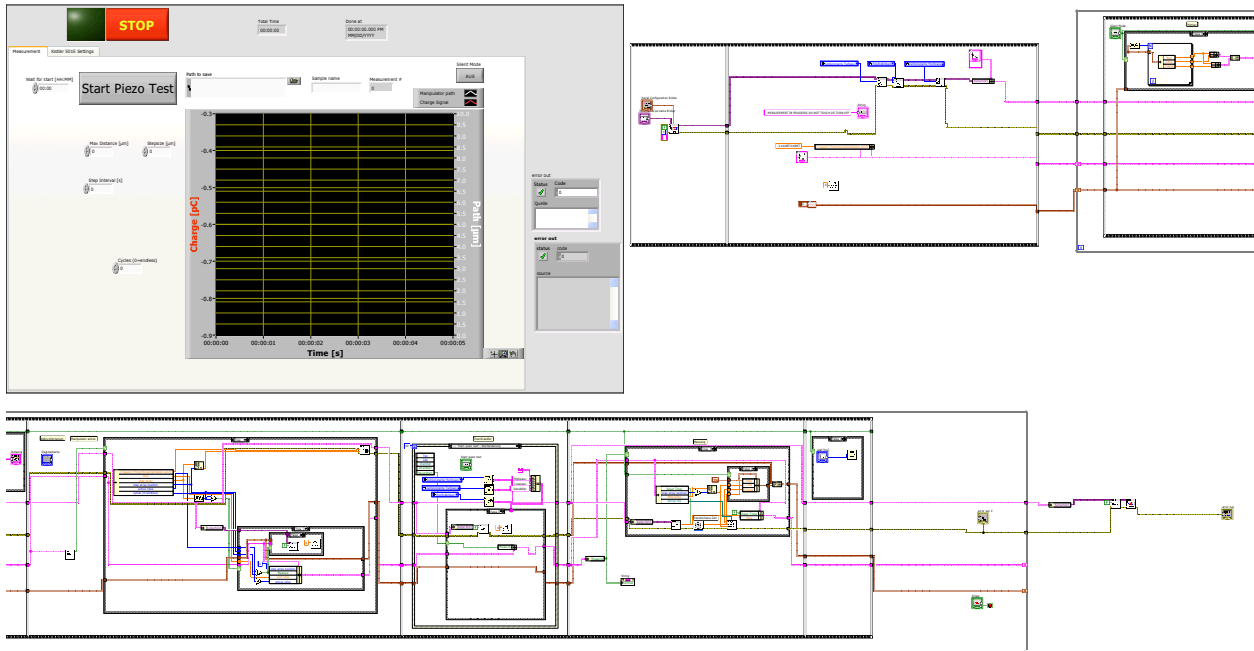
C.4 COMPLETE PIEZOTEST MULTIRUN MULTIBIAS

This software is used for measurements with the piezoelectric bending test setup introduced in *chapter 9.2.1*. The system uses a *Keithley Sourcemeter 2400* which can act as a current/voltage source and simultaneously measure. The sample is bent by a commercial piezoelectric actuator controlled with a A/D converter *Meilhaus Redlab*. The program offers the ability to define the step size, the total step distance, the interval between the steps, and the number of total cycles. A bias voltage array may be defined which allows the measurement of the sensor current response for different applied bias voltages. Additionally it is possible to measure IV curves at any moment during the measurement and by choosing *multi-UI* an IV measurement is automatically performed after every movement step. The parameters of each IV measurement can be defined in the tab *UI Curve*. The measured data is automatically saved in the defined file which will be numbered consecutively in case of repeated measurements. The resulting file contains all measurement parameters together with the measured data and can be further investigated using Matlab.



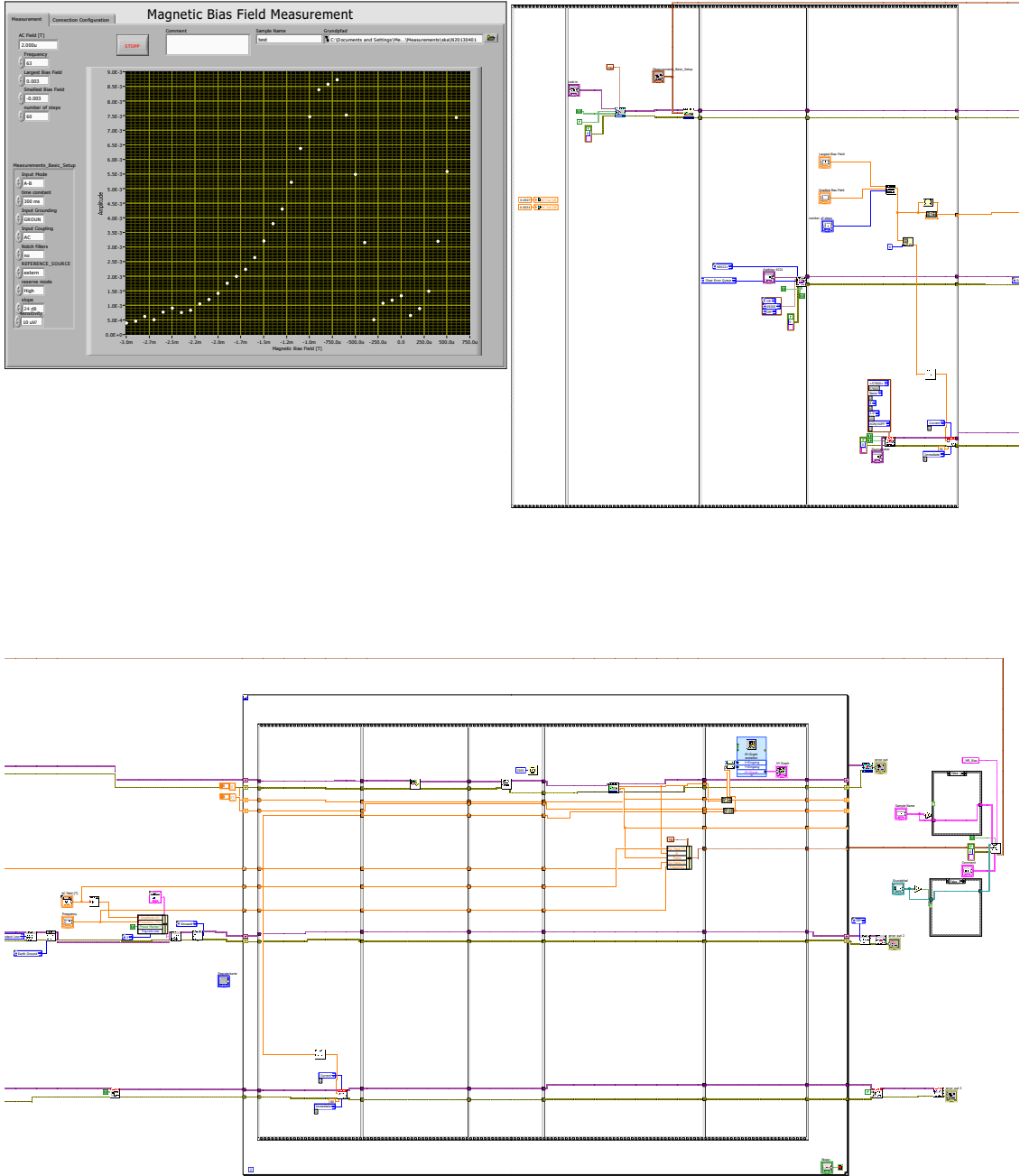
C.5 COMPLETE PIEZOTEST CHARGE

This program is similar to *Complete Piezotest Multirun Multibias* but can measure the charge response of a sample using the *Kistler 5015A* charge meter.



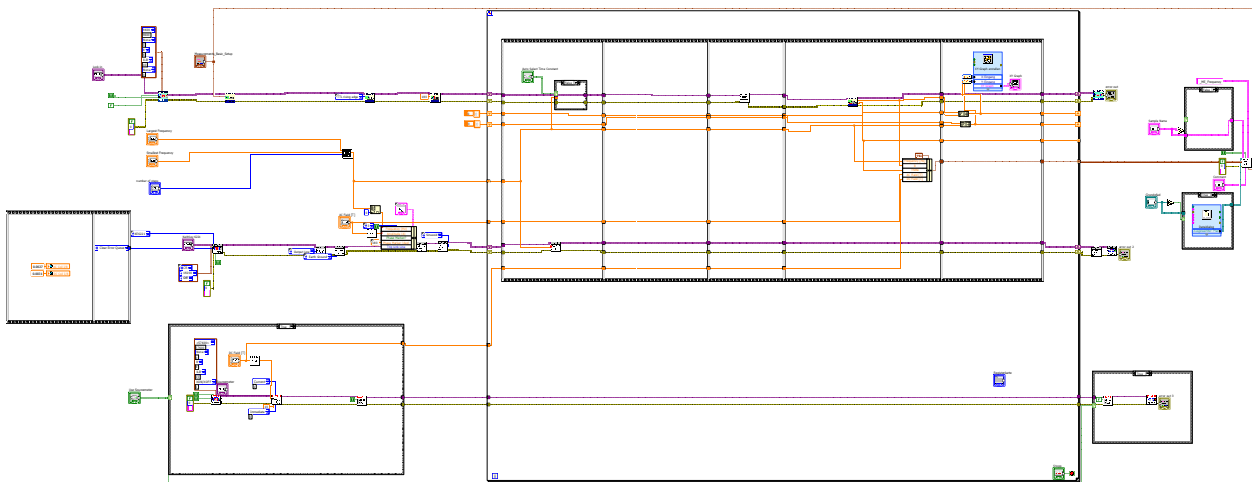
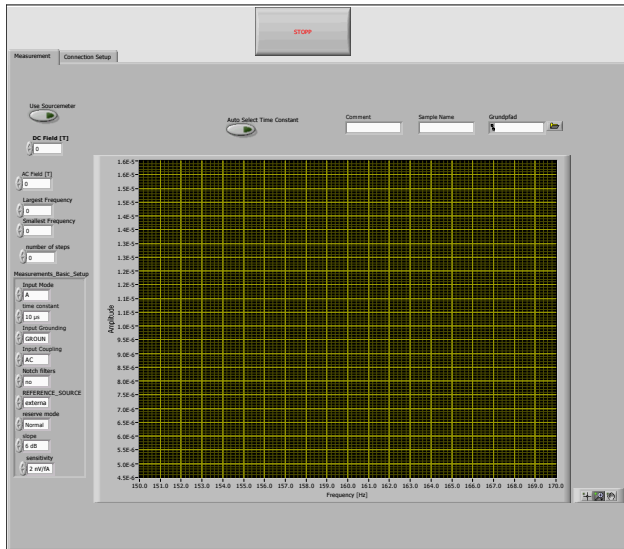
C.6 BIAS MEASUREMENT

This program measures the response of a ME sensor to a magnetic AC field at different bias fields. This allows the detection of the optimum bias for the selected frequency.



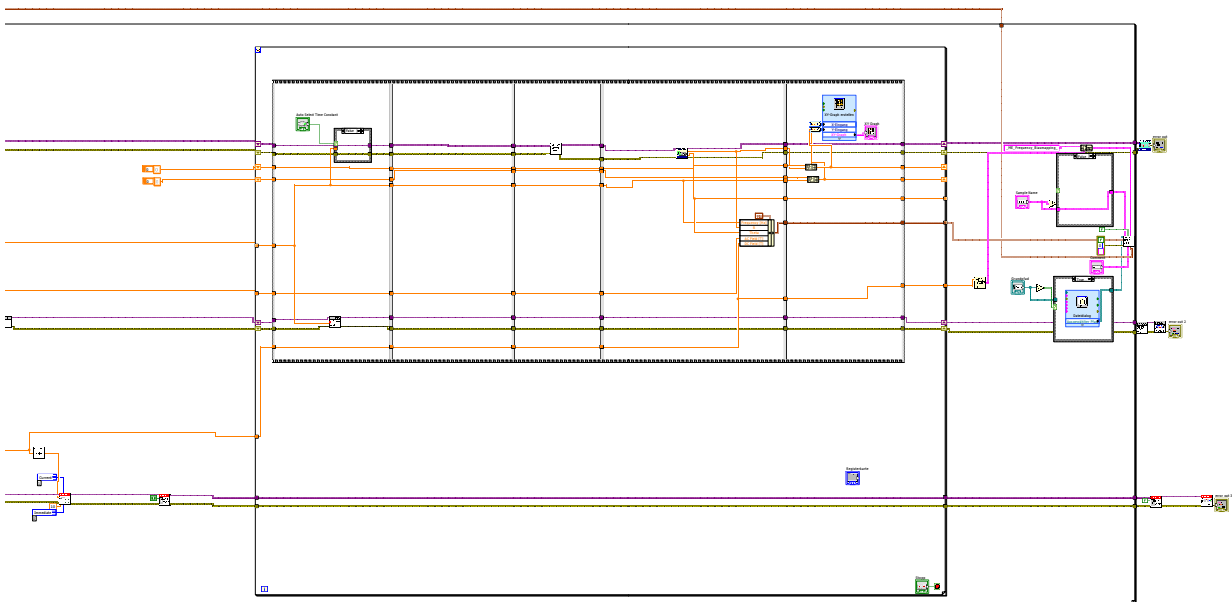
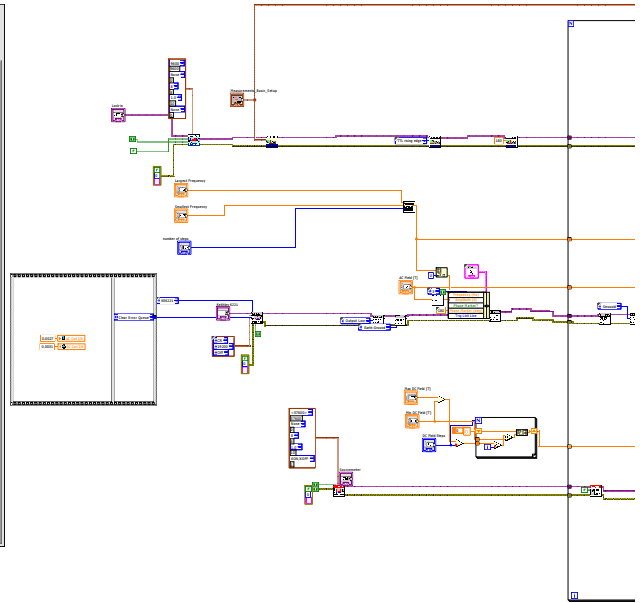
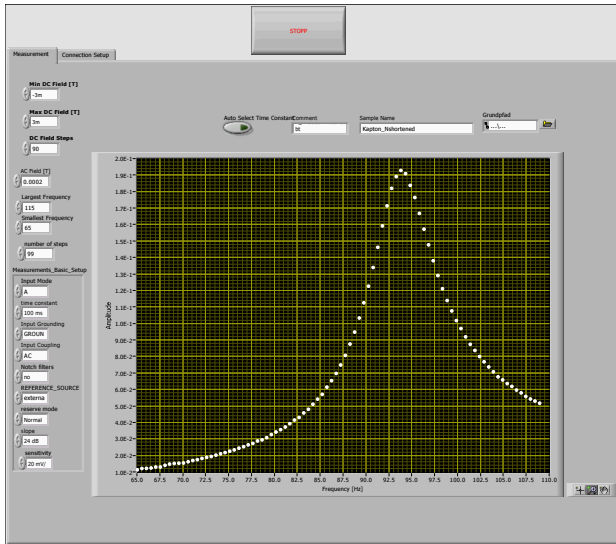
C.7 FREQUENCY SCAN

This program measures the response of a ME sensor for a varying AC frequency. This allows the detection of any resonances of the ME sensor.



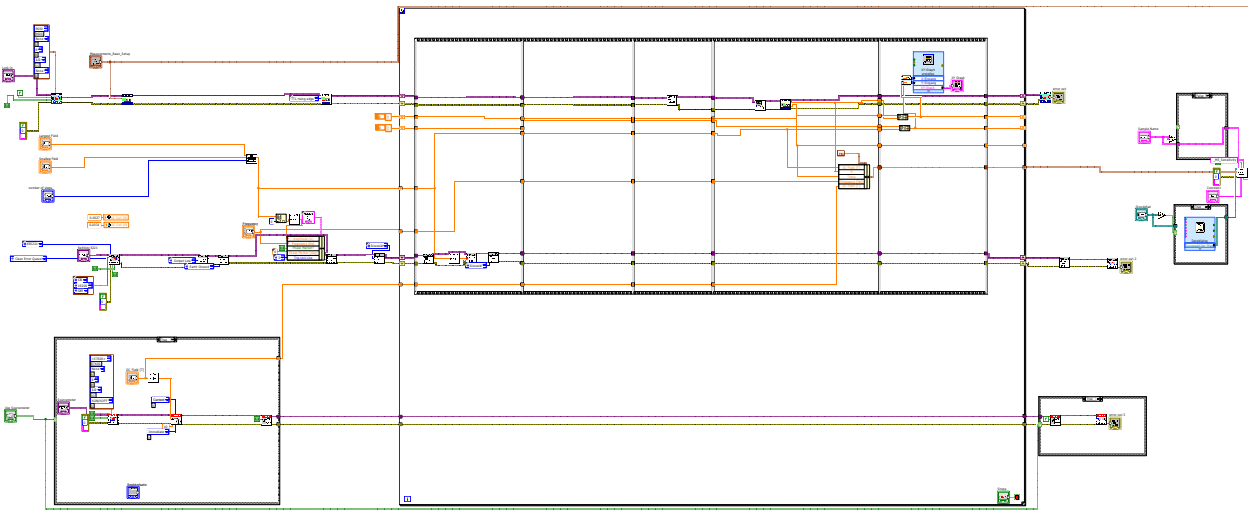
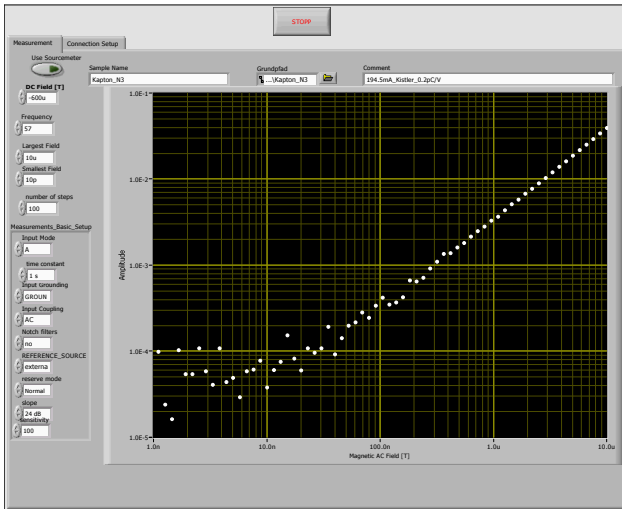
C.8 ME BIASMAPPING

This Labview software is the combination of the *Bias Measurement* and the *Frequency Scan*. For every magnetic bias field a complete frequency sweep is performed. This allows the location of the optimum bias/frequency combination.



C.9 ME SENSOR LINEARITY

This software is used to determine the linearity of a ME sensor. The response of the sensor to magnetic AC fields with different magnitudes is recorded.



D WATER JET REFLECTION EQUATIONS

Mathematics I: Cassie Baxter Young's Equation with solid-liquid interfacial energy γ_{SL} , solid-gas interfacial energy γ_{SG} and liquid-gas interfacial energy γ_{LG} :

$$\cos(\Theta_Y) = \frac{\gamma_{SG} - \gamma_{SL}}{\gamma_{LG}} \quad (\text{D.1})$$

Cassie Baxter Equation with wetted fraction f and roughness r

$$\cos(\Theta_{CB}) = rf\cos(\Theta_Y) + f - 1 \quad (\text{D.2})$$

Cassie Baxter Equation after inserting Youngs equation

$$\cos(\Theta_{CB}) = rf\frac{\gamma_{SG} - \gamma_{SL}}{\gamma_{LG}} + f - 1 \quad (\text{D.3})$$

Mathematics II: Energy before impact Surface energy of a jet with surface area A_0

$$E_{S0} = A_0\gamma_{LG} \quad (\text{D.4})$$

Surface area for circular jet with diameter d and length Δl

$$A_0 = \pi d\Delta l \quad (\text{D.5})$$

$$E_{S0} = \pi d\Delta l\gamma_{LG} \quad (\text{D.6})$$

Kinetic energy of a jet with a mass m moving with velocity v

$$E_{K0} = \frac{1}{2}mv^2 \quad (\text{D.7})$$

Mass of a jet with volume V and density ρ

$$m = \rho V \quad (\text{D.8})$$

Volume of a jet with a circular cross section, diameter d and length Δl

$$V = \pi \left(\frac{d}{2}\right)^2 \Delta l \quad (\text{D.9})$$

$$E_{K0} = \frac{1}{8}\rho\pi d^2\Delta l v^2 \quad (\text{D.10})$$

Total energy before impact E_0

$$E_0 = E_{S0} + E_{K0} \quad (\text{D.11})$$

$$\frac{E_0}{\Delta l} = \frac{1}{8}\rho\pi d^2 v^2 + \gamma_{LG}\pi d \quad (\text{D.12})$$

Mathematics III: Energy at broadest point Energy at the broadest point E_b per unit length Δl depends on the areas of the individual interfaces

$$\frac{E_b}{\Delta l} = dA_{SL}\gamma_{SL} + dA_{LG}\gamma_{LG} + dA_{SG}\gamma_{SG} \quad (\text{D.13})$$

Following standard Cassie-Baxter theory:

$$dA_{SL} = brf \quad (\text{D.14})$$

$$dA_{SG} = -brf \quad (\text{D.15})$$

Liquid-Gas interface can be written as having a overall roughness R_{LG}

$$dA_{LG} = bR_{LG} \quad (\text{D.16})$$

Inserting in equation D.13 yields

$$\frac{E_b}{\Delta l} = brf\gamma_{SL} + bR_{LG}\gamma_{LG} - brf\gamma_{SG} \quad (\text{D.17})$$

$$\frac{E_b}{\Delta l} = b(rf(\gamma_{SL} - \gamma_{SG}) + R_{LG}\gamma_{LG}) \quad (\text{D.18})$$

Mathematics IV: Water jet spreading By applying $E_0 = E_b$:

$$b(rf(\gamma_{SL} - \gamma_{SG}) + R_{LG}\gamma_{LG}) = \frac{1}{8}\rho\pi d^2 v^2 + \gamma_{LG}\pi d \quad (D.19)$$

$$rf(\gamma_{SL} - \gamma_{SG}) + R_{LG}\gamma_{LG} = \frac{1}{b} \left(\frac{1}{8}\rho\pi d^2 v^2 + \gamma_{LG}\pi d \right) \quad (D.20)$$

$$rf(\gamma_{SG} - \gamma_{SL}) - R_{LG}\gamma_{LG} = -\frac{1}{b} \left(\frac{1}{8}\rho\pi d^2 v^2 + \gamma_{LG}\pi d \right) \quad (D.21)$$

$$rf \frac{\gamma_{SG} - \gamma_{SL}}{\gamma_{LG}} - R_{LG} = -\frac{1}{b\gamma_{LG}} \left(\frac{1}{8}\rho\pi d^2 v^2 + \gamma_{LG}\pi d \right) \quad (D.22)$$

$$\underbrace{rf \frac{\gamma_{SG} - \gamma_{SL}}{\gamma_{LG}} + f - 1 - f + 1 - R_{LG}}_{\cos(\Theta_{CB})} = -\frac{1}{b\gamma_{LG}} \left(\frac{1}{8}\rho\pi d^2 v^2 + \gamma_{LG}\pi d \right) \quad (D.23)$$

$$\cos(\Theta_{CB}) - f + 1 - R_{LG} = -\frac{1}{b\gamma_{LG}} \left(\frac{1}{8}\rho\pi d^2 v^2 + \gamma_{LG}\pi d \right) \quad (D.24)$$

The wetted fraction can be expressed as:

$$f = \cos(\Theta_{CB}) + 1 - R_{LG} + \frac{\pi d}{b} \left(\frac{1}{8\gamma_{LG}} \rho d v_{\perp}^2 + 1 \right) \quad (D.25)$$

Accordingly the maximum width is:

$$b = \pi d \frac{1/(8\gamma_{LG})d\rho v_{\perp}^2 + 1}{\cos(\Theta_{CB}) - f + 1 - R_{LG}} \quad (D.26)$$

The used values for the calculation were taken from literature or directly determined by the used setup:

$$d = 600 \mu m \quad (D.27)$$

$$\rho = 1000 \text{ kg/m}^3 \quad (D.28)$$

$$\gamma_{LG} = 72.75 \cdot 10^{-3} \text{ N/m} \quad (D.29)$$

ACKNOWLEDGMENT

This work was only possible because of the support of many colleagues and friends. I would like to use the following paragraphs to thank all these people for their contribution.

I want to thank Prof. Dr. Rainer Adelung for his support and leadership in the past years and especially for giving me the opportunity to work in his group. He suggested me to become a Ph.D. student and his imaginative concepts and ideas became part of my daily life. Besides his scientific guidance he also impressed me with his kind leadership which allowed me pursue my research.

M.Sc. Arnim Schuchardt was my daily source of knowledge who was always open for any kinds of scientific discussion. His open mind strongly influenced me and working on any kind of problem with him was pure joy.

Cai Müller was hired as a supporting student for lab work. It turned out that his skills and knowledge were far beyond my expectations so that his ideas and scientific arguments became a strong influence.

I thank Dr. Ulrich Schürmann for his experienced help and especially for his fruitful comments when creating this thesis. His friendship and the daily trips to Gaarden were important and cheered me up when frustrated.

I want to thank Dr. Yogendra Kumar Mishra for his scientific support and his friendship in the past years. His experience in the scientific business was very helpful and his altruistic way of life was inspiring.

When supervising M.Sc. Jorit Gröttrup in his bachelor thesis I immediately realized his excellent skills and was lucky to recruit him afterwards. His conscientious work and his excellent theoretical knowledge were a big support.

Many thanks to Dr. Jürgen Carstensen for his support and his expertise in semiconductor physics.

I want to thank Petra Bröckers for her help and comments when writing this thesis.

Discussions with Dr. Xin Jin were a pleasure and her scientific and mental support was often putting a smile on my face.

I want to thank Prof. Dr. Franz Faupel for creating perfect initial conditions. Especially in the first years his technical equipment and his labs were the center of my daily life and I could not have started without his support.

I want to thank Prof. Dr. Klaus Rätzke for his help and support in the past years. The knowledge gain during disputation trials was immense due to his assistance.

Dipl.-Ing. Stefan Rehders was a help whenever technical problems occurred. His comments and skills improved my technical comprehension.

Christoph Ochmann helped me to understand the details of machining and discussions with him were always fruitful since he was able to enlighten me with his knowledge of technical facts.

Dipl.-Ing. Rainer Kloth introduced me to the world of computer administration and linux server systems. This strongly improved my ken and changed my way of looking at many things.

I want to thank the current and past members of *Functional Nanomaterials* Dipl.-Geol. Beate Minten, Dipl.-Wi.-Ing. Mathias Hoppe, Dr. Martina Baum, Dr. Dawit Gedamu, M.Sc. Ingo Paulowicz, M.Sc. Iris Hölken, M.Sc. Sandra Nöhren, M.Sc. Victor Kaidas, M.Sc. Fabian Schütt, M.Sc. Daria Smazna, M.Sc. Stefan Freitag, Stefan Schröder, Robert Keitel and Dr. Sebastian Wille for their support and for making every day at TF enjoyable.

Many thanks to my collaboration partners in the SFB 855 Dr. Björn Gojdka, Dipl.-Ing. Kerstin Meurisch, Dr. Iulian Teliban, Dipl.-Phys. Stjepan Hrkac, Dr. Viktor Hrkac, Dipl.-Phys. Sebastian Zabel and Dr. Enno Lage for their support.

I would also like to thank Dr. Stephan Rautenberg, Dr. Christina Pakula, Dr. Tilo Peter, M.Sc. Christian Ohrt, Dipl.-Phys. Claas Thede, Berndt Neumann and the complete staff in the TF workshop for their help.

The support of my family was very important and helpful. Special thanks to Jasmin & Jesper for reminding me of the most important thing in life, love.